

# Materials and Nanomaterials with Stimuli-Responsive Behaviour Based on the Flexibility of the Copper-Halide Chain



by  
Javier Conesa Egea

Supervised by  
Dr. Félix Zamora Abanades      Dr. Pilar Amo Ochoa

This dissertation has been submitted to  
Departamento de Química Inorgánica  
Facultad de Ciencias  
Universidad Autónoma de Madrid  
in fulfillment of the degree of Doctorate in Condensed Matter  
Physics, Nanoscience and Biophysics

Madrid, 2019

## Acknowledgments

The process of writing a PhD Thesis is not an easy one. Or, at least, it is not an easy process for a single person. For this reason, I would like to thank all the people who stood behind me, supporting me.

First of all, I would like to thank my parents and my sister M<sup>a</sup> Eugenia for giving me all the support a family can give over the years. For every recommendation, for every time you have been there when I was going through a hard situation, thank you. Thanks to my aunt and my grandmother, whose love knows no limit. And thanks to my girlfriend Marina, not only for her unconditioned love but also for giving me advice to improve figures in an artistic way.

To my supervisors, Dr. Pilar Amo Ochoa and Dr. Félix Zamora Abanades, I owe you every second you have spent to help me write and finish this thesis. Thank you Dr. Pilar Amo for every idea, for every piece of advice you have given me all along these four years to help me define the direction of my research. Thanks to both Dr. Pilar Amo and Dr. Félix Zamora for teaching me how to improve every detail when writing papers and this dissertation, and for helping me hone my skills in making figures for them.

To my lab mates and friends that have accompanied me along this road: Dr. Javier Troyano and Dr. Khaled Hassanein, who no longer belong to the Nanomaterials Lab, your work here was an inspiration for my own. To Dr. Carmen Montoro, Dr. Ana Platero, Dr. Celia Castillo, Dr. Marina Arrieta, Dr. David Rodríguez, Dr. Pablo Albacete, Dr. Carlos Gibaja, Verónica García, Íñigo Torres, Jesús Ángel Martín, Ignacio Romero and Jesús López, for our discussions in the lab or in the office, and for the times to dissipate stress. I would also like to thank the young students who temporarily became part of this family which is our research group: Jessica Gallardo, Carlos Redondo, Marta Saldaña, Noemí Nogal, Alberto Moreno and Pablo Parra.

To all the people who have contributed to the realization of our research and, therefore, to achieve the goal of finishing this thesis: thanks to Dr. Josefina Perles and Dr. Mario Ramírez from the Inter-Department Research Service (SIdI) of the UAM and Dr. Óscar Castillo from Universidad del País Vasco for their invaluable knowledge on X-ray diffraction and for the resolution of the crystal structures of my compounds. To Isidoro Poveda and Esperanza Salvador, for our times in front of the Scanning Electron Microscope taking images of my nanomaterials and discussing what we saw in them. Thanks to Dr. J. Ignacio Martínez, from Materials Science Institute of Madrid (ICMM), for the theoretical calculations that allowed us to justify the properties of our compounds. To Dr. Concepción Gimeno and Dr. Vanesa Fernández, from Universidad de Zaragoza, for their measurements of the thermoluminescent behavior of my samples, and to Prof. Salomé Delgado from Universidad Autónoma de Madrid for her interpretation of these results. To Prof. Carlos Gómez, from Universidad de Valencia, for his measurements of the electrical conductivity of my compounds with variable temperature, and to Prof. Pilar Ocón from Universidad Autónoma de Madrid for her

measurements of their electrical response upon exposure to gases. Thanks to Prof. Javier González Platas and to Dr. Ulises Rodríguez, from Universidad de La Laguna, for their studies on the crystal structure of my compounds with variable pressure and their mechanoluminescent behavior. Thanks to Dr. Marta Muñoz, from Universidad Politécnica de Madrid, for helping us in the manufacture of our first samples of composite materials, and to Dr. Yolanda Ballesteros from ICAI for the mechanical testing of these composites. Thanks to Prof. Reyes Jiménez, Dr. José Luis Priego, Dr. Rodrigo González and Dr. Santiago Herrero from Universidad Complutense de Madrid, and Dr. Deseada Díaz from Universidad Autónoma de Madrid, for their guidance upon registering and interpreting the diffuse reflectance UV-visible spectra of my compounds. Thanks to Prof. Julio Gómez and Dr. Miriam Moreno for teaching me how to use an optic microscope to take images preliminary to AFM experiments. And thanks to Prof. Hiroshi Nishihara and Dr. Ryota Sakamoto of the University of Tokyo, and the members, present and past, of their research group (Mr. Ryo Shiotsuki, Mr. Ryojun Toyoda, Mr. Shun Kimura, Mr. Kenichiro Omoto, Mr. Jo Komeda, Ms. Risa Aoki, Ms. Yiou Pei, Mr. Daiki Nishiori and many more), for having accepted me among them for four months.

Thanks to the lab technicians Miguel Ángel Fernández and Ismael Moreno and the secretaries Margarita Verdier and Cristina Rodríguez for their priceless assistance in research and administrative procedures. I would also like to thank Miguel Ángel Fernández for taking his time to record the AFM images of my nanoscaled samples.

I would also like to thank my Chemistry teacher at high school, Mr. Javier Linaje, for it was him who inspired me to study a Chemistry Degree.

Finally, it is worth to acknowledge that this thesis has been funded by the FPI-MINECO program of the Spanish Ministerio de Economía y Competitividad (and, therefore, the current Ministerio de Ciencia, Innovación y Universidades) with the grant BES-2015-071534, as well as projects MAT2016-77608-C3-1-P, MAT2016-75883-C2-2-P, MAT2016-75586-C4-4-P and CTQ2016-75816-C2-1P.

For all this, and all which is yet to come, THANK YOU.

## Abstract

The present PhD Thesis has been realized in the Inorganic Chemistry Department of the Autonomous University of Madrid (Universidad Autónoma de Madrid), under the supervision of Dr. Félix Zamora Abanades and Dr. Pilar Amo Ochoa of the Nanomaterials Research Group. To achieve the completion of this thesis, a series of materials based on coordination polymers (CPs) has been designed, synthesized and characterized. These compounds present electrical and luminescent properties which can be tuned by the presence of physical or chemical stimuli. These materials are commonly known to possess a dynamic or stimuli-responsive behavior. Apart from the experiments conducted in the presence of several stimuli, theoretical calculations have been used when necessary in order to rationalize the observed behaviors.

This thesis will be divided into six chapters: an introduction to CPs and stimuli-responsive materials, accompanied by the purposes of the thesis (Chapter 1); three chapters where the results of the thesis and the subsequent discussion are detailed (Chapters 2-4); the conclusions (Chapter 5) and, finally, the experimental section (Chapter 6).

The compounds described in chapter 2 share a common building block: copper(I) iodide and functionalized nitrogen-donor ligands. Aiming to obtain new materials based on one- and two-dimensional CPs with double *zigzag* Cu-I chains, this metal salt has been combined with the following organic ligands: methyl isonicotinate (MeIN), methyl 2-aminoisonicotinate (NH<sub>2</sub>-MeIN), aminopyrazine (Apyz) and 3-chloroisonicotinic acid (Cl-HIN). The obtained compounds have been characterized by means of infrared spectroscopy (IR), elemental analysis, single crystal X-ray diffraction (SCXRD) and powder X-ray diffraction (PXRD), and their electrical and luminescent properties have been evaluated. Afterwards, they have been prepared as nanostructures. Similarly, we have been able to obtain nanostructures of three previously described CPs, obtained by combining copper(I) iodide and isonicotinic acid (HIN), ethyl isonicotinate (EtIN) or 2-amino-5-nitropyridine (ANP).

In chapter 3, a new compound based on a double Cu-I chain, where the terminal ligand is 3,5-dichloropyridine (Cl<sub>2</sub>-py), is described. This compound presents itself in two different forms depending on the synthetic method followed to achieve its preparation. In this chapter, the difference in the luminescent properties showed by the two forms of this compound will be explained, and it will be proven that these differences are caused by the presence of defects in one of them.

Chapter 4 discloses the preparation of new composite materials based on two of the already outlined CPs and flexible organic matrices such as polyvinylidene difluoride (PVDF) and polylactic acid (PLA). The homogeneity and the luminescent and mechanical properties of these new materials will be studied, in order to present them as candidates for industrial or daily-life applications.



## Resumen

La presente tesis doctoral se ha realizado en el Departamento de Química Inorgánica de la Universidad Autónoma de Madrid bajo la dirección de los doctores Félix Zamora Abanades y Pilar Amo Ochoa, del Grupo de Nanomateriales. Para la consecución de esta tesis se han diseñado, sintetizado y caracterizado una serie de materiales basados en polímeros de coordinación (CPs) con propiedades eléctricas y luminiscentes modulables por la presencia de estímulos físicos o químicos, lo que se conoce como materiales con comportamiento dinámico o estímulo-respuesta. Además de los experimentos llevados a cabo frente a diferentes estímulos, en los casos necesarios se han realizado cálculos teóricos con el fin de racionalizar los comportamientos observados.

Esta tesis se dividirá en seis capítulos: una introducción a los CPs y a los materiales estímulo-respuesta, acompañada de los objetivos de la tesis (Capítulo 1); tres capítulos detallando los resultados de la tesis y su discusión (Capítulos 2-4); las conclusiones (Capítulo 5) y, finalmente, la sección experimental (Capítulo 6).

Los compuestos descritos en el capítulo 2 comparten uno de los bloques de construcción: el yoduro de cobre(I) y ligandos nitrógeno-dadores funcionalizados. Con el fin de obtener nuevos materiales basados en CPs monodimensionales y bidimensionales con cadenas dobles en zigzag Cu-I, dicha sal metálica se ha combinado con los ligandos orgánicos isonicotinato de metilo (MeIN), 2-aminoisonicotinato de metilo (NH<sub>2</sub>-MeIN), aminopirazina (Apyz) y ácido 3-cloroisonicotínico (Cl-HIN). Los compuestos obtenidos se han caracterizado mediante espectroscopía infrarroja (IR), análisis elemental y difracción de rayos X de monocristal (SCXRD) y de polvo (PXRD), y se han estudiado sus propiedades eléctricas y luminiscentes en cristal. Seguidamente se han preparado en forma de nanoestructuras. De la misma forma, se han fabricado nanoestructuras de tres compuestos ya descritos con anterioridad, procedentes de la combinación de yoduro de cobre(I) con ácido isonicotínico (HIN), isonicotinato de etilo (EtIN) y 2-amino-5-nitropiridina (ANP).

En el capítulo 3 se describe un nuevo compuesto basado en una cadena doble Cu-I, en el que el ligando terminal es la 3,5-dicloropiridina (Cl<sub>2</sub>-py). Este compuesto se presenta en dos formas distintas según el método de síntesis empleado para su obtención. En este capítulo se explicarán las diferencias en propiedades luminiscentes de ambas formas, y se demostrará que la causa de estas diferencias es la presencia de defectos en una de ellas.

En el capítulo 4 se describirá la preparación de nuevos materiales compuestos basados en dos de estos polímeros de coordinación y matrices poliméricas orgánicas flexibles como son el polifluoruro de vinilideno (PVDF) y el poliácido láctico (PLA). Se estudiará la homogeneidad de estos nuevos materiales, así como sus propiedades luminiscentes y mecánicas, con el fin de demostrar su potencial uso en aplicaciones industriales o cotidianas.

## Publications derived from this thesis

1. Hassanein, K.; Conesa-Egea, J.; Delgado, S.; Castillo, O.; Benmansour, S.; Martinez, J. I.; Abellan, G.; Gomez-Garcia, C. J.; Zamora, F.; Amo-Ochoa, P., Electrical Conductivity and Strong Luminescence in Copper Iodide Double Chains with Isonicotinato Derivatives. *Chemistry - A European Journal* **2015**, *21* (48), 17282-17292.
2. Conesa-Egea, J.; Gallardo-Martinez, J.; Delgado, S.; Martinez, J. I.; Gonzalez-Platas, J.; Fernandez-Moreira, V.; Rodriguez-Mendoza, U. R.; Ocon, P.; Zamora, F.; Amo-Ochoa, P., Multistimuli Response Micro- and Nanolayers of a Coordination Polymer Based on Cu<sub>2</sub>I<sub>2</sub> Chains Linked by 2-Aminopyrazine. *Small* **2017**, *13* (33), 1700965.
3. Conesa-Egea, J.; Hassanein, K.; Munoz, M.; Zamora, F.; Amo-Ochoa, P., Fast and efficient direct formation of size-controlled nanostructures of coordination polymers based on copper(i)-iodine bearing functional pyridine terminal ligands. *Dalton Transactions* **2018**, *47* (16), 5607-5613.
4. Conesa-Egea, J.; Redondo, C. D.; Martinez, J. I.; Gomez-Garcia, C. J.; Castillo, O.; Zamora, F.; Amo-Ochoa, P., Supramolecular Interactions Modulating Electrical Conductivity and Nanoprocessing of Copper-Iodine Double-Chain Coordination Polymers. *Inorganic Chemistry* **2018**, *57* (13), 7568-7577.
5. Conesa-Egea, J.; Nogal, N.; Martinez, J. I.; Fernandez-Moreira, V.; Rodriguez-Mendoza, U. R.; Gonzalez-Platas, J.; Gomez-Garcia, C. J.; Delgado, S.; Zamora, F.; Amo-Ochoa, P., Smart composite films of nanometric thickness based on copper-iodine coordination polymers. Toward sensors. *Chemical Science* **2018**, *9* (41), 8000-8010.
6. Conesa-Egea, J.; Zamora, F.; Amo-Ochoa, P., Perspectives of the smart Cu-Iodine coordination polymers: A portage to the world of new nanomaterials and composites. *Coordination Chemistry Reviews* **2019**, *381*, 65-78.
7. Conesa-Egea, J.; Moreno-Vazquez, A.; Fernandez-Moreira, V.; Ballesteros, Y.; Castellanos, M.; Zamora, F.; Amo-Ochoa, P., Micro and Nano Smart Composite Films Based on Copper-Iodine Coordination Polymer as Thermochromic Biocompatible Sensors. *Polymers* **2019**, *11* (6), 1047.

## Publications under preparation

8. Conesa-Egea, J.; González-Platas, J.; Rodríguez-Mendoza, U. R.; Martínez, J. I.; Ocon, P.; Fernández-Moreira, V.; Costa, R.; Fernandez-Cestay, J.; Zamora, F.; Amo-Ochoa, P., Cunning defects: Emission control by structural point defects on a Cu(I) double chain Coordination Polymer. *Journal of Materials Chemistry C* (sent).

9. Conesa-Egea, J.; Sakamoto, R.; Zamora, F.; Amo-Ochoa, P., Manuscript under preparation.

### **Presentations at conferences**

1. Conesa-Egea, J.; Donati, G.; López, S. G.; Toffanin, S.; Delgado, S.; Amo-Ochoa, P.; Zamora, F., Luminescent nanoribbons based on 1D coordination polymers with Cu-I chains (poster). Presented at NanoSpain 2016, Logroño (Spain), March 14-18, 2016.
2. Conesa-Egea, J.; Gallardo-Martínez, J.; Delgado, S.; Amo-Ochoa, P.; Zamora, F., Influence of the thermal variation of the structure on the properties of a Cu-I based coordination polymer (poster). Presented at ISC Granada 2016, Granada (Spain), May 29-June 2, 2016.
3. Conesa-Egea, J.; Gallardo-Martínez, J.; Delgado, S.; Martínez, J. I.; González-Platas, J.; Fernández-Moreira, V.; Rodríguez-Mendoza, U. R.; Zamora, F.; Amo-Ochoa, P., Stimuli-Responsive Materials Based on the Flexibility of the Copper-Halide Chain (oral contribution). Presented at XXXVI Reunión Bienal de la Real Sociedad Española de Química, Sitges (Barcelona, Spain), June 25-29, 2017.
4. Conesa-Egea, J.; López-Molina, J.; Moreno-Vázquez, A.; Fernández-Moreira, V.; Ballesteros, Y.; Guerrero-Lemus, R.; Zamora, F.; Amo-Ochoa, P., Materiales Compuestos Inteligentes basados en Polímeros de Coordinación con Cadenas Dobles Cobre(I)-Yodo (poster). Presented at I IAdChem Workshop, Madrid (Spain), May 9-10, 2019.
5. Conesa-Egea, J.; López-Molina, J.; Moreno-Vázquez, A.; Fernández-Moreira, V.; Ballesteros, Y.; Guerrero-Lemus, R.; Zamora, F.; Amo-Ochoa, P., Smart Composite Materials Based on Coordination Polymers with Copper(I)-Halide Double Chains (oral contribution). Presented at XXXVII Reunión Bienal de la Real Sociedad Española de Química, Donostia-San Sebastián (Guipúzcoa, Spain), May 26-30, 2019.

## List of Abbreviations and Acronyms

0D	Zero-dimensional
1D	One-dimensional
2D	Two-dimensional
3D	Three-dimensional
$^3(\text{I} + \text{M})\text{LCT}$	Triplet-arising Iodide-Metal-skeleton-to-Ligand Charge Transfer
$^3(\text{X} + \text{M})\text{LCT}$	Triplet-arising Halide-Metal-skeleton-to-Ligand Charge Transfer
$^3\text{CC}$ ( $^3\text{MCC}$ )	Triplet-arising metallophilic (Cluster-Centered) transition
$^3\text{ILCT}$	Triplet-arising Iodide-to-Ligand Charge Transfer
$^3\text{IMCT}$	Triplet-arising Iodide-to-Metal Charge Transfer
$^3\text{MLCT}$	Triplet-arising Metal-to-Ligand Charge Transfer
$^3\text{XLCT}$	Triplet-arising Halide-to-Ligand Charge Transfer
$^3\text{XMCT}$	Triplet-arising Halide-to-Metal Charge Transfer
6mq	6-methylquinoline
AC	Alternate Current
AFM	Atomic Force Microscopy
ANP	2-amino-5-nitropyridine
Apyz	Aminopyrazine (2-aminopyrazine)
bpy	Bipyridine
CB	Conduction band
Cl-HIN	3-chloroisonicotinic acid
Cl <sub>2</sub> -py	3,5-dichloropyridine
CP	Coordination Polymer
DC	Direct Current
DFT	Density Functional Theory
DMF	Dimethylformamide
dmpyz	Dimethylpyrazine

DMSO	Dimethylsulfoxide
DOS	Density of States
DR	Diffuse Reflectance
EDX	Energy-Dispersive X-ray spectroscopy
EIS	Electrochemical Impedance Spectroscopy
EoS	Equation of State
EtIN	Ethyl isonicotinate
FE-SEM	Field-Emission Scanning Electron Microscopy
FT-IR	Fourier Transform-Infrared spectroscopy
GW-BSE	Quasi-particle approximation Bethe-Salpeter equation
HIN	Isonicotinic acid
HOPG	Highly oriented pyrolytic graphite
HT	High temperature
IN	Isonicotinate
LT	Low temperature
lut	lutidine (dimethylpyridine)
MeIN	Methyl isonicotinate
MMM	Mixed-Matrix Membrane
MOF	Metal-Organic Framework
MS	Mass Spectrometry
NCP	Nanoscaled Coordination Polymer
NH <sub>2</sub> -MeIN	Methyl 2-aminoisonicotinate
pic	Picoline (methylpyridine)
PLA	Polylactic acid
PVDF	Polyvinylidene difluoride
py	Pyridine
pym	Pyrimidine

pyz	Pyrazine
RT	Room temperature
SDS	Sodium Dodecylsulfate
SEM	Scanning Electron Microscopy
TDDFT	Temperature-dependent Density Functional Theory
TGA	Thermogravimetric Analysis
THF	Tetrahydrofuran
UV-vis	Ultraviolet-visible spectroscopy
VB	Valence band
VdW	Van der Waals

# Table of contents

## Chapter 1: Introduction to coordination polymers and stimuli-responsive materials.

Aims of the thesis .....	1
1.1. Coordination Polymers (CPs) .....	2
1.1.1. Synthesis of CPs.....	7
1.1.2. Properties of CPs.....	9
1.2. Stimuli-responsive materials.....	22
1.3. Objectives of the thesis .....	27
1.4. References.....	29

## Chapter 2. Coordination Polymers based on the flexibility of the copper(I)-iodide double *zigzag* chain .....

2.1. Introduction: the double <i>zigzag</i> Cu(I)-I chain.....	46
2.1.1. Stimuli-responsive behavior of Cu(I)-I compounds.....	48
2.1.2. Nanoprocessing of Cu-X CPs .....	55
2.2. Results and discussion .....	58
2.2.1. Synthesis and structural characterization .....	58
2.2.2. Electrical conductivity .....	76
2.2.3. Luminescent properties .....	84
2.3. Conclusions.....	100
2.4. References.....	102

## Chapter 3. The effect of defects on the properties of a Cu(I)-I coordination polymer. 109

3.1. Introduction to defects. ....	110
3.2. Results and discussion. ....	115
3.2.1. Synthesis and structural characterization. ....	115
3.2.2. Luminescent properties .....	121
3.2.3. Point defects: Theoretical calculations.....	125
3.2.4. Electrical conductivity .....	129
3.3. Conclusions.....	131
3.4. References.....	131

## Chapter 4. Smart composite films based on Cu(I)-I CPs .....

4.1. Introduction to composite materials and mixed-matrix membranes (MMMs)..	136
4.2. Results and discussion .....	138

4.2.1. Preparation of MMMs of different thicknesses.....	138
4.2.2. Luminescent response to temperature and pressure .....	145
4.2.3. Mechanical properties .....	148
4.3. Conclusions.....	155
4.4. References.....	156
Chapter 5. Conclusions.....	159
Chapter 6: Experimental procedures .....	161
6.1. Materials .....	162
6.2. Methods .....	162
6.2.1. Fourier-Transform Infrared Spectroscopy (FT-IR).....	162
6.2.2. Elemental Analysis.....	162
6.2.3. Powder X-ray Diffraction (PXRD). ....	162
6.2.4. Thermogravimetric analysis (TGA) and TGA coupled with mass spectrometry (TG-MS).....	162
6.2.5. Raman Spectroscopy.....	163
6.2.6. Proton Nuclear Magnetic Resonance Spectroscopy ( $^1\text{H}$ -NMR). ....	163
6.2.7. Diffuse reflectance UV-visible spectroscopy.....	163
6.2.8. X-ray Photoelectron Spectroscopy (XPS).....	163
6.2.9. Single Crystal X-ray Diffraction (SC-XRD).....	163
6.2.10. Luminescence Spectroscopy. ....	164
6.2.11. Electrical Conductivity and Electrochemical Impedance Spectroscopy (EIS). ....	165
6.2.12. Field-Emission Scanning Electron Microscopy (FE-SEM). ....	166
6.2.13. Scanning Electron Microscopy coupled with analysis by Energy-Dispersive X-ray Spectroscopy (SEM-EDX). ....	166
6.2.14. Atomic Force Microscopy (AFM). ....	166
6.2.15. Theoretical Methodology. ....	167
6.3. Synthetic procedures.....	167
6.3.1. Synthesis of CPs with double <i>zigzag</i> Cu-I chains. ....	167
6.3.2. Preparation of composite materials based on CPs engulfed in a flexible organic polymeric matrix. ....	173
6.4. References.....	174
Appendix A: Crystallographic tables .....	177
Appendix B: Pressure-dependent SC-XRD studies .....	187



B1. Compound <b>5</b> .....	187
B2. Compound <b>6</b> .....	190
B3. Compound <b>8</b> .....	194
References.....	202
Appendix C: PXRD patterns .....	203
Appendix D: TGA analyses.....	210
D1. Pristine CPs .....	210
D2. Composite thin films.....	215
Appendix E: <sup>1</sup> H-RMN studies of compound <b>8</b> .....	219

# **Chapter 1: Introduction to coordination polymers and stimuli-responsive materials. Aims of the thesis**

## 1.1. Coordination Polymers (CPs)

Coordination polymers (CPs), also known as metal-organic coordination networks (MOCNs),<sup>1</sup> are compounds which can be defined as extended arrays based on the self-assembly of the following building blocks: metal centers, which act like nodes, and organic molecules and/or inorganic fragments, which act like linkers or ligands. The union of these building blocks leads to the formation of 1D, 2D or 3D frameworks (**Figure 1.1**), depending on the coordination number of the metal and the coordination modes of the ligands.<sup>2</sup> Reversible coordination bonds are crucial tools for the design and construction of well-ordered CPs; however, the presence of weaker intermolecular interactions such as hydrogen bonds, halogen bonds<sup>3-6</sup> and  $\pi$ - $\pi$  interactions will define the order of all the elements of the final network.<sup>7</sup> Reaction conditions, including the starting building blocks and solvents,<sup>8</sup> any counterion present in the reaction medium,<sup>9</sup> and the values of temperature and pressure, play a fundamental role in directing the dimensionality and topology of the structure of the obtained CPs.<sup>10</sup> On the other hand, their properties will be determined by the nature of the metal center, as well as that of the ligands, and how all these elements are positioned within the structure in the solid state.<sup>11</sup>

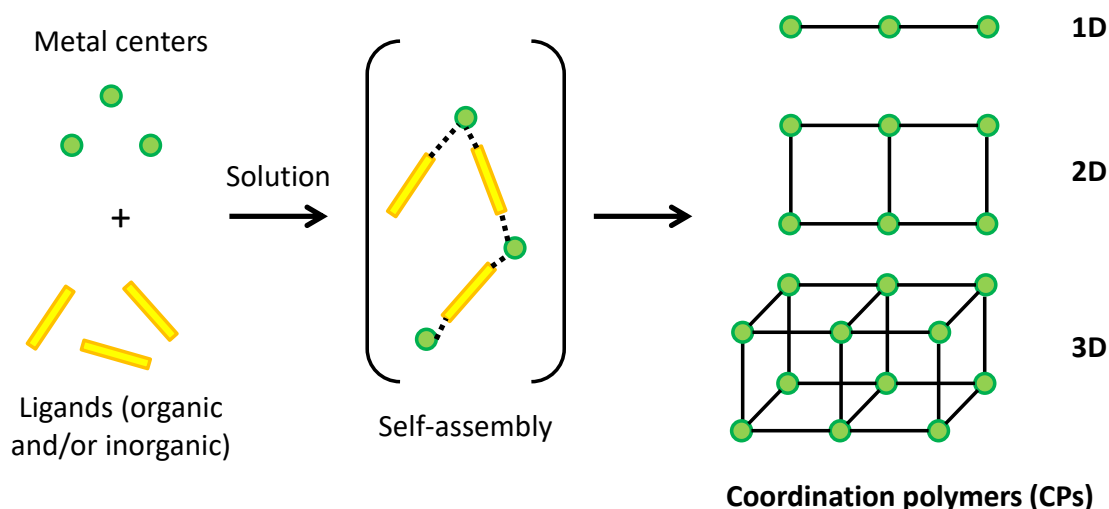


**Figure 1.1.** Schematic representation of the formation of coordination polymers and their dimensionalities. Based on a similar figure seen on reference <sup>2</sup>.

Transition metals and rare-earth elements are the most common metal centers used as nodes in the construction of coordination compounds, especially in CPs. This is due to the wide variety of oxidation states and coordination numbers that these metals can display, each one determining the geometry of the coordination bonds around them and, therefore, the final properties of the CP (**Figure 1.2**). For instance, copper presents itself mainly in two oxidation states: Cu(I)<sup>12</sup> and Cu(II);<sup>13</sup> sometimes we can find compounds where copper presents a mixed-valence oxidation state.<sup>14</sup> Properties such as magnetism, electrical conductivity or photoluminescence, as well as the coordination geometries

(trigonal, tetrahedral, square pyramidal or octahedral in the case of Cu) are determined by the oxidation state of the metal center.

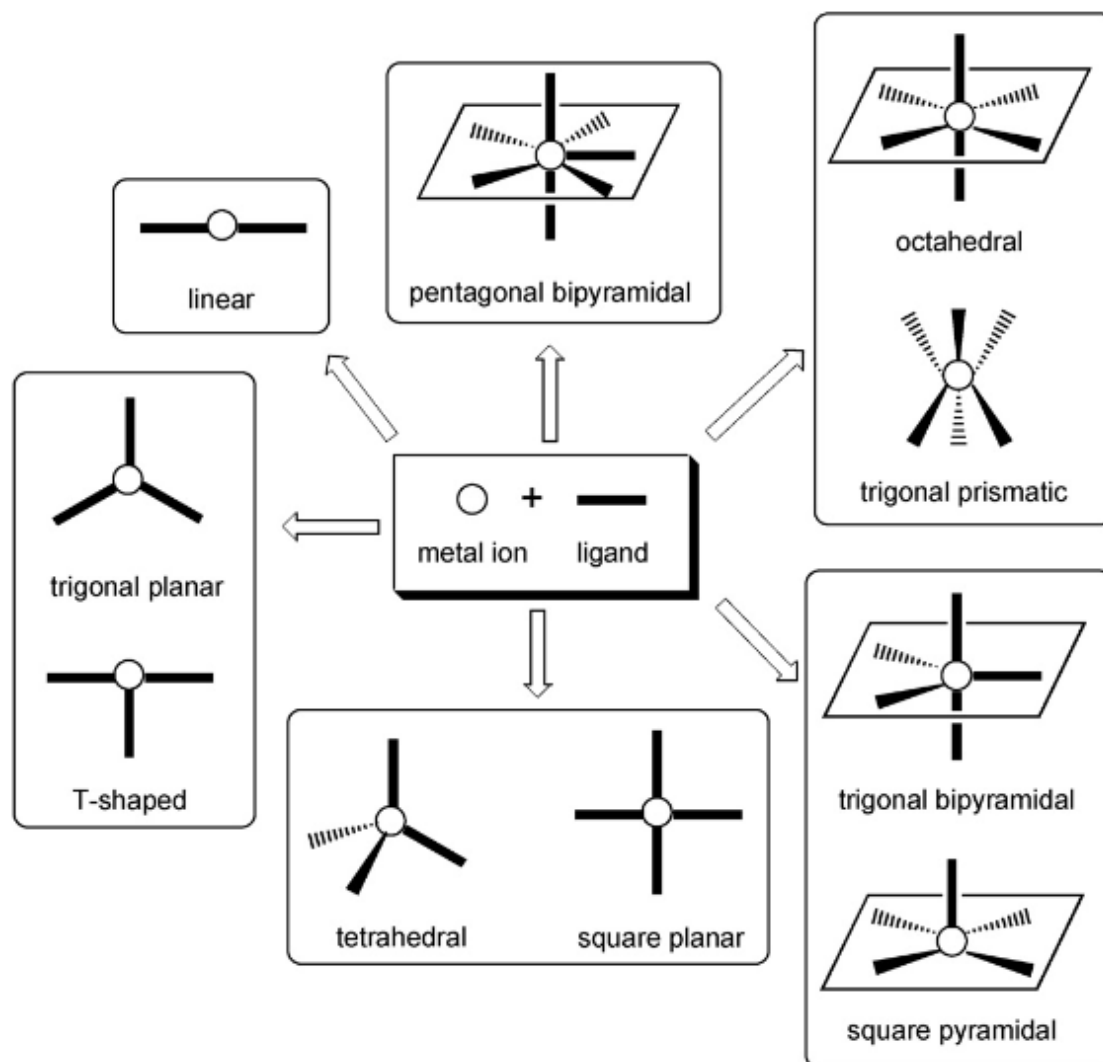


**Figure 1.2.** Coordination geometries of CPs as a function to the coordination index of the metal center (from 2 to 7). Taken from reference <sup>15</sup>.

In some cases, coordination complexes of high nuclearity where metal centers are bridged by polydentate ligands act like nodes instead of single metal ions; the clusters derived from this union are known as Secondary Building Units (SBU); this term was firstly used to refer to paddlewheel structures built from the coordination of four carboxylates around two metal centers, but many more SBUs are known nowadays (**Figure 1.3**).<sup>16-19</sup>

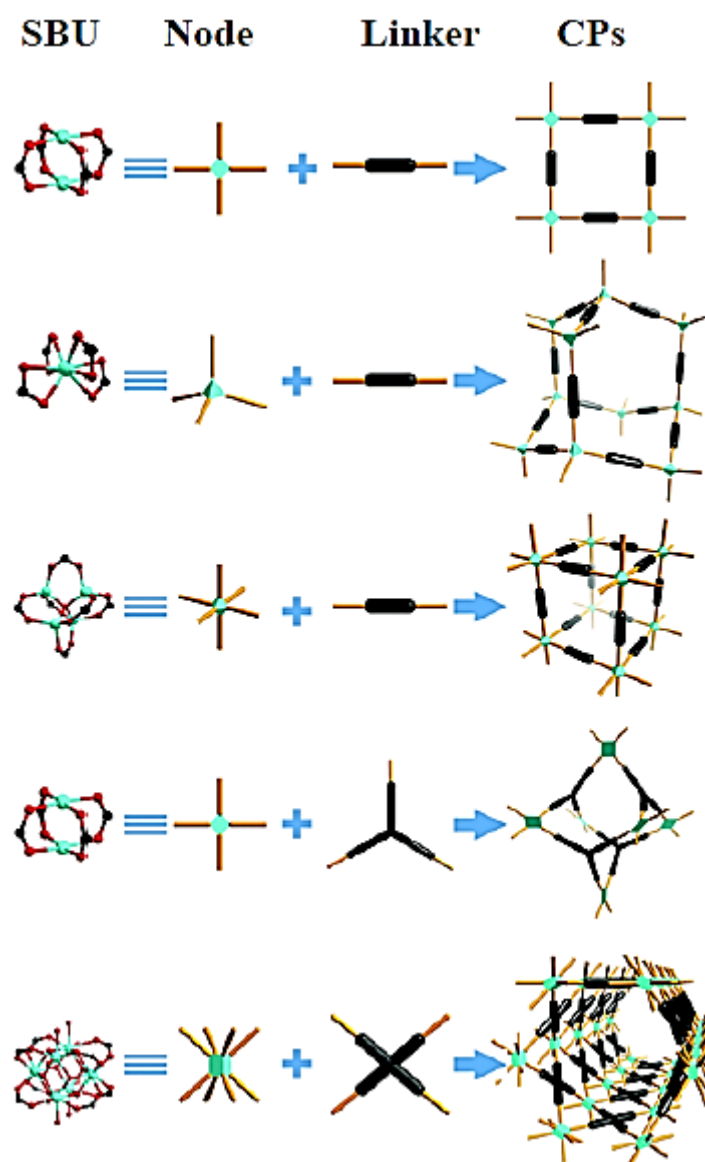


**Figure 1.3.** Examples of common SBUs and their use to form coordination polymers. Taken from reference <sup>16</sup>.

On the other hand, ligands play a critical role in defining the topology and the final properties of the resulting networks. These ligands, both organic and inorganic, can be classified as mono-, bi- or polydentate depending on the number of donor atoms that act as coordination positions. Most ligands are electrically neutral or anionic, but there are a few examples showing positive charge (**Figure 1.4**).<sup>1</sup> Other relevant aspects of the ligand design are the skeleton of the molecules, their shapes (rigid or flexible), lengths (the distance between the coordination positions will be important when designing pores with certain diameters<sup>1, 18-19</sup>), and functionalities (further presence of heteroatoms, aromatic rings, free functional groups...). In coordination compounds it is common to find halides<sup>14, 20-24</sup> and molecules with nitrogen,<sup>25-31</sup> oxygen<sup>16, 18-19</sup> and sulfur-donor atoms<sup>32</sup> in their structure; however, from the point of view of crystal engineering, the way organic ligands coordinate to the metal centers plays a key role. In this regard,

heterocyclic aromatic molecules, and especially pyridine<sup>25-29</sup> and pyrazine<sup>25, 30-31</sup> derivatives (**Figure 1.5**), including pyrimidines and biomolecules such as nucleobases,<sup>33-39</sup> have proven themselves as worthy candidates to determine the final structure of CPs.

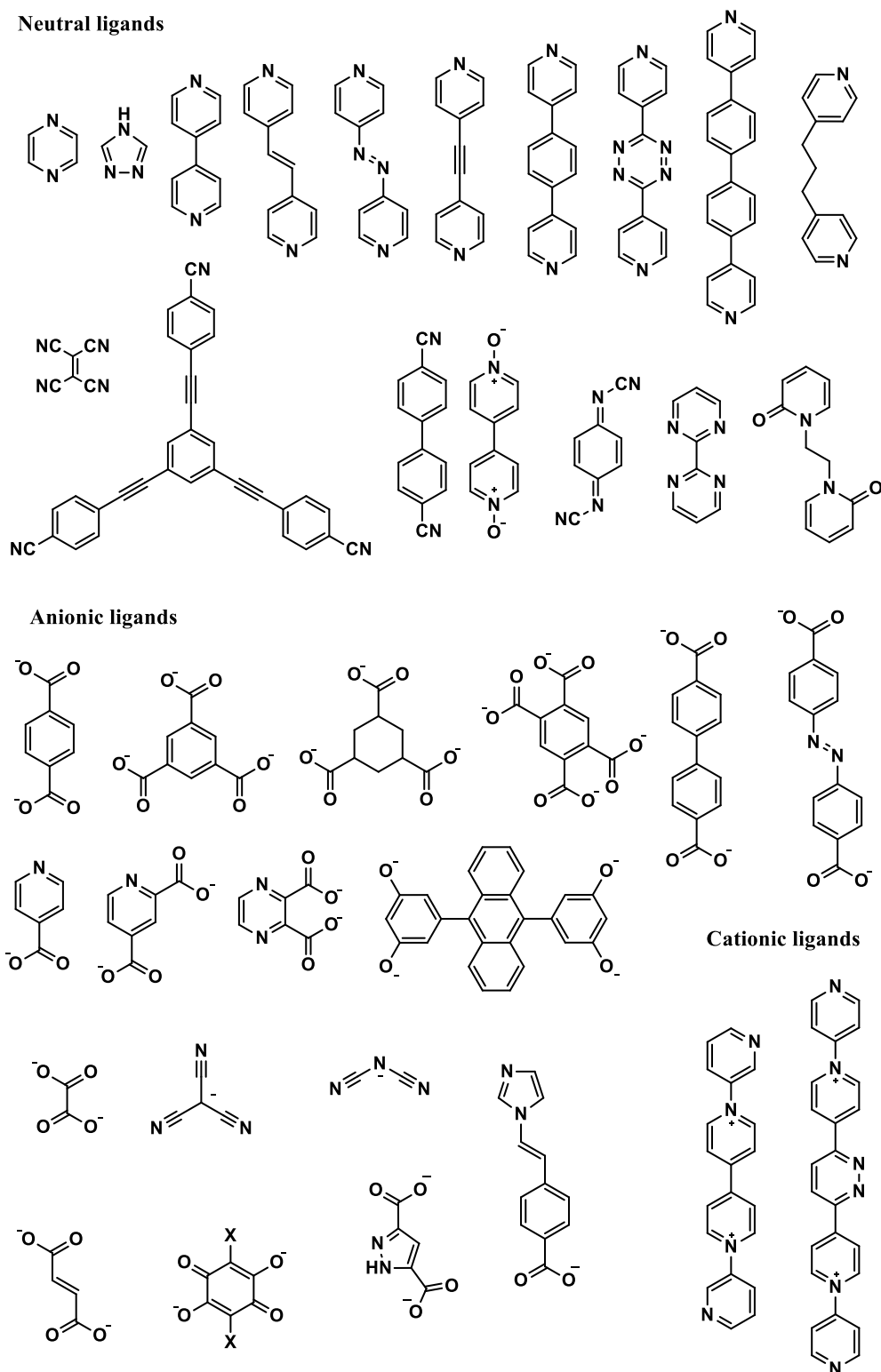


**Figure 1.4.** Examples of ligands with bridging capability used in the synthesis of coordination polymers. Taken from reference <sup>1</sup>.

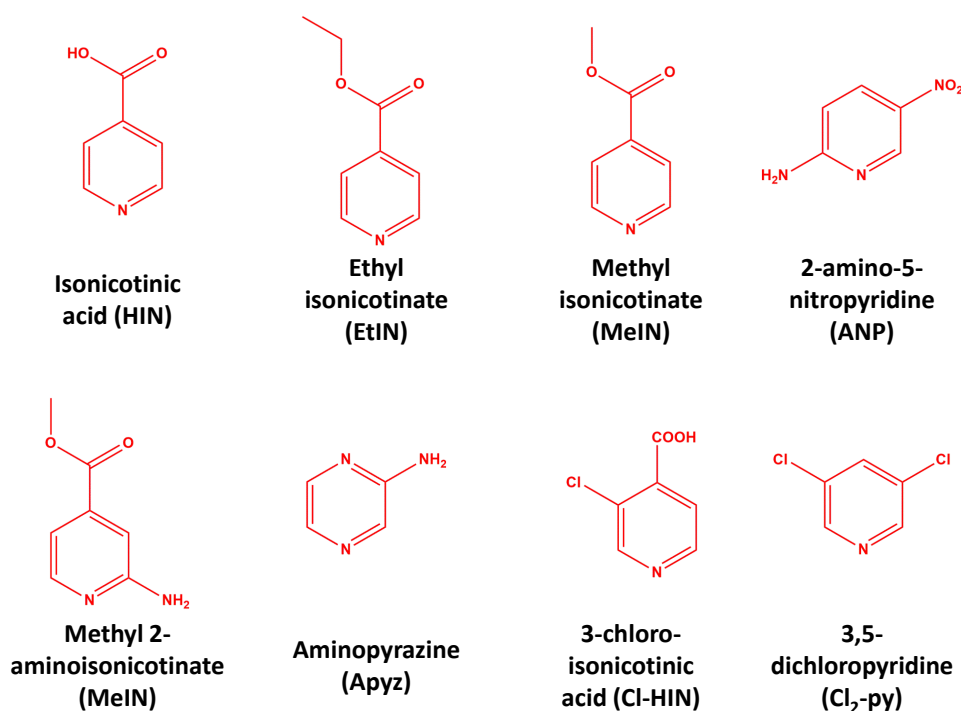


**Figure 1.5.** Examples of N-donor aromatic ligands, those used in this thesis.

Apart from these two essential building blocks, namely ligands and metal centers, other molecules present in the reaction medium can strongly influence the final structure. For instance, solvent molecules can co-crystallize and increase the number of possible weak interactions in the final packing, or can act as guest molecules in the vacant space inside the polymeric network.<sup>40</sup>

As it has been already mentioned, building blocks are essential to determine the final features of a CP. Thus, the strength of the bonds present in a CP will determine its rigidity, ranging from robust frameworks of enhanced stability to flexible solids. The latter can respond to external physical or chemical stimuli, thanks to reversible structural transformations that are intrinsically related to the structural flexibility of the bonds linking metal and ligands and the ability of the coordination sites to accept, release and/or exchange coordinating molecules.<sup>41-43</sup> In fact, this flexible nature was firstly observed for porous coordination polymers (PCPs), a subclass of CPs, also known as metal-organic frameworks (MOFs).<sup>44-45</sup> In addition, some non-porous coordination compounds show structural flexibility, to the point of suffering single-crystal to single-crystal transformations (SCSC).<sup>46-47</sup> These CPs are part of what is known as dynamic materials or stimuli-responsive materials. These materials undergo reversible structural changes when an external stimulus is applied, therefore being exceptionally useful in the preparation of functional materials with tunable or switchable physical properties. Consequently, they are particularly interesting for potential applications in the fabrication of electric,<sup>48-50</sup> magnetic<sup>51</sup> and photoluminescent devices,<sup>52</sup> since their physical properties are extremely sensitive to minor structural changes provoked by an external stimulus.

### 1.1.1. Synthesis of CPs

Traditionally, the main goal pursued in the synthesis of CPs has been the formation of high quality single crystals for structural analysis, which will hence enable the understanding of their structure and properties. However, CPs are generally insoluble in common solvents, and often the recrystallization is not plausible.<sup>10</sup> In a surprisingly short period of time, the structural chemistry of CPs has reached a mature level, due to the application of useful and novel crystallization and synthetic methods such as slow diffusion and solvothermal or microwave-assisted solvothermal synthesis.<sup>53-54</sup>

Depending on the desired structure of our CPs, we will choose among different synthetic procedures. The most common synthetic method is conventional synthesis; here, a solution containing the building blocks is stirred either at room temperature or another desired temperature value (reflux conditions are usually preferred), followed by a crystallization process in order to obtain single crystals suitable for single-crystal X-ray diffraction (SCXRD). These crystallization processes (**Figure 1.6**) are based on the self-assembly of the building blocks under supersaturation conditions caused by a diminishing of the volume (slow evaporation) or temperature, or by the presence of vapors of a poor solvent. Sometimes, it can be found that the desired product crystallizes in the reaction medium, due to the immediate generation of supersaturation. Another synthetic method used to create supersaturation is the diffusion method, where layers of the reactants dissolved in miscible solvents slowly diffuse to come in contact through an intermediate layer. This is particularly useful for the crystallization of poorly soluble products.<sup>55</sup>

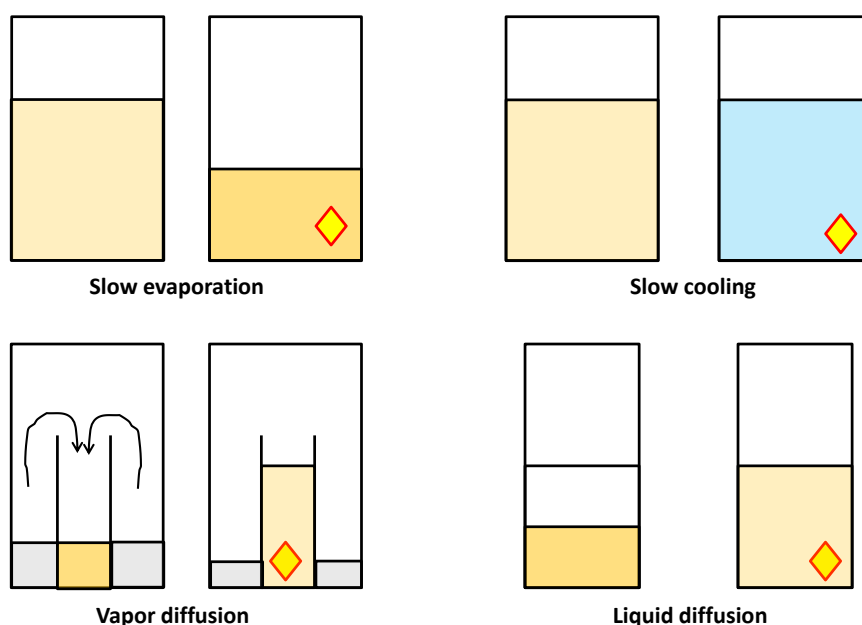


**Figure 1.6.** Scheme of the most widely used methods which lead to the obtainment of single crystals valid for X-ray diffraction analysis. The crystals are represented by the yellow rhomb.



In the cases where the immediate obtainment of single crystals is required, the solvothermal method is used. Herein, the reactions are carried out at high temperature under autogenous pressure and the reaction time and temperature are adjusted to allow the *in-situ* crystallization of the product.<sup>56</sup> However, reaction times in solvothermal syntheses are very long (several days); consequently, the microwave-assisted synthesis technique has arisen as an alternative to provide an efficient way to synthesize pure crystalline materials with short reaction times (several hours).<sup>15</sup>

It is important to mention that, by changing the synthetic procedure and/or the reaction conditions for the same starting materials, the formation of different products or polymorphs of a same substance can occur. Polymorphism is defined as the existence of the same chemical substance in more than one crystal structure, owing to the fact that the forces acting in the arrangement and/or conformation of the crystalline solids lead to different networks.<sup>57</sup> Polymorphism is an interesting phenomenon that plays an important role in understanding crystal packing and structure-property relationships.<sup>58-59</sup> One interesting example of polymorphism in CPs has been reported by Zhang,<sup>60</sup> who synthesized a 1D-CP formulated as  $[\text{CdL}_2]_n$ , where L= 2-mercaptopyridine-N-oxide, in two polymorphic forms as a result of the use of glycine as guest molecule in the starting reactants. The two crystallographic polymorphs show similar 1D polymeric chains but they are significantly different in the binding modes of the 2-mercaptopyridine-N-oxide ligand and the 3D packing modes (**Figure 1.7**).

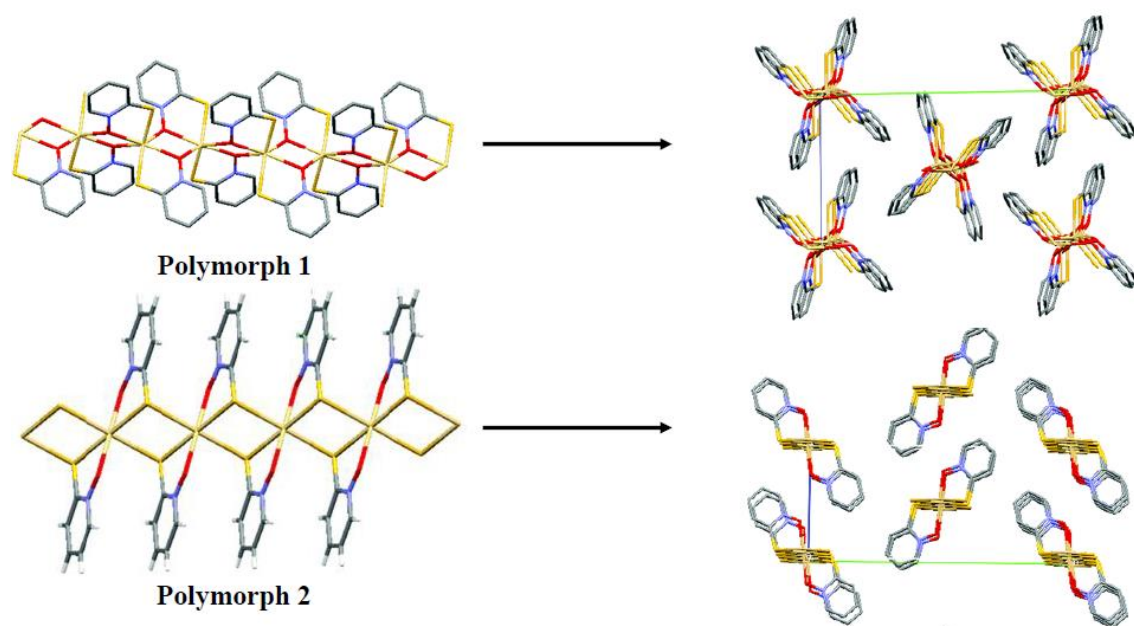


**Figure 1.7.** Crystal structures of the two polymorphs of  $[\text{CdL}_2]_n$  (L= 2-mercaptopyridine-N-oxide). Taken from reference <sup>60</sup>.

CPs can be classified according to their dimensionalities into one-dimensional (1D-CPs), two-dimensional (2D-CPs) and three-dimensional coordination polymers (3D-CPs). The dimensionality of CPs is often determined by the geometry of metal centers. The packing of the crystal structures and, therefore, the morphology of the crystals, are

strongly influenced by weak interactions such as H-bonds,  $\pi$ - $\pi$  stacking, and Van der Waals forces, but the dimensionality is based on the coordination bonds between ligand molecules and metal ions. 1D-CPs are considered to be the simplest ones in terms of dimensionality, but they have been found to have interesting electric, magnetic and optical properties.<sup>30, 37, 61-63</sup>

### 1.1.2. Properties of CPs

Currently, CPs are one of the fastest growing fields in chemistry and material science. It has attracted researchers from several areas of science due to their structural diversity, tunable properties, and the wide range of potential applications such as catalysis, electronics, magnetism, sensing, opto-electronics and nanoprocessing.<sup>64-71</sup> They can also combine multiple properties, e.g. electrical-optical or electrical-magnetic, being an interesting source of multifunctional materials. Since this thesis is focused on Cu(I)-iodide CPs, the following sections will outline, from a general point of view, those properties which are most commonly described for these CPs: electrical conductivity and luminescent properties, as well as nanoprocessing methods and size-dependent properties.

#### *1.1.2.1. Electrical conductivity*

The electrical conductivity of a material is a measure of its ability to conduct electric current. This physical magnitude depends on parameters such as temperature, pressure or the applied voltage. The measurements of the resistance and, hence, the resistivity, of a sample requires the application of a current ( $I$ ) and measuring the voltage drop across the sample ( $V$ ). According to Ohm's law of conductivity,  $V = R \times I$ ; where  $V$  is the voltage,  $I$  is the intensity of the electric current, and the proportionality constant,  $R$ , is the resistance.  $R$  depends on geometrical parameters (therefore, it is sample-dependent) and is commonly expressed as resistivity ( $\rho$ ), which is defined as  $\rho = R(A/l)$ , where  $A$  is the cross-sectional area of the conductor ( $A = a \times d$ ) and  $l$  is the distance between the voltage-drop measuring points (**Figure 1.8**). The conductivity ( $\sigma$ ) is the inverse of the resistivity ( $\sigma = 1/\rho$ ), and measured in  $\Omega^{-1} \text{ m}^{-1} = \text{S m}^{-1}$  ( $\Omega^{-1} = \text{S} = \text{Siemens}$ ). The units in which electrical conductivity is measured are often changed into  $\text{S cm}^{-1}$ .

There are two different ways to prepare samples in order to measure their electrical conductivity in the solid state: as single crystals or pressed pellets.<sup>67, 72</sup> Once the samples have been prepared, their electrical conductivity can be measured by means of the four contacts method or the two contacts method (**Figure 1.8**). The four contacts method, which is mostly used to measure single crystals, involves the connection of four parallel in-line contacts to the sample where the two external contacts are used to introduce a current ( $I+$  and  $I-$ ) and the two internal contacts are used to measure the voltage drop across the sample ( $V+$  and  $V-$ ). Its advantage over the two contacts method

(where the current is applied and the potential drop is measured through the two parallel contacts) is that it eliminates the contribution of the contacts to the resistivity, which tends to be higher than the resistivity of the sample itself. In other words, the four contacts method erases the possibility of obtaining misleading values of the electrical conductivity.

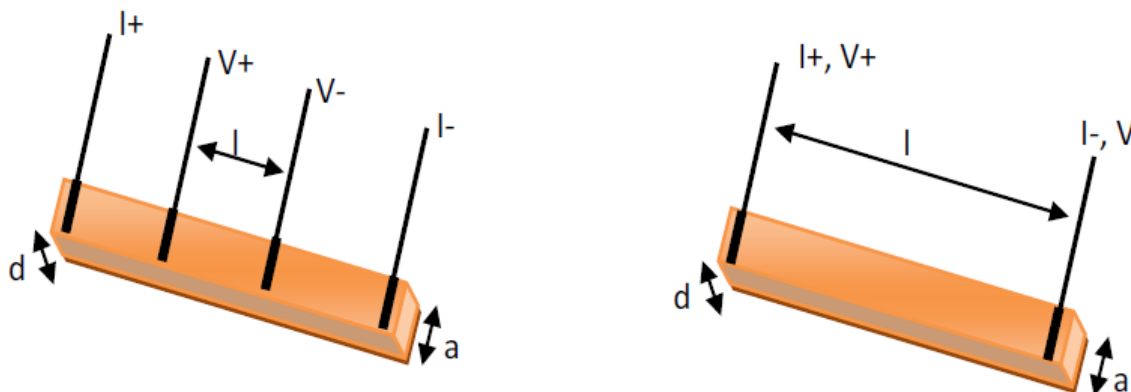


**Figure 1.8.** Scheme of the four-contacts (left) and the two-contacts method (right) used for electrical conductivity measurements. Taken from reference <sup>67</sup>.

When the sample is a pressed pellet, the effect of the anisotropy of the crystals is removed, and in these cases the resistivity is mainly dominated by the inter-grain boundary contacts, which tend to increase the resistivity, usually, between one and three orders of magnitude with respect to the values obtained in crystals. These inter-grain boundaries act as gaps that block the conductivity or as carrier accumulators. This behavior implies that true metallic materials may appear as low band-gap semiconductors or semimetals if they are measured as pressed pellets. The four contacts method is more accurate since it only measures the resistance of the sample ( $R_x$ ), ignoring that of the wires and contacts. In contrast, in two contacts method, the resistance of the sample and those of the wires and contacts are added in the measured resistance. The two contacts method is preferred for small-sized samples, with typical values of the longest dimensions of about 50  $\mu\text{m}$ , whereas the minimum size of samples to be measured by the four contacts method should be higher than 250  $\mu\text{m}$ .<sup>67</sup>

On the other hand, the experimental technique known as electrochemical impedance spectroscopy (EIS) is used to measure the impedance of a given material when applying an alternate current (AC) potential to an electrochemical cell. Like resistance, impedance is a measure of the ability of a sample to resist the flow of electrical current, but unlike resistance, it is frequency-dependent and the current and voltage are phase-shifted. The impedance ( $Z$ ) of a system is generally determined by applying a voltage perturbation with small amplitude and detecting the current response. EIS is a powerful method for analyzing the complex electrical resistance of a material and is sensitive to surface phenomena and changes of bulk properties.<sup>73</sup> Therefore, it is a useful technique to measure the conductivity of CPs, in particular those that contain solvents (especially protic ones) within their network.<sup>74</sup>

In a linear (or pseudolinear) system, the current response to a sinusoidal potential will be a sinusoid at the same frequency but shifted in phase. Therefore, it is possible to express the impedance as a complex function. The potential is described as:

$$E(t) = E_0 \exp(j\omega t)$$

$E(t)$  is the potential at time  $t$ ,  $E_0$  is the amplitude of the signal,  $j$  is the imaginary unit ( $\sqrt{-1}$ ) and  $\omega$  is the radial frequency. The relationship between radial frequency  $\omega$  (expressed in radians/second) and frequency  $\nu$  (expressed in hertz) is:

$$\omega = 2\pi\nu$$

In addition, the current response is described as:

$$I(t) = I_0 \exp(j\omega t - \varphi_0)$$

An expression analogous to Ohm's law ( $R = E/I$ ) allows to calculate the impedance of the system. The impedance is then represented as a complex number:

$$Z(\omega) = E/I = Z_0 \exp(j\varphi) = Z_0 (\cos \varphi + j \sin \varphi)$$

The impedance of a system can be graphically expressed in different ways. The most common one is the Nyquist plot, in which the real part ( $\text{Re}(Z)$  or  $Z'$ ) is plotted on the X-axis, and the imaginary part ( $\text{Im}(Z)$  or  $Z''$ ) is plotted in the Y-axis of a chart (**Figure 1.9a**). On the Nyquist plot, the impedance at a certain frequency can be represented as a vector of length  $|Z|$ . The angle between this vector and the X-axis represents the phase angle ( $\varphi$ ). The electrical conductivity can be calculated from the Nyquist plot as  $\sigma = l/a \times \text{Re}(Z)$ , Where  $l$  and  $a$  are the thickness (cm) and cross-sectional area ( $\text{cm}^2$ ) of the pellet respectively.  $\text{Re}(Z)$ , which was extracted directly from the real impedance axis, is the bulk resistance of the sample ( $\Omega$ ). Another representation of impedance measurements, less used than the Nyquist plot, is the Bode plot (**Figure 1.9b**). In this case, the logarithm of absolute values of the impedance and the phase angle are plotted in the Y-axis and the log frequency on the X-axis.

In general, the electrical behavior of materials can be distinguished by looking at the room temperature conductivity value. This is usually in the range  $10^1$ - $10^5 \text{ S cm}^{-1}$  for metallic conductors,  $10^{-10}$ - $10^1 \text{ S cm}^{-1}$  for semiconductors, and below  $10^{-10} \text{ S cm}^{-1}$  for insulators. The measurement of the thermal variation of the electrical conductivity, always within the Ohmic regime region (low potentials), is a more reliable method which gives clear picture about the electrical behavior of the targeting material. For metals, the conductivity increases or the resistivity decreases with decreasing temperature and the opposite behavior will be observed in the case of semiconductors and insulators.<sup>67</sup> This, as well as the conduction mechanisms in solid state materials, can be explained by means of the band theory.<sup>75</sup> These materials can be described, according to their band structure, as metals, semiconductors or and insulators. Because of the very large number of atoms that interact in a solid material, the discrete energy levels are so closely spaced that they form bands. The highest filled energy band is

called the valence band (VB). The closest unfilled band is called the conduction band (CB). The energy separation between these bands is called the “band gap” ( $E_g$ ). Fermi level, usually found between the valence and conduction bands, refers to the highest occupied molecular orbital at absolute zero.

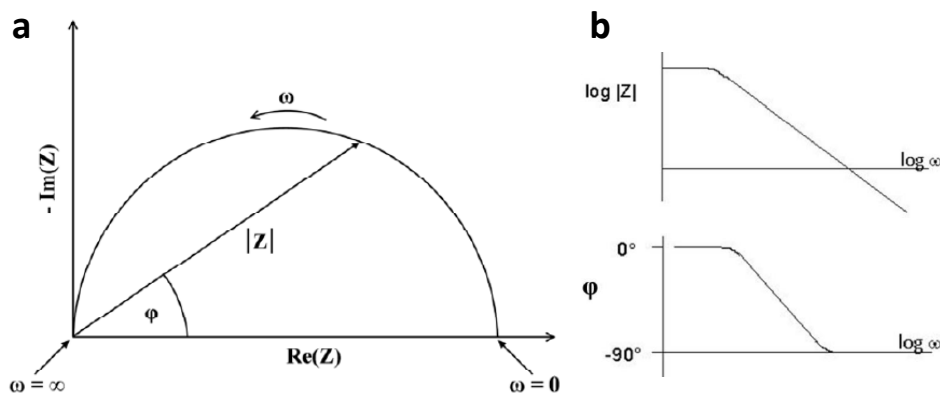


**Figure 1.9.** (a) General picture of the Nyquist plot of a single electrochemical system; the resistance of this system is calculated as the point where the semicircular curve intersects with the real part of the impedance ( $\text{Re}(Z)$ ,  $Z'$ ). (b) Bode plot graphs.

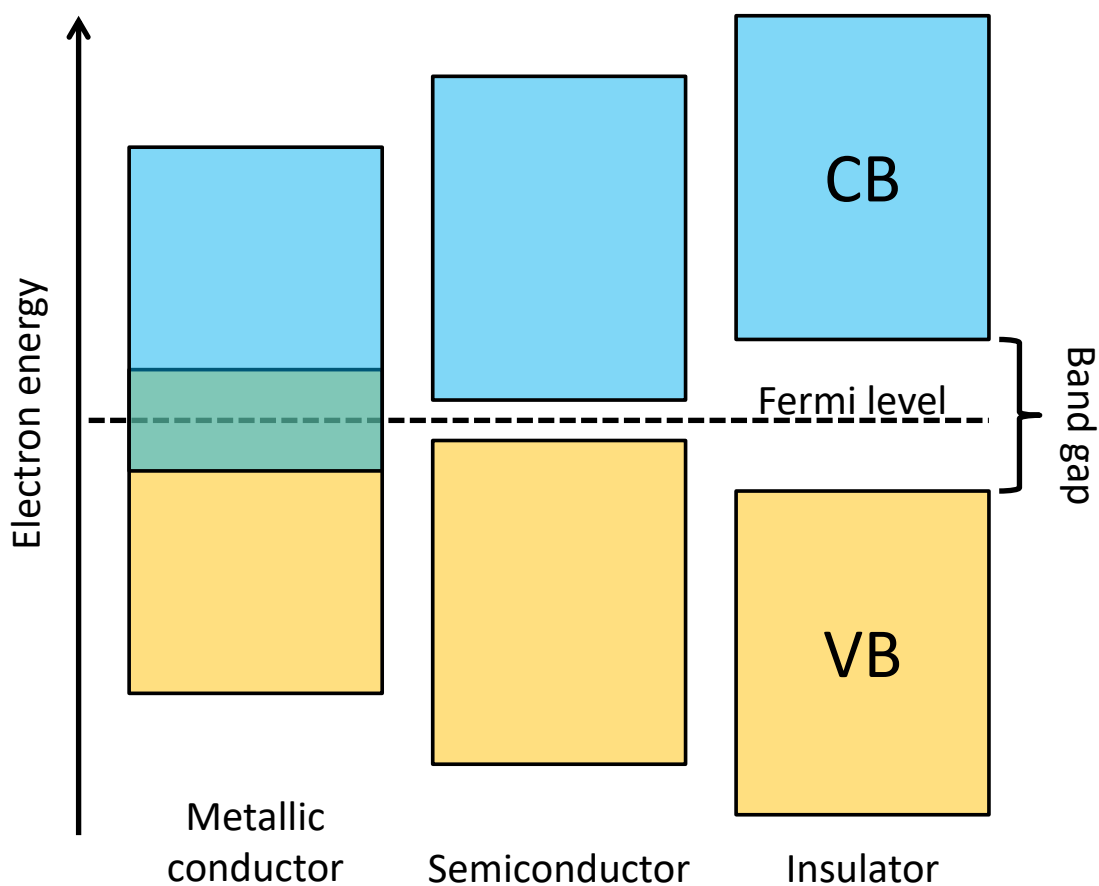


**Figure 1.10.** Schematic illustration of the band structure and band gaps of materials according to their electrical properties.

The filling of these bands and the size of the band gap determine the electronic behavior of solid materials (**Figure 1.10**). The thermal activation of semiconductors ( $E_g < 3$  eV) and insulators ( $E_g > 3$  eV) leads to a decrease in the band gap, therefore leading to an improvement in their electrical conductivity; on the other hand, metallic conductors see their conductivity decreased when temperature rises due to the discretization of the energy levels caused by the broadening of the bands. In classical semiconductors, the thermal dependence of the conductivity follows the Arrhenius law:

$$\sigma(T) = \sigma_0 \exp(-E_a/kT)$$

where  $E_a$  represents the activation energy (corresponding to half of the band gap,  $E_a = E_g/2$ ),  $k$  is Boltzmann's constant and  $\sigma_0$  is a pre-exponential factor, corresponding with the conductivity at infinite temperature. Phase transitions have been observed, in some cases, through the thermal activation of solid materials. These phase transitions, in many cases, are followed by structure rearrangements that can be detected through structure determination techniques, mainly diffractometric techniques.<sup>76</sup>

Electrical conductivity of CPs is one of the most important research areas in materials science. It is well-known that electrical conductivity of organic polymers has attracted the interest of many researchers in material science, however, the research of this property in CPs is still very scarce.<sup>67</sup> Based on recent results, some CPs systems have shown very promising macroscopic electronic properties.<sup>67</sup> In addition, the gradual incorporation of theoretical calculations in CPs has become a powerful tool for understanding the experimental measurements and for the subsequent rational design of new electrically conductive CPs.<sup>76-77</sup> One potential application of electrical conductive CPs deals with their incorporation for the fabrication of electronic devices, either at the macroscopic scale or at the nanoscale; regarding the latter, 1D-CPs have been tested as nanowires, sometimes reaching the state of molecular wires.<sup>67</sup> The electrical conductivity found in some 1D-CPs seems to be dependent on their building blocks and structure.<sup>67</sup> According to some observations, short bridging ligands are required to make metal-metal distances as short as possible in the extended structures. It has been reported that a family of CPs known as MMX chains, formed by dimetallic subunits (MM units, M = Pt, Rh, Pd, Ru...) bridged by halogens (X= I, Br, Cl), have shown reasonable electronic properties.<sup>48-49, 62, 67, 73, 78-79</sup> In particular, those MMX chains based on platinum with dithiocarboxylates and iodide with general formula  $[\text{Pt}_2(\text{RCS}_2)_4\text{I}]_n$ , where R represents alkyl groups, have shown high electrical conductivity values at room temperature. **Table 1.1** gathers the electrical conductivity values found in  $[\text{Pt}_2(\text{RCS}_2)_4\text{I}]_n$ . A thorough study of structural parameters for these MMX chains shows that the only difference between these MMX derivatives is the alkyl chain length, which governs the interchain distances and may tune the Pt-Pt and Pt-I distances that are responsible for the observed physical properties.

MMX chains have been subjected to many studies on the side of Zamora and co-workers.<sup>62, 73, 78-79</sup> For example, in the case of  $[\text{Pt}_2(n\text{-PenCS}_2)_4\text{I}]_n$ , direct current (DC) electrical conductivity measurements carried out on crystals of this CP at different

temperatures using the four contacts method, have revealed this compound's metallic behavior (**Figure 1.11**) and room temperature conductivities values in the range between 0.3 and 1.4 S cm<sup>-1</sup>. The measurements were conducted at three different temperatures: 100 (LT), 298 (RT) and 350 K (HT), and showed the existence of three different phases.<sup>73</sup> It is shown in **Table 1.1** that, due to these excellent conductivity values, these MMX compounds are excellent candidates to be used in electronic applications.

**Table 1.1.** Summary of the electrical conductivity measured for [Pt<sub>2</sub>(RCS<sub>2</sub>)<sub>4</sub>I]<sub>n</sub> CPs with different R (alkyl) groups. Unless otherwise stated, the measurement conditions are RT, 1 bar, the four contacts method and single crystals.<sup>67</sup>

Compound	$\sigma$ (S·cm <sup>-1</sup> )
[Pt <sub>2</sub> (MeCS <sub>2</sub> ) <sub>4</sub> I] <sub>n</sub>	2 <sup>a</sup> / 10 <sup>a,b</sup> / 7·10 <sup>-3 a,c</sup> / 13
[Pt <sub>2</sub> (EtCS <sub>2</sub> ) <sub>4</sub> I] <sub>n</sub>	5-30
[Pt <sub>2</sub> ( <i>n</i> -PrCS <sub>2</sub> ) <sub>4</sub> I] <sub>n</sub>	0.23
[Pt <sub>2</sub> ( <i>n</i> -BuCS <sub>2</sub> ) <sub>4</sub> I] <sub>n</sub>	17-83
[Pt <sub>2</sub> ( <i>n</i> -PenCS <sub>2</sub> ) <sub>4</sub> I] <sub>n</sub>	0.3-1.4
[Pt <sub>2</sub> ( <i>n</i> -HexCS <sub>2</sub> ) <sub>4</sub> I] <sub>n</sub>	2·10 <sup>-3</sup>

(a) Two-contact method; (b) RT, 7 GPa; (c) Pressed pellet

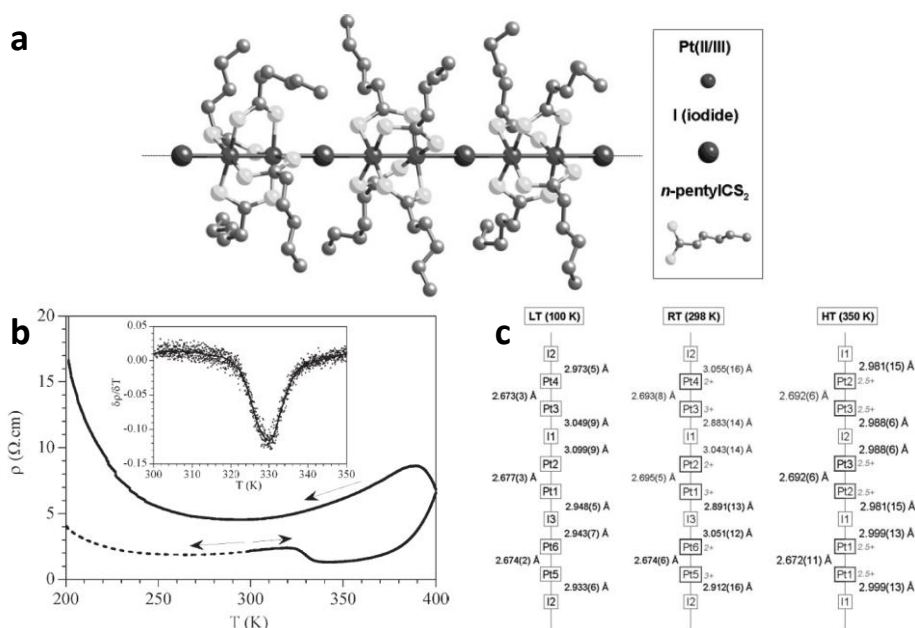


**Figure 1.11.** (a) Structure of a single chain of [Pt<sub>2</sub>(*n*-PenCS<sub>2</sub>)<sub>4</sub>I]<sub>n</sub>. (b) Thermal variation of the electrical resistivity of [Pt<sub>2</sub>(*n*-PenCS<sub>2</sub>)<sub>4</sub>I]<sub>n</sub>. The dashed line shows the behavior of a non-heated sample. The inset shows the derivative of the resistivity as a function of the temperature around the RT-HT transition. (c) Distribution of bond distances and formal oxidation states of platinum along the chain of [Pt<sub>2</sub>(*n*-PenCS<sub>2</sub>)<sub>4</sub>I]<sub>n</sub> at different temperatures. Taken from reference <sup>73</sup>.

### 1.1.2.2. Luminescent properties

Luminescence can be defined as the emission of light stimulated by the absorption of energy. Electron excitations result in different forms of luminescence, which include photoluminescence, thermoluminescence, electroluminescence and chemiluminescence, depending on the nature of the energy absorbed for the excitation process. Photoluminescence can be defined as light emission from any form of matter triggered by the absorption of photons (electromagnetic radiation). The processes that occur between the absorption and emission of light are usually illustrated by the Jablonski diagram (**Figure 1.12**).<sup>80</sup> The singlet ground electronic state is called  $S_0$ . Following light absorption, several processes usually occur. A fluorophore is usually excited to some higher vibrational level; according to the selection rules, they must move to another singlet state ( $S_1$  or  $S_2$ ). Molecules in higher excited states rapidly relax to the lowest vibrational level of  $S_1$ . If the molecule was excited to the  $S_2$  level, the molecule rapidly relaxes to its lowest vibrational level and immediately changes to an isoenergetic vibrational level of  $S_1$ , in a process called internal conversion (IC). This process is non-radiative and generally occurs within  $10^{-12}$  s or less. IC is always completed prior to emission. If the molecule in  $S_2$  cannot find an isoenergetic level of  $S_1$ , it changes to the closest level of this state, with a lower energy value; then the process is called external conversion (EC). Return to an excited vibrational state at the  $S_0$  state is the reason for the emission process, which is called fluorescence. This emission is usually accompanied by a non-radiative decay which is not registered in the emission spectrum.

Molecules in the  $S_1$  state can also undergo a spin conversion to the first triplet state,  $T_1$ . Emission from  $T_1$  is termed as phosphorescence, and is generally shifted to longer wavelengths (lower energy) relative to the fluorescence emission. Conversion of  $S_1$  to  $T_1$  is called intersystem crossing (ISC). Transition from  $T_1$  to the singlet ground state is forbidden, and as a result, the rate constants for triplet emission are several orders of magnitude smaller than those for fluorescence. Therefore, we can conclude that there are two basic types of luminescence: fluorescence, which is spin-allowed between the energetic states and has typical lifetimes approximately 10 ns; and phosphorescence, which is spin-forbidden and has lifetimes with values ranging from a few microseconds to several seconds.<sup>80</sup>

The luminescent properties of any material are characterized by several parameters, which are depicted in their respective luminescence spectra. The clearest one is defined as emission (fluorescence or phosphorescence) intensity, which is measured as a function of the wavelength. A second parameter is the quantum yield, which gives the efficiency of the fluorescence process and is defined as the ratio of the number of emitted photons released in the process of fluorescence with respect to the number of photons absorbed in the excitation process; the remaining energy is dispersed as heat by means of a non-radiative decay. Finally, the emission lifetime, which refers to the average time the molecule stays in its excited state before emitting a photon and is determined as being inversely proportional to the sum of all rate constants of a radiative process and the non-radiative processes.<sup>80</sup>



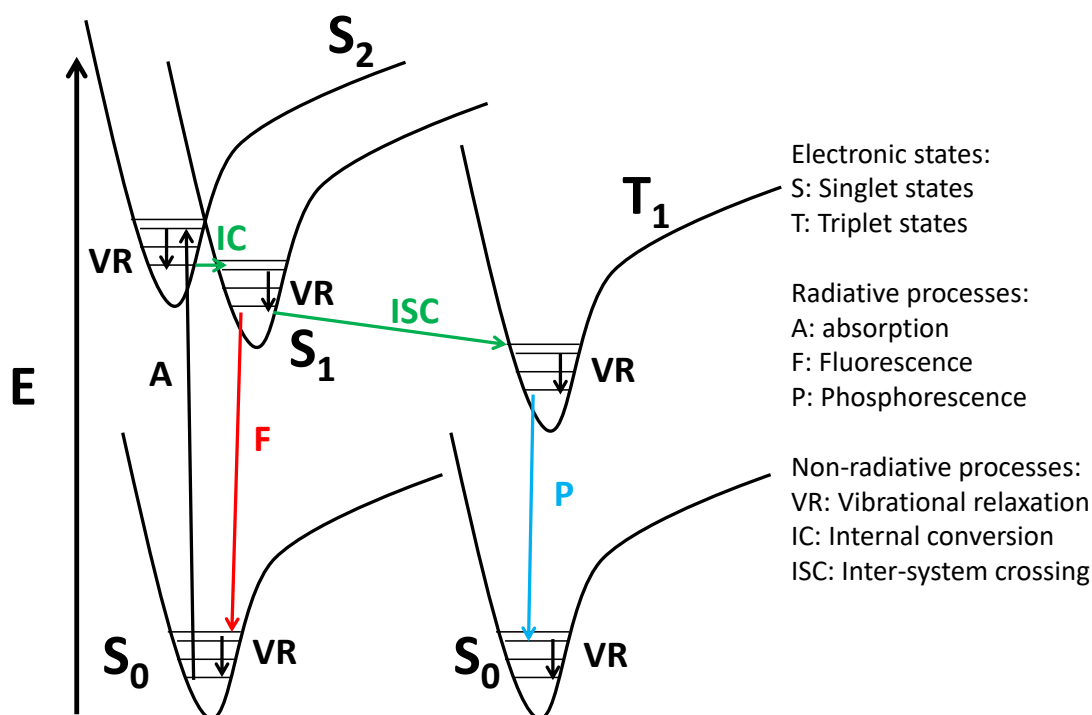


**Figure 1.12.** Schematic representation of the Jablonski diagram. External conversion (EC) has been omitted for clarity.<sup>80</sup>

CPs are considered to be very promising photoluminescent materials where both the inorganic and the organic moieties can contribute to generate radiative emission. Photoluminescence properties depend on the composition of the materials, the structure, and intermolecular packing that stabilizes these materials. Currently, polynuclear d<sup>10</sup> metal complexes have attracted considerable attention for their diverse structural and rich photoluminescence properties, even at room temperature, that give rise to potential applications as light-emitting diodes.<sup>81-85</sup> One of the most prominent classes of photoluminescent coordination compounds, which state as the main theme of this thesis, is the one integrated by copper(I) halide<sup>21-24, 27-29, 32, 52, 86-95</sup> and pseudo-halide<sup>29, 96</sup> compounds, namely Cu(I)-X. The variety of available coordination numbers for copper and bridging modes for halides and pseudohalides (from terminal to  $\mu^2$ - and up to  $\mu^8$ -bridging modes), as well as the flexibility of these parameters, have introduced great structural diversity in copper(I)-halide compounds.<sup>97</sup> Consequently, copper(I) halides can adapt to various structural motifs including square Cu<sub>2</sub>X<sub>2</sub> dimers, cubane or stepped cubane Cu<sub>4</sub>X<sub>4</sub> tetramers, zig-zag [CuX]<sub>n</sub> chains, and double stranded [Cu<sub>2</sub>X<sub>2</sub>]<sub>n</sub> ladders (X = Cl, Br, or I anions (**Figure 1.13**)).<sup>97-100</sup> They are very easy to synthesize and their emission color is easily tunable,<sup>101-102</sup> with high emission quantum yields in the solid state.<sup>103-104</sup> From the economic point of view, copper is also more abundant and less expensive than rare-earth and noble metals and is less environmentally problematic than the former.<sup>105</sup>

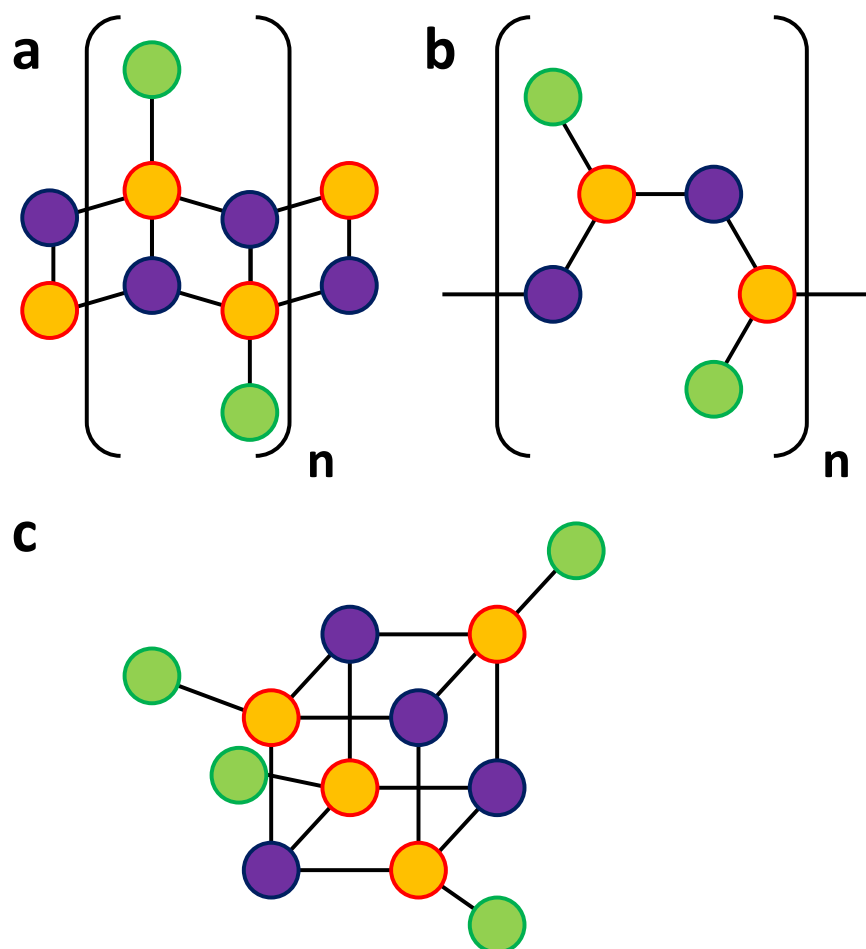


**Figure 1.13.** Representation of three of the most common structures displayed by Cu(I)-halide compounds: (a) Polymeric double *zigzag* chain (or staircase chain); (b) Polymeric single *zigzag* chain; (c) Discrete cubane-like cluster ( $\text{Cu}_4\text{X}_4$ ), acting like a SBU tetrahedrally linked to four ligand molecules. Cu: orange; halogen (X): purple; N-donor ligand (L): green.

In general, possible assignments for the excited states that are responsible for emission phenomena of Cu(I) complexes are ligand-centered (LC)  $\pi \rightarrow \pi^*$  transitions and metal-centered ones (MC). In addition, ligand-to-metal charge transfers (LMCT), involving electronic transitions from an orbital of the organic ligand to a metal-centered orbital, and metal-to-ligand charge-transfer transitions (MLCT), corresponding to the electronic transition from a metal-centered orbital to an orbital of the organic ligand, are commonly found in these compounds.<sup>106</sup> Ford *et al.* have shown that the photoluminescent behavior and geometries of copper(I)-halide aggregates are strictly related.<sup>106</sup> Cu(I)-X aggregates of tetranuclear units  $[\text{Cu}_4\text{I}_4\text{L}_4]$  (L is a substituted pyridine)<sup>21-22</sup> and rhombic  $[\text{Cu}_2(\mu\text{-X})_2]$  dimeric units<sup>107</sup> are of special interest as they have been known to be emissive. Ford *et al.* studied the case of the cluster compound  $[\text{Cu}_4\text{I}_4\text{py}_4]$  (py = pyridine), where two different emission bands have been observed. The high-energy band (HE) dominating at low temperature (77 K) was attributed to a halide-to-ligand charge transfer (XLCT) that may show up in the presence of

unsaturated ligands with accessible  $\pi$ -orbitals.<sup>108</sup> The low-energy band (LE), dominating at room temperature, has been assigned to a cluster centered (CC) transition which is a mixture of halide-to-metal charge transfer (XMCT) and ( $d \rightarrow s,p$ ) metal centered transitions. The term ‘metal-cluster-centered’ was coined to emphasize that the transition is localized on the  $\text{Cu}_4\text{I}_4$  cluster and is essentially independent of the ligand. The  $\text{Cu}\cdots\text{Cu}$  distance is a fundamental parameter which determines the presence of CC bands and must be shorter than the orbital interaction radius (which is equal to the sum of Van der Waals radii of two copper atoms), estimated to be 2.8 Å.<sup>109</sup> Usually, at room temperature the CC transition is combined with a metal-to-ligand charge transfer (MLCT).<sup>109-110</sup>

### 1.1.2.3. Nanoprocessing and size-dependent properties

The typical approaches to generate miniaturized systems in a controlled and repeatable way are *top-down* and *bottom-up* approaches.<sup>111-115</sup> Top-down methods employ tools that reduce the size of bulk materials using different strategies to produce nanostructures with the desired geometry. This approach faces many challenges such as complexity, size limitation around 10-15 nm, and high cost of clean rooms, operation and maintenance of the equipment. On the other hand, bottom-up strategies take the advantage of self-assembly processes of the atomic and molecular components into nanoscale structures by means of covalent and/or non-covalent interactions. This concept somehow tries to mimic the biological systems, for instance, the formation of the double helix in the deoxyribonucleic acid (DNA) molecules is based on the self-assembly of the DNA bases.<sup>116</sup>

The miniaturization of CPs to the nanometer size is an area of growing interest which is trying to develop a new class of highly tailorable functional materials that keep the classical characteristic of bulk CPs with the advantages of nanometer features.<sup>14, 20, 48-49, 54, 62, 73, 78-79, 117-121</sup> According to their dimensionality, nanoscale coordination polymers (NCPs) can be classified as 0D (nanoparticles, including nanospheres and particles with polyhedral shape),<sup>122-123</sup> 1D (fibers, tubes, rods, tapes...)<sup>124-125</sup> and 2D (thin films and membranes).<sup>126</sup> On the other hand, NCPs can be classified, based on their structural regularity, into amorphous or crystalline. Crystalline NCPs offer a good understanding of their composition and structure, and greatly facilitate the determination of structure-property relationships in this class of nanomaterials. Indeed, many strategies have been reported to prepare crystalline NCPs. For instance, crystalline NCPs can be obtained controlling the nucleation and growth of the building blocks through the self-assembly process, and their interactions at specific locations on surfaces.<sup>127-128</sup>

Among these strategies, the fast precipitation approach, where nanoparticles are insoluble in the solvent system whereas the individual precursors are soluble, is widely used for the synthesis of crystalline NCPs.<sup>127</sup> In addition, hydrothermal synthesis, water-in-oil (or reverse) micelles, and microemulsions<sup>129</sup> (the micelles in the

microemulsion act as nanoreactors that assist in controlling the kinetics of particle nucleation and growth), have been successfully used to prepare crystalline NCPs. As far as 2D NCPs are concerned, it is not unusual to find examples of thin films of these nanostructures prepared by liquid-liquid interfacial synthesis; this method is suitable for both 1D and 2D CPs, like those described by Nishihara *et al.*<sup>130-142</sup>

Due to the important role that 1D nanostructures can play in many applications, including electronics,<sup>125</sup> optics,<sup>143</sup> magnetic devices,<sup>144</sup> sensors,<sup>145-146</sup> and as template for functional species,<sup>124</sup> a great effort has been directed toward the development of methods to get control in the formation of 1D-CPs nanostructures (1D-NCPs), such as wires, rods, tubes, and fibres. However, this field of research is still in its infancy, so very few examples have been reported so far.

The development in the nanofabrication techniques has given rise to a revolution in the nanoelectronics industry by scaling down the electronic chips and devices. Most of the interest in nanotechnology is directed toward the precise organization of such nanostructures into more complex nano-architectures and devices. In order to manufacture electronic devices or integrated circuits in molecular scale, different molecular components are required. Molecular wire candidates have to fit some requirements, namely good electrical properties, control over the synthesis conditions, and nanoscale self-organization. If all these requirements are fulfilled, it will be possible to inter-connect and organize them into a molecular circuit.<sup>147-148</sup>

On the other hand, the endless tailorability of CPs that results from the infinite choice of building blocks suggest their potential use for electronic applications.<sup>149</sup> Thus, conductive nanofibers or single chain of 1D-CPs are of great importance for molecular electronics, since they can act as molecular wires. The selected building blocks have to produce 1D-NCPs with two essential features so as to be accessible for molecular electronics applications: firstly, they have to possess high electrical conductivity at the nanometer scale; secondly, they must be able to participate in molecular recognition processes to assemble complex structures.

New methodologies have been developed to isolate few/single chains of 1D-NCPs on insulator substrates (**Figure 1.14**) in order to enable their electrical characterization. In this regard, few examples of 1D-NCPs have been tested as molecular wires.<sup>150</sup> Once again, MMX have been revealed as some of the most suitable candidates to be subjected to these studies, due to their excellent electrical properties.<sup>48-49, 62, 73, 78-79</sup> Recently, Zamora and co-workers<sup>151</sup> were able to isolate nanoribbons of  $[\text{Pt}_2\text{I}(\text{dta})_4]_n$  ( $\text{dta} = \text{MeCS}_2 = \text{dithioacetate}$ ) on mica or highly oriented pyrolytic graphite (HOPG) surfaces. The preparation of the samples was performed by sublimation of single crystals of this CP under high vacuum conditions, obtaining nanoribbons with thicknesses of 3.5 nm and a metallic behavior coincident with that of the bulk crystals. The measurement of the electrical conductivity of the nanowires was achieved in the AFM device, by using as electrodes a gold layer connected to the nanostructures and the AFM probe itself (**Figure 1.15**).

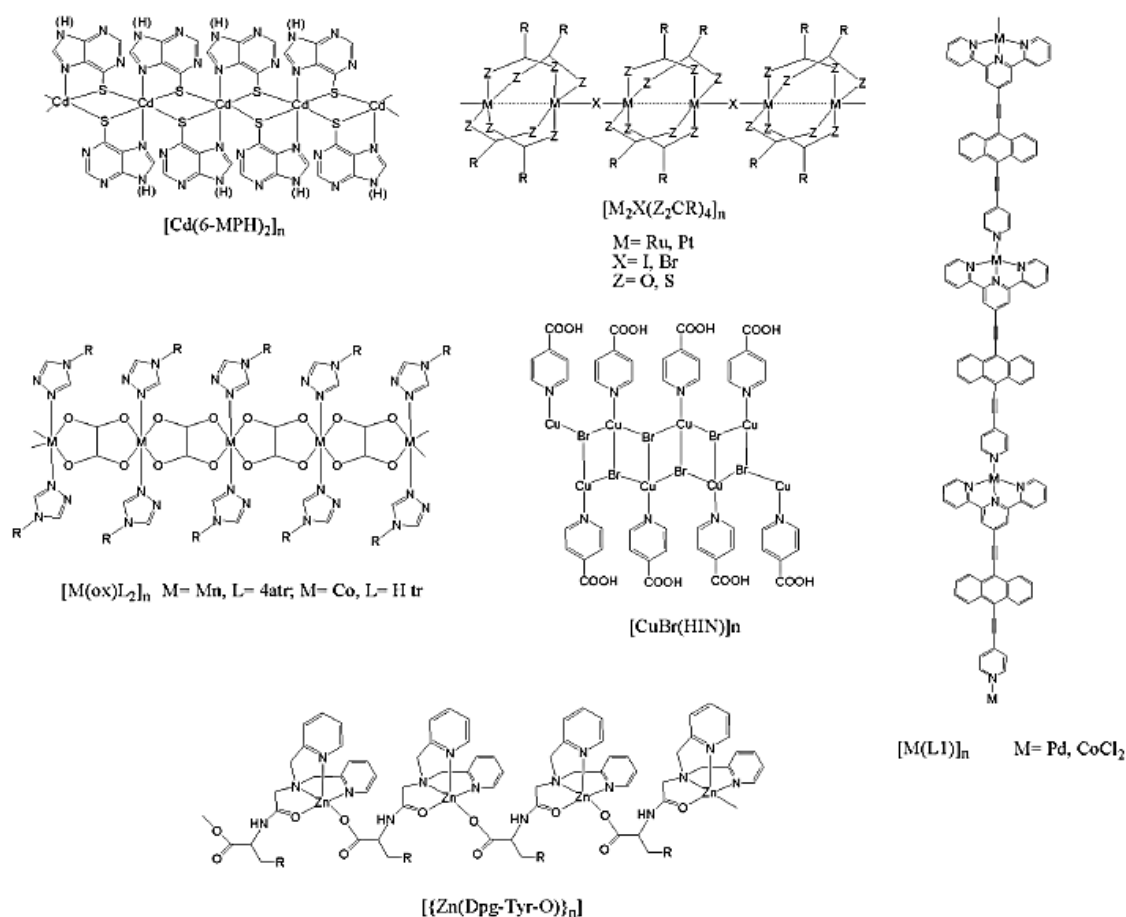


**Figure 1.14.** Examples of 1D-CPs which have been deposited on surfaces as nanostructures, considered as potential candidates to act as nanowires.<sup>125</sup>

From a different point of view, CPs containing biomolecules or bioinspired molecules (Bio-CPs) present great advantages in terms of biocompatibility, turning them into excellent candidates to be used in biomedical applications. These applications include biosensing<sup>152</sup> or delivery of certain molecules such as oligonucleotides or DNA itself.<sup>153</sup> An example of the latter has recently been reported by Vegas *et al.*<sup>154</sup> It consisted of a 1D-CP with copper(II) as metal center, a modified nucleobase (thymine-1-acetic acid, TAcOH) as terminal ligand and 4,4'-bipyridyl (bpy) as bridging ligand, namely  $[Cu(OAc)_2(\mu-bpy)(OH_2)]_n$ . By a simple bottom-up approach it was possible to obtain this CP in the shape of nanofibers with thicknesses equivalent to 12 to 50 single chains, widths of 185 nm and lengths of a few microns. The width of the nanofibers could be tuned when changing synthetic conditions such as the pH of the starting solution, never reaching values over 300 nm. These nanofibers proved to interact with oligonucleotide chains, showing preference for Poly-deoxyadenosine (Poly-A). The fact that the terminal ligands of the CP could recognize their complementary base, as well as the low sizes of the nanostructures (which would allow them to enter the body of a living being), opens them the door to be used as nanocarriers (**Figure 1.16**).

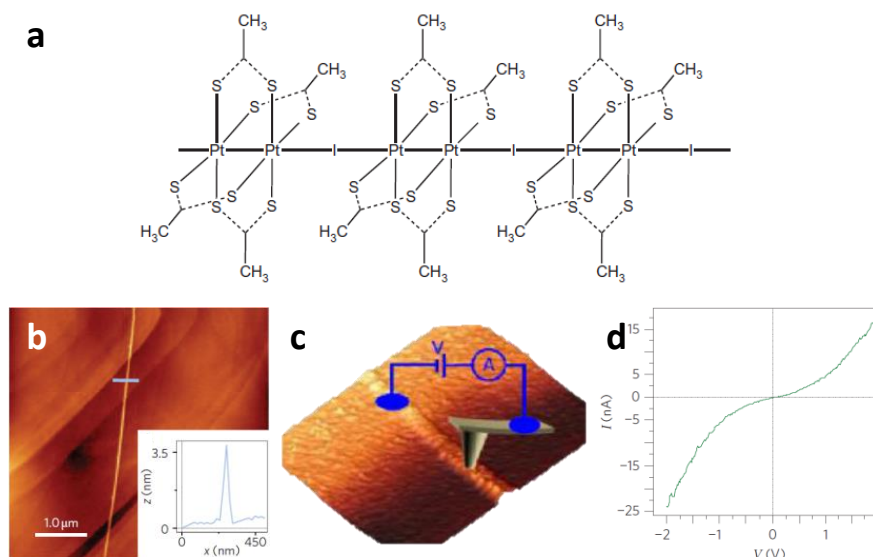


**Figure 1.15.** (a) Schematic representation of a single chain of  $[\text{Pt}_2\text{I}(\text{dta})_4]_n$ . (b) AFM image of single nanoribbon on a HOPG surface directly sublimated from  $[\text{Pt}_2\text{I}(\text{dta})_4]_n$  crystals. The inset shows its height profile taken across one of the nanoribbons. (c) Scheme of the electronic circuit used to measure the current flowing through the nanoribbons (the gold electrode has been omitted for clarity). (d)  $I$ - $V$  curve taken by contacting the nanoribbon at a distance of 100 nm from the gold electrode.<sup>151</sup>

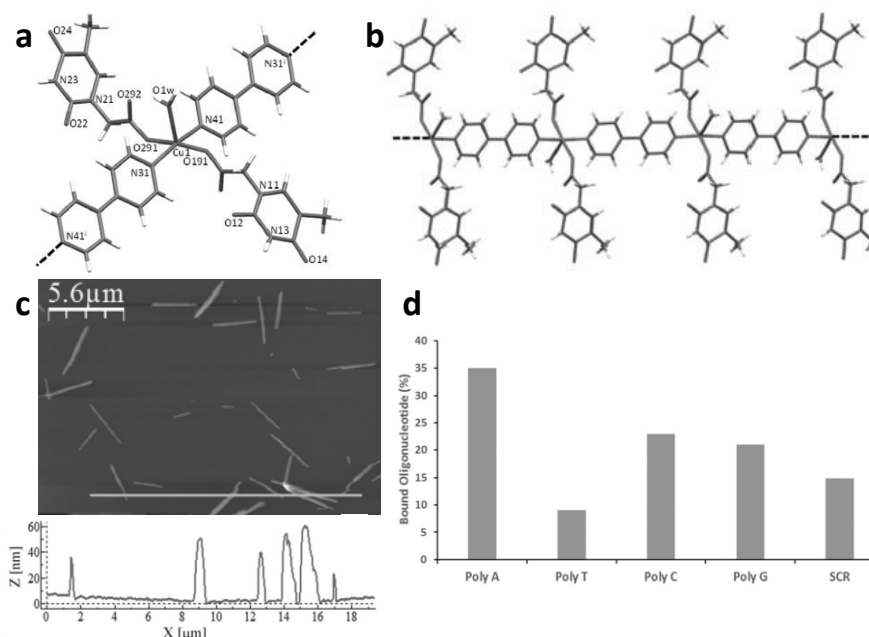


**Figure 1.16.** (a,b) Crystal structure of  $[\text{Cu}(\text{OAcT})_2(\mu\text{-bpy})(\text{OH}_2)]_n$ : (a) asymmetric unit with an extra bpy molecule; (b) Schematic representation of the 1D chain which conforms the CP. (c) AFM image of  $[\text{Cu}(\text{OAcT})_2(\mu\text{-bpy})(\text{OH}_2)]_n$  nanofibers, with its height profile across the white horizontal line. (d) Affinity of different oligonucleotides towards the CP. Equivalence: Poly-A = 5'-(dA)<sub>10</sub>-3'; Poly-T = 5'-(dT)<sub>10</sub>-3'; Poly-C = 5'-(dC)<sub>10</sub>-3'; Poly-G: 5'-(dG)<sub>10</sub>-3'; SCR = 5'-dTdCdGdTdAdAdGdCdAdT-3'. Taken from reference<sup>154</sup>.

## 1.2. Stimuli-responsive materials

Some materials show what is known as a dynamic structure. This means that small variations in physical stimuli, such as temperature or pressure, or chemical ones, such as the presence of a certain molecule as a vapor, induces slight variations in the distances and angles present in their structure, therefore causing a change in one or more properties of these materials, which is called a response. This is why these compounds are known as stimuli-responsive materials. The study of stimuli-responsive features has its origin in biological systems, where the presence of a stimulus triggers a series of reactions within the organism.<sup>94</sup> Starting from this basis, the field of dynamic materials has become a multidisciplinary one.<sup>155</sup>

Many materials have been proven to act as stimuli-responsive materials. This section will be focused on those metal-organic compounds which show this interesting behavior.

Many coordination compounds show a responsive behavior when exposed to a physical stimulus, such as temperature or pressure. When the affected property is luminescence, the terms “luminescence thermochromism” and “luminescence mechanochromism” arise. Compounds with metal centers showing a  $d^{10}$  electronic configuration ( $\text{Cu}^+$ ,  $\text{Au}^+$ ,  $\text{Zn}^{2+}$ ...) with flexible ligands or moieties are very likely to exhibit such features. As an example, herein we present a gold(I) compound,  $[(\text{C}_6\text{F}_5\text{Au})_2(\mu\text{-1,4-diisocyanobenzene})]$ , where  $\text{C}_6\text{F}_5^-$  is pentafluorophenyl.<sup>156</sup> The as-prepared compound showed a blue luminescence, but when it was ground its emission shifted to a yellow color, as an effect of the variation in the aurophilic interactions. This behavior could be reverted to its original state when the compound was exposed to a liquid solvent.

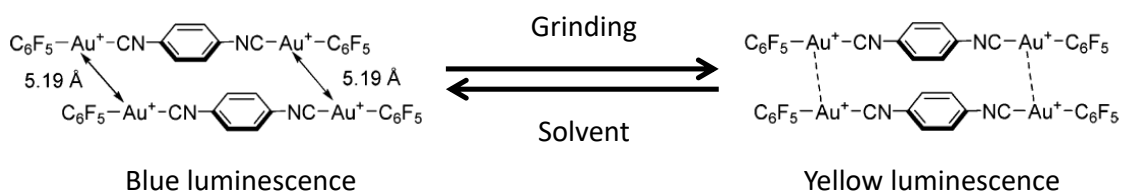


**Figure 1.17.** Schematic explanation of the luminescent mechanochromic behavior of  $[(\text{C}_6\text{F}_5\text{Au})_2(\mu\text{-1,4-diisocyanobenzene})]$ . Taken from references <sup>156</sup> and <sup>94</sup>.

Another kind of iconic dynamic materials are the so-called molecular machines, integrated by catenanes and rotaxanes. This research field, developed by Prof. Sauvage and Prof. Stoddart, made these two scientists be awarded with the Nobel Prize for Chemistry in year 2018. Focusing on catenanes, these entities consist of two interlocked macrocycles; to create these structures, the macrocycles must be synthesized starting from a precursor which acts as a ligand in a coordination compound. Once the macrocycles are generated, the demetallation of the coordination compound in an acidic medium yields the final structure of the catenane (**Figure 1.18**). These molecules are

known to be sensitive to metals in solution, such as lithium, to which the functional groups of the macrocycles can coordinate. Metals can be removed again in an acidic medium.<sup>157</sup>

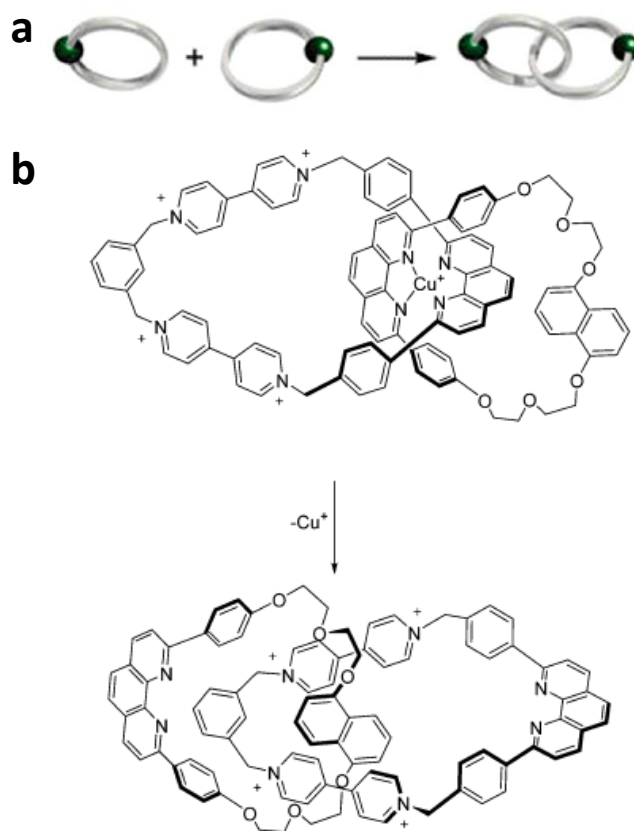


**Figure 1.18.** (a) Schematic representation of the concept of catenane. (b) An example of a catenane synthesized by Sauvage and co-workers.<sup>157</sup> Taken from reference <sup>94</sup>.

As far as CPs are concerned, their study as stimuli-responsive materials is a wide and well known research matter. Since Hardt and co-workers discovered the thermochromic properties of  $[\text{Cu}(\text{py})\text{I}]_n$ ,<sup>158</sup> many other compounds with flexible structures have been thoroughly studied. Even though Cu(I)-X compounds are the clearest examples of coordination polymers and clusters with stimuli-responsive behavior, with changes in their luminescent properties when exposed to temperature, pressure or chemical stimuli, they will not be discussed in this chapter, but in section 2.1. Instead, herein we will illustrate other examples of stimuli-responsive CPs.

One of the most commonly known and widely studied classes of CPs are those with pores in their structures, namely Metal-Organic Frameworks (MOFs). According to Férey and Serre (2009),<sup>159</sup> a MOF will show a stimuli-responsive (or *breathing*) behavior if it shows a tendency to expand and contract with the presence of a chemical or physical stimulus, derived from the flexibility of the organic bridging moieties. When applying a chemical stimulus, *i.e.* the presence of a guest molecule which can



accommodate in the pores of the lattice, the interaction of the functional groups of the flexible organic linkers with the guest molecule causes several scenarios to take place. In general words, these scenarios, discussed by Kitagawa,<sup>160</sup> involve the expansion of the crystal structure of the MOF when the guest is linked, and its contraction when the guest is freed (**Figure 1.19**).

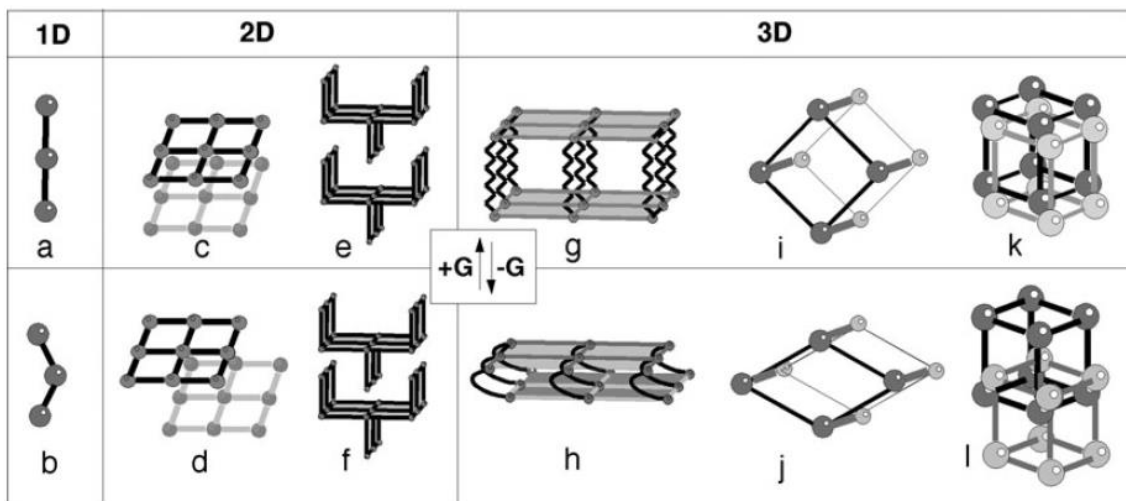


**Figure 1.19.** The “six classes” of Kitagawa; the upper panel represents the situations where the guest molecule (G) is linked to the MOF; the lower panel illustrates the opposite. In all cases, circles represent the metal centers or SBUs, and lines stand for the organic linkers. (a,b) Elongation and shrinking of the 1D chain of a CP (the spaces between chains are occupied by G). (c,d) Superimposed (c) and shifted (d) 2D sheets. (e,f) Shifting of interdigitated moieties in (e), forming 1D channels where G accommodates. (g,h) Elongation and shrinking of flexible pillars (in (g), G is located between the layers). (i,j) Widening and flattening of cages delimited by rigid linkers. (k,l) Interpenetrated grids. Taken from reference <sup>159</sup>, based on Kitagawa’s papers.<sup>160</sup>

One example of this behavior, and an illustration of situations *g* and *h* in **Figure 1.19**, is the case of zirconium phosphates anchored with alkanediphosphonates which act as flexible pillars linking layers of these phosphates. Alberti<sup>161</sup> and Clearfield<sup>162</sup> demonstrated that the phosphate groups in ZrP layers could be partially substituted by alkanediphosphonates when treated at moderately high temperatures (350 K). When the substitution degree is low, a porous 3D moiety is generated, and water molecules can accommodate inside the pores if the correct conditions (300 K, atmosphere with 100% relative humidity) take place. When water is removed, the flexible nature of the alkane chains makes them fold, causing the pores to dramatically shrink (**Figure 1.20**). This behavior is reversible.

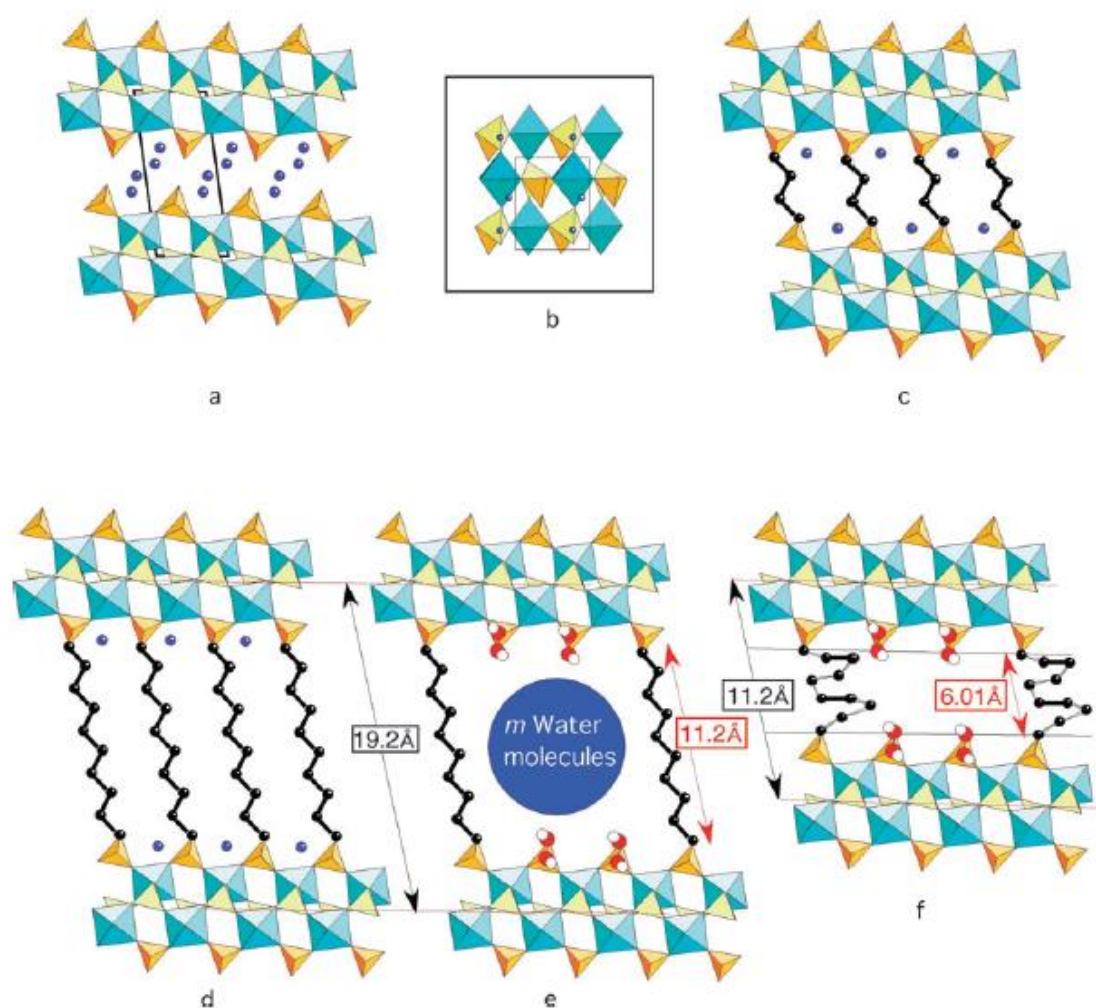


**Figure 1.20.** (a) Polyhedral projection of the structure of  $\gamma$ -ZrP along [010] and (b) along [001]; (c) and (d) [010] projections of the completely pillared Zr 1,4- and 1,10-alkane diphosphonates, (e) a schematic view of the fully hydrated phosphate/diphosphonate and (f) of the corresponding dehydrated sample showing the contraction of the carbon chain. Zr octahedra are in pale blue, phosphate groups in yellow, water molecules in dark blue, OH groups in red and white and the carbons in black. Taken from reference <sup>159</sup>.

As explained before for the general cases of metal-organic entities, it is usual to find that a stimuli-responsive behavior induces a reversible shift in a property of the material. An example of a CP with such characteristics is the electrically responsive MOF [Cu(TCNQ)], where TCNQ<sup>•-</sup> is the radical anion of 7,7,8,8-tetracyanoquinodimethane. This MOF was synthesized as two polymorphs, namely forms I and II, with radically different electrical conductivities: I is a semiconductor with a room-temperature electrical conductivity of  $4.8 \cdot 10^{-3} \text{ S} \cdot \text{cm}^{-1}$ , whereas II is almost an insulator, showing a conductivity of  $5.8 \cdot 10^{-7} \text{ S} \cdot \text{cm}^{-1}$ . When a sample of II is subjected to a voltage in the range between 0 and 6 V, a curious behavior is observed: when reaching 3 V, the compound acts as a switch, changing to a different polymorph which was named as III, which shows a conducting behavior. At 6 V, this intermediate

phase transforms into polymorph I, with the highest conductivity. This behavior is reversible, so when the electric potential is removed, the MOF gradually reverts to its original state (phase II) (**Figure 1.21**).<sup>163</sup>

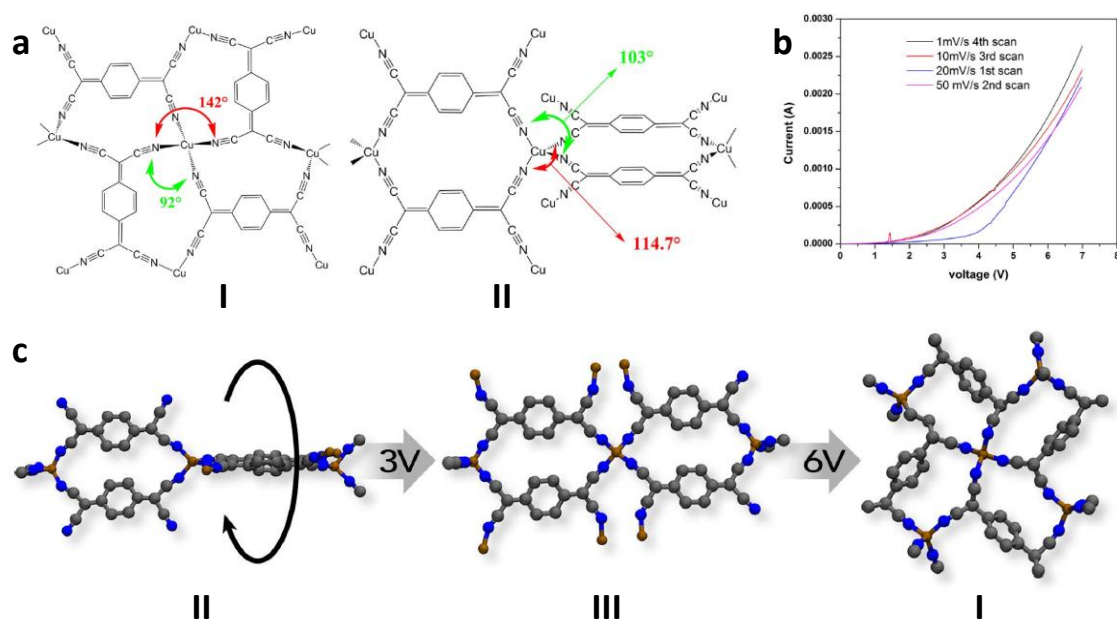


**Figure 1.21.** (a) Schematic representation of  $[\text{Cu}(\text{TCNQ})]_n$  in its polymorphic forms I (left) and II (right). (b) I-V curves of  $[\text{Cu}(\text{TCNQ})]_n$  under applied voltages between 0 and 6 V; the first scan illustrates the switch-like behavior of this MOF. (c) Ball-and-stick representation of the voltage-dependent transitions between the three phases of  $[\text{Cu}(\text{TCNQ})]_n$ . Adapted from reference <sup>163</sup>.

### 1.3. Objectives of the thesis

The purpose of this thesis can be summarized in the following statement:

*The design and synthesis of new stimuli-responsive materials and nanomaterials based on CPs with different dimensionalities (one- or two-dimensional), structures bearing flexible copper(I)-halogen chains and terminal ligands with molecular recognition capability, enabling them to show electrical and luminescent properties which can be tuned with physical or chemical stimuli.*

To achieve this goal, we have selected as building blocks copper(I) iodide and several nitrogen-donor aromatic ligands. The aim of Cu(I) as metal center is to provide luminescent behavior to our CPs thanks to its  $d^{10}$  electronic configuration; moreover, the presence of iodide as bridging ligand imbues the CPs with very flexible structures.

As far as the organic ligands are concerned, N-donor aromatic ligands such as pyridines, pyrimidines and pyrazines are soft bases which easily coordinate to Cu(I), thus enabling the formation of 1D chains where these aromatic molecules act as terminal ligands. The functional groups present in the structure of these ligands will add molecular recognition capability to our CPs, and therefore they will be able to respond to chemical stimuli as well as physical ones. The selected ligands and precursors have been isonicotinic acid (HIN), ethyl isonicotinate (EtIN), 2-amino-5-nitropyridine (ANP), methyl isonicotinate (MeIN), methyl 2-aminoisonicotinate ( $\text{NH}_2$ -MeIN), aminopyrazine (Apyz), 3-chloroisonicotinic acid (Cl-HIN) and 3,5-dichloropyridine ( $\text{Cl}_2$ -py).

In order to implement these new compounds in industrial or daily-life applications, they will also be used as dopants in composite materials by mixing them with organic polymers which will act as matrices. The selected organic matrices are the flexible polymers polyvinylidene difluoride (PVDF) and polylactic acid (PLA), the latter having the advantage of being biodegradable.

In order to fulfill this general purpose, several specific objectives have been established:

#### **1. Synthesis and characterization of CPs as multifunctional and stimuli-responsive materials and nanomaterials:**

- a) Synthesis of coordination polymers via room-temperature and solvothermal methods, and characterization of the products by means of spectroscopic and other complementary techniques.
- b) Study of their luminescent and electrical properties in bulk, and of the influence of physical and chemical stimuli in these properties.
- c) Nanoprocessing of the CPs and study of their properties in the nanoscale.

## **2. Preparation of smart and flexible composite materials**

- a) Combination of nanostructures of the CPs with flexible organic matrices; control over the thickness of the resulting films by varying the deposition method.
- b) Morphological characterization and study of the luminescent and mechanical properties of the composites.

## 1.4. References

1. Evans, O. R.; Lin, W., Crystal Engineering of NLO Materials Based on Metal–Organic Coordination Networks. *Accounts of Chemical Research* **2002**, *35* (7), 511-522.
2. Kitagawa, S.; Noro, S., Coordination Polymers: Infinite Systems. In *Comprehensive Coordination Chemistry II*, Meyer, J. A. M. J., Ed. Pergamon: Oxford, 2003; pp 231-261.
3. Allendorf, M. D.; Stavila, V., Crystal engineering, structure–function relationships, and the future of metal–organic frameworks. *CrystEngComm* **2015**, *17* (2), 229-246.
4. Biradha, K., Crystal engineering: from weak hydrogen bonds to co-ordination bonds. *CrystEngComm* **2003**, *5* (66), 374-384.
5. Mukherjee, A.; Tothadi, S.; Desiraju, G. R., Halogen bonds in crystal engineering: like hydrogen bonds yet different. *Accounts of Chemical Research* **2014**, *47* (8), 2514-2524.
6. Tothadi, S.; Sanphui, P.; Desiraju, G. R., Obtaining Synthron Modularity in Ternary Cocrystals with Hydrogen Bonds and Halogen Bonds. *Crystal Growth & Design* **2014**, *14* (10), 5293-5302.
7. Desiraju, G. R., A bond by any other name. *Angewandte Chemie International Edition* **2011**, *50* (1), 52-59.
8. Li, C. P.; Wu, J. M.; Du, M., Exceptional crystallization diversity and solid-state conversions of Cd(II) coordination frameworks with 5-bromonicotinate directed by solvent media. *Chemistry - A European Journal* **2012**, *18* (39), 12437-12445.
9. Blake, A. J.; Baum, G.; Champness, N. R.; Chung, S. S. M.; Cooke, P. A.; Fenske, D.; Khlobystov, A. N.; Lemenovskii, D. A.; Li, W.-S.; Schröder, M., Long-range chain orientation in 1-D co-ordination polymers as a function of anions and intermolecular aromatic interactions. *Journal of the Chemical Society, Dalton Transactions* **2000**, (23), 4285-4291.
10. Janiak, C., Engineering coordination polymers towards applications. *Dalton Transactions* **2003**, (14), 2781-2804.
11. Coronado, E.; Giménez-Saiz, C.; Martí-Gastaldo, C., Crystal Engineering of Multifunctional Molecular Materials. In *Engineering of Crystalline Materials Properties*, Novoa, J.; Braga, D.; Addadi, L., Eds. Springer: The Netherlands, 2008; pp 173-191.
12. Yu, J.-H.; Xu, J.-Q.; Ye, L.; Ding, H.; Jing, W.-J.; Wang, T.-G.; Xu, J.-N.; Jia, H.-B.; Mu, Z.-C.; Yang, G.-D., Hydrothermal synthesis and characterization of a

copper(I) halide coordination polymer with isonicotinic acid (IN) ligand as a template possessing three-dimensional supramolecular network structure. *Inorganic Chemistry Communications* **2002**, 5 (8), 572-576.

13. Lu, J. Y.; Babb, A. M., An unprecedented interpenetrating structure with two covalently bonded open-frameworks of different dimensionality. *Chemical Communications* **2001**, (9), 821-822.

14. Amo-Ochoa, P.; Welte, L.; Gonzalez-Prieto, R.; Sanz Miguel, P. J.; Gomez-Garcia, C. J.; Mateo-Marti, E.; Delgado, S.; Gomez-Herrero, J.; Zamora, F., Single layers of a multifunctional laminar Cu(I,II) coordination polymer. *Chemical Communications* **2010**, 46 (19), 3262-3264.

15. Noro, S.-i.; Kitagawa, S.; Akutagawa, T.; Nakamura, T., Coordination polymers constructed from transition metal ions and organic N-containing heterocyclic ligands: Crystal structures and microporous properties. *Progress in Polymer Science* **2009**, 34 (3), 240-279.

16. Lu, W.; Wei, Z.; Gu, Z. Y.; Liu, T. F.; Park, J.; Park, J.; Tian, J.; Zhang, M.; Zhang, Q.; Gentle, T., 3rd; Bosch, M.; Zhou, H. C., Tuning the structure and function of metal-organic frameworks via linker design. *Chemical Society Reviews* **2014**, 43 (16), 5561-5593.

17. Zhang, W.-X.; Liao, P.-Q.; Lin, R.-B.; Wei, Y.-S.; Zeng, M.-H.; Chen, X.-M., Metal cluster-based functional porous coordination polymers. *Coordination Chemistry Reviews* **2015**, 293-294, 263-278.

18. Eddaoudi, M.; Moler, D. B.; Li, H.; Chen, B.; Reineke, T. M.; O'Keeffe, M.; Yaghi, O. M., Modular Chemistry: Secondary Building Units as a Basis for the Design of Highly Porous and Robust Metal–Organic Carboxylate Frameworks. *Accounts of Chemical Research* **2001**, 34 (4), 319-330.

19. Tranchemontagne, D. J.; Mendoza-Cortes, J. L.; O'Keeffe, M.; Yaghi, O. M., Secondary building units, nets and bonding in the chemistry of metal-organic frameworks. *Chemical Society Reviews* **2009**, 38 (5), 1257-1283.

20. Mateo-Marti, E.; Welte, L.; Amo-Ochoa, P.; Sanz Miguel, P. J.; Gomez-Herrero, J.; Martin-Gago, J. A.; Zamora, F., Direct evidence of nanowires formation from a Cu(I) coordination polymer. *Chemical Communications* **2008**, (8), 945-947.

21. Cariati, E.; Bourassa, J., Luminescence response of the solid state polynuclear copper(i) iodide materials [CuI(4-picoline)]<sub>x</sub> to volatile organic compounds. *Chemical Communications* **1998**, (16), 1623-1624.

22. Cariati, E.; Bu, X.; Ford, P. C., Solvent- and Vapor-Induced Isomerization between the Luminescent Solids [CuI(4-pic)]<sub>4</sub> and [CuI(4-pic)]<sub>∞</sub> (pic = methylpyridine).

The Structural Basis for the Observed Luminescence Vapochromism. *Chemistry of Materials* **2000**, *12* (11), 3385-3391.

23. Benito, Q.; Le Goff, X. F.; Maron, S.; Fargues, A.; Garcia, A.; Martineau, C.; Taulelle, F.; Kahlal, S.; Gacoin, T.; Boilot, J. P.; Perruchas, S., Polymorphic copper iodide clusters: insights into the mechanochromic luminescence properties. *Journal of the American Chemical Society* **2014**, *136* (32), 11311-11320.

24. Maderlehner, S.; Leitzl, M. J.; Yersin, H.; Pfitzner, A., Halocuprate(I) zigzag chain structures with N-methylated DABCO cations--bright metal-centered luminescence and thermally activated color shifts. *Dalton Transactions* **2015**, *44* (44), 19305-19313.

25. Kitada, N.; Ishida, T., Polymeric one- and two-dimensional copper(i) iodide complexes showing photoluminescence tunable by azaaromatic ligands. *CrystEngComm* **2014**, *16* (34), 8035-8040.

26. Näther, C.; Jeß, I., Crystal Structure of  $\text{infin};2[\text{Cu}_2\text{I}_2(\mu\text{-}4\text{'-}4\text{'-bipyridine})]$  and Investigations on the Thermal Decomposition of  $\text{CuX-}4,4\text{'-bipyridine}$  Coordination Polymers. *Monatshefte für Chemie / Chemical Monthly* **2001**, *132* (8), 897-910.

27. Hassanein, K.; Conesa-Egea, J.; Delgado, S.; Castillo, O.; Benmansour, S.; Martinez, J. I.; Abellan, G.; Gomez-Garcia, C. J.; Zamora, F.; Amo-Ochoa, P., Electrical Conductivity and Strong Luminescence in Copper Iodide Double Chains with Isonicotinato Derivatives. *Chemistry - A European Journal* **2015**, *21* (48), 17282-17292.

28. Amo-Ochoa, P.; Hassanein, K.; Gomez-Garcia, C. J.; Benmansour, S.; Perles, J.; Castillo, O.; Martinez, J. I.; Ocon, P.; Zamora, F., Reversible stimulus-responsive Cu(I) iodide pyridine coordination polymer. *Chemical Communications* **2015**, *51* (76), 14306-14309.

29. Hassanein, K.; Amo-Ochoa, P.; Gomez-Garcia, C. J.; Delgado, S.; Castillo, O.; Ocon, P.; Martinez, J. I.; Perles, J.; Zamora, F., Halo and Pseudohalo Cu(I)-Pyridinato Double Chains with Tunable Physical Properties. *Inorganic Chemistry* **2015**, *54* (22), 10738-10747.

30. Pospisil, J.; Jess, I.; Näther, C.; Necas, M.; Taborsky, P., Luminescence properties of "double-stranded staircase" copper(i) halide coordination polymers with N-containing ligands. *New Journal of Chemistry* **2011**, *35* (4), 861-864.

31. Jeß, I.; Taborsky, P.; Pospíšil, J.; Näther, C., Synthesis, crystal structure, thermal and luminescence properties of  $\text{CuX(2,3-dimethylpyrazine)}$  ( $\text{X} = \text{Cl, Br, I}$ ) coordination polymers. *Dalton Transactions* **2007**, (22), 2263-2270.

32. Troyano, J.; Perles, J.; Amo-Ochoa, P.; Martinez, J. I.; Concepcion Gimeno, M.; Fernandez-Moreira, V.; Zamora, F.; Delgado, S., Luminescent Thermochromism of 2D



Coordination Polymers Based on Copper(I) Halides with 4-Hydroxythiophenol. *Chemistry - A European Journal* **2016**, 22 (50), 18027-18035.

33. Amo-Ochoa, P.; Zamora, F., Coordination polymers with nucleobases: From structural aspects to potential applications. *Coordination Chemistry Reviews* **2014**, 276, 34-58.

34. Verma, S.; Mishra, A. K.; Kumar, J., The many facets of adenine: coordination, crystal patterns, and catalysis. *Accounts of Chemical Research* **2010**, 43 (1), 79-91.

35. Lippert, B., Multiplicity of metal ion binding patterns to nucleobases. *Coordination Chemistry Reviews* **2000**, 200-202, 487-516.

36. Sivakova, S.; Rowan, S. J., Nucleobases as supramolecular motifs. *Chemical Society Reviews* **2005**, 34 (1), 9-21.

37. Amo-Ochoa, P.; Castillo, O.; Alexandre, S. S.; Welte, L.; de Pablo, P. J.; Rodriguez-Tapiador, M. I.; Gomez-Herrero, J.; Zamora, F., Synthesis of designed conductive one-dimensional coordination polymers of Ni(II) with 6-mercaptopurine and 6-thioguanine. *Inorganic Chemistry* **2009**, 48 (16), 7931-7936.

38. Amo-Ochoa, P.; Alexandre, S. S.; Hribesh, S.; Galindo, M. A.; Castillo, O.; Gomez-Garcia, C. J.; Pike, A. R.; Soler, J. M.; Houlton, A.; Zamora, F.; Harrington, R. W.; Clegg, W., Coordination chemistry of 6-thioguanine derivatives with cobalt: toward formation of electrical conductive one-dimensional coordination polymers. *Inorganic Chemistry* **2013**, 52 (9), 5290-5299.

39. Beobide, G.; Castillo, O.; Cepeda, J.; Luque, A.; Pérez-Yáñez, S.; Román, P.; Thomas-Gipson, J., Metal-carboxylato-nucleobase systems: From supramolecular assemblies to 3D porous materials. *Coordination Chemistry Reviews* **2013**, 257 (19-20), 2716-2736.

40. Li, C. P.; Du, M., Role of solvents in coordination supramolecular systems. *Chemical Communications* **2011**, 47 (21), 5958-5972.

41. Kole, G. K.; Vittal, J. J., Solid-state reactivity and structural transformations involving coordination polymers. *Chemical Society Reviews* **2013**, 42 (4), 1755-1775.

42. Zhang, J. P.; Liao, P. Q.; Zhou, H. L.; Lin, R. B.; Chen, X. M., Single-crystal X-ray diffraction studies on structural transformations of porous coordination polymers. *Chemical Society Reviews* **2014**, 43 (16), 5789-5814.

43. Zhao, N.; Sun, F.; He, H.; Jia, J.; Zhu, G., Solvent-Induced Single Crystal To Single Crystal Transformation and Complete Metal Exchange of a Pyrene-Based Metal-Organic Framework. *Crystal Growth & Design* **2014**, 14 (4), 1738-1743.

44. Kitagawa, S.; Kitaura, R.; Noro, S., Functional porous coordination polymers. *Angewandte Chemie International Edition in English* **2004**, 43 (18), 2334-2375.

45. Schneemann, A.; Bon, V.; Schwedler, I.; Senkovska, I.; Kaskel, S.; Fischer, R. A., Flexible metal-organic frameworks. *Chemical Society Reviews* **2014**, *43* (16), 6062-6096.
46. Du, M.; Li, C. P.; Wu, J. M.; Guo, J. H.; Wang, G. C., Destruction and reconstruction of the robust [Cu<sub>2</sub>(OOCR)<sub>4</sub>] unit during crystal structure transformations between two coordination polymers. *Chemical Communications* **2011**, *47* (28), 8088-8090.
47. Motreff, A.; Correa da Costa, R.; Allouchi, H.; Duttine, M.; Mathonière, C.; Duboc, C.; Vincent, J.-M., A fluorous copper(II)-carboxylate complex which magnetically and reversibly responds to humidity in the solid state. *Journal of Fluorine Chemistry* **2012**, *134*, 49-55.
48. Iguchi, H.; Kitao, S.; Seto, M.; Takaishi, S.; Yamashita, M., Predominance of covalency in water-vapor-responsive MMX-type chain complexes revealed by (129)I Mossbauer spectroscopy. *Dalton Transactions* **2014**, *43* (23), 8767-8773.
49. Iguchi, H.; Takaishi, S.; Miyasaka, H.; Yamashita, M.; Matsuzaki, H.; Okamoto, H.; Tanaka, H.; Kuroda, S., Water-vapor-induced reversible switching of electronic states in an MMX-type chain complex with retention of single crystallinity. *Angewandte Chemie International Edition* **2010**, *49* (3), 552-555.
50. Talin, A. A.; Centrone, A.; Ford, A. C.; Foster, M. E.; Stavila, V.; Haney, P.; Kinney, R. A.; Szalai, V.; El Gabaly, F.; Yoon, H. P.; Leonard, F.; Allendorf, M. D., Tunable electrical conductivity in metal-organic framework thin-film devices. *Science* **2014**, *343* (6166), 66-69.
51. Coronado, E.; Minguez Espallargas, G., Dynamic magnetic MOFs. *Chemical Society Reviews* **2013**, *42* (4), 1525-1539.
52. Shan, X.-C.; Jiang, F.-L.; Chen, L.; Wu, M.-Y.; Pan, J.; Wan, X.-Y.; Hong, M.-C., Using cuprophilicity as a multi-responsive chromophore switching color in response to temperature, mechanical force and solvent vapors. *Journal of Materials Chemistry C* **2013**, *1* (28), 4339-4349.
53. Gallego, A.; Castillo, O.; Gomez-Garcia, C. J.; Zamora, F.; Delgado, S., Electrical conductivity and luminescence in coordination polymers based on copper(I)-halides and sulfur-pyrimidine ligands. *Inorganic Chemistry* **2012**, *51* (1), 718-727.
54. Gallego, A.; Hermosa, C.; Castillo, O.; Berlanga, I.; Gomez-Garcia, C. J.; Mateo-Marti, E.; Martinez, J. I.; Flores, F.; Gomez-Navarro, C.; Gomez-Herrero, J.; Delgado, S.; Zamora, F., Solvent-induced delamination of a multifunctional two dimensional coordination polymer. *Advanced Materials* **2013**, *25* (15), 2141-2146.
55. Spingler, B.; Schnidrig, S.; Todorova, T.; Wild, F., Some thoughts about the single crystal growth of small molecules. *CrystEngComm* **2012**, *14* (3), 751-757.

56. Zhou, W.-W.; Zhao, W.; Zhao, X.; Wang, F.-W.; Wei, B., A New 1-D Cu(I) Pyridinate Complex [CuBr(anp)]<sub>n</sub>(anp = 2-amino-5-nitropyridine). *Synthesis and Reactivity in Inorganic, Metal-Organic, and Nano-Metal Chemistry* **2013**, *43* (9), 1171-1174.
57. Moulton, B.; Zaworotko, M. J., From Molecules to Crystal Engineering: Supramolecular Isomerism and Polymorphism in Network Solids. *Chemical Reviews* **2001**, *101* (6), 1629-1658.
58. Heintz, R. A.; Zhao, H.; Ouyang, X.; Grandinetti, G.; Cowen, J.; Dunbar, K. R., New Insight into the Nature of Cu(TCNQ): Solution Routes to Two Distinct Polymorphs and Their Relationship to Crystalline Films That Display Bistable Switching Behavior. *Inorganic Chemistry* **1999**, *38* (1), 144-156.
59. Tao, J.; Wei, R. J.; Huang, R. B.; Zheng, L. S., Polymorphism in spin-crossover systems. *Chemical Society Reviews* **2012**, *41* (2), 703-737.
60. Zhang, G., Polymorphism in unusual one-dimensional coordination polymers based on cadmium(ii) and 2-mercaptopyridine N-oxide. *CrystEngComm* **2013**, *15* (33), 6453-6456.
61. Leong, W. L.; Vittal, J. J., One-dimensional coordination polymers: complexity and diversity in structures, properties, and applications. *Chemical Reviews* **2011**, *111* (2), 688-764.
62. Calzolari, A.; Alexandre, S. S.; Zamora, F.; Di Felice, R., Metallicity in individual MMX chains. *Journal of the American Chemical Society* **2008**, *130* (16), 5552-5562.
63. Chen, C.-T.; Suslick, K. S., One-dimensional coordination polymers: Applications to material science. *Coordination Chemistry Reviews* **1993**, *128* (1-2), 293-322.
64. Canivet, J.; Fateeva, A.; Guo, Y.; Coasne, B.; Farrusseng, D., Water adsorption in MOFs: fundamentals and applications. *Chemical Society Reviews* **2014**, *43* (16), 5594-5617.
65. Cui, Y.; Yue, Y.; Qian, G.; Chen, B., Luminescent functional metal-organic frameworks. *Chemical Reviews* **2012**, *112* (2), 1126-1162.
66. Falcaro, P.; Ricco, R.; Doherty, C. M.; Liang, K.; Hill, A. J.; Styles, M. J., MOF positioning technology and device fabrication. *Chemical Society Reviews* **2014**, *43* (16), 5513-5560.
67. Givaja, G.; Amo-Ochoa, P.; Gomez-Garcia, C. J.; Zamora, F., Electrical conductive coordination polymers. *Chemical Society Reviews* **2012**, *41* (1), 115-147.

68. Gómez-Herrero, J.; Zamora, F., Coordination Polymers for Nanoelectronics. *Advanced Materials* **2011**, *23* (44), 5311-5317.
69. James, S. L., Metal-organic frameworks. *Chemical Society Reviews* **2003**, *32* (5), 276-288.
70. Qiu, S.; Xue, M.; Zhu, G., Metal-organic framework membranes: from synthesis to separation application. *Chemical Society Reviews* **2014**, *43* (16), 6116-6140.
71. Stavila, V.; Talin, A. A.; Allendorf, M. D., MOF-based electronic and optoelectronic devices. *Chemical Society Reviews* **2014**, *43* (16), 5994-6010.
72. Tominaka, S.; Henke, S.; Cheetham, A. K., Coordination polymers of alkali metal trithiocyanurates: structure determinations and ionic conductivity measurements using single crystals. *CrystEngComm* **2013**, *15* (45), 9400-9407.
73. Guijarro, A.; Castillo, O.; Welte, L.; Calzolari, A.; Miguel, P. J. S.; Gómez-García, C. J.; Olea, D.; di Felice, R.; Gómez-Herrero, J.; Zamora, F., Conductive Nanostructures of MMX Chains. *Advanced Functional Materials* **2010**, *20* (9), 1451-1457.
74. Sanda, S.; Biswas, S.; Konar, S., Study of proton conductivity of a 2D flexible MOF and a 1D coordination polymer at higher temperature. *Inorganic Chemistry* **2015**, *54* (4), 1218-22.
75. Neamen, D. A., *An introduction to semiconductor devices*. McGraw-Hill: New York, 2006.
76. Alexandre, S. S.; Soler, J. M.; Sanz Miguel, P. J.; Nunes, R. W.; Yndurain, F.; Gómez-Herrero, J.; Zamora, F., Design of molecular wires based on one-dimensional coordination polymers. *Applied Physics Letters* **2007**, *90* (19), 193107.
77. Castro, M. A.; Roitberg, A. E.; Cukiernik, F. D., Electronic Delocalization in Coordination Polymers Based on Bimetallic Carboxylates. *Journal of Chemical Theory and Computation* **2013**, *9* (6), 2609-2616.
78. Olea, D.; Gonzalez-Prieto, R.; Priego, J. L.; Barral, M. C.; de Pablo, P. J.; Torres, M. R.; Gomez-Herrero, J.; Jimenez-Aparicio, R.; Zamora, F., MMX polymer chains on surfaces. *Chemical Communications* **2007**, (16), 1591-1593.
79. Welte, L.; Gonzalez-Prieto, R.; Olea, D.; Torres, M. R.; Priego, J. L.; Jimenez-Aparicio, R.; Gomez-Herrero, J.; Zamora, F., Time-dependence structures of coordination network wires in solution. *ACS Nano* **2008**, *2* (10), 2051-2056.
80. Albrecht, C., Joseph R. Lakowicz: Principles of fluorescence spectroscopy, 3rd Edition. *Analytical and Bioanalytical Chemistry* **2008**, *390* (5), 1223-1224.

81. Dumur, F., Recent advances in organic light-emitting devices comprising copper complexes: A realistic approach for low-cost and highly emissive devices? *Organic Electronics* **2015**, *21*, 27-39.
82. Liu, W.; Fang, Y.; Wei, G. Z.; Teat, S. J.; Xiong, K.; Hu, Z.; Lustig, W. P.; Li, J., A Family of Highly Efficient CuI-Based Lighting Phosphors Prepared by a Systematic, Bottom-up Synthetic Approach. *Journal of the American Chemical Society* **2015**, *137* (29), 9400-9408.
83. Liu, Z.; Qayyum, M. F.; Wu, C.; Whited, M. T.; Djurovich, P. I.; Hodgson, K. O.; Hedman, B.; Solomon, E. I.; Thompson, M. E., A codeposition route to CuI-pyridine coordination complexes for organic light-emitting diodes. *Journal of the American Chemical Society* **2011**, *133* (11), 3700-3703.
84. Liu, Z.; Qiu, J.; Wei, F.; Wang, J.; Liu, X.; Helander, M. G.; Rodney, S.; Wang, Z.; Bian, Z.; Lu, Z.; Thompson, M. E.; Huang, C., Simple and High Efficiency Phosphorescence Organic Light-Emitting Diodes with Codeposited Copper(I) Emitter. *Chemistry of Materials* **2014**, *26* (7), 2368-2373.
85. Yam, V. W.; Au, V. K.; Leung, S. Y., Light-Emitting Self-Assembled Materials Based on d(8) and d(10) Transition Metal Complexes. *Chemical Reviews* **2015**, *115* (15), 7589-7728.
86. Zhao, Q.; Li, F.; Huang, C., Phosphorescent chemosensors based on heavy-metal complexes. *Chemical Society Reviews* **2010**, *39* (8), 3007-3030.
87. You, Y.; Lee, S.; Kim, T.; Ohkubo, K.; Chae, W. S.; Fukuzumi, S.; Jhon, G. J.; Nam, W.; Lippard, S. J., Phosphorescent sensor for biological mobile zinc. *Journal of the American Chemical Society* **2011**, *133* (45), 18328-18342.
88. Cui, Y.; Yue, Y.; Qian, G.; Chen, B., Luminescent functional metal-organic frameworks. *Chemical Reviews* **2012**, *112* (2), 1126-1162.
89. Wenger, O. S., Vapochromism in organometallic and coordination complexes: chemical sensors for volatile organic compounds. *Chemical Reviews* **2013**, *113* (5), 3686-3733.
90. Hu, Z.; Deibert, B. J.; Li, J., Luminescent metal-organic frameworks for chemical sensing and explosive detection. *Chemical Society Reviews* **2014**, *43* (16), 5815-5840.
91. Benito, Q.; Baptiste, B.; Polian, A.; Delbes, L.; Martinelli, L.; Gacoin, T.; Boilot, J. P.; Perruchas, S., Pressure Control of Cuprophilic Interactions in a Luminescent Mechanochromic Copper Cluster. *Inorganic Chemistry* **2015**, *54* (20), 9821-9825.
92. Benito, Q.; Goff, X. F.; Nocton, G.; Fargues, A.; Garcia, A.; Berhault, A.; Kahlal, S.; Saillard, J. Y.; Martineau, C.; Trebosc, J.; Gacoin, T.; Boilot, J. P.;

- Perruchas, S., Geometry flexibility of copper iodide clusters: variability in luminescence thermochromism. *Inorganic Chemistry* **2015**, *54* (9), 4483-4494.
93. Coudert, F.-X., Responsive Metal–Organic Frameworks and Framework Materials: Under Pressure, Taking the Heat, in the Spotlight, with Friends. *Chemistry of Materials* **2015**, *27* (6), 1905-1916.
  94. McConnell, A. J.; Wood, C. S.; Neelakandan, P. P.; Nitschke, J. R., Stimuli-Responsive Metal-Ligand Assemblies. *Chemical Reviews* **2015**, *115* (15), 7729-7793.
  95. Zeng, G.; Xing, S.; Han, X.; Xin, B.; Yang, Y.; Wang, X.; Li, G.; Shi, Z.; Feng, S., Reversible photoluminescence switching behavior and luminescence thermochromism of copper(I) halide cluster coordination polymers. *RSC Advances* **2015**, *5* (51), 40792-40797.
  96. Tronic, T. A.; deKrafft, K. E.; Lim, M. J.; Ley, A. N.; Pike, R. D., Copper(I) cyanide networks: synthesis, luminescence behavior and thermal analysis. Part 1. Diimine ligands. *Inorganic Chemistry* **2007**, *46* (21), 8897-8912.
  97. Peng, R.; Li, M.; Li, D., Copper(I) halides: A versatile family in coordination chemistry and crystal engineering. *Coordination Chemistry Reviews* **2010**, *254* (1-2), 1-18.
  98. Slabbert, C.; Rademeyer, M., One-dimensional halide-bridged polymers of metal cations with mono-heterocyclic donor ligands or cations: A review correlating chemical composition, connectivity and chain conformation. *Coordination Chemistry Reviews* **2015**, *288*, 18-49.
  99. Arnby, C. H.; Jagner, S.; Dance, I., Questions for crystal engineering of halocuprate complexes: concepts for a difficult system. *CrystEngComm* **2004**, *6* (46) 257-275.
  100. Graham, P. M.; Pike, R. D.; Sabat, M.; Bailey, R. D.; Pennington, W. T., Coordination polymers of copper(I) halides. *Inorganic Chemistry* **2000**, *39* (22), 5121-5132.
  101. Maini, L.; Braga, D.; Mazzeo, P. P.; Maschio, L.; Rerat, M.; Manet, I.; Ventura, B., Dual luminescence in solid CuI(piperazine): hypothesis of an emissive 1-D delocalized excited state. *Dalton Transactions* **2015**, *44* (29), 13003-13006.
  102. Hashimoto, M.; Igawa, S.; Yashima, M.; Kawata, I.; Hoshino, M.; Osawa, M., Highly efficient green organic light-emitting diodes containing luminescent three-coordinate copper(I) complexes. *Journal of the American Chemical Society* **2011**, *133* (27), 10348-10351.
  103. Volz, D.; Hirschbiel, A. F.; Zink, D. M.; Friedrichs, J.; Nieger, M.; Baumann, T.; Bräse, S.; Barner-Kowollik, C., Highly efficient photoluminescent Cu(I)–PyrPHOS-metallopolymers. *Journal of Materials Chemistry C* **2014**, *2* (8) 1457-1462.

104. Volz, D.; Zink, D. M.; Bocksrocker, T.; Friedrichs, J.; Nieger, M.; Baumann, T.; Lemmer, U.; Bräse, S., Molecular Construction Kit for Tuning Solubility, Stability and Luminescence Properties: Heteroleptic MePyrPHOS-Copper Iodide-Complexes and their Application in Organic Light-Emitting Diodes. *Chemistry of Materials* **2013**, 25 (17), 3414-3426.
105. Barbieri, A.; Accorsi, G.; Armaroli, N., Luminescent complexes beyond the platinum group: the d10 avenue. *Chemical Communications* **2008**, (19), 2185-2193.
106. Ford, P. C.; Cariati, E.; Bourassa, J., Photoluminescence Properties of Multinuclear Copper(I) Compounds. *Chemical Reviews* **1999**, 99 (12), 3625-3648.
107. Tsuge, K.; Chishina, Y.; Hashiguchi, H.; Sasaki, Y.; Kato, M.; Ishizaka, S.; Kitamura, N., Luminescent copper(I) complexes with halogenido-bridged dimeric core. *Coordination Chemistry Reviews* **2016**, 306, 636-651.
108. Tran, D.; Bourassa, J. L.; Ford, P. C., Pressure-Induced Luminescence Rigidochromism in the Photophysics of the Cuprous Iodide Cluster Cu<sub>4</sub>I<sub>4</sub>py<sub>4</sub>. *Inorganic Chemistry* **1997**, 36 (3), 439-442.
109. Vitale, M.; Ford, P. C., Luminescent mixed ligand copper(I) clusters (CuI)<sub>n</sub>(L)<sub>m</sub> (L=pyridine, piperidine): thermodynamic control of molecular and supramolecular species. *Coordination Chemistry Reviews* **2001**, 219-221, 3-16.
110. Braga, D.; Grepioni, F.; Maini, L.; Mazzeo, P. P.; Ventura, B., Solid-state reactivity of copper(I) iodide: luminescent 2D-coordination polymers of CuI with saturated bidentate nitrogen bases. *New Journal of Chemistry* **2011**, 35 (2), 339-344.
111. Rodriguez-San-Miguel, D.; Amo-Ochoa, P.; Zamora, F., MasterChem: cooking 2D-polymers. *Chemical Communications* **2016**, 52 (22), 4113-4127.
112. Barth, J. V.; Costantini, G.; Kern, K., Engineering atomic and molecular nanostructures at surfaces. *Nature* **2005**, 437 (7059), 671-679.
113. Biswas, A.; Bayer, I. S.; Biris, A. S.; Wang, T.; Dervishi, E.; Faupel, F., Advances in top-down and bottom-up surface nanofabrication: techniques, applications & future prospects. *Advanced Colloid and Interface Science* **2012**, 170 (1-2), 2-27.
114. Mailly, D., Nanofabrication techniques. *The European Physical Journal Special Topics* **2009**, 172 (1), 333-342.
115. Santos, A.; Deen, M. J.; Marsal, L. F., Low-cost fabrication technologies for nanostructures: state-of-the-art and potential. *Nanotechnology* **2015**, 26 (4), 042001.
116. Olea, D.; Alexandre, S. S.; Amo-Ochoa, P.; Guijarro, A.; de Jesús, F.; Soler, J. M.; de Pablo, P. J.; Zamora, F.; Gómez-Herrero, J., From coordination polymer macrocrystals to nanometric individual chains. *Advanced Materials* **2005**, 14, 1761-1765.

117. Meng, L. R.; Mo, R.; Zhou, H.; Wang, G.; Chen, W.; Wang, D.; Peng, Q., Synthesis of Luminescent Cubic Phase One-Dimensional CuI Nanostructures in Solution. *Crystal Growth & Design* **2010**, *10* (8), 3387-3390.
118. Troyano, J.; Perles, J.; Amo-Ochoa, P.; Martínez, J. I.; Zamora, F.; Delgado, S., Reversible recrystallization process of copper and silver thioacetamide–halide coordination polymers and their basic building blocks. *CrystEngComm* **2014**, *16* (35), 8224-8231.
119. Hermosa, C.; Horrocks, B. R.; Martinez, J. I.; Liscio, F.; Gomez-Herrero, J.; Zamora, F., Mechanical and optical properties of ultralarge flakes of a metal-organic framework with molecular thickness. *Chemical Science* **2015**, *6* (4), 2553-2558.
120. Otero-Irurueta, G.; Hernandez-Rodriguez, I.; Martinez, J. I.; Palacios-Rivera, R.; Palomares, F. J.; Lopez, M. F.; Gallego, A. I.; Delgado, S.; Zamora, F.; Mendez, J.; Martin-Gago, J. A., On-surface self-organization of a robust metal-organic cluster based on copper(I) with chloride and organosulphur ligands. *Chemical Communications* **2015**, *51* (15), 3243-3246.
121. Troyano, J.; Castillo, Ó.; Amo-Ochoa, P.; Fernández-Moreira, V.; Gómez-García, C. J.; Zamora, F.; Delgado, S., A crystalline and free-standing silver thiocarboxylate thin-film showing high green to yellow luminescence. *Journal of Materials Chemistry C* **2016**, *4* (36), 8545-8551.
122. Oh, M.; Mirkin, C. A., Chemically tailorable colloidal particles from infinite coordination polymers. *Nature* **2005**, *438* (7068), 651-654.
123. Furukawa, S.; Reboul, J.; Diring, S.; Sumida, K.; Kitagawa, S., Structuring of metal-organic frameworks at the mesoscopic/macrosopic scale. *Chemical Society Reviews* **2014**, *43* (16), 5700-5734.
124. Puigmarti-Luis, J.; Rubio-Martinez, M.; Hartfelder, U.; Imaz, I.; MasPOCH, D.; Dittrich, P. S., Coordination polymer nanofibers generated by microfluidic synthesis. *Journal of the American Chemical Society* **2011**, *133* (12), 4216-4219.
125. Mas-Balleste, R.; Gomez-Herrero, J.; Zamora, F., One-dimensional coordination polymers on surfaces: towards single molecule devices. *Chemical Society Reviews* **2010**, *39* (11), 4220-4233.
126. Beldon, P. J.; Tominaka, S.; Singh, P.; Saha Dasgupta, T.; Bithell, E. G.; Cheetham, A. K., Layered structures and nanosheets of pyrimidinethiolate coordination polymers. *Chemical Communications* **2014**, *50* (30), 3955-7.
127. Carne, A.; Carbonell, C.; Imaz, I.; MasPOCH, D., Nanoscale metal-organic materials. *Chemical Society Reviews* **2011**, *40* (1), 291-305.



128. Lin, W.; Rieter, W. J.; Taylor, K. M., Modular synthesis of functional nanoscale coordination polymers. *Angewandte Chemie International Edition in English* **2009**, *48* (4), 650-658.
129. Taylor, K. M.; Jin, A.; Lin, W., Surfactant-assisted synthesis of nanoscale gadolinium metal-organic frameworks for potential multimodal imaging. *Angewandte Chemie International Edition* **2008**, *47* (40), 7722-7725.
130. Kambe, T.; Sakamoto, R.; Hoshiko, K.; Takada, K.; Miyachi, M.; Ryu, J. H.; Sasaki, S.; Kim, J.; Nakazato, K.; Takata, M.; Nishihara, H., pi-Conjugated nickel bis(dithiolene) complex nanosheet. *Journal of the American Chemical Society* **2013**, *135* (7), 2462-2465.
131. Matsuoka, R.; Toyoda, R.; Sakamoto, R.; Tsuchiya, M.; Hoshiko, K.; Nagayama, T.; Nonoguchi, Y.; Sugimoto, K.; Nishibori, E.; Kawai, T.; Nishihara, H., Bis(dipyrinato)metal(ii) coordination polymers: crystallization, exfoliation into single wires, and electric conversion ability. *Chemical Science* **2015**, *6* (5), 2853-2858.
132. Takada, K.; Sakamoto, R.; Yi, S. T.; Katagiri, S.; Kambe, T.; Nishihara, H., Electrochromic bis(terpyridine)metal complex nanosheets. *Journal of the American Chemical Society* **2015**, *137* (14), 4681-4689.
133. Sakamoto, R.; Hoshiko, K.; Liu, Q.; Yagi, T.; Nagayama, T.; Kusaka, S.; Tsuchiya, M.; Kitagawa, Y.; Wong, W. Y.; Nishihara, H., A photofunctional bottom-up bis(dipyrinato)zinc(II) complex nanosheet. *Nature Communications* **2015**, *6*, 6713.
134. Sakamoto, R.; Takada, K.; Sun, X.; Pal, T.; Tsukamoto, T.; Phua, E. J. H.; Rapakousiou, A.; Hoshiko, K.; Nishihara, H., The coordination nanosheet (CONASH). *Coordination Chemistry Reviews* **2016**, *320-321*, 118-128.
135. Mustafar, S.; Wu, K.-H.; Toyoda, R.; Takada, K.; Maeda, H.; Miyachi, M.; Sakamoto, R.; Nishihara, H., Electrochemical fabrication of one-dimensional porphyrinic wires on electrodes. *Inorganic Chemistry Frontiers* **2016**, *3* (3), 370-375.
136. Sakamoto, R.; Yagi, T.; Hoshiko, K.; Kusaka, S.; Matsuoka, R.; Maeda, H.; Liu, Z.; Liu, Q.; Wong, W. Y.; Nishihara, H., Photofunctionality in Porphyrin-Hybridized Bis(dipyrinato)zinc(II) Complex Micro- and Nanosheets. *Angewandte Chemie International Edition* **2017**, *56* (13), 3526-3530.
137. Sakamoto, R., Bottom-up Creation of Functional Low-Dimensional Materials Based on Metal Complexes. *Bulletin of the Chemical Society of Japan* **2017**, *90* (3), 272-278.
138. Rapakousiou, A.; Sakamoto, R.; Shiotsuki, R.; Matsuoka, R.; Nakajima, U.; Pal, T.; Shimada, R.; Hossain, A.; Masunaga, H.; Horike, S.; Kitagawa, Y.; Sasaki, S.; Kato, K.; Ozawa, T.; Astruc, D.; Nishihara, H., Liquid/Liquid Interfacial Synthesis of a Click Nanosheet. *Chemistry - A European Journal* **2017**, *23* (35), 8443-8449.

139. Maeda, H.; Sakamoto, R.; Nishihara, H., Interfacial synthesis of electrofunctional coordination nanowires and nanosheets of bis(terpyridine) complexes. *Coordination Chemistry Reviews* **2017**, *346*, 139-149.
140. Aoki, R.; Toyoda, R.; Kogel, J. F.; Sakamoto, R.; Kumar, J.; Kitagawa, Y.; Harano, K.; Kawai, T.; Nishihara, H., Bis(dipyrrinato)zinc(II) Complex Chiroptical Wires: Exfoliation into Single Strands and Intensification of Circularly Polarized Luminescence. *Journal of the American Chemical Society* **2017**, *139* (45), 16024-16027.
141. Tsukamoto, T.; Takada, K.; Sakamoto, R.; Matsuoka, R.; Toyoda, R.; Maeda, H.; Yagi, T.; Nishikawa, M.; Shinjo, N.; Amano, S.; Iokawa, T.; Ishibashi, N.; Oi, T.; Kanayama, K.; Kinugawa, R.; Koda, Y.; Komura, T.; Nakajima, S.; Fukuyama, R.; Fuse, N.; Mizui, M.; Miyasaki, M.; Yamashita, Y.; Yamada, K.; Zhang, W.; Han, R.; Liu, W.; Tsubomura, T.; Nishihara, H., Coordination Nanosheets Based on Terpyridine-Zinc(II) Complexes: As Photoactive Host Materials. *Journal of the American Chemical Society* **2017**, *139* (15), 5359-5366.
142. Matsuoka, R.; Sakamoto, R.; Hoshiko, K.; Sasaki, S.; Masunaga, H.; Nagashio, K.; Nishihara, H., Crystalline Graphdiyne Nanosheets Produced at a Gas/Liquid or Liquid/Liquid Interface. *Journal of the American Chemical Society* **2017**, *139* (8), 3145-3152.
143. Zhang, X.; Chen, Z. K.; Loh, K. P., Coordination-assisted assembly of 1-D nanostructured light-harvesting antenna. *Journal of the American Chemical Society* **2009**, *131* (21), 7210-7211.
144. Coronado, E.; Galán-Mascarós, J. R.; Monrabal-Capilla, M.; García-Martínez, J.; Pardo-Ibáñez, P., Bistable Spin-Crossover Nanoparticles Showing Magnetic Thermal Hysteresis near Room Temperature. *Advanced Materials* **2007**, *19* (10), 1359-1361.
145. An, J.; Shade, C. M.; Chengelis-Czegan, D. A.; Petoud, S.; Rosi, N. L., Zinc-adeninate metal-organic framework for aqueous encapsulation and sensitization of near-infrared and visible emitting lanthanide cations. *Journal of the American Chemical Society* **2011**, *133* (5), 1220-1223.
146. Guo, S.; Wang, E., Functional micro/nanostructures: simple synthesis and application in sensors, fuel cells, and gene delivery. *Accounts of Chemical Research* **2011**, *44* (7), 491-500.
147. Robertson, N.; McGowan, C. A., A comparison of potential molecular wires as components for molecular electronics. *Chemical Society Reviews* **2003**, *32* (2), 96-103.
148. James, D.; Tour, J., In *Molecular Wires and Electronics*, Springer-Heidelberg: Berlin, 2005; Vol. 257, pp 33-62.

149. Hendon, C. H.; Tiana, D.; Walsh, A., Conductive metal-organic frameworks and networks: fact or fantasy? *Physical Chemistry and Chemical Physics* **2012**, *14* (38), 13120-13132.
150. Garcia-Couceiro, U.; Olea, D.; Castillo, O.; Luque, A.; Roman, P.; de Pablo, P. J.; Gomez-Herrero, J.; Zamora, F., Scanning probe microscopy characterization of single chains based on a one-dimensional oxalato-bridged manganese(II) complex with 4-aminotriazole. *Inorganic Chemistry* **2005**, *44* (23), 8343-8348.
151. Gentili, D.; Givaja, G.; Mas-Balleste, R.; Azani, M. R.; Shehu, A.; Leonardi, F.; Mateo-Marti, E.; Greco, P.; Zamora, F.; Cavallini, M., Patterned conductive nanostructures from reversible self-assembly of 1D coordination polymer. *Chemical Science* **2012**, *3* (6), 2047-2051.
152. Tan, H.; Zhang, L.; Ma, C.; Song, Y.; Xu, F.; Chen, S.; Wang, L., Terbium-based coordination polymer nanoparticles for detection of ciprofloxacin in tablets and biological fluids. *ACS Applied Materials and Interfaces* **2013**, *5* (22), 11791-11796.
153. Wang, F.; Liu, B.; Huang, P. J.; Liu, J., Rationally designed nucleobase and nucleotide coordinated nanoparticles for selective DNA adsorption and detection. *Analytical Chemistry* **2013**, *85* (24), 12144-12151.
154. Vegas, V. G.; Lorca, R.; Latorre, A.; Hassanein, K.; Gomez-Garcia, C. J.; Castillo, O.; Somoza, A.; Zamora, F.; Amo-Ochoa, P., Copper(II)-Thymine Coordination Polymer Nanoribbons as Potential Oligonucleotide Nanocarriers. *Angewandte Chemie International Edition* **2017**, *56* (4), 987-991.
155. *Intelligent Stimuli-Responsive Materials*. Li, Q., Ed.; John John Wiley and Sons: Hoboken, NJ, 2013.
156. Ito, H.; Saito, T.; Oshima, N.; Kitamura, N.; Ishizaka, S.; Hinatsu, Y.; Wakeshima, M.; Kato, M.; Tsuge, K.; Sawamura, M., Reversible mechanochromic luminescence of [(C<sub>6</sub>F<sub>5</sub>Au)<sub>2</sub>( $\mu$ -1,4-diisocyanobenzene)]. *Journal of the American Chemical Society* **2008**, *130* (31), 10044-10045.
157. Amabilino, D. B.; Dietrich-Buchecker, C. O.; Livoreil, A.; Perez-Garcia, L.; Sauvage, J. P.; Stoddart, J. F., A Switchable Hybrid [2]-Catenane Based on Transition Metal Complexation and pi-Electron Donor-Acceptor Interactions. *Journal of the American Chemical Society* **1996**, *118* (16), 3905-3913.
158. Hardt, H. D.; Pierre, A., Fluorescence thermochromism and symmetry of copper(I) complexes. *Inorganica Chimica Acta* **1977**, *25*, L59-L60.
159. Ferey, G.; Serre, C., Large breathing effects in three-dimensional porous hybrid matter: facts, analyses, rules and consequences. *Chemical Society Reviews* **2009**, *38* (5), 1380-1399.

160. Kitagawa, S.; Uemura, K., Dynamic porous properties of coordination polymers inspired by hydrogen bonds. *Chemical Society Reviews* **2005**, 34 (2), 109-119.
161. Alberti, G.; Murcia-Mascarós, S.; Vivani, R., Pillared Derivatives of  $\gamma$ -Zirconium Phosphate Containing Nonrigid Alkyl Chain Pillars. *Journal of the American Chemical Society* **1998**, 120 (36), 9291-9295.
162. Byrd, H.; Clearfield, A.; Poojary, D.; Reis, K. P.; Thompson, M. E., Crystal Structure of a Porous Zirconium Phosphate/Phosphonate Compound and Photocatalytic Hydrogen Production from Related Materials. *Chemistry of Materials* **1996**, 8 (9), 2239-2246.
163. Fernandez, C. A.; Martin, P. C.; Schaef, T.; Bowden, M. E.; Thallapally, P. K.; Dang, L.; Xu, W.; Chen, X.; McGrail, B. P., An electrically switchable metal-organic framework. *Scientific Reports* **2014**, 4, 6114.

## **Chapter 2. Coordination Polymers based on the flexibility of the copper(I)-iodide double *zigzag* chain**

## 2.1. Introduction: the double *zigzag* Cu(I)-I chain.

Among coordination polymers (CPs), those containing copper(I) ascend to thousands, with as many discrete compounds formed by clusters of this metal center. Within this family of CPs arises a large sub-family, formed by compounds with the general formula  $[\text{CuXL}]_n$ , where X is a halide and L is an organic ligand, generally a N-donor or S-donor ligand. Although these compounds were discovered for around a century,<sup>1</sup> it was not until the 1970s that the scientific community started showing a massive interest for their synthesis, structure and properties. This was propitiated by a great advance in the development of X-ray diffraction techniques.<sup>2-30</sup>

$[\text{CuXL}]_n$  CPs can present a wide variety of structural motifs (**Figure 2.1**), but one of the most common ones is the double *zigzag* chain (**Figure 2.2**).<sup>10</sup> These compounds are characterized for showing short  $\text{Cu}\cdots\text{Cu}$  distances, close to (or lower than) the sum of Van der Waals radii (2.80 Å), as well as great flexibility, arising from a very good overlapping between the orbitals of copper and halogen (which is even better when the halogen is iodine). As explained in section 1.2, most stimuli-responsive materials show this kind of behavior due to slight, but critical, structure changes caused by the effect of stimuli such as pressure, temperature or certain chemical compounds present in the environment surrounding them. In this case, when these external stimuli exert their effects on Cu(I)-I based compounds, they will behave like elastic springs (**Figure 2.3**), with a subsequent modification in the  $\text{Cu}\cdots\text{Cu}$  and Cu-X distances and in the angles. Thus, a slight shrinking of the  $\text{Cu}\cdots\text{Cu}$  distances improves the metallophilic interactions between the copper atoms, also known as cuprophilic interactions. The term *cuprophilicity* was coined in the 1990s, and this phenomenon has been studied for years as the cause of the variations in the luminescent properties of these compounds.<sup>31-33</sup>

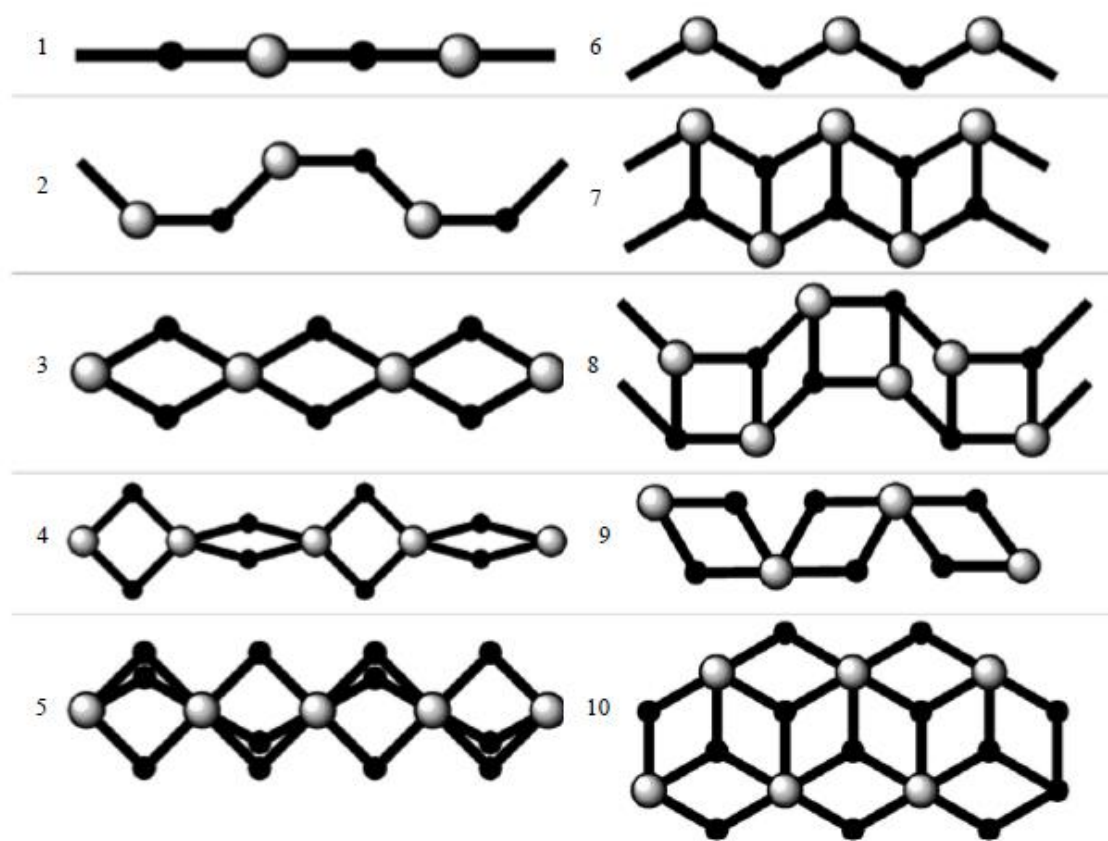


**Figure 2.1.** Compilation of all the structures displayed by CPs based on metal-halogen chains (Metal center:  $\circ$ ; Halide ligand:  $\bullet$ ). (1) Linear chain. (2) Single bound chain. (3) Ribbon-shaped chain (common in anionic chains). (4) Twisted ribbon. (5) Knotted string. (6) Single *zigzag* chain. (7) **Double *zigzag* chain**. (8) Double bent chain. (9) *Zigzag* ribbon. (10) Double ribbon. Taken from reference <sup>10</sup>.

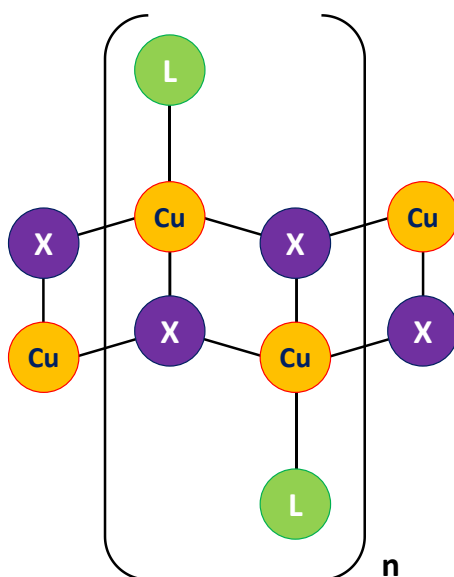


**Figure 2.2.** Scheme of the double *zigzag* chain. Taken from reference <sup>34</sup>.

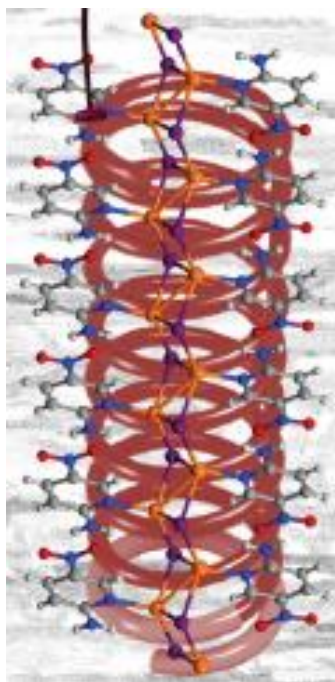


**Figure 2.3.** Representation of a 1D Cu(I)-I CP behaving like an elastic spring. Cu: orange; I: purple; C: grey; H: white; N: blue; O: red Taken from reference <sup>13</sup> (front cover).

### 2.1.1. Stimuli-responsive behavior of Cu(I)-I compounds

As explained above, the presence of stimuli such as temperature, pressure or certain vapors can induce structural changes in the Cu(I)-I chains. The aim of this section is to outline the effects of these stimuli over several examples of Cu(I)-X based compounds studied over the years.

#### *2.1.1.1. Temperature-dependent properties*

Cu(I)-I double chains are especially sensitive to temperature changes, since the usual structural contraction that compounds suffer when temperature decreases, this originates a shortening of Cu...Cu and Cu-I distances, typically allowing a better interaction between these atoms.

The first Cu(I)-I compound found to show luminescence thermochromism is [CuI(py)]<sub>4</sub> (py = pyridine) a discrete cluster compound discovered by Hardt and co-workers in 1977.<sup>35</sup> The features of this compound consist of a shift in the luminescence maximum, from 600 nm (orange-yellow) at 300 K to 450 nm (blue) at 77 K. Since this discovery, many more cluster-based compounds containing substituted pyridines as terminal ligands have been synthesized and studied.<sup>31, 36-37</sup> In all cases, luminescence at room temperature is associated with a combination of a halide-to-metal charge transfer



(<sup>3</sup>XMCT) and a cluster-centered  $3d^{10} \rightarrow 3d^9 4(s,p)^1$  transition (<sup>3</sup>CC), whereas at low temperatures a higher energy transition associated to a halide-to-ligand charge transfer (<sup>3</sup>XLCT) arises. All these transitions have triplet states as their origin so, according to the Jablonski diagram (see section 1.1.2.2, **Figure 1.12**), they correspond to phosphorescence.

These findings have been verified for CPs where the  $[Cu_xI_x]$  cluster is part of the structural moiety. Sometimes the emission of this cluster finds itself combined to the emissive behavior of another feature of the same compound, including other metal entities. This is the case of the 3-dimensional metal-organic framework (MOF)  $[(CuI_4I_4)_3(Cu^I_6)_2(3\text{-ptt})_{12}]_n \cdot 24n\text{DEF} \cdot 12n\text{H}_2\text{O}$  (3-ptt = 5-(3-pyridyl)-1H-1,2,4-triazole-3-thiolate; DEF = diethylformamide), described by Hong and co-workers.<sup>38</sup> In this CP, the thermochromic behavior displayed by the  $[Cu_4I_4]$  cluster coexists with the near infrared (NIR) emission of the  $[Cu_6S_6]$  clusters, creating a compound with an extremely rare dual emission which exists because the electronic states involving each metal cluster do not interfere. Thus, at room temperature, this compound displays only a NIR emission corresponding to that of the  $[Cu_6S_6]$  cluster, whereas at low temperatures this NIR band shifts to lower energies and a new intense emission centered at 590 nm shows up (**Figure 2.4**).

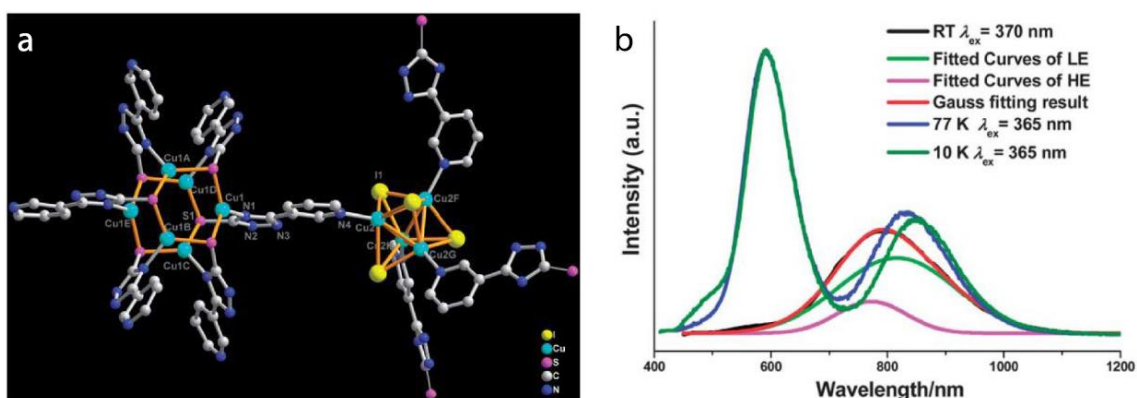


**Figure 2.4.** (a) Asymmetric unit of  $[(CuI_4I_4)_3(Cu^I_6)_2(3\text{-ptt})_{12}]_n \cdot 24n\text{DEF} \cdot 12n\text{H}_2\text{O}$ ; hydrogen atoms are omitted for clarity. (b) Experimental emission spectra of  $[(CuI_4I_4)_3(Cu^I_6)_2(3\text{-ptt})_{12}]_n \cdot 24n\text{DEF} \cdot 12n\text{H}_2\text{O}$  at room temperature (black) and low temperatures (blue and dark green), and theoretical fits of the room temperature spectrum. Taken from reference<sup>38</sup>.

The luminescent thermochromic properties of CPs based on Cu(I)-I double zig-zag chains follow the similar principles than those of cluster-based compounds, since  $Cu \cdots Cu$  distances, or at least half of them, also tend to be closely similar to  $2.80 \text{ \AA}$ , twice the van der Waals radius of Cu(I), and therefore they display the same <sup>3</sup>XMCT and <sup>3</sup>CC transitions at room temperature, although the transition at low temperatures implies a charge transfer between the metal-halide skeleton and the ligand, namely <sup>3</sup>(M + X)LCT. Still, depending on the terminal ligands of the Cu(I)-I double chains, the thermochromism displayed by each CP may drastically vary (**Table 2.1**). Some of the

compounds presented in this thesis (like, for example, **4** and **5**), are examples of the dramatic changes in properties caused by the presence of a single functional group in the terminal ligands.

**Table 2.1.** Temperature-dependent emissive behavior data of some Cu(I)-I double-chain-based coordination polymers. Taken from reference <sup>34</sup>.

CP	Dimensionality	T (K)	$\lambda_{em}$ (nm)	Cu...Cu distances (Å)	Reference
[Cu <sub>2</sub> I <sub>2</sub> (pyz)] <sub>n</sub>	2D	300	560	2.805	<sup>39</sup>
		80	606	(unpublished)	
[Cu <sub>2</sub> I <sub>2</sub> (2-Clpyz)] <sub>n</sub>	2D	300	628	(Structure not available)	<sup>39</sup>
		80	616		
[Cu <sub>2</sub> I <sub>2</sub> (2,3-dmpyz)] <sub>n</sub>	2D	300	544	2.736	<sup>40</sup>
[Cu <sub>2</sub> I <sub>2</sub> (2,5-dmpyz)] <sub>n</sub>	2D	300	570	2.797	<sup>18</sup>
[Cu(2,6-dmpyz)I] <sub>n</sub>	1D	300	533	2.748	<sup>18</sup>
[Cu(4,6-dmpym)I] <sub>n</sub>	1D	300	512	2.986	<sup>18</sup>
[Cu(3,5-lut)I] <sub>n</sub>	1D	300	436	2.889; 3.051	<sup>18</sup>
[Cu <sub>2</sub> I <sub>2</sub> (4,4'-bpy)] <sub>n</sub>	2D	300	541	2.845	<sup>41</sup>
		80	568	(unpublished)	
[Cu(EtIN)I] <sub>n</sub>	1D	300	567	2.797; 2.813	<sup>42</sup>

Legend: py = pyridine; pym = pyrimidine; pyz = pyrazine; dmpyz = dimethylpyrazine; lut = lutidine (dimethylpyridine); bpy = bipyridine; EtIN = ethyl isonicotinate.

Apart from their luminescent properties, Cu(I)-I double chain-based CPs usually show semiconductive behavior, with electrical conductivities ranging from 10<sup>-9</sup> Scm<sup>-1</sup> to 10<sup>-3</sup> Scm<sup>-1</sup>.<sup>13, 43-44</sup> Following this principle, when lowering the temperature, the electronic band gap will grow and, therefore, the electrical conductivity of these CPs will decrease. This semiconductive behavior arises from the electronic delocalization along the Cu-I chains, favored by the large size of the iodide ligands. If the asymmetry of the chain changes due to a phase transition provoked by a variation of temperature, some changes in the electrical conductivity will appear, and eventually this can encompass the presence of a hysteresis cycle (*vide infra*, section 2.2.2).

It is important to know that these studies are limited at temperatures higher than 100 °C because, according to the thermogravimetric analyses of these CPs, they start decomposing at this temperature.<sup>42</sup>

#### 2.1.1.2. Pressure-dependent properties

Mechanical stresses can also affect Cu-I double chains, causing modifications in the Cu...Cu and Cu-I distances just like temperature does. The effect of pressure on Cu(I)-I was first studied in 1977. Vogler and co-workers<sup>45</sup> coined the term “luminescence rigidochromism” referring to a change in the luminescence when the rigidity of the medium changed, e. g., when freezing a solution containing the compound by applying pressure. Ford et al.<sup>46</sup> deepened in the study of the tetranuclear compound [CuI(py)]<sub>4</sub>, (py = pyridine); in benzene solution at 1 bar, this compound presents an emission centered at 695 nm, corresponding to a <sup>3</sup>CC excited state. When freezing this solution, due to the action of pressure (at  $P > 72$  MPa), this emission band sharply shifts to 575 nm (**Figure 2.5**), close to that observed for the compound in the solid state (580 nm). This behavior was confirmed for solutions of this cluster-based complex in other solvents.

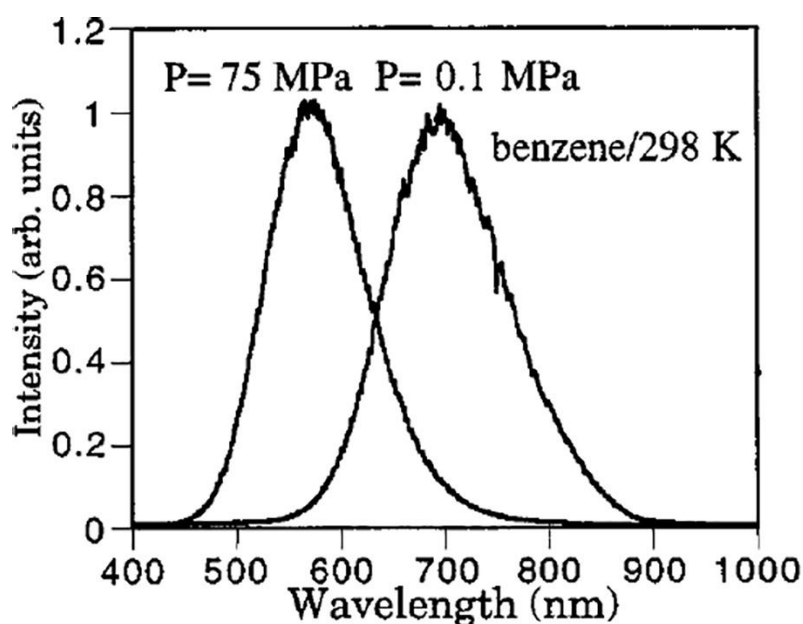


**Figure 2.5.** Normalized emission spectra of [CuI(py)]<sub>4</sub> (py = pyridine) in benzene solution, at 1 bar and at 75 MPa. Taken from reference <sup>46</sup>.

However, unlike clusters, when a CP is dissolved, two different scenarios can take place. On the one hand, it undergoes solvolysis; on the other hand, it dissociates into its building blocks. In both cases, it gives rise to the cleavage of the CP and the formation of different species in solution. Therefore, the studies of the pressure in solution are hampered and the pressure-dependent behavior of a CP must be carried out in the solid state.

Prior to the description of the mechanochromism of Cu(I)-I chains, it has to be noticed that not all these compounds present this kind of behavior. The variations in the distances and angles in the structure and the ligands which decorate the chains limit this feature.

Initially, the simplest way to put one of these CPs through a mechanical stress is to grind it. Many studies carried out on Cu-I clusters and CPs show that, when they are ground, they suffer a loss of crystallinity or a phase transition which causes a sharp variation of their emission intensity and wavelength.<sup>15-16</sup> However, grinding does not always imply a loss of crystallinity, so more complex approaches are needed to study CPs which keep being crystalline when pressure increases.

One of these complex approaches consists of the use of a diamond anvil cell (DAC), allowing the use of ultra-high pressures with a suitable control of the measurement. This experimental set-up allows both the measurement of the changes in emission of the material at different pressures and its structural variations, therefore allowing establishing a comparison to rationalize the observed variations. Thus, González-Platas and co-workers<sup>47</sup> used this approach to report a 1D CP with 6-methylquinoline (6mq) as terminal ligand, namely  $[\text{Cu}(\text{6mq})\text{I}]_n$ . This CP showed an emission centered at 550 nm at ambient conditions, arising from a halide-to-ligand charge transfer excited state ( $^3\text{XMCT}$ ); as pressure is raised above 800 MPa, and up to 6.45 GPa, three new emission bands centered at 515, 647 and 712 nm appear (**Figure 2.6**). The structural changes observed under pressure confirmed that  $\text{Cu}\cdots\text{Cu}$  distances shrank as pressure increased, from values of 2.796 and 2.466 Å at 1 bar to 2.683 and 2.932 Å at 6.45 GPa, in this case. Then, the appearance of these new bands was attributed to an enhancement of the cluster-centered transition ( $^3\text{CC}$ ).

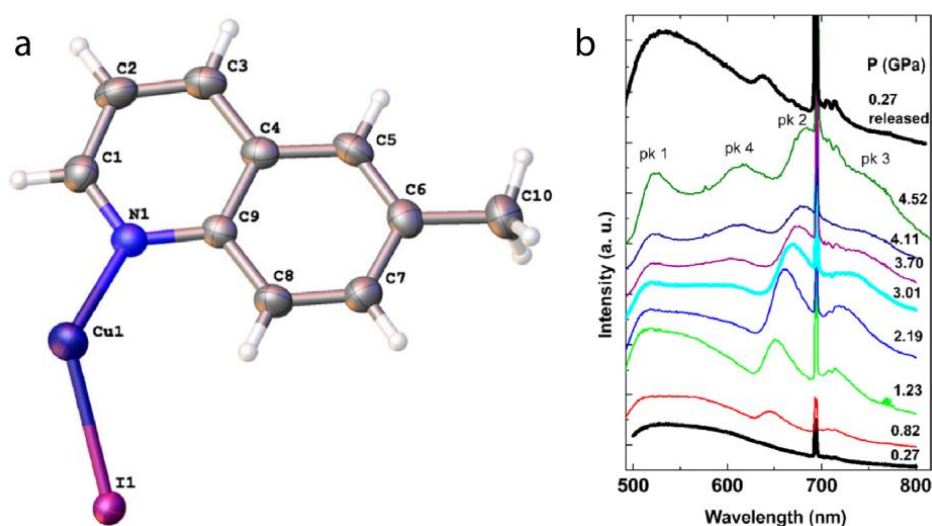


**Figure 2.6.** (a) Asymmetric unit of the crystal structure of  $[\text{Cu}(\text{6mq})\text{I}]_n$  (6mq = 6-methylquinoline); C: gray, H: white, N: blue, Cu: indigo; I: purple. (b) Pressure-dependent emissive behavior of  $[\text{Cu}(\text{6mq})\text{I}]_n$ ; the sharp peak at 690 nm corresponds to the emission of a ruby sphere used as pressure sensor. Taken from reference <sup>47</sup>.

Sometimes the application of pressure to a Cu(I)-I CP leads to a quenching of the luminescence, caused by a bad overlapping of the hybridized  $d_z^2$  orbitals of the copper atoms. This phenomenon will be explained in further detail for compounds **5** and **6** (*vide infra*, section 2.2.3).

#### 2.1.1.3. Response to vapors

As afore mentioned, Cu-I chain-based CPs can also be sensitive to chemical stimuli. For instance, the presence of certain vapors of molecules can interact with these materials and produce a significant change in its physical properties *i.e.* emission and/or electrical conductivity. These vapor-to-solid interactions induce structural changes in the Cu-I chain CPs driven by the molecular recognition capabilities of certain terminal ligands. The interactions between the terminal ligands and the vapors can occur via  $\pi$ - $\pi$  stacking, van der Waals forces and/or hydrogen bonds.

Since the discovery of  $[\text{Cu}(\text{py})\text{I}]_n$  (py = pyridine) (with  $n = 4$  or  $\infty$ ),<sup>48-49</sup> many Cu(I)-I based CPs and clusters have been studied, but it was not until 1998 when Ford et al.<sup>50</sup> found out the first example of these compounds which showed a vapochromic behavior.  $[\text{Cu}(4\text{-pic})\text{I}]_\infty$  (4-pic = 4-methylpyridine, or 4-pycoline) suffered a reversible transformation from its polymeric staircase motif into a four-member cluster,  $[\text{Cu}(4\text{-pic})\text{I}]_4$ , when exposed to toluene, both in liquid or vapor phase. On the contrary, when exposing  $[\text{Cu}(4\text{-pic})\text{I}]_4$  to pentane, it reverted to the polymeric form  $[\text{Cu}(4\text{-pic})\text{I}]_\infty$ . This induced an evident change in the luminescent properties of the compound (**Figure 2.7**).

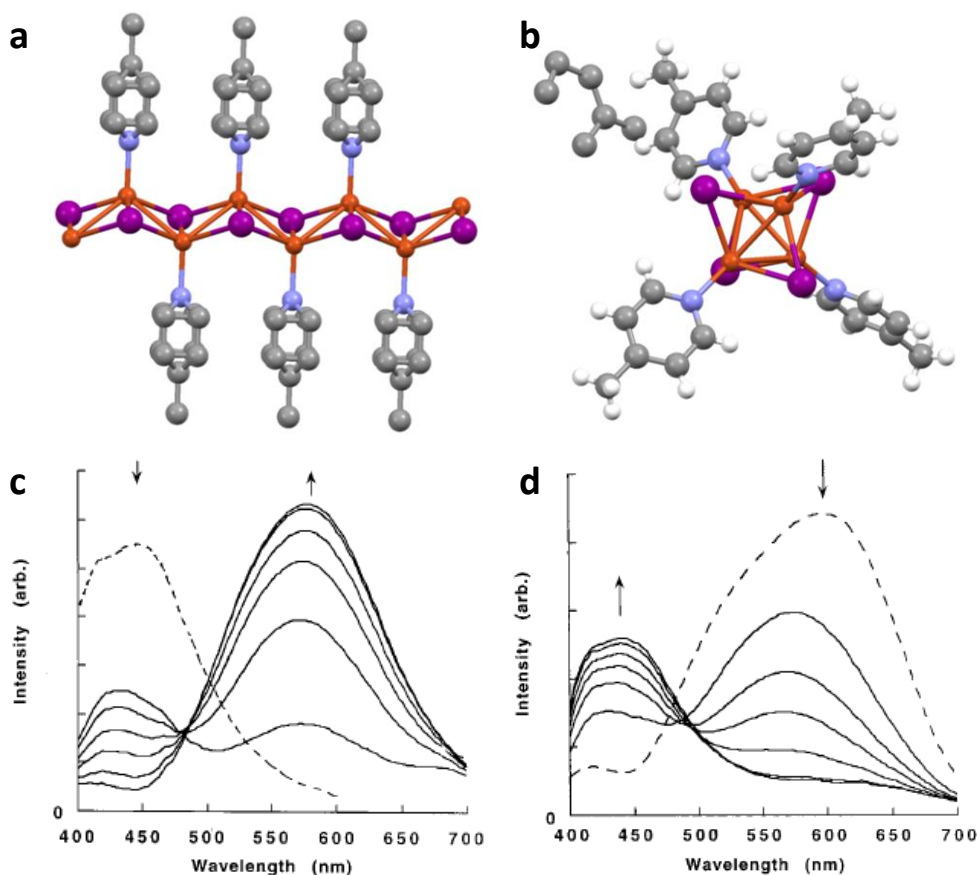


**Figure 2.7.** Crystal structures of  $[\text{Cu}(\text{4-pic})\text{I}]_\infty$  (4-pic = 4-methylpyridine) (a) and  $[\text{Cu}(\text{4-pic})\text{I}]_4 \cdot \text{Toluene}$  (b). (c) Variation of the luminescence spectrum of  $[\text{Cu}(\text{4-pic})\text{I}]_\infty$  as it transforms into  $[\text{Cu}(\text{4-pic})\text{I}]_4$  in the presence of toluene. (d) Variation of the luminescence spectrum of  $[\text{Cu}(\text{4-pic})\text{I}]_4$  as it transforms into  $[\text{Cu}(\text{4-pic})\text{I}]_\infty$  in the presence of n-pentane. The shapes of the aromatic rings in (a) are due to a 50% delocalization for their orientation. (c, d) Taken from reference <sup>51</sup>.

This study has been extended to many other compounds since then. In 2000, Ford et al.<sup>51</sup> extended their studies to the similar compounds  $[\text{Cu}(\text{3-pic})\text{I}]_\infty$  and  $[\text{Cu}(\text{3-pic})\text{I}]_4$  (3-pic = 3-methylpyridine, or 3-pycoline), observing no response to gases.

More recently, Hassanein et al.<sup>13-14</sup> reported a 1D CP with 2-amino-5-nitropyridine (ANP) in its structure (**3**). Its high ability to establish hydrogen bonding interactions with some molecules proved it to be an excellent sensor for vapors of methanol, ethanol or, specially, acetic acid. When exposed to these molecules, the conductivity of this CP raised drastically, up to three orders of magnitude (**Figure 2.8**). In this thesis we will describe how the presence of acetic vapors affects the lateral dimensions of nanostructures of this compound.

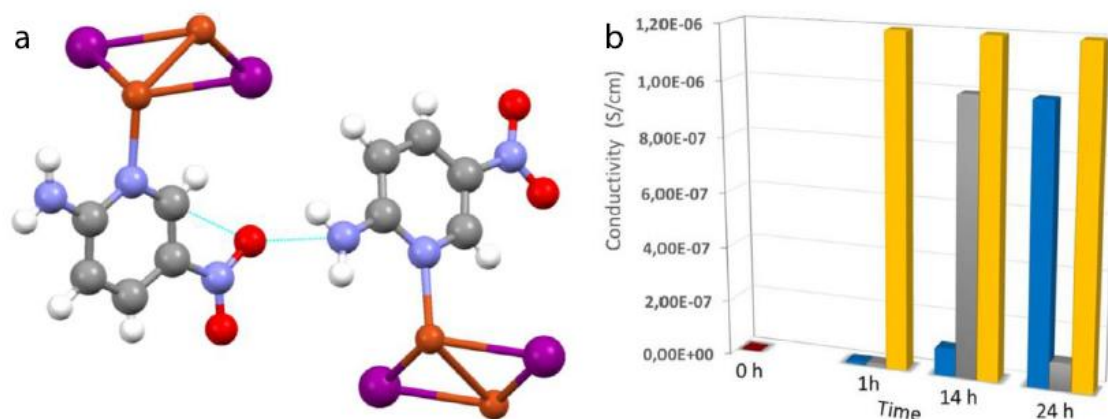


**Figure 2.8.** (a) Crystal structure of [Cu(ANP)I]<sub>n</sub> (ANP = 2-amino-5-nitropyridine) along the *a* axis. White: H; gray: C; blue: N; red: O; orange: Cu; purple: I. Dashed blue lines indicate hydrogen bonds. (b) Variation of the electrical conductivity of [Cu(ANP)I]<sub>n</sub>: pristine (red), exposed to methanol (blue), ethanol (gray) or acetic acid (yellow). Taken from reference <sup>13</sup>.

### 2.1.2. Nanoprocessing of Cu-X CPs

To date there are two fundamental approaches for nanoprocessing compounds based on the approaches of bottom-up and top-down synthesis. Bottom-up methodologies usually enclose on-surface (solid substrates) and interfacial syntheses (in liquid-liquid or liquid-air interfaces), whereas the most common top-down methods are micromechanical exfoliation and liquid phase exfoliation.<sup>52</sup>

In the case of Cu-X CPs, the general insolubility of this type of compounds allows the use of a top-down methodology based on sonication techniques in liquid phase (liquid phase exfoliation). This methodology gave its first fruits about 10 years ago, with interesting results like the ones obtained by Welte et al. for the 1D CP [Cu(HIN)Br]<sub>n</sub>, where HIN is isonicotinic acid (**Figure 2.9**)<sup>44</sup> and for the mixed valence 2D CP [Cu<sub>2</sub>Br(IN)<sub>2</sub>]<sub>n</sub> (**Figure 2.10**).<sup>53</sup>



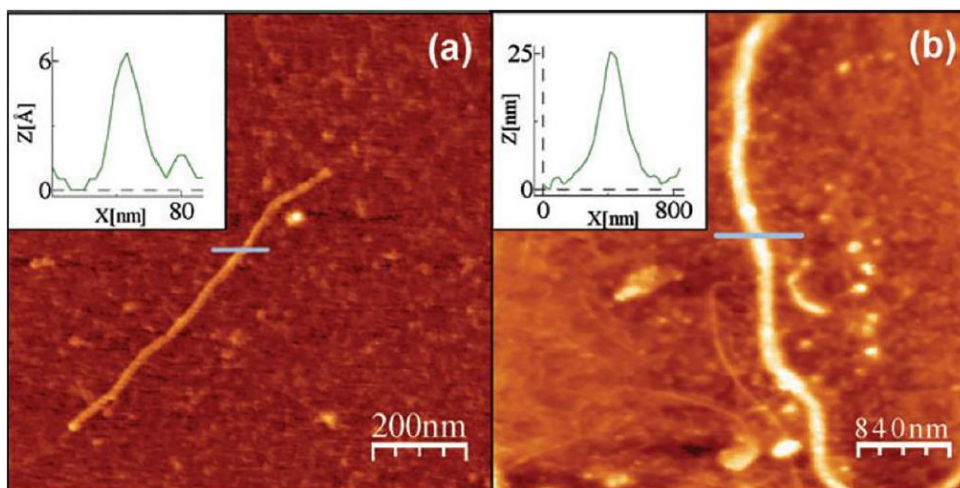


**Figure 2.9.** AFM topography images of  $[\text{CuBr}(\text{HIN})]_n$  (HIN = isonicotinic acid) nanowires deposited on polylysine treated mica (a) and gold (b) surfaces, with their respective height profiles across the blue lines on the upper-left corner.<sup>44</sup>

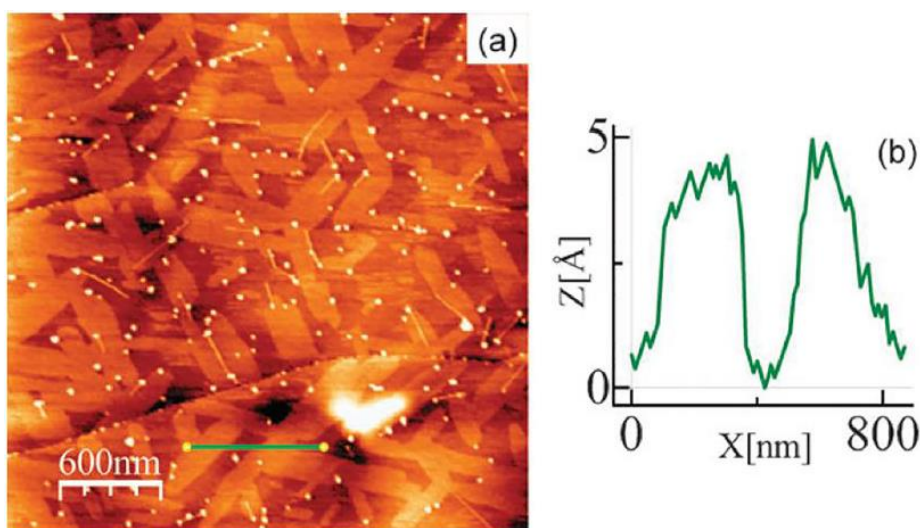


**Figure 2.10.** AFM topography image of  $[\text{Cu}_2\text{Br}(\text{IN})_2]_n$  (IN = isonicotinate) nanosheets deposited on highly oriented pyrolytic graphite (HOPG) (a), with its height profile across the line (b).<sup>53</sup>

The second approach is based on the bottom-up method, although this methodology is truncated by the known insolubility of the CPs. In a preliminary work, the CP formation-solution reversibility process based on its solubility in specific solvents was successfully demonstrated in related MMX chains.<sup>54-56</sup> One-dimensional mixed-valence CPs  $[\text{Pt}_2(\text{RCS}_2)_4\text{I}]_n$  (where  $\text{RCS}_2^-$  is a dithiocarboxylate with  $\text{R} = n\text{-pentyl}$ ) could be synthesized as nanowires with lengths of several microns and heights between 1.5 and 2.5 nm, corresponding to one to three MMX chains, by drop-casting of saturated solutions of their respective building blocks in THF over mica surfaces.<sup>55</sup> On the other hand, other MMX-based 1D CPs, namely  $[\text{Ru}_2(\text{EtCO}_2)_4\text{X}]_n$  (where  $\text{EtCO}_2^-$  is propionate and  $\text{X}^-$  is  $\text{Br}^-$  or  $\text{I}^-$ ), the morphology of the obtained nanostructures depends on the bridging halide and the surface where they are deposited.  $[\text{Ru}_2(\text{EtCO}_2)_4\text{Br}]_n$  structures



deposited in mica starting from a solution of its building blocks in aqueous SDS show a typical nanofiber shape, whereas those deposited on highly oriented pyrolytic graphite (HOPG) show a helical structure derived from their interaction with the HOPG steps.<sup>56</sup> In the case of  $[\text{Ru}_2(\text{EtCO}_2)_4\text{I}]_n$ , sonication of ethanol solutions of its building blocks gave rise to different nanostructures depending on the subsequent incubation time at 20 °C before depositing the solution over mica surfaces. Thus, immediately after the ultrasound treatment, nanostructures of this CP showed irregular shapes, progressively evolving into well-defined nanowires after 43 days of incubation.<sup>57</sup>

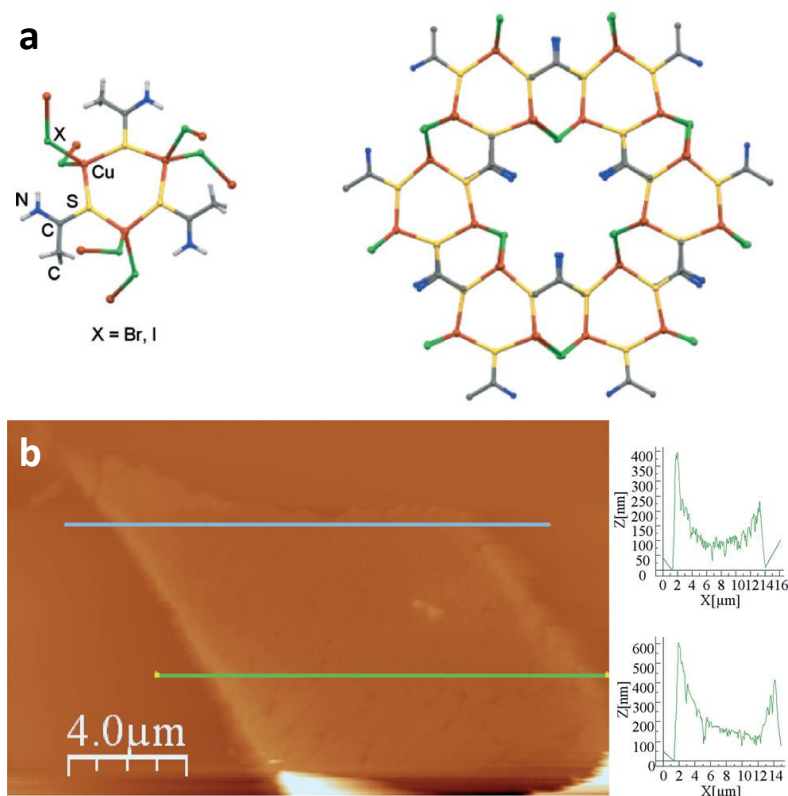


**Figure 2.11.** (a) Crystal structure of  $[\text{CuX}(\text{TAA})]_n$  (with  $\text{X} = \text{Br}$  or  $\text{I}$ ), showing the basic  $\text{Cu}_6\text{S}_6$  ring (left) and its connection with other rings via the halogen atoms to conform the 3-dimensional structure (right). (b) Topological AFM image of a  $[\text{CuI}(\text{TAA})]_n$  sheet formed by drop-casting of a saturated solution of the building blocks in acetonitrile, with its height profiles across the blue (up) and green lines (down). Taken from reference <sup>58</sup>.

More recently, Troyano et al.<sup>58</sup> carried out a solubility study on some CPs based on CuI and organosulphur ligands. It is well known that, when you dissolve a coordination polymer, it dissociates into its building blocks. Common solvents used to dissolve CPs are strongly coordinative (this is the case of DMF and DMSO), so the original structure of the CP cannot be recovered. However, when these Cu(I)-I based CPs are dissolved in acetonitrile, as the solvent evaporates they reorganize to form CP crystals. Therefore, when a drop of a saturated solution of these CPs is cast on a surface and allowed to evaporate, it leads to the formation of sub-micron structures with the same chemical

composition and structure found for the analogous microcrystals, like the films obtained for  $[\text{CuI}(\text{TAA})]_n$  (TAA = thioacetamide) (**Figure 2.11**). Subsequent studies performed on other CuI CPs<sup>42</sup> confirmed that most of these compounds show the same reversible behavior. This finding has been a key fact that has allowed the fruition of further studies on the preparation of Cu-X CP based nanostructures by bottom-up methods, including a more recent approach based on the direct synthesis of the desired nanostructures in the reaction medium, taking advantage of the insolubility of the CPs.

In this chapter, four new compounds based on Cu(I)-I double *zigzag* chains will be synthesized, structurally characterized and nanoprocessed, and their luminescent and electrical properties will be studied. Moreover, three compounds which have already been described will be re-synthesized as nanostructures, with the aim to compare their properties to those of the corresponding bulk crystals.

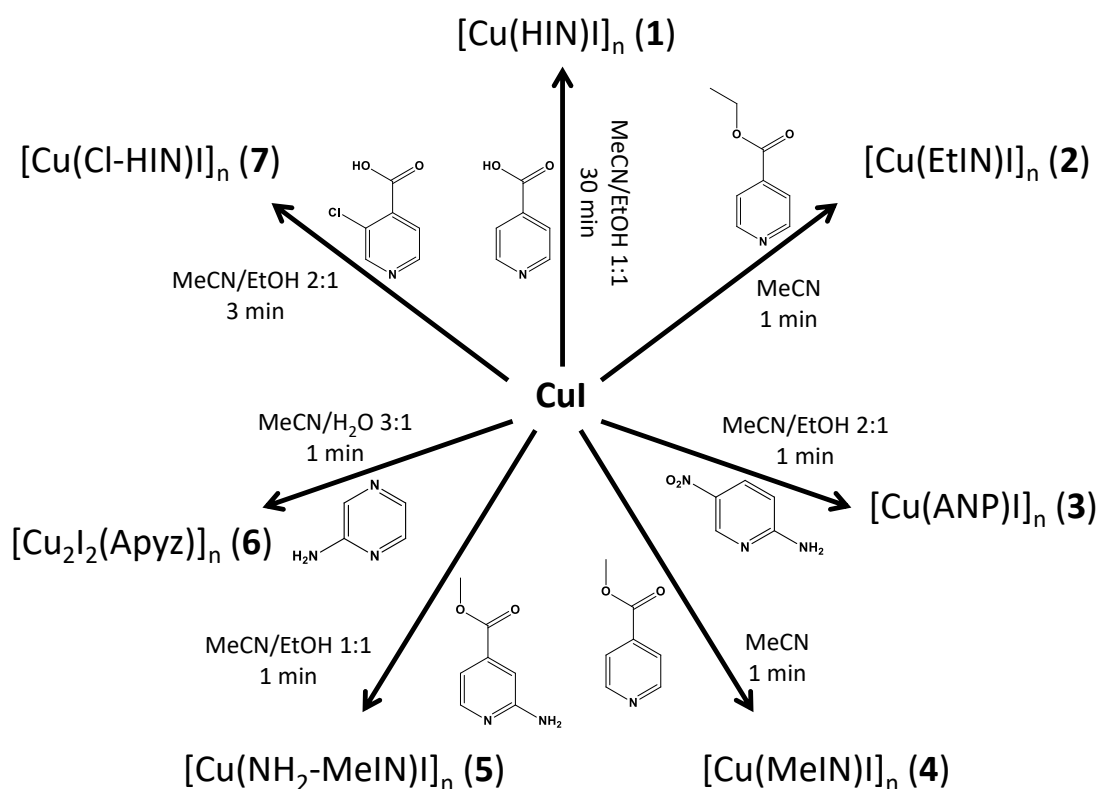
## 2.2. Results and discussion

### 2.2.1. Synthesis and structural characterization

The direct reactions between copper(I) iodide and seven different N-donor aromatic ligands leads to the formation of compounds **1-7**. For these compounds, a conventional synthetic approach consisting of reactions at room temperature with magnetic stirring is enough to obtain these compounds with reasonable yields and a high degree of purity, confirmed by powder X-ray diffraction (PXRD; see appendix B). The selected solvent was acetonitrile, or a mixture containing it, mainly because it is the best solvent which can dissolve copper(I) iodide. The election of a second solvent depends mainly on the solubility of the organic ligand, taking into account that, when both reactants are mixed in solution, they react faster. **Scheme 2.1** summarizes the synthetic conditions leading to the obtainment of compounds **1-7**.

Another well-known synthetic method that is commonly used to prepare CPs is solvothermal synthesis. Although we have made several attempts to create different compounds by changing the reaction conditions, no positive results were obtained in any case. Instead, solvothermal reactions always led to the obtainment of the same compounds, but in poor yields and quality. Only a solvothermal reaction between CuI and aminopyrazine (Apyz) gave rise to crystals of **6**, suitable for single crystal X-ray diffraction (SC-XRD).

If we observe the infrared (IR) spectra of compounds **1-7**, they all share typical  $\nu_{\text{C}=\text{N}}$  bands, proper of the stretching of the aromatic rings. The rest of the bands depend on the functional groups linked to these rings; for instance, compounds **4**, **5** and **7** present  $\nu_{\text{C}=\text{O}}$  bands arising from the carbonyl groups, and compounds **5** and **6** present  $\nu_{\text{N-H}}$  bands coming from the amino groups (**Table 2.2**)



**Scheme 2.1.** Summary of the synthetic methods leading to the obtainment of compounds **1-7**.

**Table 2.2.** Most significant stretching bands observed in the IR spectra of compounds **1-7**.

Compound	$\nu_{\text{C=N}}$ ( $\text{cm}^{-1}$ )	Other $\tilde{\nu}$ values ( $\text{cm}^{-1}$ )	Type of bond and vibration corresponding to the other $\tilde{\nu}$ values
<b>1</b>	1290	2400-3100 1692	$\nu_{\text{O-H}}$ with H-bonds $\nu_{\text{C=O}}$
<b>2</b>	1290	1716	$\nu_{\text{C=O}}$
<b>3</b>	1330, 1286	3447, 3325 1625, 1602 1126	$\nu_{\text{N-H}}$ $\delta_{\text{N-H}}$ $\nu_{\text{N=O}}$
<b>4</b>	1319, 1282	1724	$\nu_{\text{C=O}}$
<b>5</b>	1308, 1270	3450, 3345 1716 1634, 1603	$\nu_{\text{N-H}}$ $\nu_{\text{C=O}}$ $\delta_{\text{N-H}}$
<b>6</b>	1316	3419, 3316 1613, 1604	$\nu_{\text{N-H}}$ $\delta_{\text{N-H}}$
<b>7</b>	1274, 1263	2400-3100 1697	$\nu_{\text{O-H}}$ with H-bonds $\nu_{\text{C=O}}$

### 2.2.1.1. XRD structures description

Although the structures of compounds **1-3** have already been described by Dr. Hassanein,<sup>13-14, 42</sup> they will also be explained herein, since they will serve to establish a comparative study with compounds **4-7**, not only of the packing, but also of the properties displayed by these compounds.

All compounds **1-7** share as structural motif the Cu(I)-I double *zigzag* chain (**Figures 2.12-2.18**). The copper centers are coordinated to three iodides and the iminic nitrogen of the terminal organic ligands, with a distorted tetrahedral geometry. On the other hand, iodides act like bridging ligands, linking themselves to three copper centers. However, the intermolecular forces between chains, arising from the different functional groups present in the ligands, give rise to different packings.

The carboxylic acid groups present in isonicotinic acid allow the 1D chains of compound **1** to form a 2D supramolecular array *via* the formation of complementary hydrogen bonds between adjacent carboxylic acid residues. This complementary H-bonding model is a well-known supramolecular synthon which directs the supramolecular structure of organic molecules and coordination compounds containing carboxylic acid groups.<sup>59</sup> The 2D supramolecular sheets are parallel to the (102) plane and are linked together by weak Van der Waals forces. The double chain can be described as Cu<sub>2</sub>I<sub>2</sub> trapezoids sharing opposite sides with dihedral angles of 119.3°. The isonicotinic acid ligands are arranged in a way that they are tilted (90.6°) and twisted (61.0°) with respect to (w.r.t.) the propagation direction of the double chain (**Figure 2.12; Tables A1-A2** in appendix A).

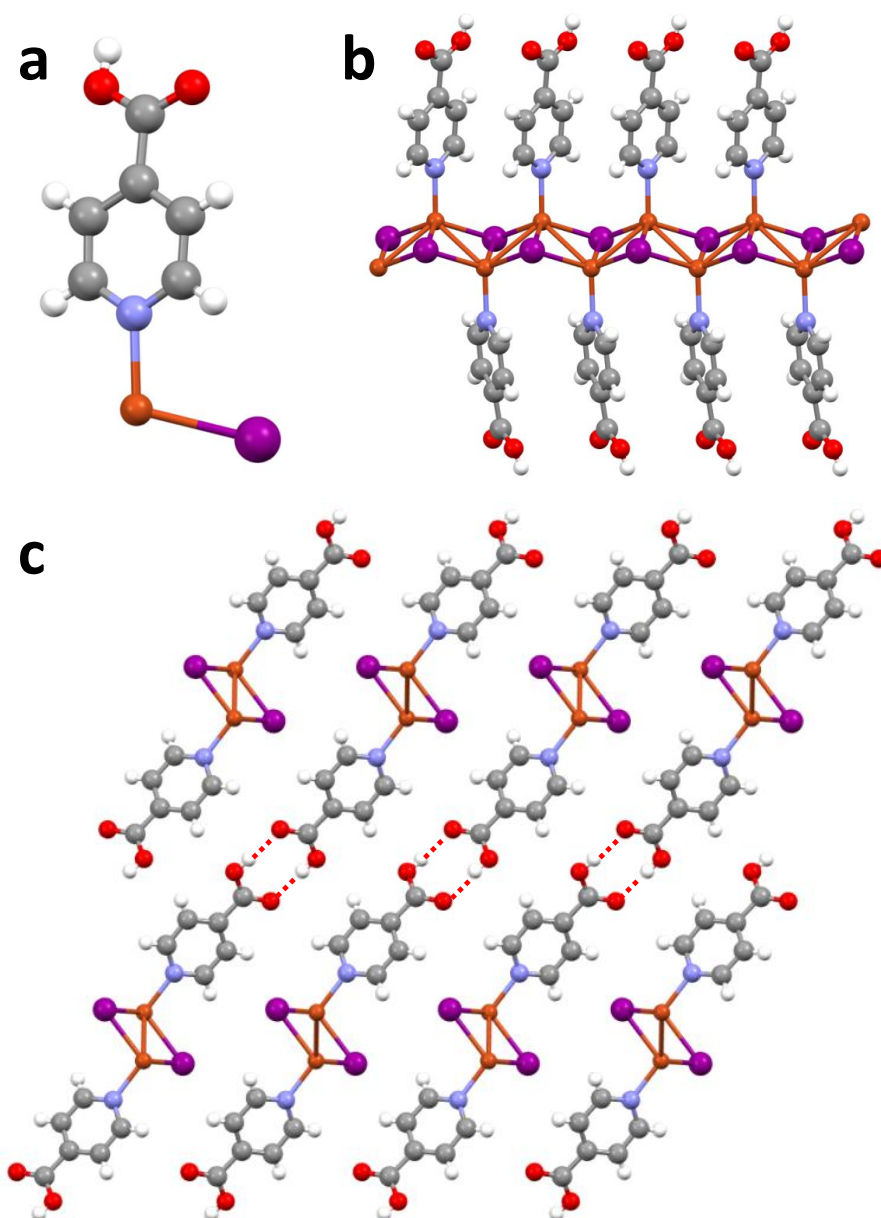


**Figure 2.12.** Crystal structure of compound **1**: (a) asymmetric unit; (b) lateral view of a Cu(I)-I double *zigzag* chain; (c) View of the packing of the crystal structure from the crystallographic *b* axis. Cu: orange; I: purple; C: grey; H: white; N: blue; O: red. Dashed red lines indicate the presence of H-bonding interactions.

An ethoxycarbonyl group instead of a carboxylic acid totally changes the packing of the structure of compound **2** w.r.t. compound **1**. In this case, the ethyl group makes this ligand bulky enough to even prevent the formation of intra-chain  $\pi$ - $\pi$  stacking interactions, so the 1D chains are linked together by weak Van der Waals interactions. The double chain can be described as Cu<sub>2</sub>I<sub>2</sub> rhomboids sharing opposite sides with dihedral angles of 120.9°. The tilt and twist angles of the ethyl isonicotinate ligands show values of 82.0° and 62.5°, respectively (**Figure 2.13**).

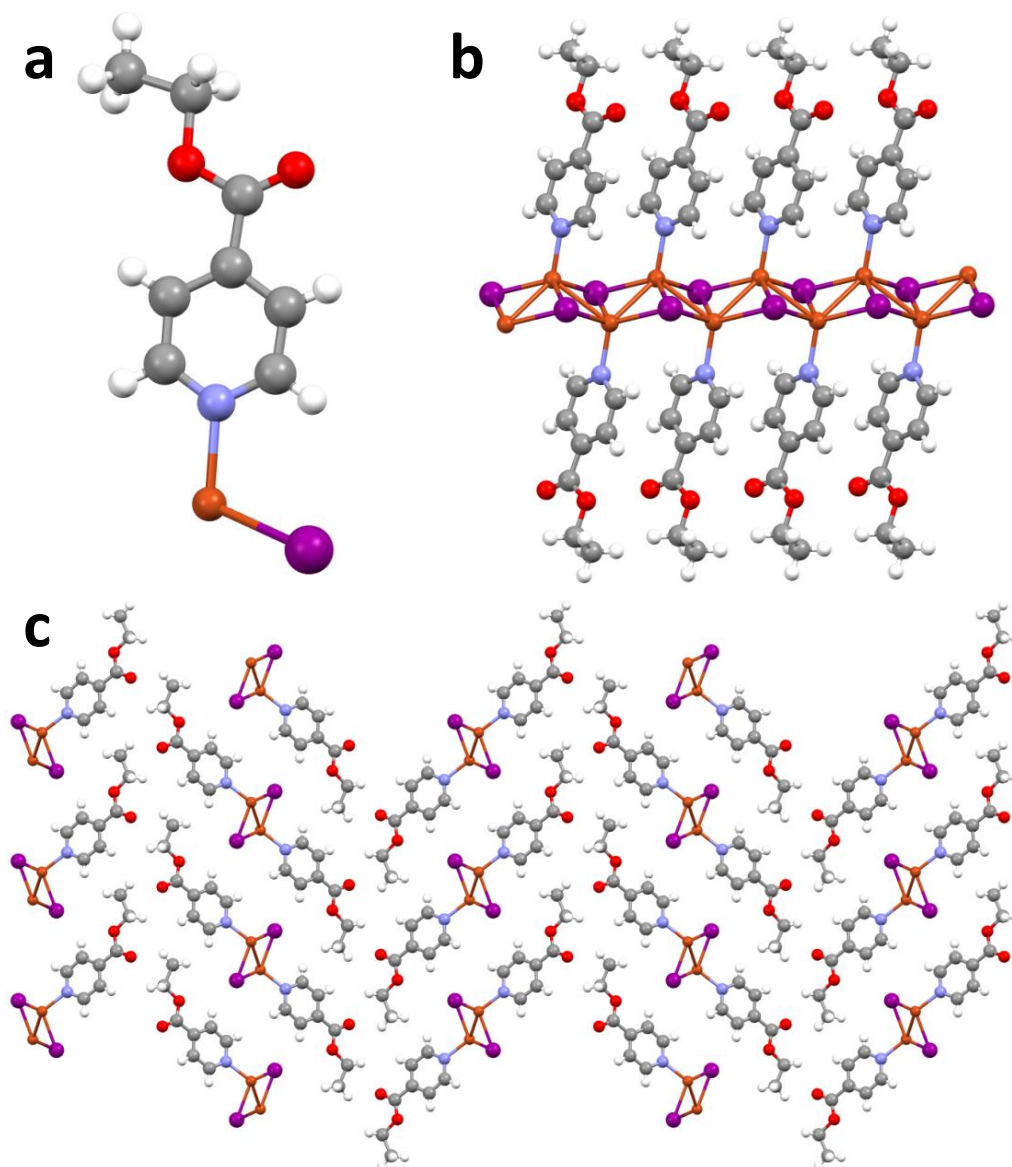


**Figure 2.13.** Crystal structure of compound **2**: (a) asymmetric unit; (b) lateral view of a Cu(I)-I double *zigzag* chain; (c) View of the packing of the crystal structure from the crystallographic *a* axis. Cu: orange; I: purple; C: grey; H: white; N: blue; O: red.

Compound **3** shows two polymorphs depending on the reaction conditions used for its synthesis.<sup>13</sup> In this case we are going to focus on the room temperature polymorph, since it is the one which has been prepared and subjected to further studies. The supramolecular arrangement of this CP is strongly directed by the presence of hydrogen bonds between the amino group of an ANP residue and an adjacent nitro group of a neighboring chain. Moreover, weak intra-chain interactions between amino groups and iodide ligands increase the strength of the structure. The double chain can be described as  $\text{Cu}_2\text{I}_2$  rhomboids sharing opposite sides with dihedral angles of  $120.9^\circ$  (**Figure 2.14**).

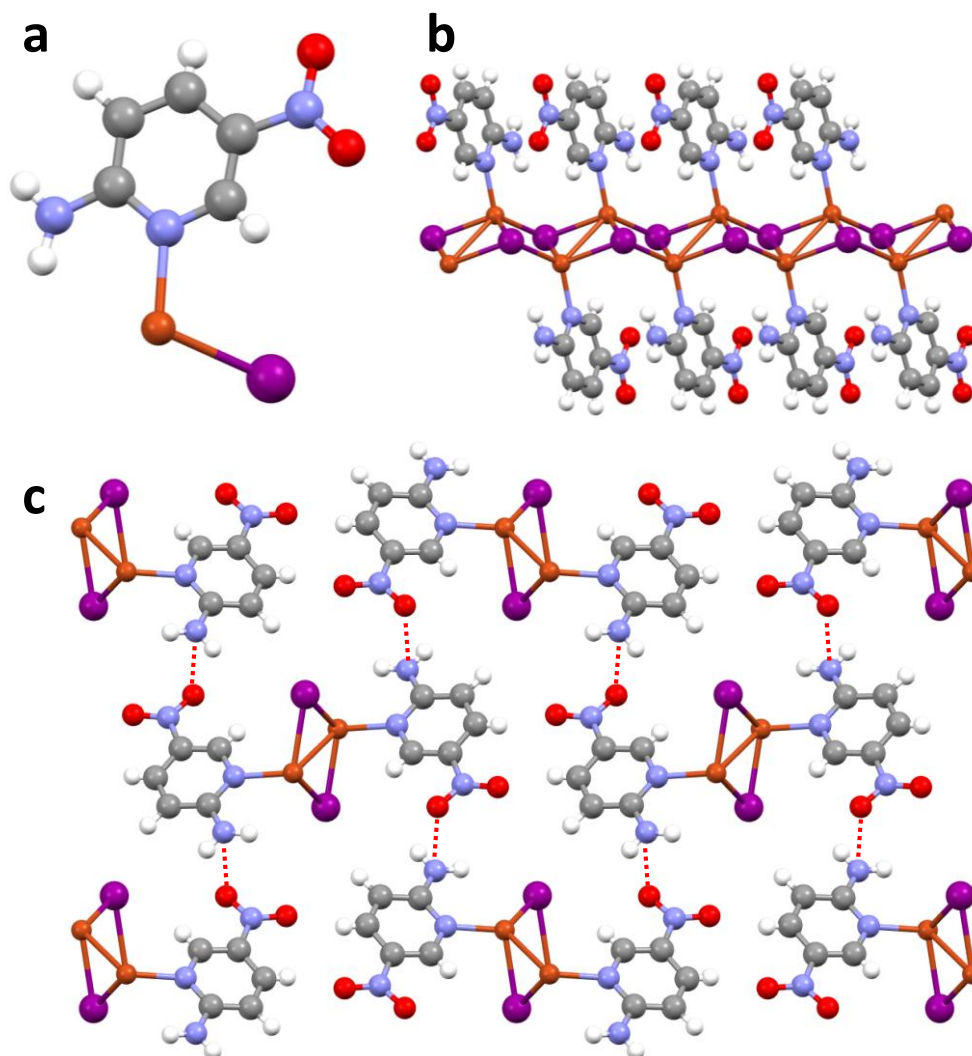


**Figure 2.14.** Crystal structure of compound **3**: (a) asymmetric unit; (b) lateral view of a Cu(I)-I double *zigzag* chain; (c) View of the packing of the crystal structure from the crystallographic *a* axis. Cu: orange; I: purple; C: grey; H: white; N: blue; O: red. Dashed red lines indicate the presence of H-bonding interactions.

Compound **4** behaves in a similar way to compound **2**, but since the methoxycarbonyl group of methyl isonicotinate is less bulky than the ethoxycarbonyl group, the double chains in compound **4** are reinforced by the presence of intra-chain  $\pi$ - $\pi$  stacking interactions, and the chains are linked by weak H-bonding interactions between the free oxygen atom of an organic residue and the hydrogens linked to the aromatic ring of an adjacent molecule. The double chain can be described as  $\text{Cu}_2\text{I}_2$  rhomboids sharing opposite sides with dihedral angles of  $122.1^\circ$ . The tilt and twist angles of the methyl isonicotinate ligands show values of  $88.7^\circ$  and  $59.1^\circ$ , respectively (**Figure 2.15**; **Tables A3-A4** in appendix A).

When the temperature is lowered, compound **4** experiences a phase transition which takes place between 125 and 145 K (this phase transition causes a hysteresis cycle in its electrical behavior, as will be explained below). To rationalize this phase transition, the



crystal structure of this CP has been solved at 200 and 110 K (Tables A3-A4 in appendix A). As can be observed, all distances experience the expected reduction; however, when going from 200 to 110 K, a Cu-I<sub>rail</sub> distance slightly grows (0.0020 Å). As a consequence, the asymmetry of the chain changes and, with it, the properties of the compound. All these changes are reversible.

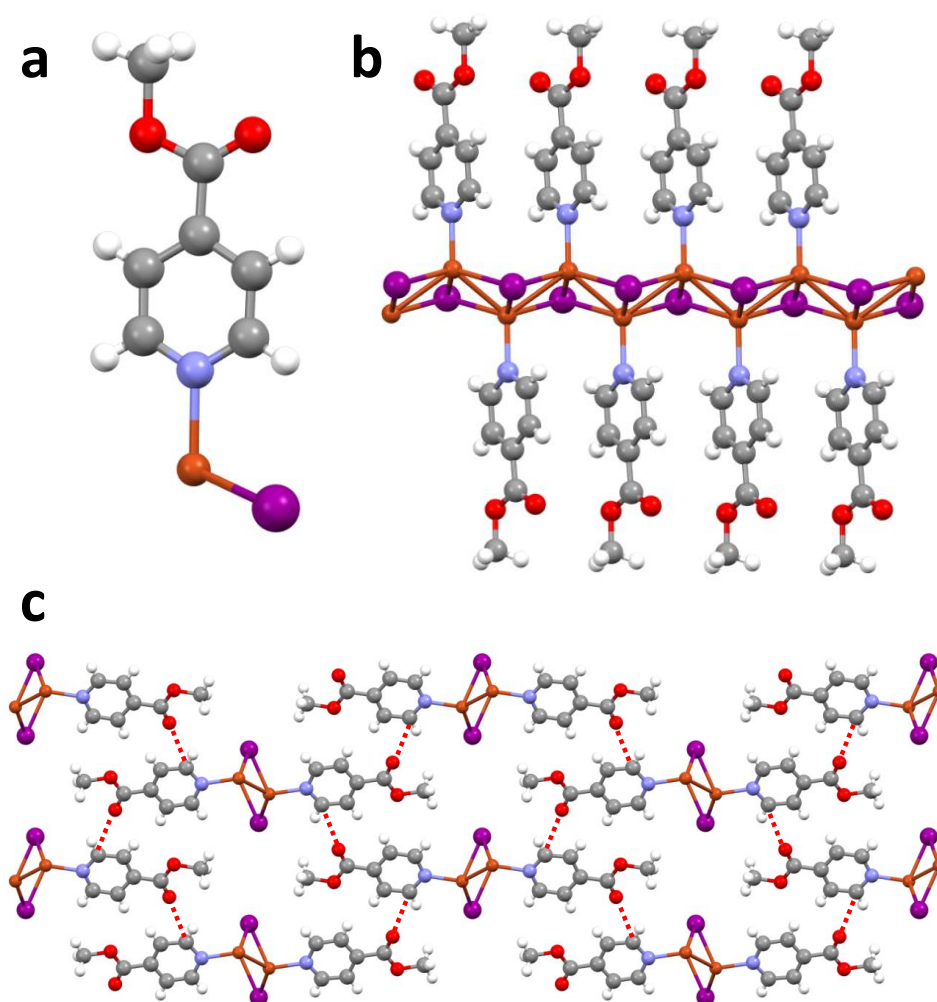


**Figure 2.15.** Crystal structure of compound **4**: (a) asymmetric unit; (b) lateral view of a Cu(I)-I double *zigzag* chain; (c) View of the packing of the crystal structure from the crystallographic *a* axis. Cu: orange; I: purple; C: grey; H: white; N: blue; O: red. Dashed red lines indicate the presence of H-bonding interactions.

At first sight, compound **5** differs from compound **4** only by the presence of an amino group in the organic residues of the former. However, this induces significant differences both in Cu...Cu distances and in the way their structures are packed. The amino group in the methyl 2-aminoisonicotinate ligands allows it to establish H-bonds with carbonylic oxygen atoms in nearby chains (Figure 2.16); these interactions are stronger than those observed for compound **4** due to the higher electronegativity of nitrogen versus a  $sp^2$  carbon. As a consequence of these inter-chain interactions, the Cu...Cu distances suffer important alterations: compound **4** is almost symmetric, with Cu...Cu distances of 2.751 and 2.818 Å, whereas compound **5** shows values of 2.682



and 3.514 Å for these distances (**Tables A3-A4** in appendix A). Therefore, one way to describe the chains of compound **5** is as an array of Cu<sub>2</sub>I<sub>2</sub> dimers connected by weak Cu...Cu interactions. These structural differences are the main cause of the characteristic luminescent behavior observed for each compound.

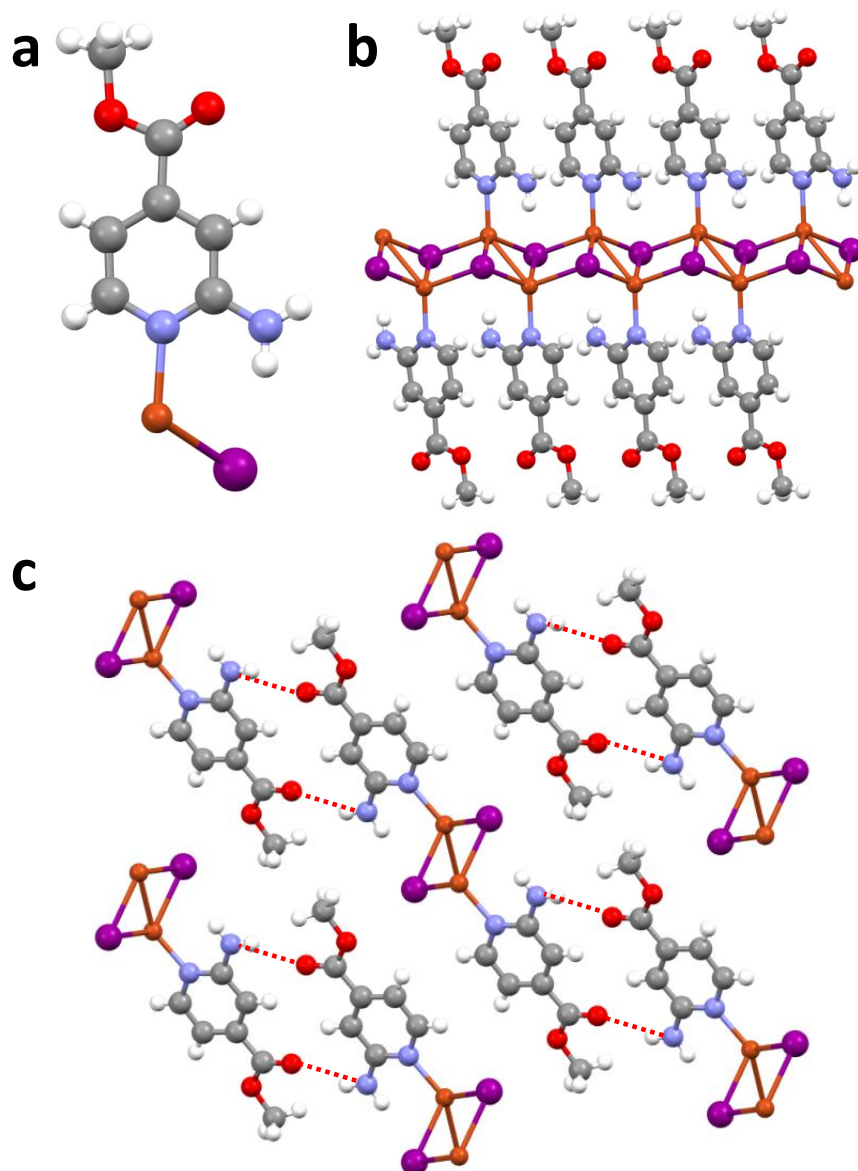


**Figure 2.16.** Crystal structure of compound **5**: (a) asymmetric unit; (b) lateral view of a Cu(I)-I double *zigzag* chain; (c) View of the packing of the crystal structure from the crystallographic *a* axis. Cu: orange; I: purple; C: grey; H: white; N: blue; O: red. Dashed red lines indicate the presence of H-bonding interactions.

As temperature is lowered, all distances in compound **5** suffer the expected reversible shrinking. This CP also suffers reversible structural variations when it is subjected to hydrostatic pressure. Studies carried out in a diamond anvil cell (DAC) using a methanol-ethanol-water 16:3:1 mixture as pressure-transmitting medium (it remains hydrostatic at pressures up to 10 GPa and above<sup>60</sup>) have allowed calculating the equations of state (EoS) and the bulk modulus ( $K_0$ ) of this compound, thus explaining

the degree of compressibility of this material (Section B1 in appendix B). The usual range of bulk modulus values of organometallic compounds oscillates between 10 and 20 GPa,<sup>61-63</sup> and it is usual that Cu-I based CPs show values within this range, thus explaining the elasticity and flexibility of the chains.<sup>47</sup> Compound **5** shows a  $K_0$  value of 9.7 GPa, close to the lower limit of this range, due to the deformability of the inter-chain interactions. Another consequence of the application of pressure is a drastic shrinking of all distances. Cu $\cdots$ Cu distances are the softest ones, suffering reductions of up to a 10.33% when pressure is increased to 7.16 GPa (**Table A7** in appendix A).

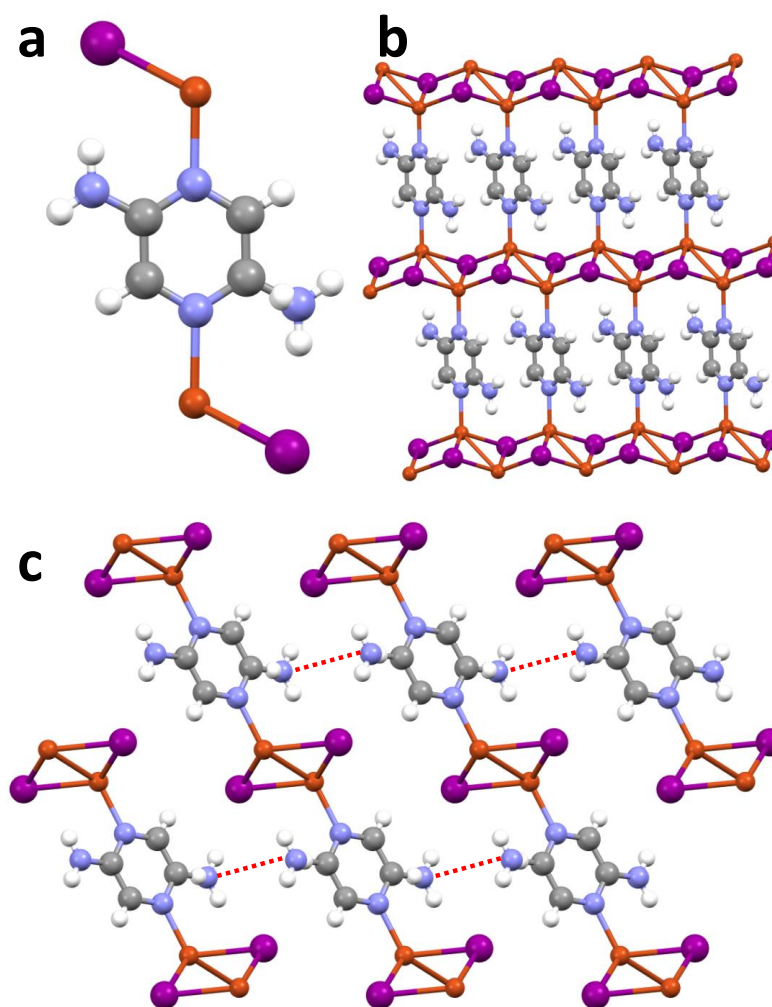


**Figure 2.17.** Crystal structure of compound **6**: (a) asymmetric unit; (b) lateral view of a 2D sheet containing three Cu(I)-I double *zigzag* chains; (c) View of the packing of the crystal structure from the crystallographic *a* axis. Cu: orange; I: purple; C: grey; H: white; N: blue; O: red. Dashed red lines indicate the presence of H-bonding interactions. Amino groups appear twice in every ligand residue due to a delocalization between two positions with 50% probability.

So far we have seen CPs where the terminal ligand is a pyridine derivative, with a single coordination position available for an intermediate-soft acid like copper(I). However, aminopyrazine presents two iminic nitrogen atoms, which makes compound **6** the only 2D CP among the compounds presented in this thesis. The two-dimensional sheets are

conformed by 1D double *zigzag* chains linked together by the aminopyrazine residues, with the free amino groups establishing hydrogen bonds with neighboring groups from nearby sheets. These amino groups are delocalized between two positions with 50% probability. The Cu $\cdots$ Cu distances display an asymmetry which is similar to that of compound **5**, but less accused, with values of 2.715 and 3.253 Å (**Figure 2.17**, **Tables A5-A6** in appendix A).

Similar to what was observed for compound **5**, when lowering the temperature with the help of liquid nitrogen we observe a reduction in all the distances present in the structure of compound **6**. As far as its response to pressure is concerned, pressures as high as 8.35 GPa cause, again, a drastic shrinking of all distances, especially Cu $\cdots$ Cu distances, which acquire values of 2.543 and 2.693 Å (**Table A8** in appendix A). Its bulk modulus (14.3 GPa) lies within the range outlined above, given the flexibility of the Cu-I chain but with a low deformability of the inter-chain interactions.

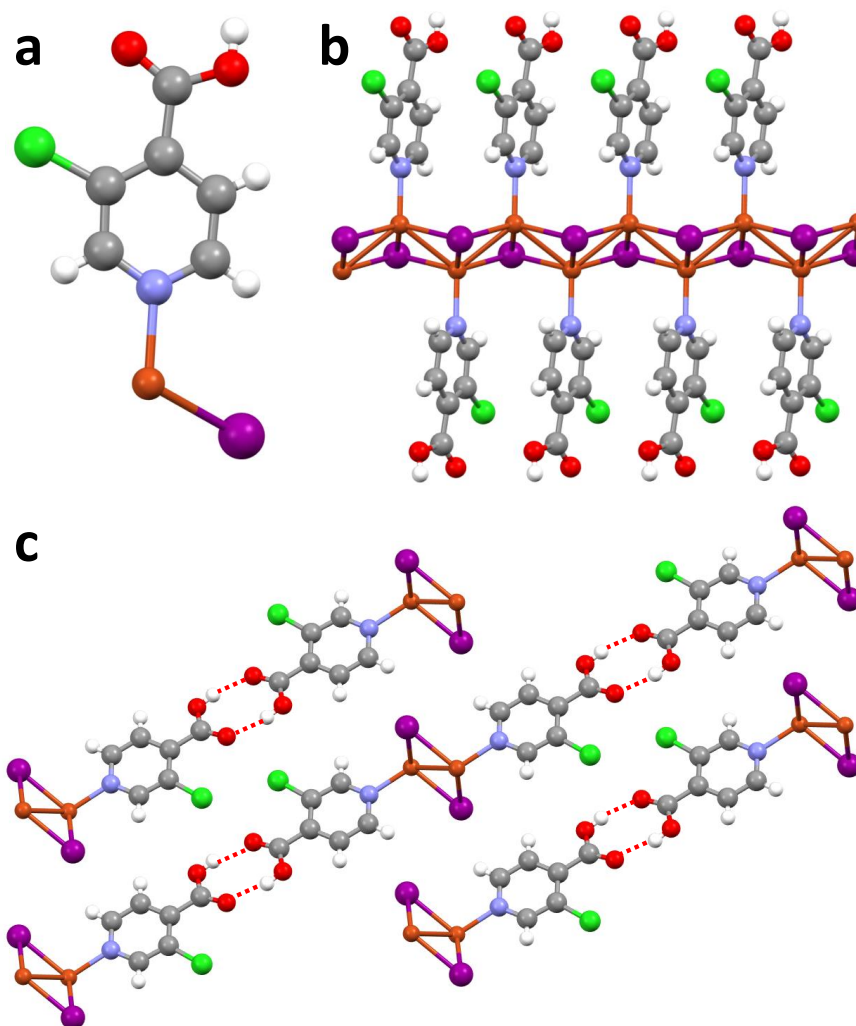


**Figure 2.18.** Crystal structure of compound **7**: (a) asymmetric unit; (b) lateral view of a Cu(I)-I double *zigzag* chain; (c) View of the packing of the crystal structure from the crystallographic *a* axis. Cu: orange; I: purple; C: grey; H: white; N: blue; O: red. Dashed red lines indicate the presence of H-bonding interactions.

Compound **7** shows a structure with features closer to those of compound **1**. The packing is directed by complementary H-bonds between the carboxylic groups of neighboring 3-chloroisonicotinic acid ligands, but this CP shows an additional feature, consisting of weak intra-molecule chlorine-oxygen interactions which strengthen the structure (**Figure 2.18**, **Tables A1-A2** in appendix A).

#### 2.2.1.2. Morphological characterization of nanoscale CPs

The low solubility of coordination polymers **2-7** in their reaction medium allows the immediate formation of precipitates consisting of nanostructures of these compounds. Depending on the structures of each compound, these nanostructures will show different morphologies.

The remarkable insolubility of isonicotinic acid in all solvents, caused by extremely strong hydrogen bonds, turns compound **1** into the most difficult one to nanoprocess. The fact that it does not precipitate in the reaction medium and, when adding a poor solvent, the white precipitate that forms is formed uniquely by isonicotinic acid, limits the nanoprocessing methods available to these two options: i) a top-down methodology consisting of the treatment of crystals of **1** with ultrasounds, or ii) the fast evaporation of a saturated solution of the building blocks (the mother solution isolated after the reaction is complete). However, opposite to what was expected, the sonication of crystals both in ultrasound bath and probe was fruitless, since the crystals tended to cleave along the chain, resulting in a shortening of the crystals without a significant reduction of the lateral dimensions (directed by H-bonds and VdW forces). This can be explained by the fact that inter-chain hydrogen bonding interactions are favored w.r.t. chain-solvent ones,<sup>64-66</sup> and has been observed for all the CPs presented in this thesis. On the other hand, the fast evaporation of a 20  $\mu\text{L}$  drop of the mother solution results in the formation of razor and needle-like structures with dimensions of  $(1.7 \pm 0.9) \times (11 \pm 7) \mu\text{m}^2$  and  $(0.304 \pm 0.082) \times (6 \pm 1) \mu\text{m}^2$ , respectively. This implies a significant reduction w.r.t. the length and lateral dimension of single crystals obtained by slow evaporation of the mother solution for 72 h, with values of  $(85 \pm 63) \times (1244 \pm 549) \mu\text{m}^2$  (**Figure 2.19**).

H-bonds present in 3-chloroisonicotinic acid are less strong than those of isonicotinic acid, so its lower insolubility allows compound **7** to be obtained as nanofibers directly in the reaction medium. The fibers observed by SEM show mean dimensions of  $(0.08 \pm 0.02) \times (0.8 \pm 0.3) \times (40 \pm 11) \mu\text{m}^3$ , in contrast with the dimensions of the micrometric crystals obtained by the slow evaporation of the mother solution:  $(33 \pm 11) \times (387 \pm 40) \mu\text{m}^2$  (**Figure 2.20**). The direct evidence of the formation of nanostructures of **7** was confirmed by AFM. In order to prepare the samples in a way that inter-chain interactions are minimized, the bottom-up methodology consisting of the direct reaction with magnetic stirring at a speed of 1200 rpm was selected, followed by a dilution of the

reaction medium. As a result, nanofibers with thicknesses between 5 and 15 nm, corresponding to arrays of 5 to 14 single chains, were obtained (**Figure 2.21**).

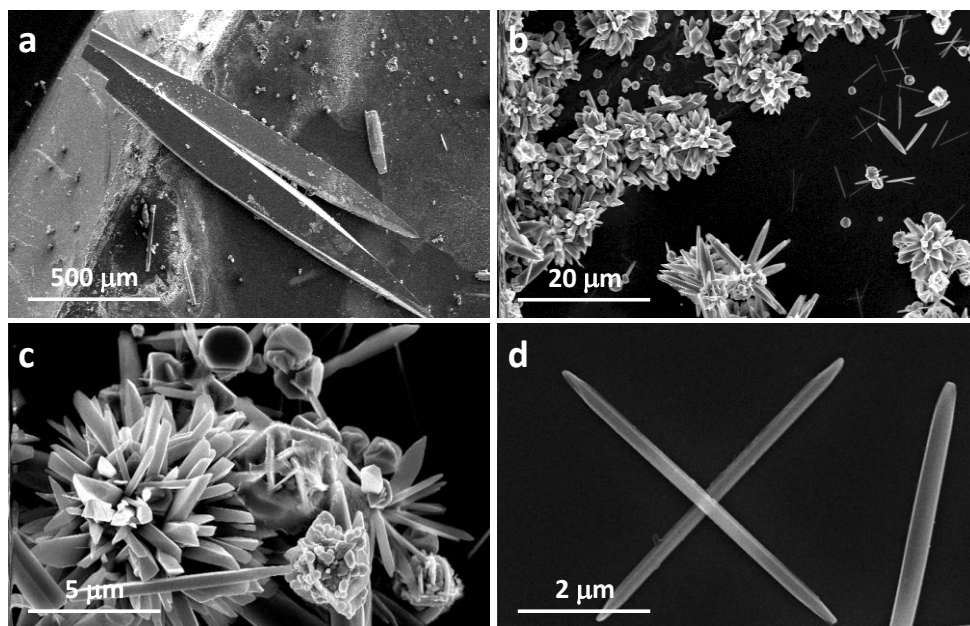


**Figure 2.19.** (a) SEM image of compound **1** microcrystals obtained by slow evaporation of the mother solution. (b) General SEM image of compound **1** micro- and submicrofibers obtained by fast evaporation of a 20  $\mu\text{L}$  drop of the mother solution (52 mM). (c) Detailed SEM image of the razor-like microfibers of compound **1**. (d) Detailed SEM image of the needle-like submicrofibers of compound **1**.

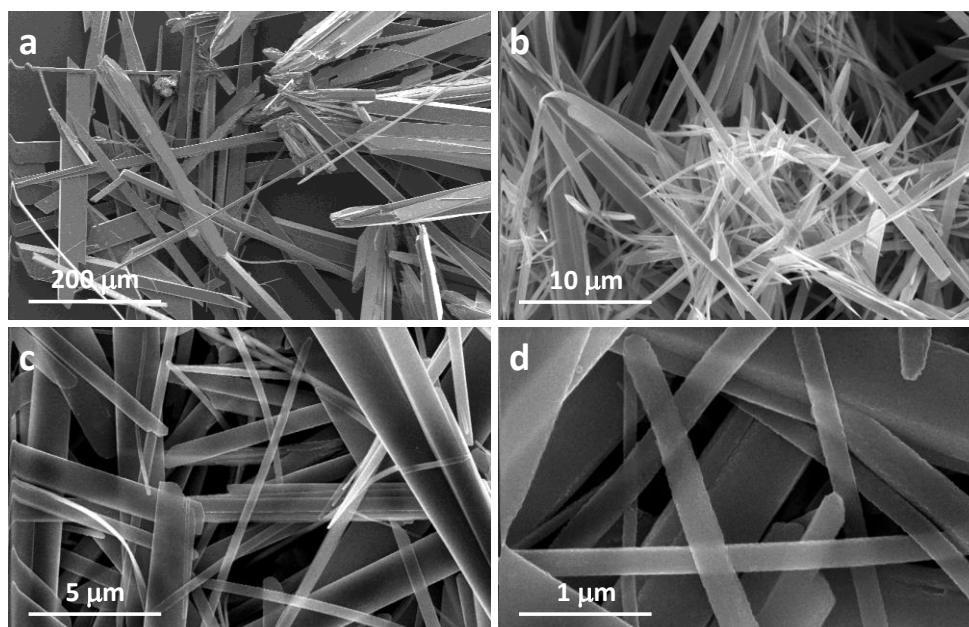


**Figure 2.20.** (a) SEM image of microcrystals of compound **7** obtained by direct reaction at 25  $^{\circ}\text{C}$  between CuI and the Cl-HIN ligand in MeCN/EtOH, after 2 days of slow evaporation: large area (bar-scale 200  $\mu\text{m}$ ). (b–d) General and detailed SEM images of compound **7** nanofibers obtained after 3 min of reaction time.



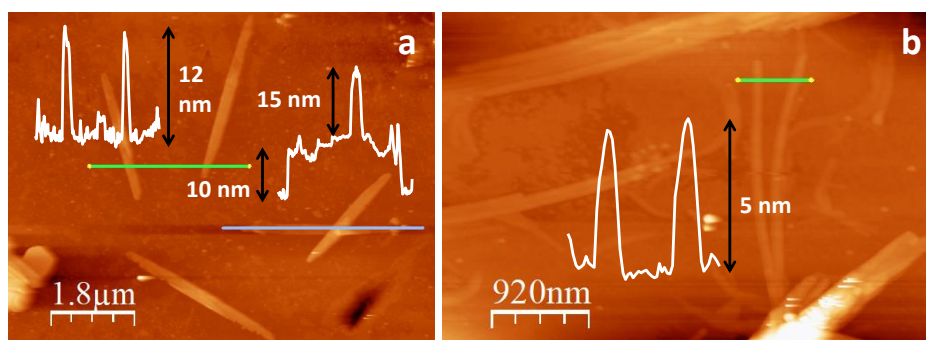


**Figure 2.21.** AFM images of nanofibers of compound **7** on SiO<sub>2</sub> prepared by magnetic stirring (1200 rpm) and drop-casting, with their height profiles across the green and blue lines.

Compounds **2** and **3** were also obtained by simple one-pot synthetic procedures. By mixing copper(I) iodide and liquid ethyl isonicotinate in acetonitrile, compound **2** was obtained in the shape of nanoribbons. The SEM and AFM images of these nanoribbons (**Figure 2.22**) show lateral dimensions of  $(60 \pm 28) \times (3 \pm 2) \mu\text{m}^2$  and thicknesses between 6 and 25 nm, in clear contrast with the regular dimensions of the micrometric crystals, these ones being  $(61 \pm 15) \times (1700 \pm 400) \mu\text{m}^2$ .

On the other hand, the reaction between CuI and 2-amino-5-nitropyridine (ANP) in acetonitrile-ethanol 2:1 leads to the formation of nanofibers of compound **3**. The mean dimensions of these fibers have been checked by SEM and AFM (**Figure 2.23**), finding lengths of over 100  $\mu\text{m}$ , widths of  $(0.3 \pm 0.2) \mu\text{m}$  and thicknesses between 50 and 250 nm. The respective micrometric crystals showed dimensions of  $(22 \pm 12) \times (1000 \pm 500) \mu\text{m}^2$ .

Although we have been able to obtain nanostructures of these compounds, they need to be shortened in order to be useful in different applications. Following this principle, we have studied the influence of the reaction conditions in the lateral dimensions of these nanostructures (**Table 2.3**). Taking into account the errors made in the measurements, we can conclude that sonication and an increase in the initial concentration of the building blocks does not produce significant variation in the lateral dimensions of our nanostructures, with one exception: the lateral dimensions of compound **3** show significantly higher values when they are subjected to sonication in ultrasound bath (compare experiment *b3* vs. *e3*). As explained before for compound **1**, ultrasounds seem to favor the formation of hydrogen bonds, and as temperature increases the rate of formation of these H-bonds grows faster, so longer reaction times will provoke an increase in the lateral dimensions of the nanofibers of **3**. Higher reactant concentrations favor agglomeration processes, so the highest width values are obtained for experiment *f3*. Compound **2** does not suffer these variations since it does not have an intrinsic capacity to establish hydrogen bonding interactions.

The use of a mixture of solvents containing water (MeCN/H<sub>2</sub>O 1:1) for these reactions induces a significant decrease in the lengths of the nanostructures of both **2** and **3**

(experiments *g2* and *g3*). Therefore, the use of a poor solvent seems to play a crucial role in the fast precipitation of the CPs once they are formed in a water containing medium. Indeed, size reduction using a poor solvent is well-known for nanoparticles of CPs, including MOFs.<sup>67-68</sup>

**Table 2.3.** Effect of the reaction time, concentration, solvent and stirring method on the lateral dimensions of the nanostructures of compounds **2** and **3** at 20 °C for magnetic stirring and between 20 and 30 °C for the sonication in ultrasound bath. The means and standard deviations have been calculated from data corresponding to 60 nanocrystals.

Experiment	Reaction method	Solvent	Reaction Time (min.)	[CuI] and [ANP] or [EtIN] (mM)	Mean fibre width (μm)	Mean fibre length (μm)
<b>a3</b>	Magnetic stirring	CH <sub>3</sub> CN/EtOH	1	35	0.3 ± 0.2	>100
<b>b3</b>	Magnetic stirring	CH <sub>3</sub> CN/EtOH	9	35	0.3 ± 0.1	>100
<b>c3</b>	Magnetic stirring	CH <sub>3</sub> CN/EtOH	9	70	0.5 ± 0.1	>100
<b>d3</b>	Ultrasound bath	CH <sub>3</sub> CN/EtOH	1	35	0.3 ± 0.2	>100
<b>e3</b>	Ultrasound bath	CH <sub>3</sub> CN/EtOH	9	35	1.3 ± 0.7	>100
<b>f3</b>	Ultrasound bath	CH <sub>3</sub> CN/EtOH	9	70	2 ± 1	>100
<b>g3</b>	Ultrasound bath	CH <sub>3</sub> CN/H <sub>2</sub> O	9	35	0.6 ± 0.4	65 ± 28
<b>a2</b>	Magnetic stirring	CH <sub>3</sub> CN	1	35	3 ± 2	60 ± 28
<b>b2</b>	Magnetic stirring	CH <sub>3</sub> CN	9	35	7 ± 3	31 ± 18
<b>c2</b>	Magnetic stirring	CH <sub>3</sub> CN	9	70	7 ± 2	20 ± 4
<b>d2</b>	Ultrasound bath	CH <sub>3</sub> CN	1	35	7 ± 2	23 ± 5
<b>e2</b>	Ultrasound bath	CH <sub>3</sub> CN	9	35	5 ± 3	46 ± 5
<b>f2</b>	Ultrasound bath	CH <sub>3</sub> CN	9	70	9 ± 3	22 ± 7
<b>g2</b>	Ultrasound bath	CH <sub>3</sub> CN/H <sub>2</sub> O	9	35	2 ± 0.6	9±2

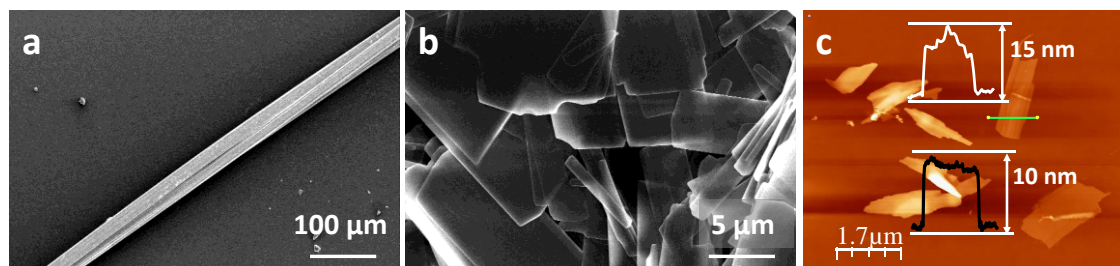


**Figure 2.22.** (a, b) SEM images of compound **2**: microcrystals (a) and nanofibres prepared by magnetic stirring at 500 rpm (b). (c) AFM image of fibers of compound **2** with their height profiles across the lines (insets).

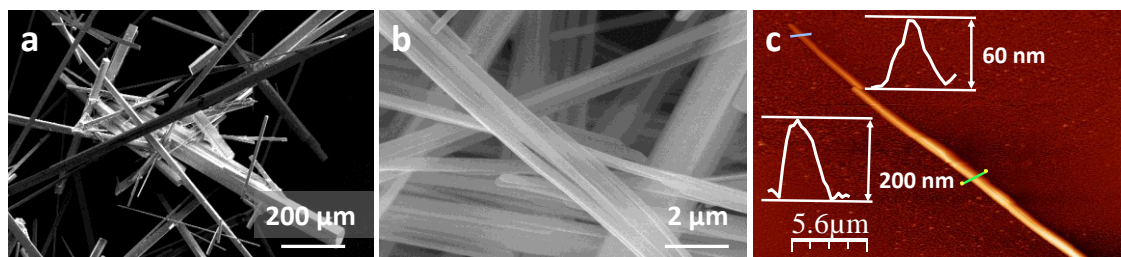


**Figure 2.23.** (a, b) SEM images of compound **3**: microcrystals (a) and nanofibres prepared by magnetic stirring at 500 rpm (b). (c) AFM image of fibers of compound **3** with their height profiles across the lines (insets).

When crystals of compound **3** are exposed to acetic acid vapors, they experience a sorption process and, consequently, they become amorphous but their electrical conductivity increases by three orders of magnitude. This process is reversible, and can be reverted by leaving the crystals in the open air. This is the consequence of the outstanding capacity of the ANP residues to selectively recognize certain molecules by establishing hydrogen bonding interactions with them, and it is translated in slight variations of the distances and angles within the double Cu-I chains.

In order to check if the nanofibers of compound **3** suffer the same sorption process than the single crystals, a sample containing these nanofibers was exposed to acetic acid vapors for 72 hours. The new **3**·AcOH material was characterized by elemental analysis, IR, PXRD and SEM. Elemental analysis quantifies an acetic acid adsorption of *ca.* 10 wt%. The IR spectrum of **3**·AcOH shows one additional band to those observed in the initial material at  $1715\text{ cm}^{-1}$ , corresponding to the C=O stretching of acetic acid. The PXRD pattern did not show any significant changes (**Figure C4** in appendix C) with respect to that of the pristine **3**. When studying the nanostructures by SEM, the morphology of the fibers after exposure to acetic acid changed, with their widths doubled to  $(740 \pm 468)\text{ nm}$  (**Figure 2.24a**). Consequently, acetic acid links to the ANP terminal ligands via hydrogen bonding interactions, favoring the broadening of the fibers without changing their crystal structure. Therefore, it can be stated that the interaction between **3** and the AcOH molecules takes place at the surface of the nanofibers leading to an enhancement in the width while retaining its crystal structure.

Finally, the reversibility of the acetic acid adsorption by these nanofibers was studied. For this purpose, **3**·AcOH was allowed to stay in air for 30 days. The SEM characterization of the new material shows lateral dimensions of  $(600 \pm 497)\text{ nm}$ , which are slightly thinner in width than **3**·AcOH but wider than the starting material (**Figure 2.24b**). The IR spectrum in this state still shows the vibration assigned to the carboxylic group. Desorption of AcOH molecules from **3**·AcOH is completed upon heating at  $50\text{ }^{\circ}\text{C}$  for 2 hours. IR spectroscopy confirms the absence of carboxylic groups. Morphological characterization of the desorbed crystalline material shows widths of  $(443 \pm 332)\text{ nm}$  (**Figure 2.24c**) which agrees with those observed in the starting nanofibers of **3**.



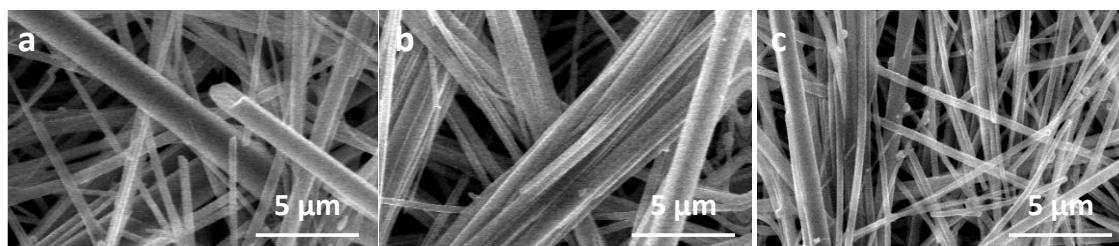


**Figure 2.24.** (a) SEM image of nanofibers of **3** after being exposed to acetic acid (AcOH) vapors for 72 h. (b) SEM image of the same nanofibers exposed to AcOH vapors upon standing in air for 30 d. (c) SEM image of the same nanofibres exposed to AcOH vapors upon standing in air for 30 d and heated at 50 °C for 2 h.

Nanofibers of compounds **4** and **5** can easily be obtained in a similar way to those outlined for compounds **2** and **3**, this is, by direct reactions between their building blocks. The micrometric crystals obtained by the slow evaporation of the mother liquors show dimensions of  $(2000 \pm 500) \times (150 \pm 50) \mu\text{m}^2$  for compound **4** (**Figure 2.25a**) and  $(1500 \pm 500) \times (78 \pm 30) \mu\text{m}^2$  for compound **5** (**Figure 2.26a**). When these compounds are reduced to the nanometric scale they still show lengths higher than 100  $\mu\text{m}$ , but their lateral dimensions are significantly lower, these ones being  $(811 \pm 348) \text{ nm}$  and  $(501 \pm 389) \text{ nm}$ , respectively (**Figures 2.25b-d** and **2.26b-d**). The AFM images of these nanofibers show thicknesses between 50 and 550 nm for compound **4** (**Figure 2.27a,b**) and between 5 and 15 nm for compound **5** (**Figure 2.27c,d**).

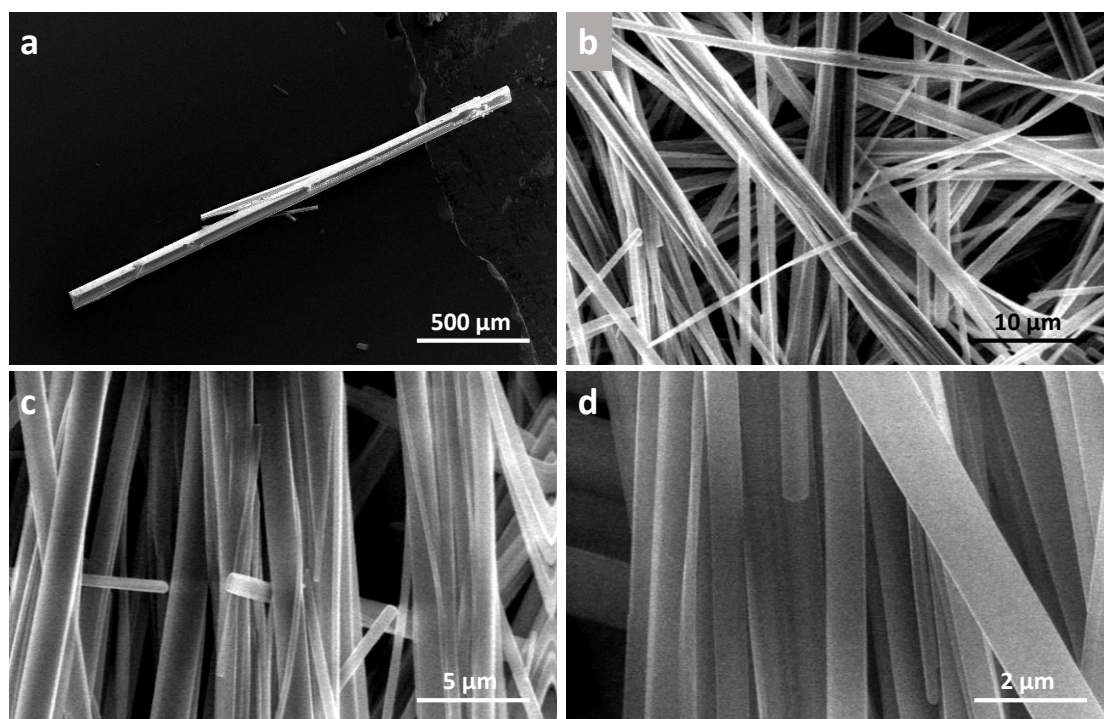


**Figure 2.25.** (a) SEM image of compound **4** microcrystals obtained by slow evaporation at 25 °C. (b-d) SEM images of compound **4** nanofibers obtained by fast precipitation at 25 °C.

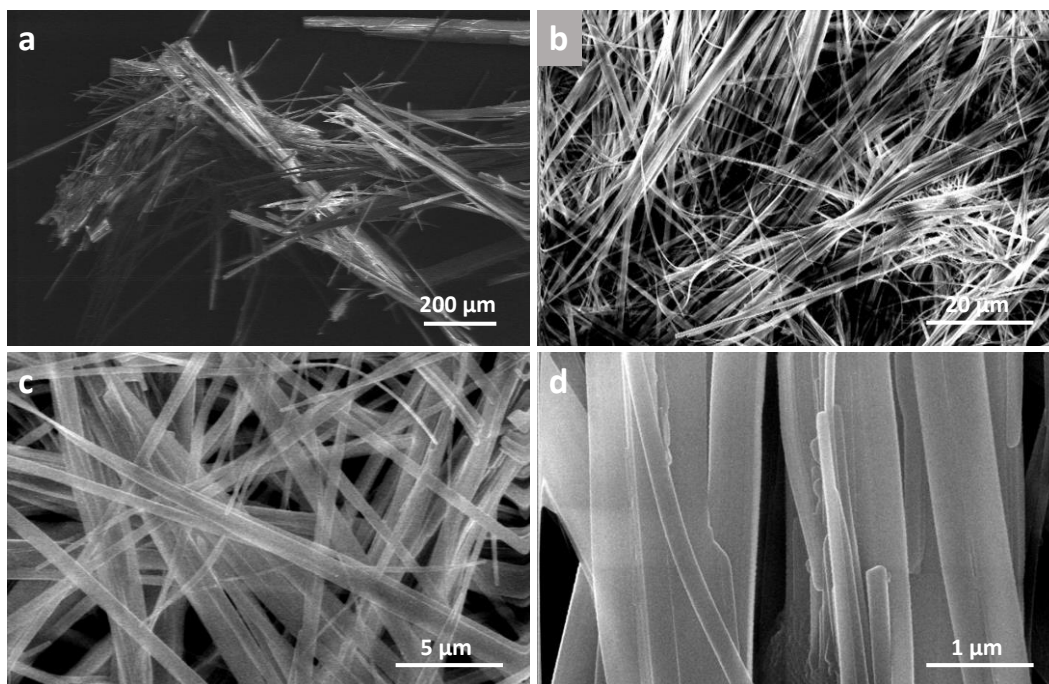


**Figure 2.26.** (a) SEM image of compound **5** microcrystals obtained by slow evaporation at 25 °C. (b-d) SEM images of compound **5** nanofibers obtained by fast precipitation at 25 °C.

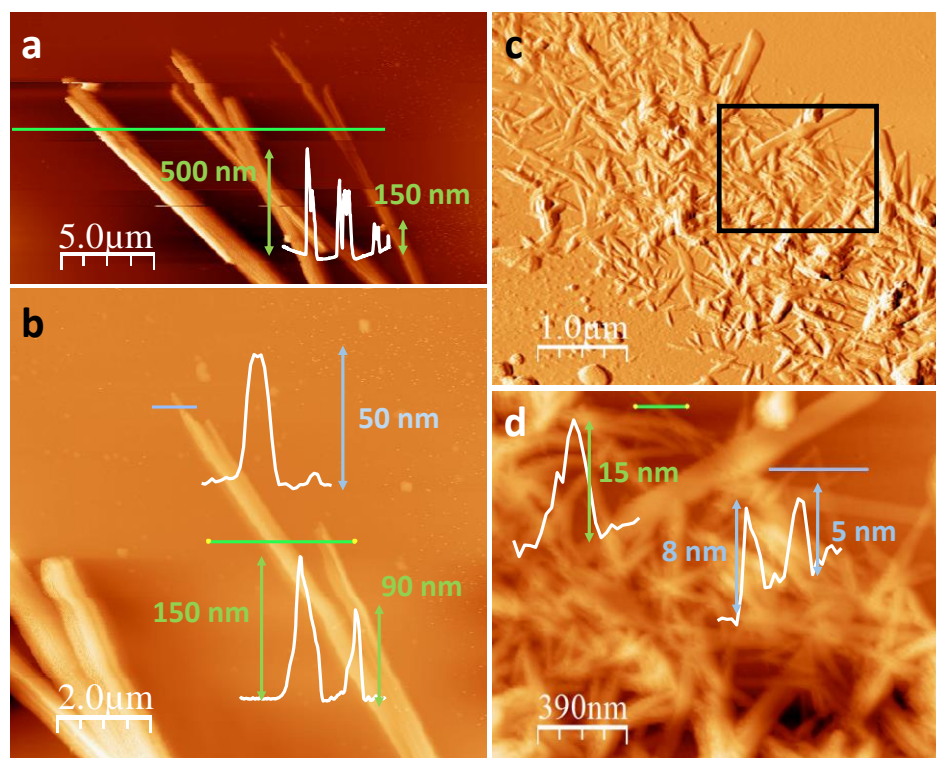


**Figure 2.27.** (a) AFM image of nano- and sub-microfibers of compound **4** on SiO<sub>2</sub> prepared by drop casting, with their height profile across the green line. (b) A zoomed area of (a), with its height profiles across the blue and green lines. (c) AFM image of compound **5** nanofibers on SiO<sub>2</sub> prepared by dip-coating. (d) A zoomed area of (c), the black rectangle, with its height profiles across the green and blue lines.



Due to its two-dimensional nature, compound **6** is the only one in this thesis which crystallizes in the shape of sheets. Compound **6** nanosheets can be obtained by the direct reaction of CuI and aminopyrazine in acetonitrile/water 3:1. Whereas crystals show lateral dimensions of  $(38 \pm 10) \times (21 \pm 7) \mu\text{m}^2$  (**Figure 2.28a,b**), nanosheets present dimensions of  $(372 \pm 127) \times (1209 \pm 300) \text{nm}^2$ , observed by SEM (**Figure 2.28c,d**). An AFM study allows determining the thicknesses of these nanosheets, these ones being in the range between 5 and 20 nm, corresponding to 10-32 stacked layers (**Figure 2.29**). However, in the process that leads to the formation of the nanosheets, they can pile up to form aggregates with thicknesses from 100 to 300 nm. The advantage of these aggregates is that they can be studied by confocal microscopy (see section 2.2.3).

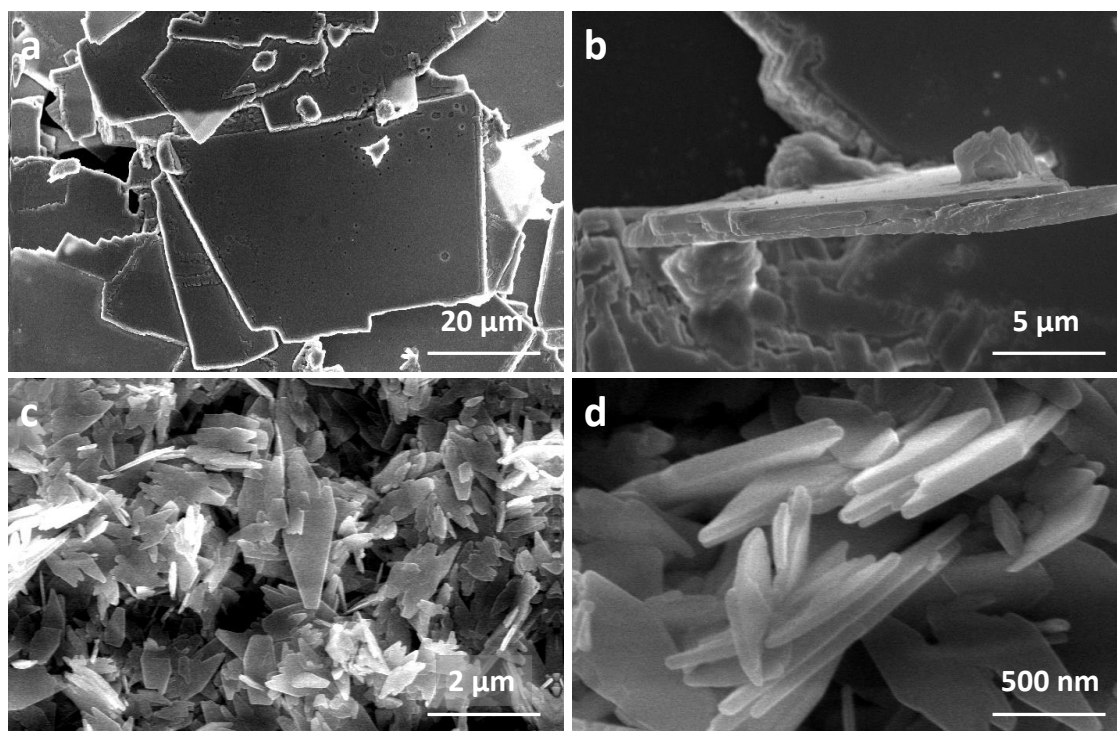


**Figure 2.28.** (a,b) General (a) and detailed (b) SEM images of compound **6** microcrystals. (c,d) General (c) and detailed (d) SEM images of compound **6** microcrystals.

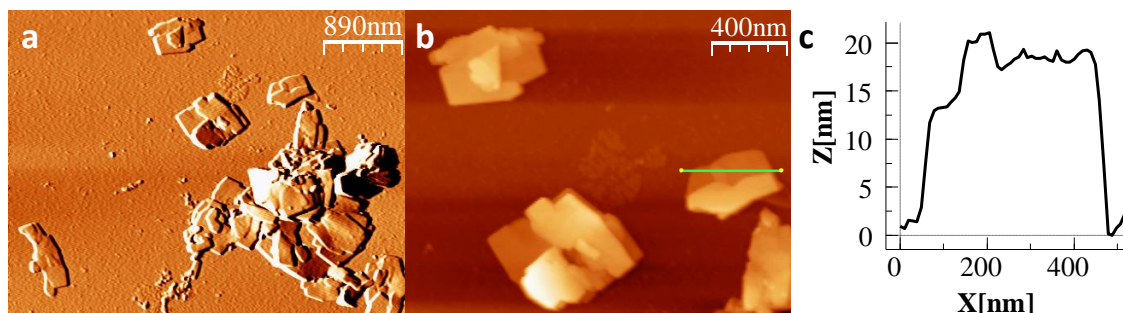


**Figure 2.29.** a) AFM image of compound **6** nanosheets on SiO<sub>2</sub>. b) A zoomed area of (a). c) A typical height profile of a nanosheet across the green line represented in (b).

### 2.2.2. Electrical conductivity

In this section, the electrical conductivity values of compounds **4-7** will be outlined and explained by means of theoretical calculations of the electronic band-gap. In order to experimentally determine the electrical conductivity of all compounds, a two-contact method was used, contacting crystals of every compound with graphite paste and tungsten wires, and applying a voltage between -10 and 10 V. This same method was used to study the thermal dependence of their electrical conductivity, but using four contacts instead of two (see Experimental Section, chapter 6.2).

Compound **4** shows an electrical conductivity value of  $4 \cdot 10^{-7}$  S/cm at room temperature. In order to compare it with the electrical conductivity of compounds **1** ( $3 \cdot 10^{-3}$  S/cm) and **2** ( $2 \cdot 10^{-6}$  S/cm), we will thoroughly look at the distances and angles present in their structures (Appendix A, **Table A3**).<sup>42</sup>

Electrical conductivity in Cu(I)-I double chains is determined by the following factors: firstly, Cu-I<sub>rail</sub> distances and their dimerization; secondly, I-Cu-I angles along the chain; finally, the dihedral angle between Cu<sub>2</sub>I<sub>2</sub> rhomboid dimers. It has been proved that Cu...Cu distances (having average values of 2.872 Å for compound **1**, 2.805 Å for compound **2** and 2.787 Å for compound **4**) are too long and, therefore, the Cu...Cu are too weak to determine the electrical conductivity of these compounds. These leaves the Cu-I<sub>rail</sub> distances as the only plausible pathway for electronic delocalization.

Cu-I<sub>rail</sub> lengths are shorter in **1** (2.632 Å) than in **2** (2.662 Å) and **4** (2.661 Å), and the dimerization of these bonds along the chain is also smaller in **1** (0.001 Å) than in **2** (0.0876 Å) and **4** (0.0171 Å), in agreement with the higher conductivity value found for **1**. Additionally, although the differences are smaller, the I-Cu-I bond angle along the chain is larger in **1** (103.01(3)°) than in **2** (102.69(2)°) and **4** (102.93(3)°). This larger angle is expected to lead to a better orbital overlap and, therefore, to a high electrical conductivity, again in agreement with the observed values. Finally, the dihedral angle between the Cu<sub>2</sub>I<sub>2</sub> rhomboid dimers forming the chain also suggests that compound **1** should be a better conductor as this angle is closer to 90° in this compound (119.38°) than in **2** (120.98°) and **4** (122.18°). This eases the overlapping of hybridized d<sub>z</sub><sup>2</sup> orbitals of copper centers and the p<sub>z</sub> orbitals of iodine in **1** (**Figure 2.30**), therefore justifying its conductivity value, which is three orders of magnitude higher than that of **2**. As far as compounds **2** and **4** are concerned, although Cu-I<sub>rail</sub> lengths and their dimerization are longer in **2** and its I-Cu-I bond along the chain has a smaller value, this compound shows a lower value for the dihedral angle. All this factors compensate, yielding similar experimental values of the electrical conductivity.

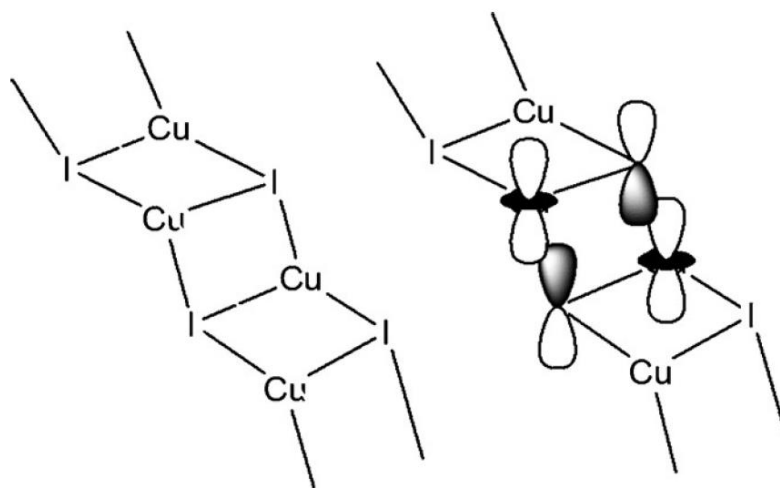


**Figure 2.30.** Schematic representation of the overlapping between the hybridized  $d_z^2$  and  $p_z$  orbitals of copper and iodine along a Cu(I)-I chain.

According to its conductivity value, a semiconducting behavior is expected for compound **4**. As can be seen in **Figure 2.31**, at temperatures between 145 and 350 K resistivity decreases with the increasing temperature, confirming this behavior. The activation energy, calculated by means of the Arrhenius equation, shows a value of 300 meV. Remarkably, between 125 and 145 K a hysteresis cycle is generated due to a phase transition (see section 2.2.1.1) between two semiconducting phases, originated by slight changes in the asymmetry of the chains. As a result, resistivity decreases by four orders of magnitude. The activation energy of this new phase is 80 meV. At temperatures above 350 K, the partial degradation of the CP, releasing  $\text{CO}_2$  with a subsequent partial reduction of Cu(I) into Cu(0), derives into an irreversible transformation of compound **4** into a quasimetallic phase which remains unaltered in the range of temperatures studied (2-400 K).

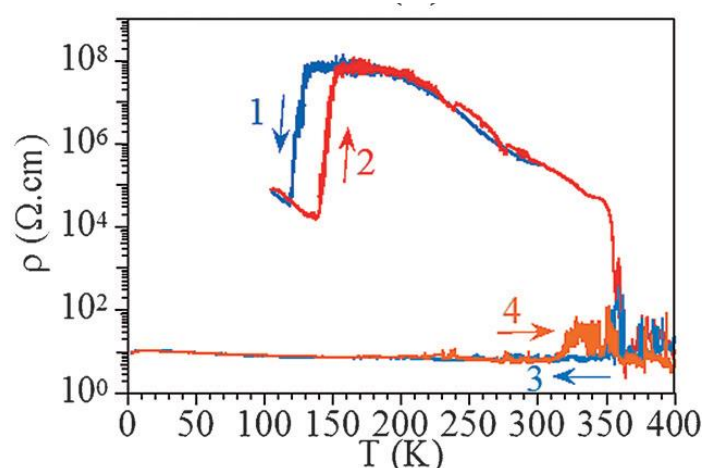


**Figure 2.31.** Thermal variation of the electrical conductivity of **4** in four successive scans (1-4). The constant horizontal resistivity between 125 and 200 K in scans 1 and 2 indicates that the resistance has reached the measuring limit of the equipment ( $5 \times 10^{11} \Omega$ ).

Another way to rationalize the electrical properties of compounds **1**, **2** and **4** is the use of theoretical calculations of the density of states (DOS) and the shape of their valence bands (VB) and conduction bands (CB). The computational details of the procedure followed for the calculations are outlined in the experimental section (section 2.2.15). In the theoretical simulations, we have used the atomic coordinates found in the X-ray structures of these CPs to evaluate the real geometry of the materials in the crystalline phase, in which the electrical measurements were carried out. For all the compounds, the residual forces acting on each atom in all the calculations were below  $0.1 \text{ eV}\text{\AA}^{-1}$ , which is low enough to guarantee perfectly converged and realistic results for such complex systems from a theoretical point of view. This noticeably good geometrical transferability between the experimental configurations and our theoretical implementation has already provided successful results for other similar CP crystals,<sup>58</sup> so it will be used for all the calculations related to the CPs presented in this thesis.

In this case, the band gap values calculated for compounds **1**, **2** and **4** (with values of 0.13 eV for compound **1**, 0.04 eV for **2**, 0.19 eV for **4** at 296 K and 0.17 eV for **4** at 110 K; **Figure 2.32**) are in good agreement with their activation energies (200, 80 and 300 meV, respectively); moreover, with these results these CPs are predicted as narrow-gap semiconductors, whose behavior is confirmed by their structure. The significant differences between their conductivity values can be justified by means of analyzing the different contributions of the *p* and *d* states of Cu and I. In the case of compound **1**, a highly effective hybridization of the  $\text{Cu-}d_z^2$  states and the  $\text{I-}p_z$  states leads to an important electronic delocalization which is the cause of its high conductivity, whereas in the case of compounds **2** and **4** this hybridization is very poor (in the case of compound **2**,  $\text{I-}d_z^2$  orbitals play a key role in the formation of its electronic states, precluding a slightly better electronic delocalization than that of **4**). The better overlapping of these  $\text{Cu-}d_z^2$  and  $\text{I-}p_z$  orbitals in **1** is due to the lower value of the dihedral angle between  $\text{Cu}_2\text{I}_2$  planes ( $119.3^\circ$  w.r.t.  $120.9^\circ$  and  $122.3^\circ$ ).

**Figure 2.33** shows the VB and CB orbital electron isodensities ( $10^{-4} \text{ e}\text{\AA}^{-3}$ ) of compounds **1**, **2** and **4**. In this figure it is possible to appreciate that, in all cases, the valence electron isodensity is mostly located along the Cu-I skeleton, whilst the conduction electron isodensity shows a continuous orbital side-to-side hybridization formed between the ligands. Thus, the conduction will be produced mainly along the one-dimensional chains. The increasing temperature enables the charge migration from the valence band towards the conduction band, as well as a temperature- induced overlapping between both bands that will ease the carrier mobility and the electronic conduction along the chains.

Additionally, a deeper inspection of **Figure 2.33** allows us to appreciate that, for the CPs showing higher conductivity values (**1** and **2**), the valence band shows some significant weight also within the organic ligands, which may ease the carriers mobility towards the conduction band, mostly located on these ligands. Conversely, this finding is not evident for compound **4**.



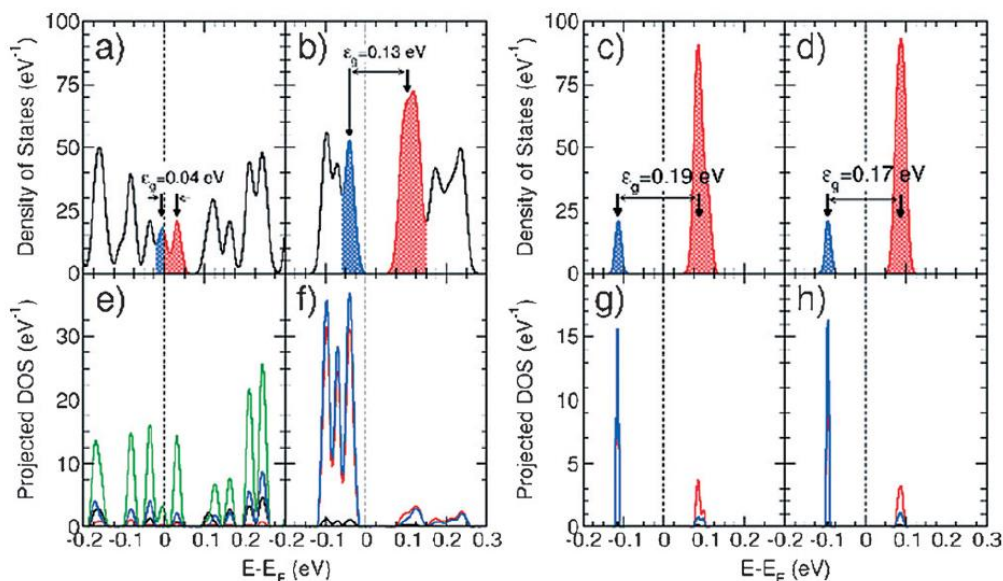


**Figure 2.32.** (a-d) Calculated total density of electronic states for **2** and **1** (a,b), and for **4** at 296 K and 110 K (c,d) as a function of the energy, relative to the Fermi level. Each energy level has been broadened with a Lorentzian profile with a linewidth of 0.01 eV, and the valence and conduction bands for both compounds have been shaded in blue and red, respectively. The transport gap is also indicated in each subpanel. (e-h) Calculated projected density of electronic states for **2** (e), **1** (f) and **4** at 296 K (g) and 110 K (h) on Cu and I atoms.  $p$  and  $d$  state contributions of all the Cu and I atoms participating in each crystal are depicted separately (black, red, blue and green lines correspond to Cu- $p$ , Cu- $d$ , I- $p$ , I- $d$  contributions, respectively).

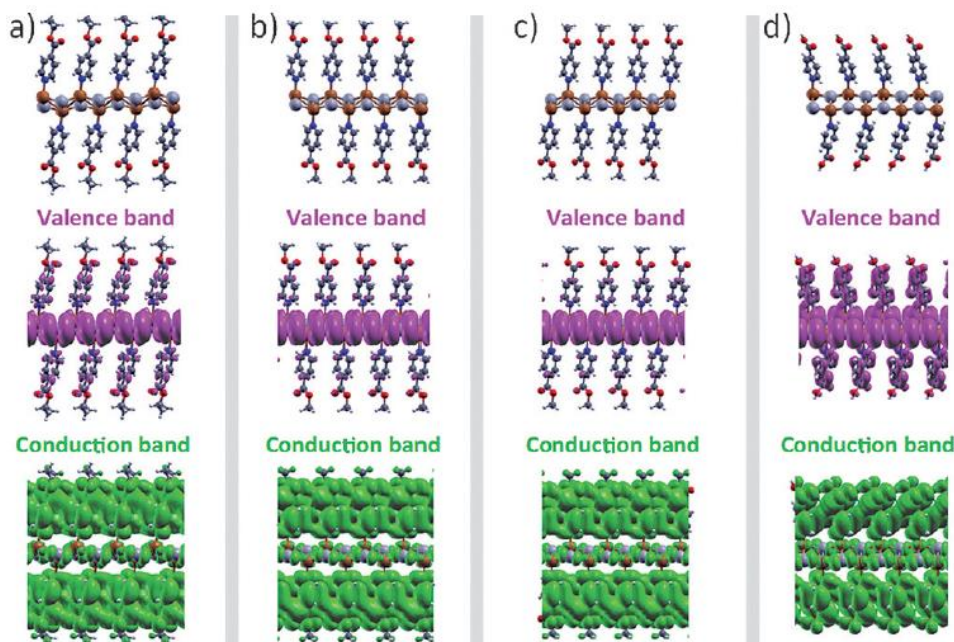


**Figure 2.33.** Computed VB (middle panels) and CB (bottom panels) orbital electron isodensities ( $10^{-4} \text{ e}\text{\AA}^{-3}$ ) for compounds **2** (a), **4** at 296 K (b) and 110 K (c), and **1** (d). Clean geometries are also shown (top panels) for better visualization.

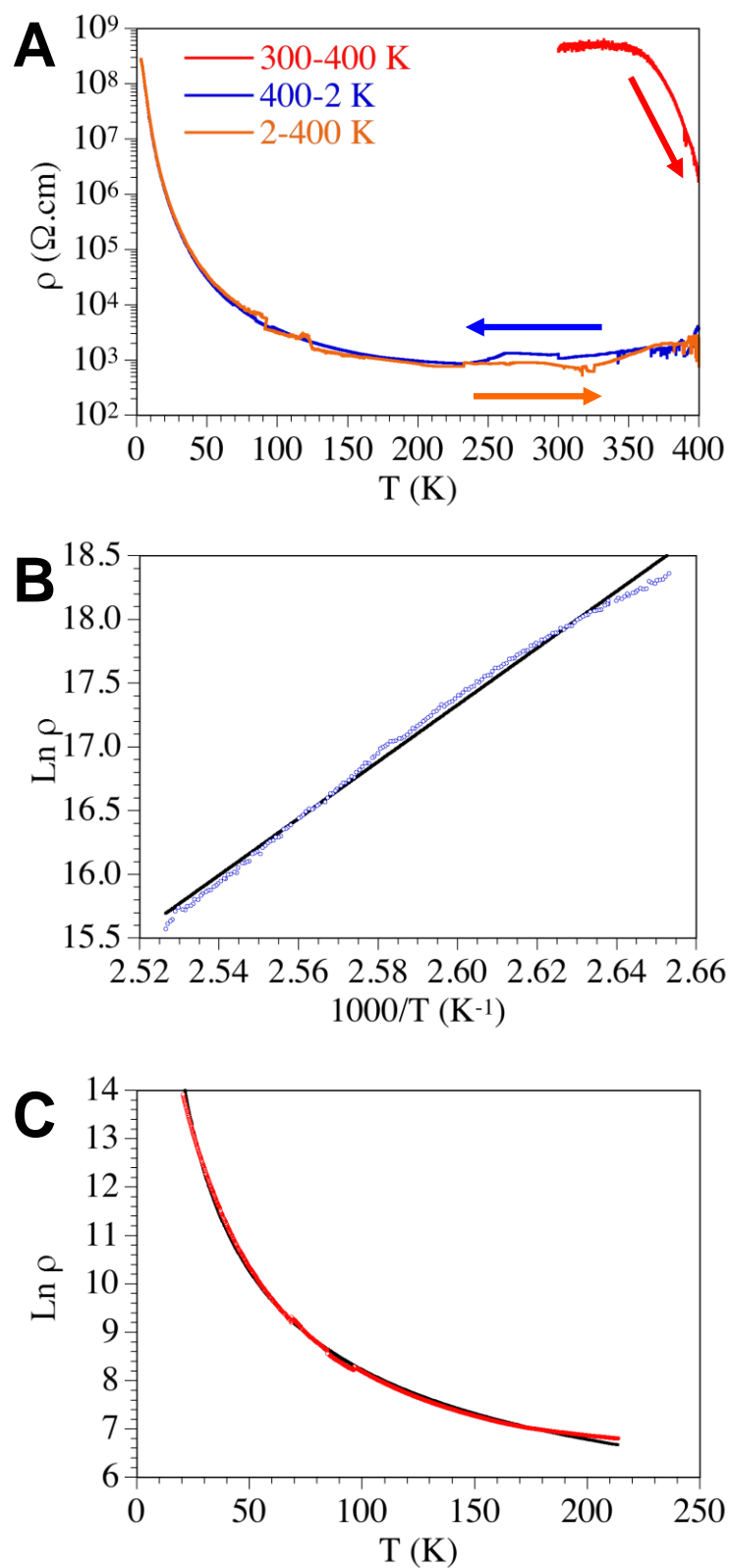


**Figure 2.34.** (a) Thermal variation of the electrical resistivity for compound **5**. (b) Arrhenius plot of compound **5** in the initial heating scan from 380 to 400 K. (c) Thermal variation of the electrical conductivity of compound **5** in the cooling scan after the initial heating at 400 K. Solid black line is the fit to the variable range hopping model.



The thermal dependence of the electrical resistivity of a single crystal of compound **5** (**Figure 2.34a**) shows that, initially, this compound is almost an insulator at room temperature, with an extrapolated conductivity value of  $\text{ca. } 10^{-15} \text{ S/cm}$ . When the sample is heated from room temperature to 400 K, the resistance remains above the detection limit of our equipment ( $5 \times 10^{11} \Omega$ ) up to  $\text{ca. } 360 \text{ K}$  and, accordingly, the resistivity ( $\rho$ ) shows a constant value below this temperature. Above  $\text{ca. } 360 \text{ K}$  the resistivity decreases and reaches a value of  $\text{ca. } 2.2 \times 10^6 \Omega \text{ cm}$  at 400 K (i.e.,  $\sigma = 1/\rho = 2.1 \times 10^{-7} \text{ S cm}^{-1}$ ), with an activation energy of 2.0 eV (**Figure 2.34b**). Interestingly, at 400 K the resistivity decreases with time and after  $\text{ca. } 10 \text{ min}$  at 400 K the resistivity reaches a constant value of  $\text{ca. } 3 \times 10^3 \Omega \text{ cm}$  ( $\sigma = 2.3 \times 10^{-4} \text{ S cm}^{-1}$ ). Once the resistivity value is stabilized, the temperature was decreased to 2 K. In this cooling scan the resistivity shows a quasi-metallic behavior and initially decreases to reach a broad minimum at  $\text{ca. } 225 \text{ K}$  with a value of  $\text{ca. } 8 \times 10^2 \Omega \text{ cm}$ . Below this temperature the resistivity increases to reach a value of  $\text{ca. } 3 \times 10^8 \Omega \text{ cm}$  at 2 K. If the crystal is heated from 2 to 400 K the resistivity shows the same values observed in the cooling scan. This behavior does not obey the Arrhenius law (**Figure 2.34c**), but rather a variable range hopping model for 1D systems:  $\sigma = \sigma_0 \exp[-(T_0/T)^\alpha]$  with  $\sigma_0 = 0.032(2) \text{ S cm}^{-1}$ ,  $T_0 = 2187(72) \text{ K}$  and  $\alpha = 0.51(1)$ , a value very close to the expected one for a 1D system ( $\alpha = 1/2$ ). Further cooling/heating cycles show a similar behavior.

The difference between the electrical conductivity values of compounds **4** and **5** can be explained by looking at their crystal structures. Although they seem identical, there is a significant difference between the average values of the Cu...Cu distances ( $2.787 \text{ \AA}$  for **4**,  $3.098 \text{ \AA}$  for **5**), which can be used to justify the lower conductivity of **5**. In this case, theoretical calculations are more suitable to justify the luminescent properties of compound **5** rather than its electrical conductivity (see section 2.2.3).

Compound **7** shows a room temperature electrical conductivity of  $3 \times 10^{-5} \text{ Scm}^{-1}$  and a typical semiconducting behavior (**Figure 2.35**) that is similar to that of compound **1**. A very slight degradation process which occurs above 380 K (hampered by the strong network of hydrogen bonds present in the structure of this compound) causes the resistivity to increase in the successive cooling scan. Afterwards, in the following heating and cooling scans show a very smooth hysteresis cycle (180-270 K) between the unaltered phase and the slightly degraded one.

In fact, compounds **1** and **7** show some of the highest electrical conductivity values registered for a Cu-X coordination polymer. Still, the differences between them are remarkable (two orders of magnitude). Fortunately, these differences can be easily explained by four structural factors: firstly, the Cu-I<sub>rail</sub> distances, which are lower in **1** ( $2.632 \text{ \AA}$  w.r.t.  $2.646 \text{ \AA}$ ); secondly, the dimerization of these Cu-I<sub>rail</sub> distances, which once again is lower in **1** ( $0.010 \text{ \AA}$  w.r.t.  $0.0217 \text{ \AA}$ ); finally, the value of the I-Cu-I angle along the chain and the dihedral angle, which in the case of **1** are closer to  $90^\circ$ , therefore easing the hybridization of Cu- $d_z^2$  and I- $p_z$  orbitals. All these factors demonstrate that compound **1** should show a higher electrical conductivity than that of **7**.

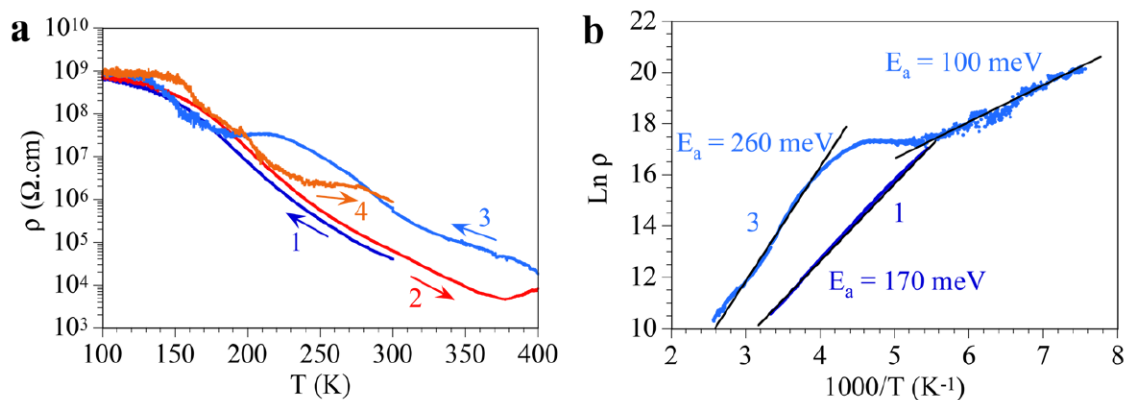


**Figure 2.35.** Electrical behavior of compound **7**. (a) Thermal dependence of the electrical resistivity in four successive cooling and heating scans. (b) Arrhenius plot of the first (dark blue) and second (light blue) cooling scans.

Theoretical calculations also endorse the higher electrical conductivity of **1**. The DOS diagrams (**Figure 2.36**) allow calculating the electronic band-gap of these compounds, these showing values of 0.13 eV for compound **1** and 0.05 eV for compound **7**. Nevertheless, the VB and CB of compound **7** are strongly localized, and this can easily be observed in a graphical representation of the 3D orbital isodensities (**Figure 2.37**): the VB is localized in the Cu-I skeleton, whereas the CB is located on the ligands. As was explained before, the VB and CB of compound **1** are effectively hybridized, so this strongly favors the electronic delocalization.

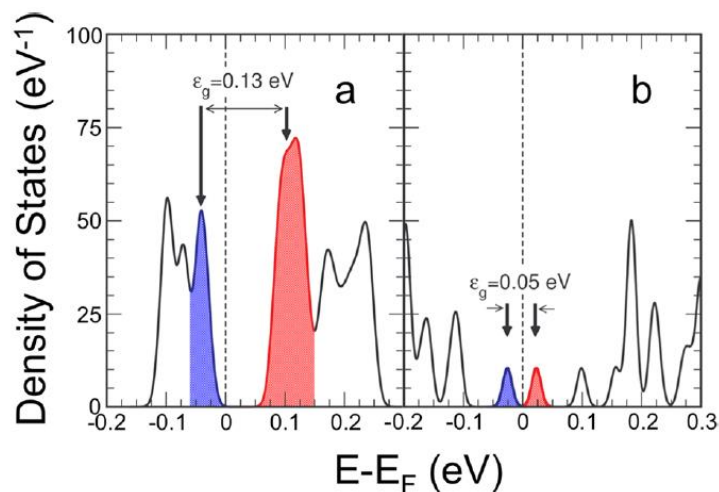


**Figure 2.36.** Computed total density of electronic states (in  $\text{eV}^{-1}$ ) for compounds **1** (a) and **7** (b) as a function of the energy (in eV), relative to the Fermi level. Each energy level has been broadened with a Lorentzian profile with a line width of 0.01 eV, and the VB and CB for both compounds have been shaded in blue and red, respectively. Values of the VB-CB band gaps are shown superimposed to each corresponding panel.

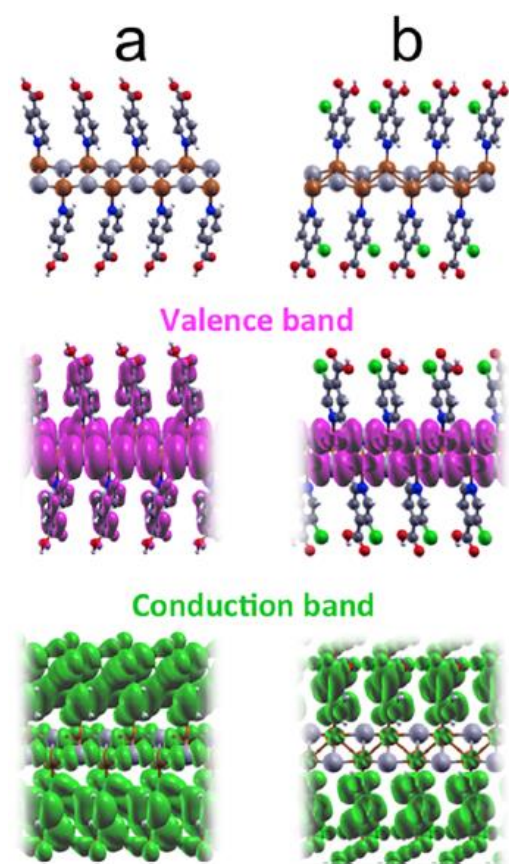


**Figure 2.37.** Computed 3D orbital isodensities corresponding to the VB (middle panels) and CB (bottom panels) (all with a value of  $10^{-4} \text{ e}^{-} \text{ \AA}^{-3}$ ) for the compounds **1** (a) and **7** (b). Clean geometries are also shown (top panels) for better visualization.

Finally, compound **6** displays a DC electrical conductivity of  $8.6 \times 10^{-7} \text{ S cm}^{-1}$  at room temperature and a classical semiconducting behavior, with an activation energy of 65 meV (**Figure 2.38**). The temperature-dependence study does not show any phase transition in the range between 100 and 400 K.

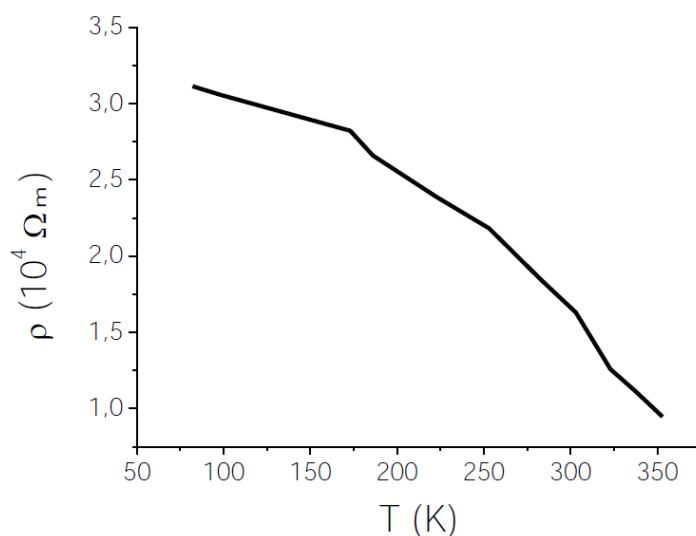


**Figure 2.38.** Electrical conductivity of **6** at temperatures ranging from 80 to 373 K.

### 2.2.2.1. Response to acetic acid vapors

As explained in the introduction of this chapter (section 2.1.1), the presence of certain functional groups in the terminal ligands of Cu-I chain based CPs allows them to interact with other molecules by means of weak forces such as H-bonds or Van der Waals forces. This is the case of compound **3**, since the free amino and nitro groups present in its structure can easily form H-bonds with vapors of volatile organic compounds such as alcohols or acetic acid. This is translated into a fast and efficient electrical response upon the presence of these vapors (see references <sup>13-14</sup> and **Figure 2.8**).

The case of compound **3** prompted us to evaluate the electrical response of compounds **4-7** upon exposure to acetic acid vapors. Among these CPs, only compound **6** exhibited a remarkable, yet slow, response. By means of an EIS study under alternate current (AC), we observed that the initial conductivity ( $t = 0\text{h}$ ) of  $1.32 \times 10^{-8} \text{ S cm}^{-1}$  is enhanced, reaching values of  $2.83 \times 10^{-8} \text{ S cm}^{-1}$  and  $2.61 \times 10^{-7} \text{ S cm}^{-1}$  after 4 and 24 h, respectively, upon exposition of pressed pellets of **6** to acetic acid vapors (**Table 2.4**). This chemical response can be ascribed to hydrogen-bonding interactions between the acetic acid and the amino group of the 2-aminopyrazine ligands.

**Table 2.4.** AC conductivity of **6**: values at 298 K and their variation with the exposition time under acetic acid (AcOH) vapors (from 0 to 48 hours).

Exposition time (h)	Pellet thickness (mm)	Pellet area (cm <sup>2</sup> )	R ( $\Omega$ )	$\sigma$ (S·cm <sup>-1</sup> )
0	0.301	0.13	$2.28 \cdot 10^{-7}$	$1.32 \cdot 10^{-8}$
4	0.303	0.13	$1.07 \cdot 10^{-7}$	$2.83 \cdot 10^{-8}$
24	0.306	0.13	$8.47 \cdot 10^{-5}$	$3.61 \cdot 10^{-7}$
48	0.304	0.13	$5.86 \cdot 10^{-5}$	$5.18 \cdot 10^{-7}$

### 2.2.3. Luminescent properties

The luminescence studies presented in this section will be focused on compounds **4-6**, since compounds **1-3** have already been reported and compound **7** does not show any emissive behavior.

### 2.2.2.1. Luminescence thermochromism

The structural analysis of compounds **4-6** suggests that they are interesting candidates to carry out emission studies at variable temperature.

From the qualitative point of view, a naked eye experiment shows that the excitation of **4** and **5** with an UV lamp ( $\lambda_{\text{exc}} = 365 \text{ nm}$  or  $312 \text{ nm}$ ) at room temperature produces a strong orange emission for **4** and weak yellow emission for **5** (**Figures 2.40** and **2.41**). Upon cooling these materials to  $80 \text{ K}$ , **4** shows a slight decrease in its emission intensity, while **5** exhibits a significant increase (**Figures 2.40** and **2.41**). These processes are reversible, and thus warming up the materials from  $80 \text{ K}$  to  $300 \text{ K}$  produces a gradual recovery of their initial properties. The comparison between micrometric and nanometric samples shows an influence only in the emission intensity, being more significant for **4**.

To evaluate in further detail these qualitative observations, emission spectra at variable temperature of **4** as well as **5** were recorded from  $80$  to  $300 \text{ K}$  (**Figure 2.41**). Thus, at  $300 \text{ K}$  the excitation of the samples with  $\lambda_{\text{exc}} = 440 \text{ nm}$  produces a strong emission with an asymmetric band centered at  $\lambda_{\text{em}} = 610 \text{ nm}$  for **4**, and a weak emission at  $\lambda_{\text{em}}$  ca.  $550 \text{ nm}$  for **5**. By lowering the temperature from  $300$  to  $80 \text{ K}$ , a progressive decrease of the emission intensity (up to 5 times lower at  $80$  than at  $300 \text{ K}$ ) is observed for **4**, while a progressive increase (up to 50 times higher at  $80$  than at  $300 \text{ K}$ ) is observed for **5**. In addition, it is remarkable that between  $140$  and  $80 \text{ K}$  a structured band with two emission maxima, of similar intensities, centered at  $593$ ,  $642 \text{ nm}$  and a shoulder at ca.  $707 \text{ nm}$  appeared for **4**. On the other hand, for **5** a very asymmetric band centered at ca.  $550 \text{ nm}$  is observed at  $140 \text{ K}$  and, as temperature decreases, the intensity of this asymmetric band increases. However, this band is not resolved like a structured band, and a maximum centered at  $550 \text{ nm}$  together with a shoulder at  $516 \text{ nm}$  can be observed.

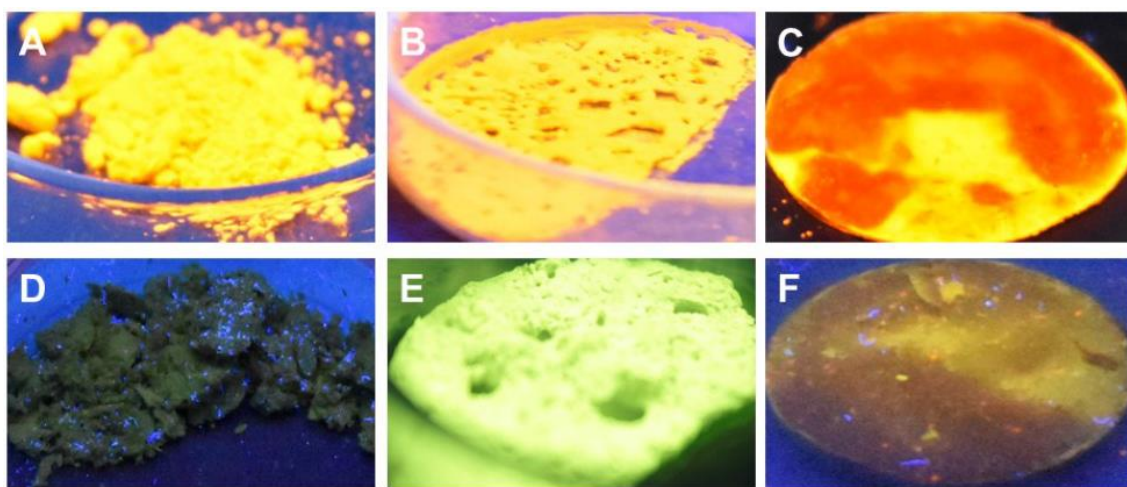


**Figure 2.40.** (a, b, c) Luminescence of **4** at  $298 \text{ K}$  (a), at  $80 \text{ K}$  (b) and at  $80 \text{ K}$  and  $2 \text{ GPa}$  (c). (d, e, f) Luminescence of **5** at  $298 \text{ K}$  (d), at  $80 \text{ K}$  (e) and at  $80 \text{ K}$  and  $2 \text{ GPa}$  (f).  $\lambda_{\text{exc}} = 312 \text{ nm}$ .

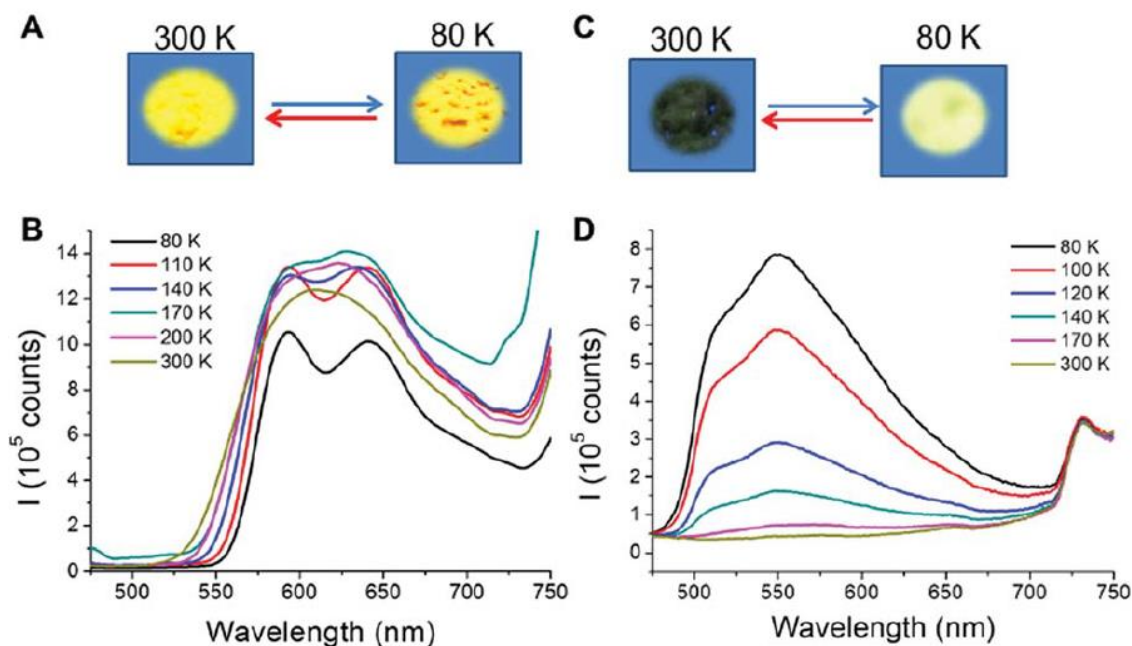


**Figure 2.41.** (a) Representation showing the temperature-dependence behavior of **4** in the solid state under UV lamp excitation ( $\lambda_{\text{exc}} = 365$  nm) at room temperature (left) and under liquid nitrogen (right). (b) Temperature-dependent luminescence spectra of **4**. (c) Representation showing the thermochromic behavior of **5** in the solid state under UV lamp excitation ( $\lambda_{\text{exc}} = 365$  nm) at room temperature (left) and under liquid nitrogen (right). (d) Temperature-dependent luminescence spectra of **5**.

The stair-type chain structure adopted by **4** and **5** is common for I-Cu-N donor ligand coordination polymers and the emission origin, centered around 520–640 nm, can be most likely due to a mixed iodide-to-ligand and metal-to-ligand charge transfer (IL/MLCT) excited state [ $^3(\text{I} + \text{M})\text{LCT}$ ].<sup>69–72</sup> This assignment is supported when comparing the emission spectra of **4** and **5**, where we can see that the emission is affected by the nature of the substituent on the pyridine ring. Thus, **5** shows emission bands at higher energies than **4**, in accordance with a higher HOMO-LUMO gap. Finally, the broad and unstructured bands observed at room temperature are also in accordance with the assignment made as a combination of  $^3(\text{I} + \text{M})\text{LCT}$  states.<sup>73</sup>

To rationalize the origin of the changes in the emission by lowering the temperature, crystal structures for **4** and **5** were solved at 110 K. While in compound **4** all metallic distances are shorter than 2.80 Å, which is twice the van der Waals radius, **5** adopts the most common disposition of the  $\text{Cu}_2\text{I}_2$  units in these stair-step chain structures, showing alternation of long (>2.80 Å) and short (<2.80 Å) distances between Cu and Cu atoms. These structural differences observed along the  $\text{Cu}_2\text{I}_2$  chains, symmetric for **4** versus asymmetric for **5**, provoke changes in the emission. Comparing the thermochromic properties of both compounds, **5** does not display emission at room temperature but, upon cooling, a bright yellow emission is observed increasing the intensity of emission with decreasing temperature. The crystal structures of compounds **4** and **5** at 296 and 110 K show that the space group and the general structural features do not change with



the temperature (**Tables A3-A4** in appendix A). Thus, the Cu-I and Cu...Cu distances show the expected decrease with decreasing temperature and the increase observed in the emission intensity upon cooling is in accordance with the increase in structural rigidity, decreasing the non-radiative rate constant.<sup>74</sup>

On the other hand, although the space group of **4** is the same at temperatures of 296, 200 and 110 K, it shows a transition at 125-145 K, confirmed by the study carried out on the thermal dependence of the unit cell parameters. Thus, this structural transition can be attributed to a slight change in the asymmetry of the Cu-I<sub>rail</sub> bond lengths along the chain, increasing from 0.0171 Å at 296 K to 0.0243 Å at 200 K but decreasing to 0.0208 Å at 110 K. These changes in the structure will likely induce a variation in the shape and energy of the HOMO and LUMO when changing from room temperature to 80 K.

The lifetimes measured for **4** at 300 and 80 K were 8.1-7.1 ms, respectively, which fall in the microsecond-order decay lifetime range and are assigned to phosphorescence, arising from a triplet state. The fact that the structured band observed at 80 K, with maxima centered at 592 and 640 nm, has similar lifetime values seems to indicate that both emissions belong to the same structured band emitting from the same excited state and, alike, lifetime measurements for both temperatures suggest that there is only one emission level without any geometrical distortions in the excited state.

For **5**, the lifetime measured at 80 K was 1.25 and 1.15 ms for the emissions centered at 516 and 550 nm, respectively. Similar values are also indicative of emissions from the same excited state. **5** has a lower lifetime than **4**, suggesting a greater rigidity in its structure due to the presence of the amino group attached to the pyridine ring.<sup>75</sup>

Theoretical calculations of the excitation spectra for the two structures of **4** and **5** resolved by X-ray diffraction at low (110 K) and high (296 K) temperatures have been carried out to rationalize the thermochromic effect evidenced by the experiments. Interestingly, our theoretical approach is able to capture the reduction in the photoluminescence performance observed in compound **4** and very weak changes in the case of compound **4** from the low-temperature to the high-temperature regime. **Figure 2.42** shows the prominent excitation feature located at around 580 nm for the case of T = 110 K. Nevertheless, the intensity of the peaks decreases by around 35(2) % for the cases of T = 296 K and T = 110 K, with the maximum of the peak located at 600 nm for compound **2** and barely any displacement for compound **1**. The decrease in the photoluminescence behavior may have its origin in the thermal fluctuations that tend to broaden both the VB and CB, subsequently reducing the efficiency of the metal-ligand transition for the case of the high-temperature regime as compared with the T = 110 K case. Indeed, the global DOS profile morphology of compound **4** (top panel of **Figure 2.43**) remains with no significant variations when moving from 296 K to 200 K or 110 K, excepting slightly for energies out from the gap region, which evinces that the structural changes induced by the increasing temperature do not substantially affect the electronic structure. In particular, the VB and CB remain practically unaltered and, thus,

the electronic band-gap as well, with a value of 0.47 eV. Nevertheless, a more pronounced effect induced by the temperature is observed in the DOS profiles for **5** (bottom panel of **Figure 2.43**). In this case, not only do evident shifts between electronic states appear for the two temperatures, but also does a visible reduction of the bandgap from 1.25 eV at RT down to 0.92 eV at  $T=110$  K. This observation will be directly related with the thermochromic effect observed for this compound, not observed for compound **4**.

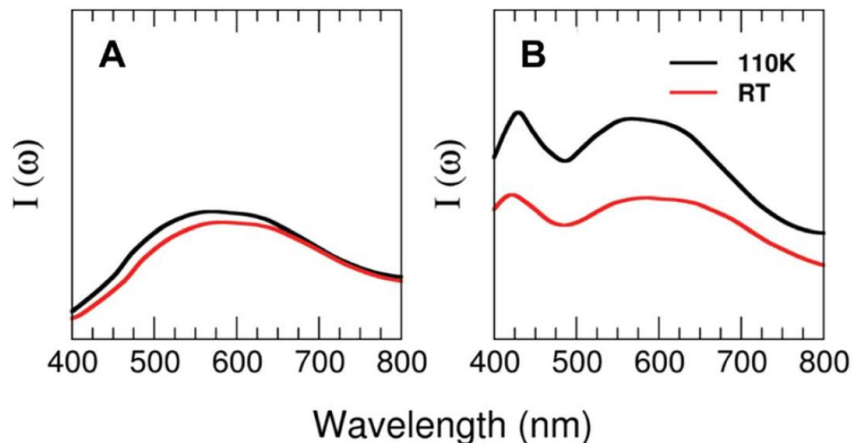


**Figure 2.42.** Computed TDDFT photoexcitation spectra (in arb. units) for **4** (a) and **5** (b) as a function of the photon wavelength (in nm) for two different temperatures at standard pressure ( $T = 110$  and  $296$  K). Ordinate-scale is the same in both graphs for a better comparison.

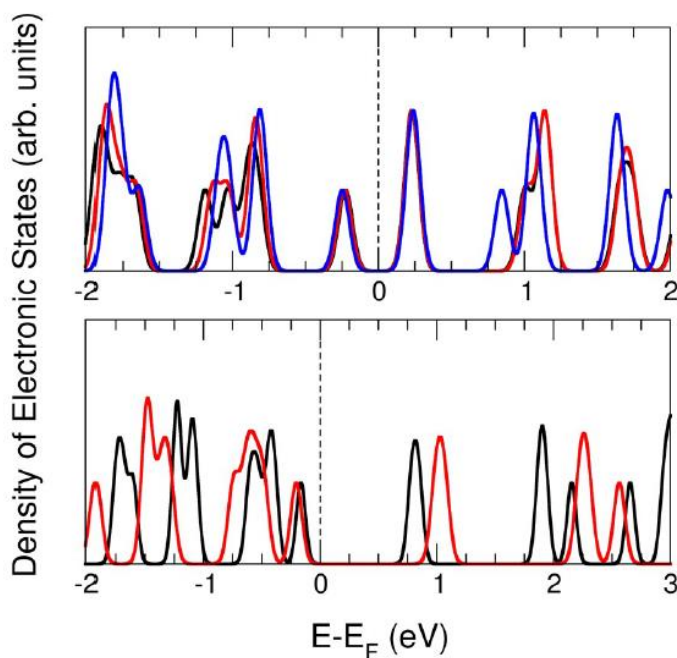


**Figure 2.43.** Computed density of electronic states (in arb. units) for compounds **4** (top panel) and **5** (bottom panel) as a function of the energy referred to the Fermi level (in eV), for different temperatures:  $T=110$  (black), 200 (red) and 296 K (blue) for **4** and  $T=110$  (black) and 296 K (red) for **5**.



As far as compound **6** is concerned, excitation of solid crystalline samples with micrometric (**6m**) and nanometric dimensions (**6n**) with an UV lamp ( $\lambda_{\text{exc}} = 365$  nm), at room temperature, produces a very weak orange emission for both materials (**Figure 2.44a,c**). However, upon cooling at 80 K, both **6m** and **6n** significantly increase their emission intensity showing a perceptible eye shift from orange to yellow (**Figure 2.44b,d**). The thermochromic process is fully reversible for **6m** and **6n**.

In order to evaluate in more detail these seminal experimental observations, emission spectra at variable temperature of **6m** and **6n** were recorded (**Figure 2.45**), observing similar results for both **6m** and **6n**. Thus, by lowering the temperature of **6m** from 300 to 80 K, a progressive increase of the emission intensity (30 times higher at 80 K than at 300 K) and a blue-shift were observed. The very weak emission observed at  $\approx 630$  nm at 300 K is progressively shifted to 566 nm at 80 K (**Figure 2.45**). The lifetime measured at 80 K was 20.9  $\mu\text{s}$ , which falls in the microsecond-order decay lifetime and is assigned to phosphorescence, arising from a triplet state. Essentially, the size of the sample seems to influence mainly in the emission intensity, which is lower in the case of **6n**.

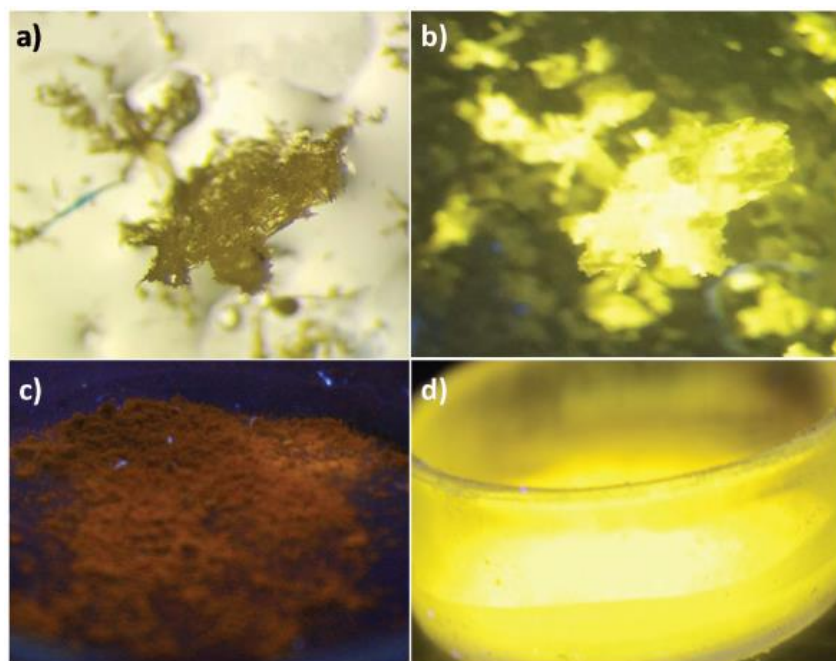


**Figure 2.44.** a) Optical microscope image of **6m** microcrystals at 300 K. b) Optical microscope image of **6m** microcrystals at 80 K. c) Photograph of **6n** crystalline powder at 300 K. d) Photograph of **6n** crystalline powder at 80 K. All images were taken under a UV lamp with  $\lambda_{\text{exc}} = 365$  nm.

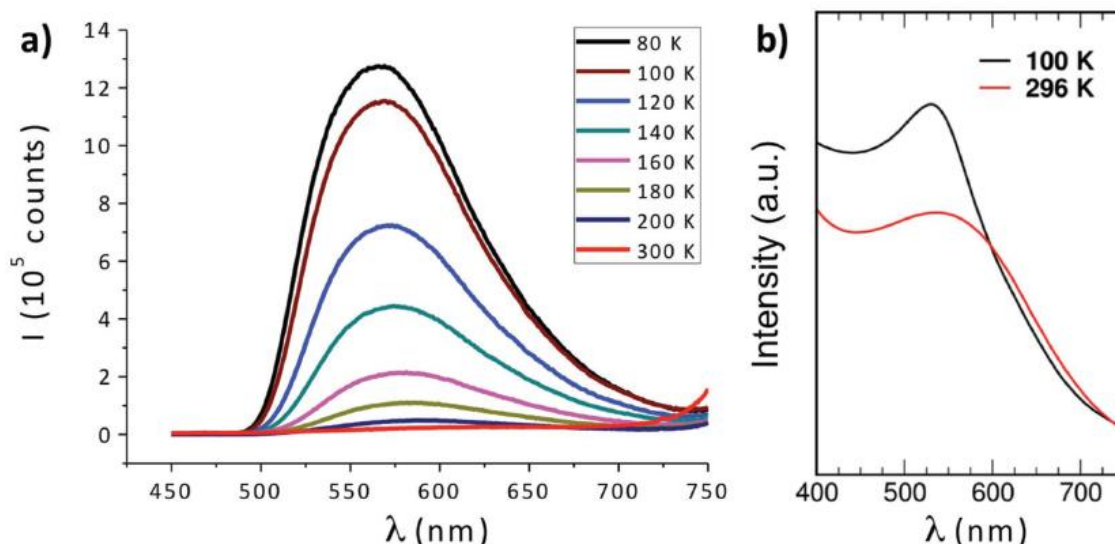


**Figure 2.45.** a) Emission spectra of compound **6m** at different temperatures. b) Computed GW-BSE (quasi-particle approximation Bethe-Salpeter equation) photoexcitation spectra of **6** as a function of the excitation wavelength (in nm) for two structures by X-ray diffraction at low (100 K) and high (296 K) temperatures.

Similar to what happened to compound **5**, the contribution of a  $^3\text{MCC}$  transition in the excited state is supported by the short  $\text{Cu}\cdots\text{Cu}$  distances observed, since the half of the  $\text{Cu}\cdots\text{Cu}$  distances are below the sum of Van der Waals radii ( $2.80 \text{ \AA}$ ) and the broad and unstructured band observed is also in accordance with the assignment made as a combination of  $^3(\text{M} + \text{I})\text{LCT}$  states.<sup>69-72</sup> Additionally, thermochromic effects can be largely affected by a change in  $\text{Cu}\cdots\text{Cu}$  distances due to the  $^3\text{MCC}$  excitation state. Once again, this shrinking of  $\text{Cu}\cdots\text{Cu}$  distances and the increase in the rigidity of the medium are the main causes of the thermochromism of **6**.

In order to rationalize the thermochromic effect evidenced by the experiments, we have performed calculations of the excitation spectra for the two structures of **6** resolved by X-ray diffraction at low (100 K) and high (296 K) temperatures (**Figure 2.45b**). Our theoretical approach is able to capture the reduction in the photoluminescence performance observed from the low-temperature to the high-temperature regimes. In this case, **Figure 2.45b** shows the prominent excitation feature located at 526 nm for the case of  $T = 100 \text{ K}$ . Nevertheless, the intensity of the peak decreases around a 30% for the case of  $T = 296 \text{ K}$  with respect to the  $T = 100 \text{ K}$  case, with the maximum of the peak located at 530 nm.

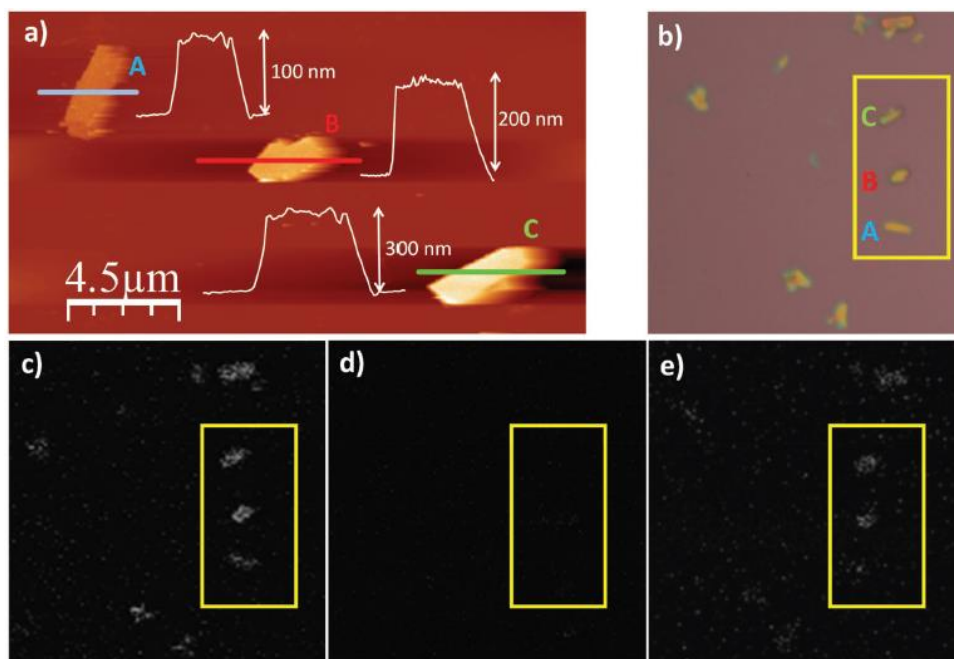


**Figure 2.46.** a) Topographic AFM image of **6n** nanolayers deposited on an SiO<sub>2</sub> substrate and their height profiles, named as A–C. b) Optical microscope image of the **6n** nanolayers (A–C) characterized in part (a) at 298 K. c) Confocal microscopy image of **6n** nanolayers (A–C) at 300 K upon irradiation with a laser with excitation wavelengths of 351 and 364 nm, at a power of 9.36 μW. d) Confocal microscopy image of **6n** nanolayers (A–C) at 300 K, when irradiated with a laser with excitation wavelengths of 351 and 364 nm, at a power of 6.34 μW. e) Confocal microscopy image of **6n** nanolayers (A–C) 7 min after being at 80 K, when irradiated with a laser with excitation wavelengths of 351 and 364 nm, at a power of 6.34 μW.

The thermochromic properties of isolated **6n** nanolayers deposited on SiO<sub>2</sub> have also been studied. **Figure 2.46a** shows topological AFM images with their corresponding height profiles showing three different **6n** nanolayers with over micrometer-sized lateral dimensions, and  $\approx 100$ , 200, and 350 nm thicknesses. **Figure 2.46b** displays an optical image of the AFM analyzed area. **Figure 2.46c–e** shows confocal microscopy images of the same region upon irradiation with a laser with excitation wavelengths of 351 and 364 nm at a power of 9.36 μW at 300 K, A–C nanolayers show bright emission between 500 and 600 nm (**Figure 2.46c**). However, the emission of the A–C nanolayers is significantly reduced (not perceptible under a confocal microscope) when laser power is reduced to 6.34 μW (**Figure 2.46d**), and it becomes more intense at 80 K (**Figure 2.46e**). The emission observed at 80 K reverses to the initial state as the sample reaches the initial temperature. Therefore, the thermochromism observed in these nanolayers is reversible.

#### 2.2.2.2. Luminescence mechanochromism

In order to study the potential mechanoluminescence behavior of compounds **4** and **5**, we have prepared pressed pellets at different pressures with the materials in the form of nano- and micrometric powders for both compounds. The pressed pellets of compound **4** show slight changes, their emission going from an intense orange to a weaker reddish orange, which does not change upon decreasing the temperature to 77 K (**Figure 2.40c**). However, the pressed pellets of **5** (at different pressures from 1 to 5 GPa) show a significant change in their luminescence. Indeed, upon applying pressure their emission is quenched at both 298 and 80 K (**Figure 2.40f**), but it is recovered when the pellet is decompressed by grinding, indicating reversibility of the emission with the pressure. To gain knowledge about this behavior, initial PXRD patterns were collected from the as-synthesized materials in the form of pressed and ground pellets. The results do not show significant differences, suggesting that the structures are the same (**Figure C7** in appendix C). This is why we performed a high-pressure SC-XRD study on compound **5** (see section 2.2.1.1).

High pressure emission has also been measured for compound **5**, both in the shape of crystals (**5m**) and a nanometric powder (**5n**). Both spectra (**Figure 2.47**) show a spectral multicomponent structure. Some similarities between them are observed, particularly under ambient conditions (300 K, 0 GPa), where we can see a band located around 500 nm. However, upon applying pressure, differences between them are clearly observed, both in intensity and in spectral shape. Under ambient conditions and with excitation at 375 nm, **5m** shows a structured and asymmetric broadband with three components centred approximately at 500 (green), 575 (yellow) and 615 (orange) nm. As pressure increases, changes in the shape and intensity are remarkable; the asymmetry and the structure of the band disappear at 1.3 GPa, retaining only the orange component, and the integrated intensity increases three fold. However, when increasing the pressure, gradual decreases of the intensity and large red-shift of the emission bands of around  $440\text{ cm}^{-1}$  per GPa are also noticeable. Above 6 GPa, intensity is almost negligible (less than 15%) compared to that obtained under ambient conditions. Upon releasing pressure, the system seems to be almost reversible (**Figure 2.47a**).

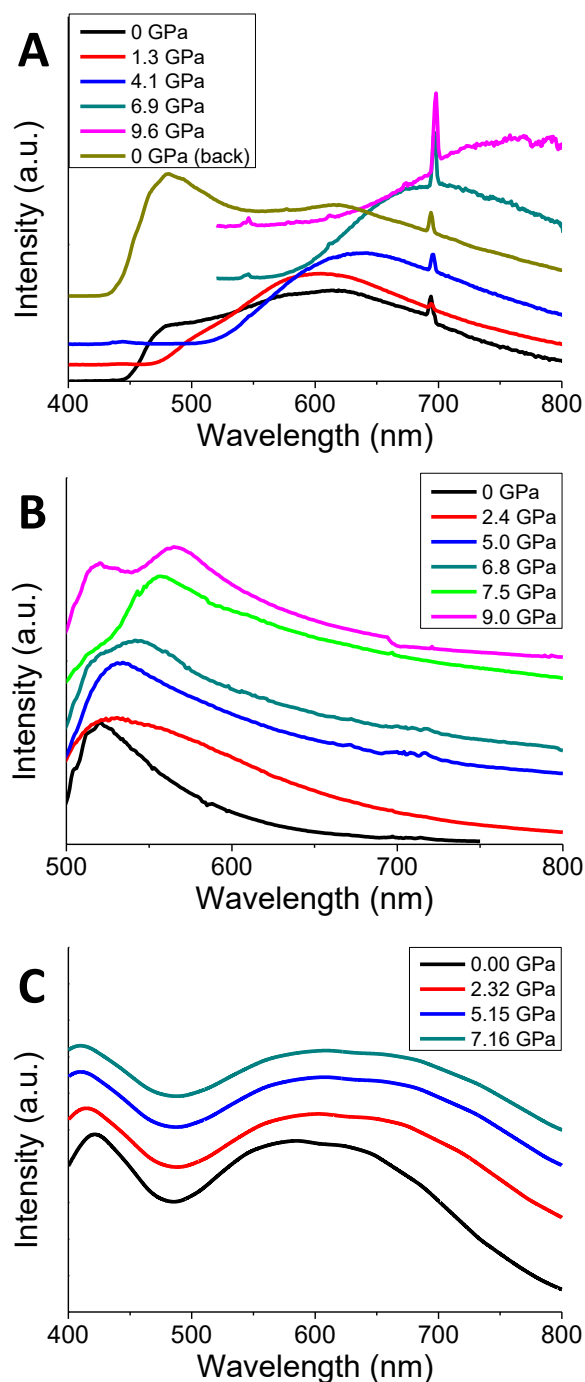


**Figure 2.47.** (a) Normalized luminescence spectra of **5m** obtained at 298 K under 375 nm laser excitation for different externally applied hydrostatic pressures ( $P = 0, 1.3, 4.1, 6.9,$  and  $9.6$  GPa, and 0 GPa after decompressing) within a range between 400 and 800 nm. (b) Normalized luminescence spectra of **5n** obtained at 298 K under 458 nm laser excitation for different externally applied hydrostatic pressures ( $P = 0, 2.4, 5.0, 6.8, 7.5,$  and  $9.0$  GPa) within a range between 500 and 800 nm. The band at 700 nm corresponds to the ruby emission. (c) Computed TDDFT photoexcitation spectra (in arb. units) for **5** as a function of the photon wavelength (in nm) for different externally applied hydrostatic pressures ( $P = 0, 2.32, 5.15$  and  $7.16$  GPa). Ordinate-scale is the same in both graphs for a better comparison.

In the case of **5n**, no emission was recorded when excited at 375 nm; however upon changing the excitation wavelength to 458 nm an intense emission was observed. Due to the proximity of the excitation wavelength and the starting wavelength of the spectrum, it is impossible to extract valuable information below 500 nm. The emission band under ambient conditions consists of an unstructured asymmetric band with two green components, centered at 520 nm and 555 nm, respectively, the former being larger in amplitude and similar in spectral position to the green component found in **5m**. At 0.11 GPa the band broadens around 9 nm and shifts to the red by about 5 nm; both tendencies continue until 1.4 GPa, with a red-shift rate of *ca.* 330 cm<sup>-1</sup> per GPa. From this point, the broadening abruptly changes from 0.6 GPa (74 nm) to 1.4 GPa (116 nm), as a consequence of the increase in the amplitude of the low-energy component, and the band is red-shifted. It seems that the low-energy component, which clearly shifts to the red, dominates up to 7.5 GPa, but beyond this pressure two components are now clearly identified, one remaining at 520 nm (high-energy component) which matches with that observed under ambient conditions, and the low-energy one with a red-shift of *ca.* 350 cm<sup>-1</sup> per GPa, from 7.5 to 9.0 GPa. Regarding intensity, the behavior is also complex, showing a 4.7-fold increase in the integrated intensity at 2.5 GPa, which after this point gradually decreases by the same amount till 6.8 GPa, just where the splitting of the two components is clear. From that pressure to the last one recorded, an increase of 1.7 times at 9 GPa is observed (**Figure 2.47b**). The features of luminescence spectra are closely related to the surrounding environment of the emitter. In this sense a high pressure technique allows gradually modifying and controlling the inter- and intramolecular interactions so that a correlation between the structure and luminescence can be made. In CuI ladder-type complexes, emission is modulated by some parameters, most of them related to bond angles and distances of the nearby surrounding ions, such as Cu···Cu, Cu-I, Cu-L (ligands), and I-Cu-I, in particular within the Cu<sub>2</sub>I<sub>2</sub> cluster core. The so-called LE emission band usually involves a [Cu<sub>2</sub>I<sub>2</sub>] cluster-centered triplet excited state (<sup>3</sup>CC), which is a combination of iodide-to-metal charge-transfer (<sup>3</sup>IMCT) and Cu 3d → 4s, 4p transitions (<sup>3</sup>MCC\*), with the latter strongly dependent on Cu···Cu (cuprophilic) interactions, when Cu···Cu distances are lower than the sum of the Van der Waals radii of Cu (2.8 Å), although other contributions can also be considered as <sup>3</sup>ILCT and <sup>3</sup>MLCT. In order to distinguish among the possible transitions involved, a high-pressure technique can be an interesting tool to check the mechanochromic effects that can be complemented with the thermochromic one, since pressure induced larger changes in bond lengths and angles as well as in interplanar distances than those achieved by changing the temperature. In this kind of complex, different non-excluding transitions can take place as is reflected in the asymmetric and structured ambient condition emission spectrum of **5m** and **5n**.

**Figure 2.47c** shows the computed TDDFT photoexcitation spectra of **5** for different externally applied hydrostatic pressures (P = 0, 2.32, 5.15 and 7.16 GPa) within a range between 400 and 800 nm. Within this wavelength range we can observe a prominent excitation feature centered around 580 nm for the case P = 0, which tends to shift to higher photon wavelengths as the pressure increases. This wide feature has its origin in

an electronic transition between the VB and the CB (84%) and the VB-1 and the CB (1%). As usual in this sort of Cu-based polymers, in this case the VB and VB-1 are mostly located in the Cu-based metal skeleton, whilst the CB and CB+1 are located in the organic ligands (**Figure 2.48**). Interestingly, as the pressure starts to increase, the intensity of this broad excitation feature progressively decays, which excellently agrees with the experimental photoluminescence spectra, where the intensity also decays for high pressures. For increasing values of the pressure, theory predicts a slight shift of the feature towards higher wavelengths until being located around 610 nm. Nevertheless, it is well known that this shift should be taken cautiously since these small variations could be framed within the accuracy of this approach. **Figure 2.47c** also shows another excitation feature located at 420 nm for  $P = 0$ . This excitation has its origin mostly in an electronic transition between the VB and the CB+1 (96%), which also decays and shifts towards lower wavelengths.

**Figure 2.48** shows the computed density of electronic states (in arb. units) for **5** as a function of the energy referred to the Fermi level (in eV), for different externally applied hydrostatic pressures. For the case in which no external pressure is applied ( $P = 0$ ), theory predicts a canonical narrow-gap p-type semiconducting character, with the Fermi level almost pinning the valence band (VB) of the compound and yielding an electronic gap of around 1.25 eV. Interestingly, as the hydrostatic pressure increases we can clearly observe different emerging effects. The first one consists of a progressive reduction of the band-gap up to a value of 0.8 eV for the case limiting of  $P = 7.16$  GPa. This situation is reached by a totally asymmetrical closure around the Fermi energy with increasing pressure, even flipping the initial p-type semiconducting character at  $P = 0$  GPa into a canonical n-type semiconducting character, with the Fermi level almost pinning the conduction band (CB) of the material at  $P = 7.16$  GPa. The second and most interesting effect is the evident breaking of the electronic degeneracy in most of the electronic states lying within the depicted energy window in the figure. The doubly electronically degenerated CB splits into two electronic states as the external pressure increases. This behavior is also observed for the, initially at  $P = 0$ , doubly degenerated CB+1, as well as for VB-1. The VB does not experience any splitting since it is, even at  $P = 0$ , a single occupied electronic state (and no additional electronic impairment effect is observed within our spin-polarized calculations).

The case of compound **6** is very similar to that of compound **5**. A qualitative experiment carried out on pellets of **6** pressed at 1-5 GPa showed that the CP lost its emissive behavior. This was reverted grinding the pellets. In any case, the PXRD patterns showed neither amorphization nor phase transitions (**Figure C9** in appendix C). In order to understand the decrease in the emission intensity as a consequence of the pressure, we subjected a crystal of **6** to a high-pressure study, analyzing the variation in its structure and emission, and performed theoretical calculations using density functional theory (DFT).



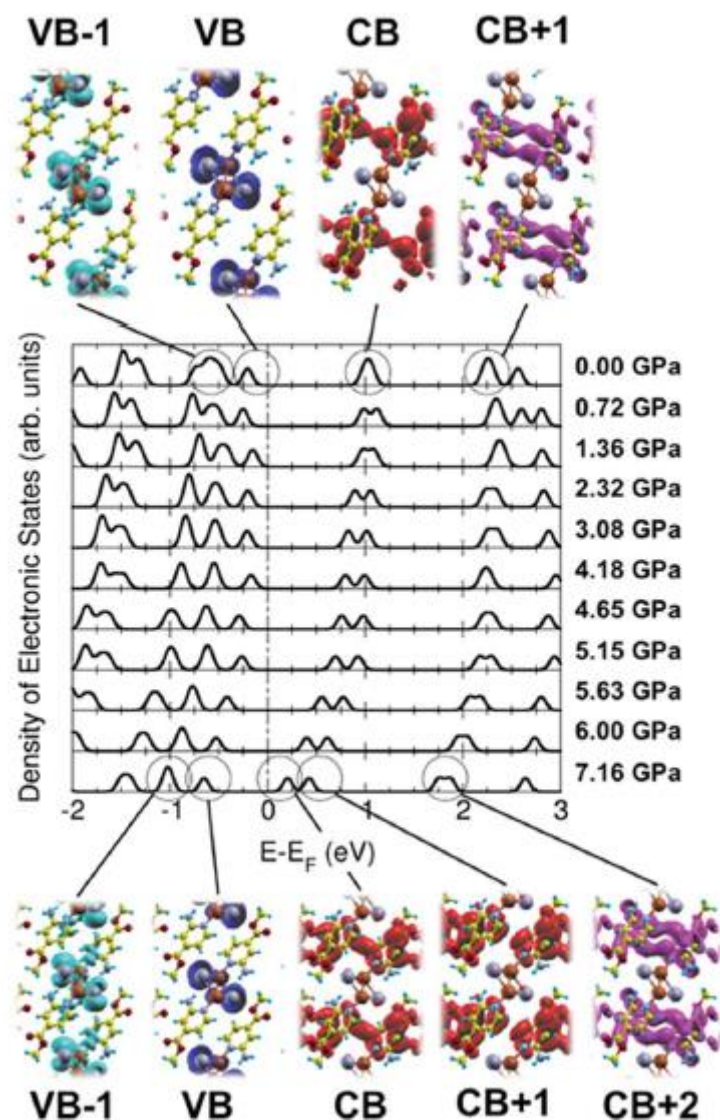


**Figure 2.48.** Computed density of electronic states (in arb. units) for **5** as a function of the energy referred to the Fermi level (in eV), for different externally applied hydrostatic pressures ( $P = 0, 0.72, 1.36, 2.32, 3.08, 4.18, 4.65, 5.15, 5.63, 6.00$  and  $7.16$  GPa). 3D orbital density isosurfaces (with a value of  $5 \times 10^{-3}$  a.u.) are also included for the most representative electronic states and represented over their respective X-ray diffraction structures obtained at 298 K.

A single crystal of compound **1m** has been subjected to an emission study versus pressure (**Figure 2.49**). The low-pressure ( $\approx 0$  GPa) spectrum consists of an asymmetric broadband peaking around 645 nm. Upon applying pressure, two different behaviors can be observed; on the one hand, there is a pronounced linear redshift of the maximum of the band of around  $15 \text{ nm GPa}^{-1}$  reaching at  $\approx 690$  nm and simultaneously a gradual quenching of its intensity up to 5 GPa appeared, vanishing beyond that pressure. At around 4 GPa, two emission bands are present with maxima at 560 nm and around 690 nm; the latter band cannot be fully characterized due to the overlapping with the ruby emission. The emergence of another broadband blue-shift with respect to the previous



one remains up to 8.7 GPa with no significant changes in its maxima at around 590 nm. Upon gradual release of pressure, the spectra tend to recover their previous emission shapes.

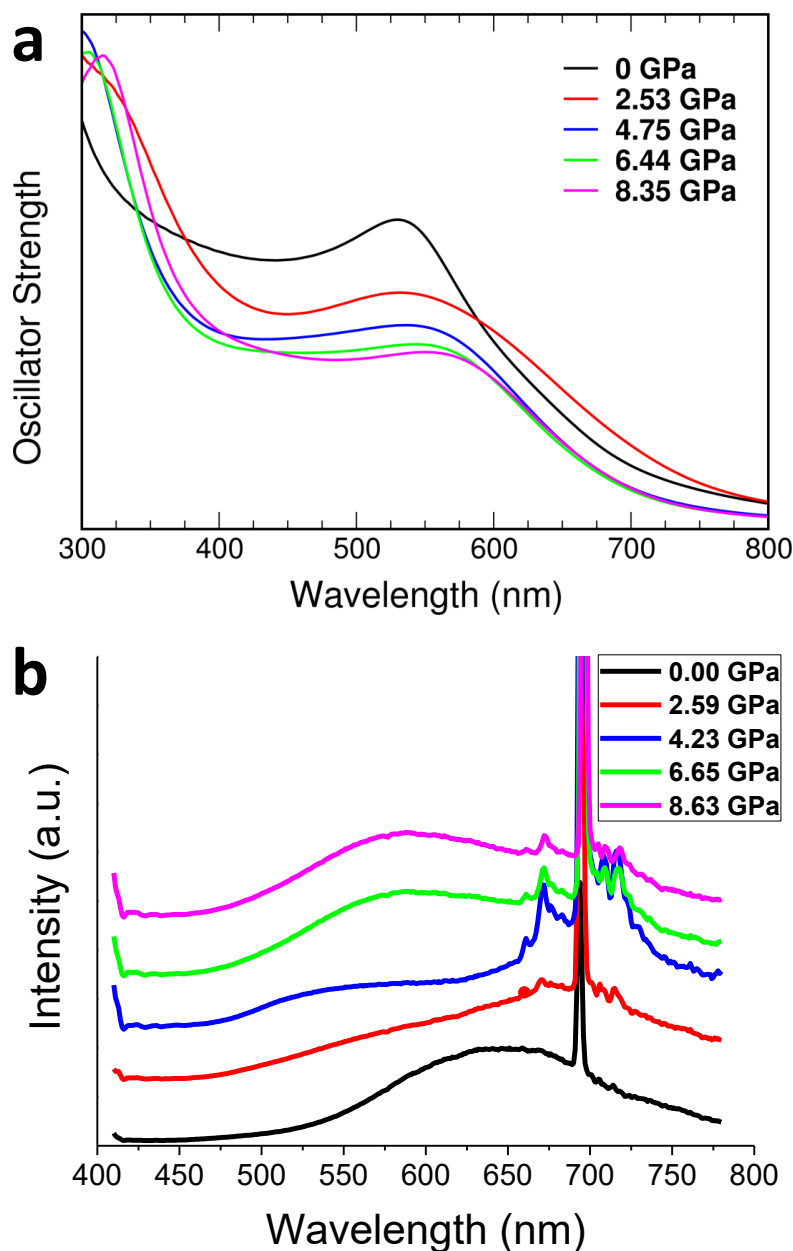


**Figure 2.49.** a) Computed GW-BSE photoexcitation spectra of **6** as a function of the excitation wavelength (in nm) for different externally applied hydrostatic pressures ( $P = 0, 2.53, 4.75, 6.44,$  and  $8.35$  GPa) within a range between 300 and 800 nm. b) Normalized luminescence spectra of **6** obtained at 25 °C under 375 nm laser excitation for different externally applied hydrostatic pressures ( $P = 0, 2.59, 4.23, 6.65,$  and  $8.63$  GPa) within a range between 400 and 800 nm. The inset shows the intensity behavior with pressure. The band at 700 nm corresponds to the ruby emission.

In both the cases of compounds **5** and **6**, the sequential asymmetrical band-gap closure and the breaking of the electronic degeneracy have their origin in a pressure-induced electronic degeneracy-rupture, which is a direct consequence of Pauli's exclusion principle. The external hydrostatic pressure effect shortens bond lengths within the compound (in particular within the metallic Cu chain), which tends to force different electrons to occupy the same electronic state, which is forbidden by Pauli's exclusion principle. Thus, the system electronically reacts by breaking the electronic degeneracy of some populated states to accommodate the pressure-induced forced electrons. Some of these states are directly involved in the visible emission processes of the material. On this basis, this interesting behavior will have a direct reflection in the optical properties of the system as the external pressure increases.

The vanishing of the broad excitation feature described in the previous paragraph as the pressure increases can be rationalized in terms of the pressure-induced electronic degeneracy-rupture explained in detail above. The degeneracy-rupture produces a loss of efficiency in the metal–ligand transition, responsible for the photoluminescence behavior since highly degenerated electronic orbitals contributing to that transition slightly modify their occupancy and symmetry by the effect of the pressure. Increasing pressure produces the compression of bond lengths within the compound, which is the case of the Cu···Cu distance (around a 20% bond-length compression followed by a reduction of around 3° in the dihedral angle from 0 to 7.16 GPa). In particular, this reduction of the Cu···Cu distance, which accommodates occupied electronic states that actively participate in the permitted metal-ligand transition (cuprophilic interaction), is reflected by a visible vanishing of the photoluminescence. Therefore, electrons belonging to the slightly hybridized occupied Cu  $d_z^2$  orbitals (within the Cu···Cu interaction) are pushed towards each other by the effect of the pressure, forcing them to occupy the same electronic state. Nevertheless, the system reacts by the electronic degeneracy-rupture slightly modifying the orbital orientation. For the case of  $P = 0$  the slightly hybridized  $d_z^2$  orbitals located in each Cu atom are oriented facing their lobes to maximize the cuprophilic interaction, and, thus, the photoluminescence is maximum. Nevertheless, for high pressures, with a reduced Cu···Cu distance, the lobes of the  $d_z^2$  orbitals spin in such a way to avoid the electronic overlapping (**Figure 2.50**). This behavior produces a reduction in the metal-ligand transition efficiency, which finally leads to the photoluminescence vanishing.

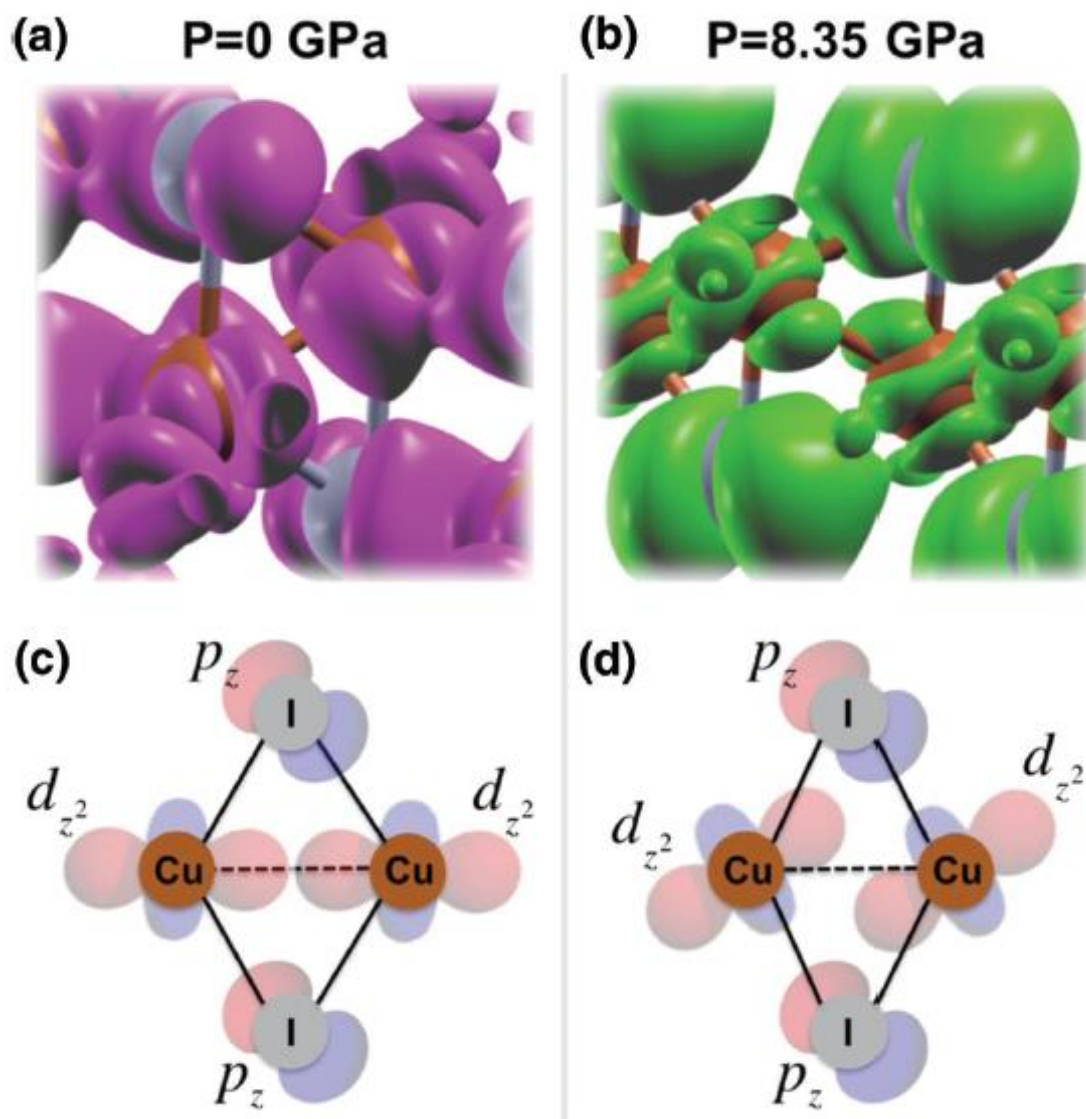


**Figure 2.50.** (a,b) Computed 3D valence band orbital isodensity (value of  $10^{-4} \text{ e}^- \text{ \AA}^{-3}$ ) of compound **6** at externally applied hydrostatic pressures of  $P = 0$  (part (a), purple) and 8.35 GPa (part (b) light green). (c,d) Pictorial sketch of both situations for a better visualization.

## 2.3. Conclusions

The direct reactions between copper(I) iodide and different N-donor ligands lead to the formation of a series of CPs sharing a structural motif: the Cu(I)-I double *zigzag* chain. The seven chosen compounds have been structurally and morphologically characterized. Due to their one-dimensionality, most of them form crystals with shapes of needles or blocks from the mother solution generated in the synthesis, and they form nanofibers and nanoribbons directly in the reaction medium; on the other hand, compound **6** is two-dimensional, so it forms sheet-shaped crystals and nanosheets. The nanofibers of compound **3** suffer variations in their lateral dimensions when they are exposed to acetic acid vapors, in an analogous manner to its electrical conductivity.

The electrical and luminescent properties of all compounds have been studied. All of them show a semiconducting behavior, with a low-energy gap, the valence band mainly localized in the Cu(I)-I chain and the conduction band localized in the ligands. Among these CPs, compounds **1** and **7** present the best electrical conductivity values, but they do not show any emission; parallelly, compound **6** shows a weak response to acetic acid vapors, raising its electrical conductivity one order of magnitude. On the other hand, compound **4** presents an intense orange emission at room temperature, with a slight and reversible variation in the intensity and wavelength of the observed bands as temperature drops to 77 K.

Compounds **5** and **6** show the most remarkable behavior among all compounds presented in this chapter: they do not show emission at room temperature, but when the temperature is lowered to 77 K they acquire a very intense yellow emission. This emission reverts to the original state when the system is warmed back to room temperature. This behavior is explained by the shortening of Cu...Cu distances, which results in a strengthening of the cuprophilic interactions. However, when high pressure values are applied to these two compounds, both of them completely (but reversibly) lose their emissive behavior, since the drastic shrinking of the Cu...Cu distances results in an ineffective orbital overlapping, and therefore the cuprophilic interactions disappear. Thus is proved that compounds **5** and **6** act like multi-stimuli-responsive materials.

## Conclusiones

Las reacciones directas entre yoduro de cobre(I) y diferentes ligandos N-dadores conduce a la formación de una serie de CPs con un motivo estructural común: la doble cadena Cu(I)-I en *zigzag*. Los siete compuestos elegidos se han caracterizado estructural y morfológicamente. Casi todos ellos, al ser monodimensionales, generan cristales en forma de agujas o bloques a partir de las aguas madres de síntesis, y se forman como nanofibras o nanocintas directamente en el medio de reacción, a excepción del compuesto **6**, ya que debido a su carácter bidimensional cristaliza en forma de láminas o nanoláminas. Las nanofibras del compuesto **3** presentan variaciones en su grosor cuando son expuestas a vapores de ácido acético, de forma análoga a como ocurre con su conductividad eléctrica.

Se han estudiado las propiedades eléctricas y luminiscentes de todos los compuestos. Todos ellos presentan un comportamiento semiconductor, con un bajo valor de energía del gap, la banda de valencia localizada fundamentalmente en las cadenas Cu-I y la banda de conducción sobre los ligandos. Los compuestos **1** y **7** presentan los mejores valores de conductividad eléctrica para este grupo de compuestos, pero no presentan emisión; por otra parte, el compuesto **6** presenta una débil respuesta eléctrica a ácido acético, mejorando su conductividad en un orden de magnitud a las 24 horas de exposición. Por su parte, el compuesto **4** presenta una importante emisión naranja a temperatura ambiente, con una ligera variación reversible en la intensidad de emisión y en la longitud de onda de las bandas observadas al bajar la temperatura hasta 77 K.

Los compuestos **5** y **6** presentan el comportamiento más llamativo para este tipo de compuestos: a temperatura ambiente presentan emisiones muy débiles, pero al bajar la temperatura a 77 K adquieren una intensa emisión en el color amarillo. La emisión revierte al anterior estado conforme vuelven a temperatura ambiente. Este comportamiento se explica por un acortamiento reversible en las distancias Cu...Cu, que implica una mejora en las interacciones cuprofilicas. Sin embargo, al aplicar presiones elevadas, la emisión desaparece por completo para ambos compuestos, también de forma reversible, debido a que la drástica reducción de las distancias Cu...Cu provoca un mal solapamiento de orbitales que impide la interacción. De esta forma se demuestra que los compuestos **5** y **6** son materiales multi-estímulo-respuesta.

## 2.4. References

1. N. Armaroli, G. A., F. Cardinali, A. Listorti, Photochemistry and Photophysics of Coordination Compounds: Copper. *Topics in Current Chemistry* **2007**, 280, 69.
2. Lebhardt, T.; Roesler, S.; Beck-Broichsitter, M.; Kissel, T., Polymeric nanocarriers for drug delivery to the lung. *Journal of Drug Delivery Science and Technology* **2010**, 20 (3), 171-180.
3. Troyano, J.; Perles, J.; Amo-Ochoa, P.; Zamora, F.; Delgado, S., Strong luminescent copper(i) halide coordination polymers and dinuclear complexes with thioacetamide and N,N'-donor ligands. *CrystEngComm* **2016**, 18 (10), 1809-1817.
4. Zhou, P.; Shi, R.; Yao, J.-f.; Sheng, C.-f.; Li, H., Supramolecular self-assembly of nucleotide-metal coordination complexes: From simple molecules to nanomaterials. *Coordination Chemistry Reviews* **2015**, 292, 107-143.
5. Festa, R. A.; Thiele, D. J., Copper: an essential metal in biology. *Current Biology* **2011**, 21, R877-R883.
6. Rana, S. V. S., Metals and apoptosis: recent developments. *Journal of Trace Elements in Medical Biology* **2008**, 22, 262-284.
7. Semisch, A.; Ohle, J.; Witt, B.; Hartwig, A., Cytotoxicity and genotoxicity of nano - and microparticulate copper oxide: role of solubility and intracellular bioavailability. *Particle and Fibre Toxicology* **2014**, 11 (1), 1-16.
8. Song, Y.; Fan, R. Q.; Wang, P.; Wang, X. M.; Gao, S.; Du, X.; Yang, Y. L.; Luan, T. Z., Copper(I)-iodide based coordination polymers: bifunctional properties related to thermochromism and PMMA-doped polymer film materials. *Journal of Materials Chemistry C* **2015**, 3 (24), 6249-6259.
9. Maderlehner, S.; Leitl, M. J.; Yersin, H.; Pfitzner, A., Halocuprate(I) zigzag chain structures with N-methylated DABCO cations - bright metal-centered luminescence and thermally activated color shifts. *Dalton Transactions* **2015**, 44 (44), 19305-19313.
10. Slabbert, C.; Rademeyer, M., One-dimensional halide-bridged polymers of metal cations with mono-heterocyclic donor ligands or cations: A review correlating chemical composition, connectivity and chain conformation. *Coordination Chemistry Reviews* **2015**, 288, 18-49.
11. Wang, J., Biomolecule-Functionalized Nanowires: From Nanosensors to Nanocarriers. *ChemPhysChem* **2009**, 10 (11), 1748-1755.
12. Hartwig, A., Metal interaction with redox regulation: an integrating concept in metal carcinogenesis? *Free Radical Biology and Medicine* **2013**, 55, 63-72.

13. Amo-Ochoa, P.; Hassanein, K.; Gomez-Garcia, C. J.; Benmansour, S.; Perles, J.; Castillo, O.; Martinez, J. I.; Ocon, P.; Zamora, F., Reversible stimulus-responsive Cu(I) iodide pyridine coordination polymer. *Chemical Communications* **2015**, 51 (76), 14306-14309.
14. Hassanein, K.; Amo-Ochoa, P.; Gomez-Garcia, C. J.; Delgado, S.; Castillo, O.; Ocon, P.; Martinez, J. I.; Perles, J.; Zamora, F., Halo and Pseudohalo Cu(I)-Pyridinato Double Chains with Tunable Physical Properties. *Inorganic Chemistry* **2015**, 54 (22), 10738-10747.
15. Benito, Q.; Goff, X. F.; Nocton, G.; Fargues, A.; Garcia, A.; Berhault, A.; Kahlal, S.; Saillard, J. Y.; Martineau, C.; Trebosc, J.; Gacoin, T.; Boilot, J. P.; Perruchas, S., Geometry flexibility of copper iodide clusters: variability in luminescence thermochromism. *Inorganic Chemistry* **2015**, 54 (9), 4483-4494.
16. Benito, Q.; Baptiste, B.; Polian, A.; Delbes, L.; Martinelli, L.; Gacoin, T.; Boilot, J. P.; Perruchas, S., Pressure Control of Cuprophilic Interactions in a Luminescent Mechanochromic Copper Cluster. *Inorganic Chemistry* **2015**, 54 (20), 9821-9825.
17. Benito, Q.; Le Goff, X. F.; Maron, S.; Fargues, A.; Garcia, A.; Martineau, C.; Taulelle, F.; Kahlal, S.; Gacoin, T.; Boilot, J. P.; Perruchas, S., Polymorphic copper iodide clusters: insights into the mechanochromic luminescence properties. *Journal of the American Chemical Society* **2014**, 136 (32), 11311-11320.
18. Kitada, N.; Ishida, T., Polymeric one- and two-dimensional copper(i) iodide complexes showing photoluminescence tunable by azaaromatic ligands. *CrystEngComm* **2014**, 16 (34), 8035-8040.
19. Zhou, W.-W.; Zhao, W.; Zhao, X.; Wang, F.-W.; Wei, B., A New 1-D Cu(I) Pyridinate Complex [CuBr(anp)]<sub>n</sub> (anp = 2-amino-5-nitropyridine). *Synthesis and Reactivity in Inorganic, Metal-Organic, and Nano-Metal Chemistry* **2013**, 43 (9), 1171-1174.
20. Liu, J.; Qin, Y.-L.; Qu, M.; Clerac, R.; Zhang, X.-M., Rung-defected ladder of azido-bridged Cu(ii) chains linked by [Cu(picolate)<sub>2</sub>] units. *Dalton Transactions* **2013**, 42 (32), 11571-11575.
21. Yam, V. W.-W.; Wong, K. M.-C., Luminescent metal complexes of d6, d8 and d10 transition metal centres. *Chemical Communications* **2011**, 47 (42), 11579-11592.
22. Peng, R.; Li, M.; Li, D., Copper(I) halides: A versatile family in coordination chemistry and crystal engineering. *Coordination Chemistry Reviews* **2010**, 254 (1-2), 1-18.
23. Wu, F.; Tong, H.; Wang, K.; Zhang, J.; Xu, Z.; Zhu, X., Luminescent monomeric and polymeric cuprous halide complexes with 1,2-bis(3,5-dimethylpyrazol-

- 1-ylmethyl)-benzene as ligand. *Inorganic Chemistry Communications* **2015**, 58, 113-116.
24. Fang, S.-M.; Zhang, Q.; Hu, M.; Xiao, B.; Zhou, L.-M.; Sun, G.-H.; Gao, L.-J.; Du, M.; Liu, C.-S., Controllable assembly of copper(i)-iodide coordination polymers by tecton design of benzotriazol-1-yl-based pyridyl ligands: from 2D layer to 3D self-penetrating or homochiral networks. *CrystEngComm* **2010**, 12 (7), 2203-2212.
25. Kim, T. H.; Shin, Y. W.; Kim, J. S.; Lee, S. S.; Kim, J., Luminescent staircase copper(I) coordination polymer based on planar Cu3I3. *Inorganic Chemistry Communications* **2007**, 10 (6), 717-719.
26. Li, J.-C.; Li, H.-X.; Li, H.-Y.; Gong, W.-J.; Lang, J.-P., Ligand Coordination Site-Directed Assembly of Copper(I) Iodide Complexes of ((Pyridyl)-1-pyrazolyl)pyridine. *Crystal Growth & Design* **2016**, 16 (3), 1617-1625.
27. Lin, P.; Henderson, R. A.; Harrington, R. W.; Clegg, W.; Wu, C.-D.; Wu, X.-T., New 1- and 2-Dimensional Polymeric Structures of Cyanopyridine Complexes of AgI and CuI. *Inorganic Chemistry* **2003**, 43 (1), 181-188.
28. Yu, J. H.; Xu, J. Q.; Ye, L.; Ding, H.; Jing, W. J.; Wang, T. G.; Xu, J. N.; Jia, H. B.; Mu, Z. C.; Yang, G. D., Hydrothermal synthesis and characterization of a copper(I) halide coordination polymer with isonicotinic acid (IN) ligand as a template possessing three-dimensional supramolecular network structure. *Inorganic Chemistry Communications* **2002**, 5 (8), 572-576.
29. Hardt, H. D.; Pierre, A., Fluorescence thermochromism of pyridine copper iodides and copper iodide. *Zeitschrift für Anorganische und Allgemeine Chemie* **1973**, 402 (1), 107-112.
30. Braga, D.; Grepioni, F.; Maini, L.; Mazzeo, P. P.; Ventura, B., Solid-state reactivity of copper(i) iodide: luminescent 2D-coordination polymers of CuI with saturated bidentate nitrogen bases. *New Journal of Chemistry* **2011**, 35 (2), 339-344.
31. Ford, P. C.; Cariati, E.; Bourassa, J., Photoluminescence Properties of Multinuclear Copper(I) Compounds. *Chemical Reviews* **1999**, 99 (12), 3625-3648.
32. Siemeling, U.; Vorfeld, U.; Neumann, B.; Stammeler, H.-G., Cuprophilicity? a rare example of a ligand-unsupported CuI–CuI interaction. *Chemical Communications* **1997**, (18), 1723-1724.
33. Singh, K.; Long, J. R.; Stavropoulos, P., Ligand-Unsupported Metal–Metal (M = Cu, Ag) Interactions between Closed-Shell d10Trinuclear Systems. *Journal of the American Chemical Society* **1997**, 119 (12), 2942-2943.
34. Conesa-Egea, J.; Zamora, F.; Amo-Ochoa, P., Perspectives of the smart Cu-Iodine coordination polymers: A portage to the world of new nanomaterials and composites. *Coordination Chemistry Reviews* **2019**, 381, 65-78.



35. Hardt, H. D.; Pierre, A., Fluorescence thermochromism and symmetry of copper(I) complexes. *Inorganica Chimica Acta* **1977**, *25*, L59-L60.
36. Cariati, E.; Lucenti, E.; Botta, C.; Giovanella, U.; Marinotto, D.; Righetto, S., Cu(I) hybrid inorganic–organic materials with intriguing stimuli responsive and optoelectronic properties. *Coordination Chemistry Reviews* **2016**, *306*, Part 2, 566-614.
37. Liu, Z.; Djurovich, P. I.; Whited, M. T.; Thompson, M. E., Cu<sub>4</sub>I<sub>4</sub> clusters supported by P<sup>^</sup>N-type ligands: new structures with tunable emission colors. *Inorganic Chemistry* **2012**, *51* (1), 230-236.
38. Shan, X.-C.; Jiang, F.-L.; Yuan, D.-Q.; Zhang, H.-B.; Wu, M.-Y.; Chen, L.; Wei, J.; Zhang, S.-Q.; Pan, J.; Hong, M.-C., A multi-metal-cluster MOF with Cu<sub>4</sub>I<sub>4</sub> and Cu<sub>6</sub>S<sub>6</sub> as functional groups exhibiting dual emission with both thermochromic and near-IR character. *Chemical Science* **2013**, *4* (4), 1484-1489.
39. Pospisil, J.; Jess, I.; Näther, C.; Necas, M.; Taborsky, P., Luminescence properties of “double-stranded staircase” copper(i) halide coordination polymers with N-containing ligands. *New Journal of Chemistry* **2011**, *35* (4), 861-864.
40. Jeß, I.; Taborsky, P.; Pospíšil, J.; Näther, C., Synthesis, crystal structure, thermal and luminescence properties of CuX(2,3-dimethylpyrazine) (X = Cl, Br, I) coordination polymers. *Dalton Transactions* **2007**, (22), 2263-2270.
41. Näther, C.; Jeß, I., Crystal Structure of  $\infty$ [Cu<sub>2</sub>I<sub>2</sub>(μ-4,4'-bipyridine)] and Investigations on the Thermal Decomposition of CuX-4,4'-bipyridine Coordination Polymers. *Monatshefte für Chemie / Chemical Monthly* **2001**, *132* (8), 897-910.
42. Hassanein, K.; Conesa-Egea, J.; Delgado, S.; Castillo, O.; Benmansour, S.; Martinez, J. I.; Abellan, G.; Gomez-Garcia, C. J.; Zamora, F.; Amo-Ochoa, P., Electrical Conductivity and Strong Luminescence in Copper Iodide Double Chains with Isonicotinato Derivatives. *Chemistry - A European Journal* **2015**, *21* (48), 17282-17292.
43. Redel, E.; Fiederle, M.; Janiak, C., Piperazinium, Ethylenediammonium or 4,4'-Bipyridinium Halocuprates(I) by Cu-II/Cu-0 Comproportionation. *Zeitschrift für Anorganische und Allgemeine Chemie* **2009**, *635* (8), 1139-1147.
44. Mateo-Marti, E.; Welte, L.; Amo-Ochoa, P.; Sanz Miguel, P. J.; Gomez-Herrero, J.; Martin-Gago, J. A.; Zamora, F., Direct evidence of nanowires formation from a Cu(I) coordination polymer. *Chemical Communications* **2008**, (8), 945-947.
45. Vogler, A.; Kunkely, H., Photoluminescence of tetrameric copper(I) iodide complexes solutions. *Journal of the American Chemical Society* **1986**, *108* (23), 7211-7212.

46. Tran, D.; Bourassa, J. L.; Ford, P. C., Pressure-Induced Luminescence Rigidochromism in the Photophysics of the Cuprous Iodide Cluster Cu<sub>4</sub>I<sub>4</sub>py<sub>4</sub>. *Inorganic Chemistry* **1997**, 36 (3), 439-442.
47. Aguirrechú-Comeron, A.; Hernandez-Molina, R.; Rodríguez-Hernández, P.; Muñoz, A.; Rodríguez-Mendoza, U. R.; Lavin, V.; Angel, R. J.; González-Platas, J., Experimental and ab Initio Study of Catena(bis(μ<sub>2</sub>)-iodo)-6-methylquinoline-copper(I) under Pressure: Synthesis, Crystal Structure, Electronic, and Luminescence Properties. *Inorganic Chemistry* **2016**, 55 (15), 7476-7484.
48. Raston, C. L.; White, A. H., Crystal structure of the copper(I) iodide–pyridine (1/1 ) tetramer. *Journal of the Chemical Society, Dalton Transactions* **1976**, (21), 2153-2156.
49. Oelkrug, E. E. u. D., Strukturisomere von Kupfer(I)iodid • Pyridin und ihre Lumineszenzeigenschaften. Darstellung und Kristallstruktur einer neuen Modifikation von CuI • NC<sub>5</sub>H. *Zeitschrift für Naturforschung* **1980**, 35B, 1247-1253.
50. Cariati, E.; Bourassa, J., Luminescence response of the solid state polynuclear copper(i) iodide materials [CuI(4-picoline)]<sub>x</sub> to volatile organic compounds. *Chemical Communications* **1998**, (16), 1623-1624.
51. Cariati, E.; Bu, X.; Ford, P. C., Solvent- and Vapor-Induced Isomerization between the Luminescent Solids [CuI(4-pic)]<sub>4</sub> and [CuI(4-pic)]<sub>∞</sub> (pic = methylpyridine). The Structural Basis for the Observed Luminescence Vapochromism. *Chemistry of Materials* **2000**, 12 (11), 3385-3391.
52. Rodríguez-San-Miguel, D.; Amo-Ochoa, P.; Zamora, F., MasterChem: cooking 2D-polymers. *Chemical Communications* **2016**, 52 (22), 4113-4127.
53. Amo-Ochoa, P.; Welte, L.; González-Prieto, R.; Sanz Miguel, P. J.; Gómez-García, C. J.; Mateo-Martí, E.; Delgado, S.; Gómez-Herrero, J.; Zamora, F., Single layers of a multifunctional laminar Cu(I,II) coordination polymer. *Chemical Communications* **2010**, 46 (19), 3262-3264.
54. Givaja, G.; Amo-Ochoa, P.; Gómez-García, C. J.; Zamora, F., Electrical conductive coordination polymers. *Chemical Society Reviews* **2012**, 41 (1), 115-147.
55. Guijarro, A.; Castillo, O.; Welte, L.; Calzolari, A.; Miguel, P. J. S.; Gómez-García, C. J.; Olea, D.; di Felice, R.; Gómez-Herrero, J.; Zamora, F., Conductive Nanostructures of MMX Chains. *Advanced Functional Materials* **2010**, 20 (9), 1451-1457.
56. Olea, D.; González-Prieto, R.; Priego, J. L.; Barral, M. C.; de Pablo, P. J.; Torres, M. R.; Gómez-Herrero, J.; Jiménez-Aparicio, R.; Zamora, F., MMX polymer chains on surfaces. *Chemical Communications* **2007**, (16), 1591-1593.

57. Welte, L.; Gonzalez-Prieto, R.; Olea, D.; Torres, M. R.; Priego, J. L.; Jimenez-Aparicio, R.; Gomez-Herrero, J.; Zamora, F., Time-dependence structures of coordination network wires in solution. *ACS Nano* **2008**, 2 (10), 2051-2056.
58. Troyano, J.; Perles, J.; Amo-Ochoa, P.; Martínez, J. I.; Zamora, F.; Delgado, S., Reversible recrystallization process of copper and silver thioacetamide–halide coordination polymers and their basic building blocks. *CrystEngComm* **2014**, 16 (35), 8224-8231.
59. Desiraju, G. R., Supramolecular Synthons in Crystal Engineering—A New Organic Synthesis. *Angewandte Chemie International Edition in English* **1995**, 34 (21), 2311-2327.
60. Klotz, S.; Chervin, J. C.; Munsch, P.; Marchand, G. L., Hydrostatic limits of 11 pressure transmitting media. *Journal of Physics D: Applied Physics* **2009**, 42 (7), 075413.
61. Spencer, E. C.; Angel, R. J.; Ross, N. L.; Hanson, B. E.; Howard, J. A. K., Pressure-Induced Cooperative Bond Rearrangement in a Zinc Imidazolate Framework: A High-Pressure Single-Crystal X-Ray Diffraction Study. *Journal of the American Chemical Society* **2009**, 131 (11), 4022-4026.
62. Funnell, N. P.; Dawson, A.; Francis, D.; Lennie, A. R.; Marshall, W. G.; Moggach, S. A.; Warren, J. E.; Parsons, S., The effect of pressure on the crystal structure of l-alanine. *CrystEngComm* **2010**, 12 (9), 2573-2583.
63. Slebodnick, C.; Zhao, J.; Angel, R.; Hanson, B. E.; Song, Y.; Liu, Z.; Hemley, R. J., High Pressure Study of Ru<sub>3</sub>(CO)<sub>12</sub> by X-ray Diffraction, Raman, and Infrared Spectroscopy. *Inorganic Chemistry* **2004**, 43 (17), 5245-5252.
64. Shen, J.; Ding, P.; Gao, L.; Gao, Y.; Zhang, Q.; Yuan, S.; Xin, X., Formation of organogels with aggregation-induced emission characteristics triggered by thermal and ultrasound. *Colloid and Polymer Science* **2017**, 295 (10), 1765-1772.
65. Maity, I.; Rasale, D. B.; Das, A. K., Sonication induced peptide-appended bolaamphiphile hydrogels for in situ generation and catalytic activity of Pt nanoparticles. *Soft Matter* **2012**, 8 (19), 5301-5308.
66. Rastogi, M.; Awasthi, A.; Shukla, J. P., Ultrasonic and IR investigations of N-H bond complexes. *Phys. Chem. Liq.* **2004**, 42 (2), 117-126.
67. Meng, L. R.; Mo, R.; Zhou, H.; Wang, G.; Chen, W.; Wang, D.; Peng, Q., Synthesis of Luminescent Cubic Phase One-Dimensional CuI Nanostructures in Solution. *Crystal Growth & Design* **2010**, 10 (8), 3387-3390.
68. Kumar, R.; Siril, P. F., Controlling the size and morphology of griseofulvin nanoparticles using polymeric stabilizers by evaporation-assisted solvent–antisolvent interaction method. *Journal of Nanoparticle Research* **2015**, 17 (6), 256.

69. Toivola, R.; Lai, P.-N.; Yang, J.; Jang, S.-H.; Jen, A. K. Y.; Flinn, B. D., Mechanochromic fluorescence in epoxy as a detection method for barely visible impact damage in CFRP composites. *Composites Science and Technology* **2017**, *139*, 74-82.
70. Guionneau, P., Crystallography and spin-crossover. A view of breathing materials. *Dalton Transactions* **2014**, *43* (2), 382-393.
71. Makiura, R.; Motoyama, S.; Umemura, Y.; Yamanaka, H.; Sakata, O.; Kitagawa, H., Surface nano-architecture of a metal-organic framework. *Nature Materials* **2010**, *9* (7), 565-571.
72. Boscher, N. D.; Choquet, P.; Duday, D.; Kerbellec, N.; Lambrechts, J.-C.; Maurau, R., Luminescent lanthanide-based hybrid coatings deposited by atmospheric pressure plasma assisted chemical vapour deposition. *Journal of Materials Chemistry* **2011**, *21* (47), 18959-18961.
73. Rashid, A.; Ananthnag, G. S.; Naik, S.; Mague, J. T.; Panda, D.; Balakrishna, M. S., Dinuclear Cu-I complexes of pyridyl-diazadiphosphetidines and aminobis(phosphonite) ligands: synthesis, structural studies and antiproliferative activity towards human cervical, colon carcinoma and breast cancer cells. *Dalton Transactions* **2014**, *43* (29), 11339-11351.
74. Valeur, B.; Berberan-Santos, M. N., *Molecular Fluorescence. Principles and Applications*. 2 ed.; Wiley-VCH Verlag GmbH & Co.: 2012.
75. Corrales, S. A.; Cain, J. M.; Uhlig, K. A.; Mowson, A. M.; Papatriantafyllopoulou, C.; Peprah, M. K.; Ozarowski, A.; Tasiopoulos, A. J.; Christou, G.; Meisel, M. W.; Lampropoulos, C., Introducing Dimensionality to the Archetypical Mn<sub>12</sub> Single-Molecule Magnet: a Family of [Mn<sub>12</sub>]<sub>n</sub> Chains. *Inorganic Chemistry* **2016**, *55* (4), 1367-1369.

### **Chapter 3. The effect of defects on the properties of a Cu(I)-I coordination polymer**

### 3.1. Introduction to defects.

When the properties of a material are studied, we usually focus on its structure in order to justify their origin and, thus, the structure-properties relationship. However, structural defects can play an essential role in determining the final values of these properties, *e.g.* luminescence, conductivity or magnetism.<sup>1</sup> Indeed, the presence of surface defects has been described as a cause of changes in the physical properties of a single compound.<sup>2-4</sup> In fact, defects of various natures and length scales are key attributes of solid-state materials and strongly affect their physical and chemical properties.<sup>4</sup>

Structural defects can be classified according to their dimensionality:<sup>1</sup>

**1. Zero-dimensional defects (point defects):** These are the most common defects we can find in any material, and they involve single atoms (**Figure 3.1**). They can be subdivided into the following categories:

a) Vacancies. Among point defects, these are the most common, since they are present in every solid substance. They are generated when an atom is missing from its position. According to thermodynamics, the presence of vacancies in a solid increases its entropy, therefore improving its stability. The amount of vacancies ( $N_v$ ) in a crystalline material is calculated via the following equation, similar to Arrhenius's law:

$$N_v = N \cdot \exp(-Q_v/kT)$$

Herein,  $N$  represents the total number of atomic sites in the material, and  $Q_v$  is the activation energy that is required for the generation of a vacancy. Since the value of  $Q_v$  is always positive, as temperature rises the factor " $\exp(-Q_v/kT)$ " will be higher, and so will be  $N_v$ .

In metals, it is common to find a ratio of vacancies of  $10^{-4}$ . In the case of ionic materials, the vanishing of an ion from its position is immediately followed by the generation of another vacancy in the position of a complementary ion, in order to keep the electroneutrality. This is called a Schottky defect.

b) Interstitial defects. This kind of defect involves the appearance of an atom in a hole (or interstitial position) of the material's lattice. Since the atom occupying this interstice is substantially bigger than the site, it generates important distortions in the surrounding lattice region. Therefore, interstitial defects are much less common than vacancies.

It is common that interstitial defects are generated by the displacement of an atom from its usual position to the interstitial site, therefore generating a vacancy as well. This combination of an interstitial defect and a vacancy is known as Frenkel defect, and its presence is predominant in ionic materials.

c) Substitutions. This kind of defect is generated when an atom in the crystal lattice is replaced by a different one, commonly known as an impurity.

In ionic materials, the electric charge of the impurity can alter the structure of the material in different ways. If its charge is equal to that of the ion it replaces, the lattice remains unaltered, unless the size of the impurity is 15% higher or lower (this would generate distortions in the lattice in a similar way than interstitial defects). If its charge is lower, vacancies of the complementary ion appear, but if it is higher, the generated vacancies will affect ions similar to that which was replaced, in order to keep the electroneutrality. An example of the latter situation involves non-stoichiometric solids, such as wüstite (iron(II) oxide, FeO). In this mineral, there is always a proportion of iron(III) atoms, and for every two Fe(III) substitutional cations, a Fe(II) vacancy is generated. Therefore, the formula of wüstite must be written as  $\text{Fe}_{1-x}\text{O}$ , where  $x$  is the ratio of vacancies and the number of Fe(III) substitutional defects is  $2x$ .

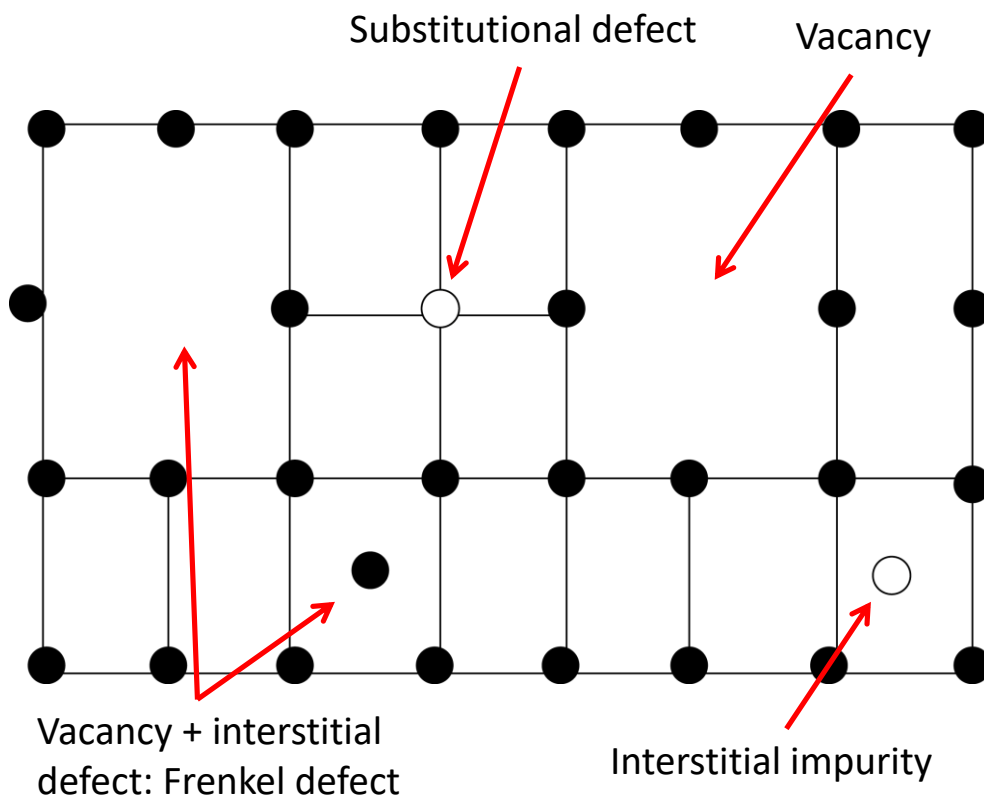


**Figure 3.1.** Schematic representation of all point defects (Schottky defects are omitted since they are exclusive of ionic materials). Based on a series of images in reference <sup>1</sup>, vectorized by Ms. Marina Prada.

**2. One-dimensional defects (linear defects):** These defects, also known as dislocations, are generated when a row of atoms in the crystal lattice disappears, therefore generating a lack of stacking which causes a misalignment of the adjacent atoms. Therefore, important distortions of the lattice appear around the dislocation line.

Depending on the nature of the dislocations, they can be divided into two groups: edge dislocations and screw dislocations. Sometimes, dislocations containing both characters (known as mixed dislocations) can be found within the structure of a material.

a) Edge dislocations. This kind of defect is characterized to be centered around the dislocation line (**Figure 3.2**). Far from the place where the dislocation is originated, the lattice structure becomes virtually perfect.

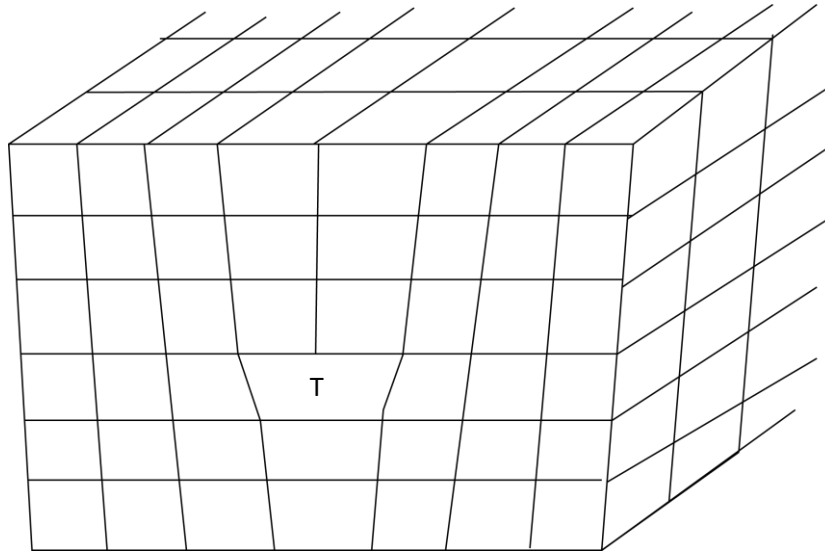


**Figure 3.2.** Schematic representation of an edge dislocation. The “T” marks the spot where this defect takes its origin. Based on a figure in reference <sup>1</sup>, vectorized by Ms. Marina Prada.

b) Screw dislocations. These defects form by the effect of shear stresses (such as those generated by grinding processes), causing the displacement of a row of atoms one position to the adjacent site, causing a helical path to be generated around the dislocation line (**Figure 3.3**).

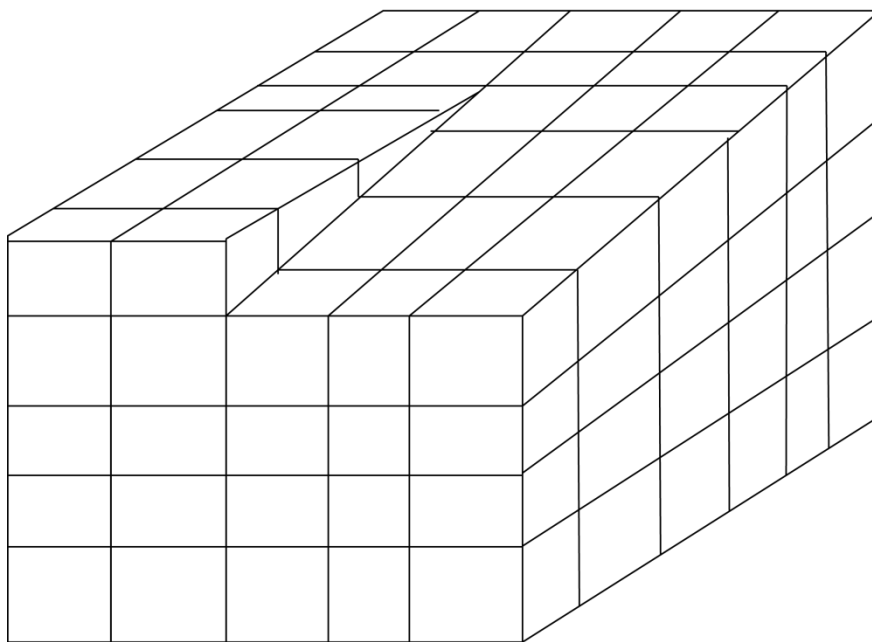


**Figure 3.3.** Schematic representation of a screw dislocation. Based on a figure in reference <sup>1</sup>, vectorized by Ms. Marina Prada.



**3. Two-dimensional defects (surface defects):** These defects, also called interfacial defects, separate different regions of a material with different crystal structure or orientations, the so-called domains.

Apart from external surfaces (where the atoms at those edges have some unoccupied bonding sites, also called unsaturations), surface defects can be divided into twin planes and grain boundaries.

a) Twin planes. These defects are formed where the separation of two crystalline domains takes place through a mirror symmetry plane (**Figure 3.4**). Due to their nature, they can be considered as a special case of grain boundary (*vide infra*). Twins are generated by shear forces, or in annealing processes, and they occur only in specific crystallographic planes.

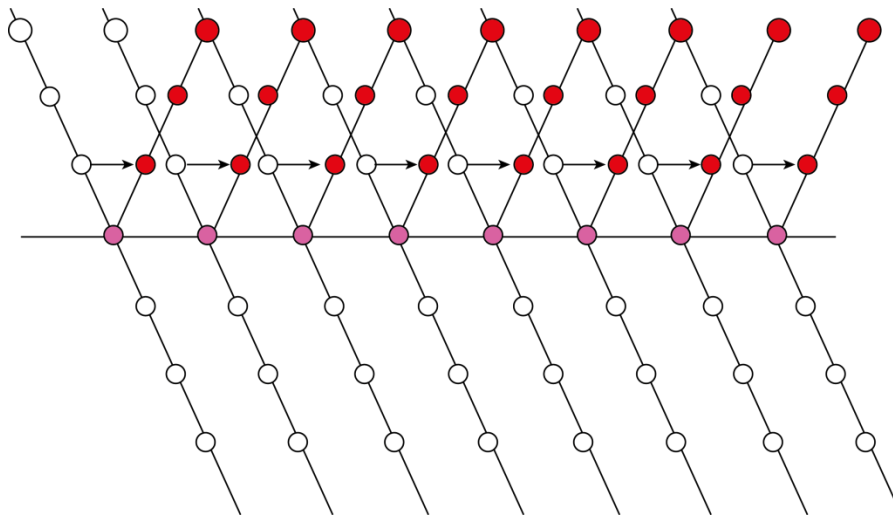


**Figure 3.4.** Schematic representation of a twin defect. The twin plane is depicted as the horizontal line. Based on a series of images in reference <sup>1</sup>, vectorized by Ms. Marina Prada.

b) Grain boundaries. This is the general term which is used to determine the two-dimensional boundary which separates two crystalline domains of a material, no matter what their orientation is. The difference in orientation of the crystal structure of the two domains generates an atomic mismatch (**Figure 3.5**).

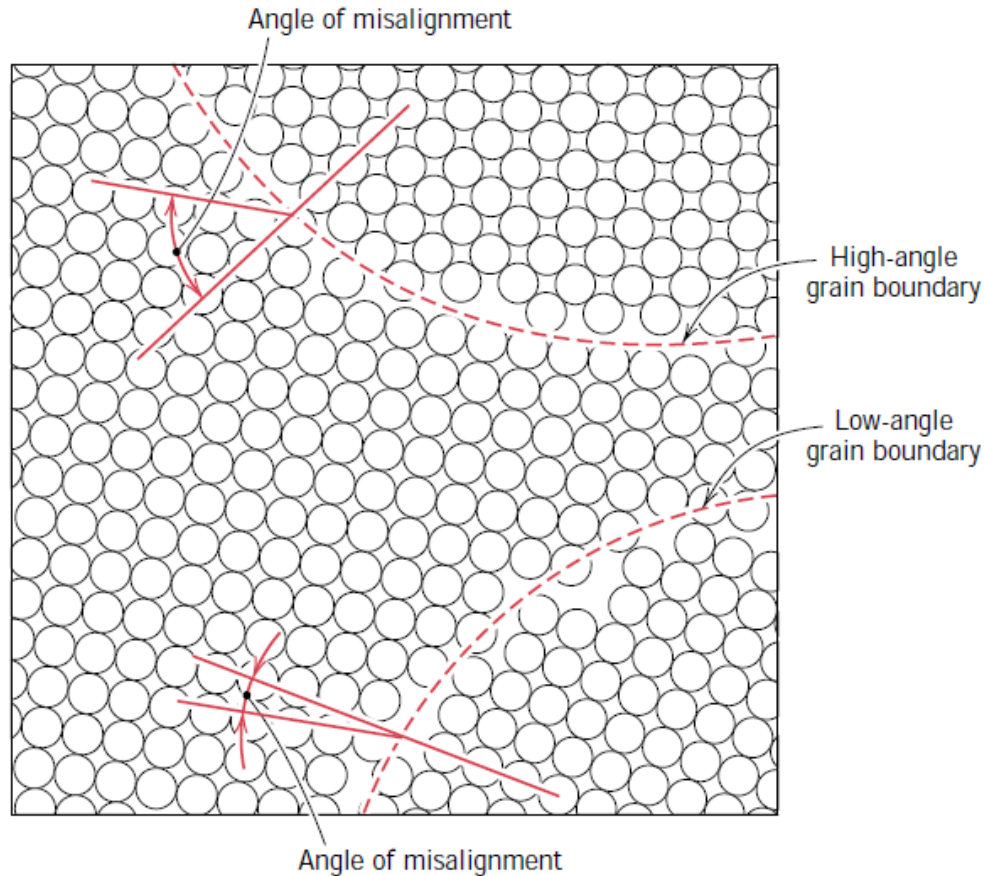


**Figure 3.5.** Schematic representation of grain boundaries. Taken from reference <sup>1</sup>.

**4. Volumetric or bulk defects:** Other defects found in all solid materials are much larger than those afore discussed. These include pores, cracks, foreign inclusions, and the presence of different phases. These are normally introduced during processing and fabrication steps.

The presence of defects in a material is of crucial importance, as has been mentioned before. Following this basis, the generation of specific defects through controlled doping, using different synthetic routes with the aim to modify the optical properties of a specific compound, has already been reported.<sup>5-6</sup> In most of these investigations, the dopant species represent *ca.* 1 to 20 % and provoke significant changes in the structure and morphology of the material that can be studied by using conventional characterization techniques.<sup>7</sup> Therefore, it seems very important to study how to control the presence of defects<sup>8-11</sup> in crystalline compounds to gain control over their properties and, therefore, improve their efficiency in any of their possible applications.<sup>12-16</sup> In fact, defect engineering is of paramount importance to manipulate crystal quality and, therefore, the specific properties desired in a material. However, the study of structural defects is very complicated in particular for low dimensionality defects present in low concentration where the usual spectroscopic and diffractometric techniques (IR, XRD,

XPS...) do not give this information.<sup>3</sup> In case of Metal Organic Frameworks (MOFs), engineered defects have gained recent attention because their implications in both catalysis and porosity.<sup>4</sup> Despite this, still very little work reports the effect of the structural defects of CPs on their electronic properties. Very recently we have shown that the electrical conductivity of MMX chains, a particular type of CPs well-related to CuI-double chains, strongly varies with the density and type of the metal-halide defects along the MMX chains (**Figure 3.6**).<sup>17</sup>

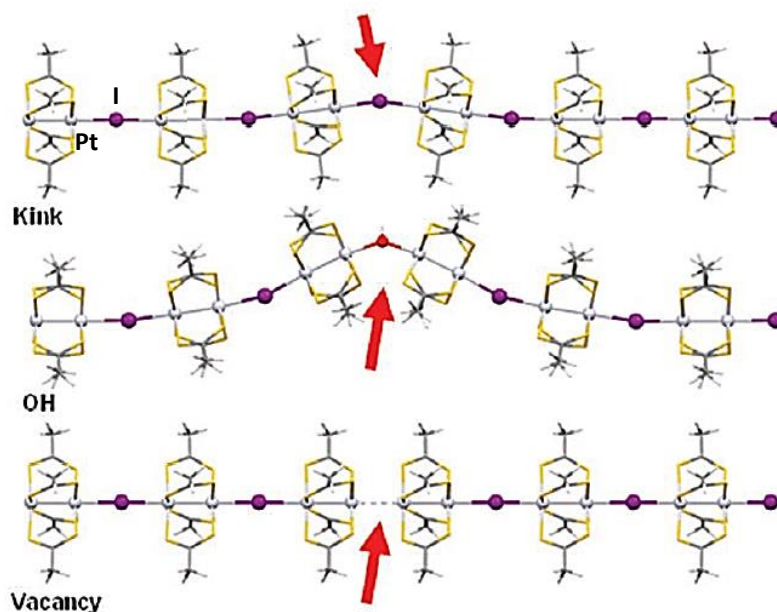
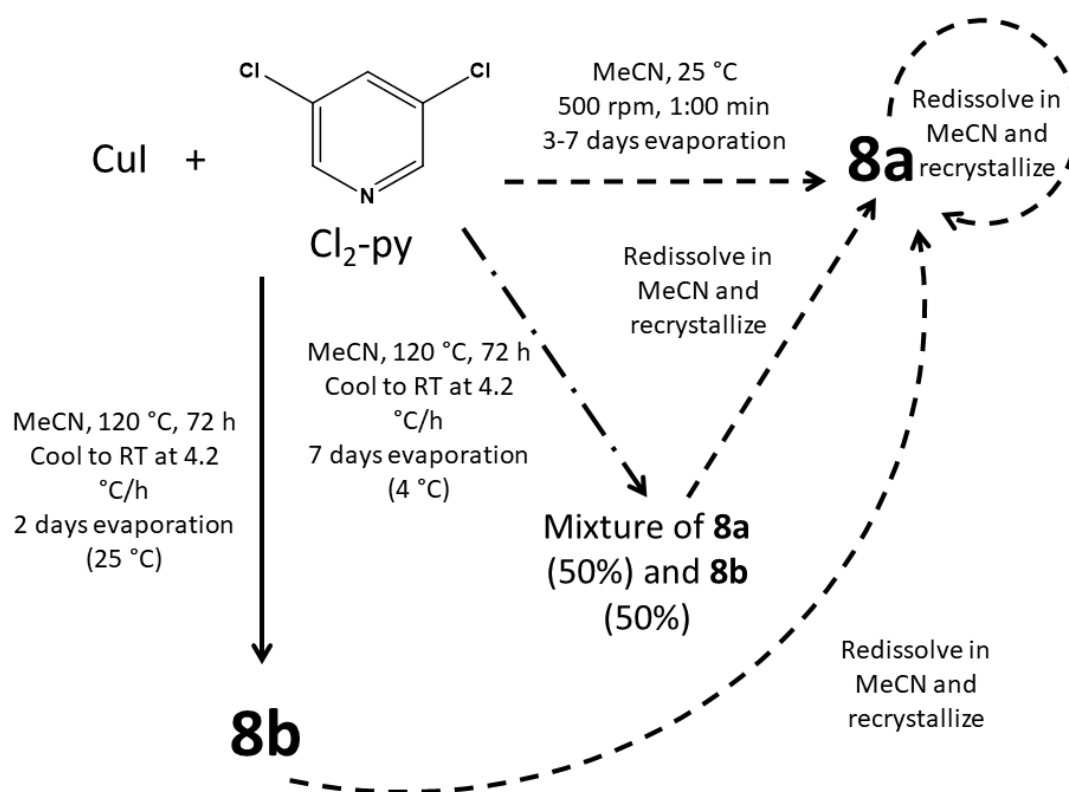


**Figure 3.6.** Representation of three possible defect types which could be found in  $[\text{Pt}_2\text{I}(\text{dta})_4]_n$  (dta = dithioacetate). Vacancies were found to be the cause of the changes in its electrical conductivity. Taken from reference <sup>17</sup>.

## 3.2. Results and discussion.

### 3.2.1. Synthesis and structural characterization.

Direct reaction between CuI and 3,5-dichloropyridine ( $\text{Cl}_2\text{-py}$ ) in acetonitrile gives rise to the isolation of the 1D CP  $[\text{Cu}(\text{Cl}_2\text{-py})\text{I}]_n$ . However, when slightly modifying the synthetic conditions this CP can be isolated as two different compounds with identical structure, named as **8a** and **8b**. Thus, when the initial CuI and  $\text{Cl}_2\text{-py}$  acetonitrile solution, in a 1:1 ratio and a range of concentration between 18 and 70 mM, is allowed to crystallize at 25 °C, yellow single crystals of **8a** are isolated. On the other hand, when the initial acetonitrile solution, in a similar range of concentrations, is first submitted to a solvothermal treatment at 120 °C for 72 h, then filtered or centrifuged and allowed to crystallize, dark-yellow crystals of **8b** are formed instead (**Scheme 3.1**).



**Scheme 3.1.** Synthetic routes which lead to the formation of **8a** and **8b**.

Single crystal X-ray analyses of **8a** and **8b** show that these structures do not present any significant difference neither in structure parameters nor distances nor angles (**Appendix A, Tables A9-A10**). The structure of **8a** and **8b** corresponds to the general formula  $[\text{Cu}(\text{Cl}_2\text{-py})\text{I}]_n$  which, same as compounds **1-7** outlined in chapter 2 and many other reported Cu(I)-I CPs,<sup>18-19</sup> consists of a polymeric staircase motif of edge-sharing  $\text{Cu}_2\text{I}_2$  rhomboids. In this case, the polymeric chain runs parallel to the *b* axis, and it is anchored with 3,5-dichloropyridine as N-donor terminal ligand (**Figure 3.7**).

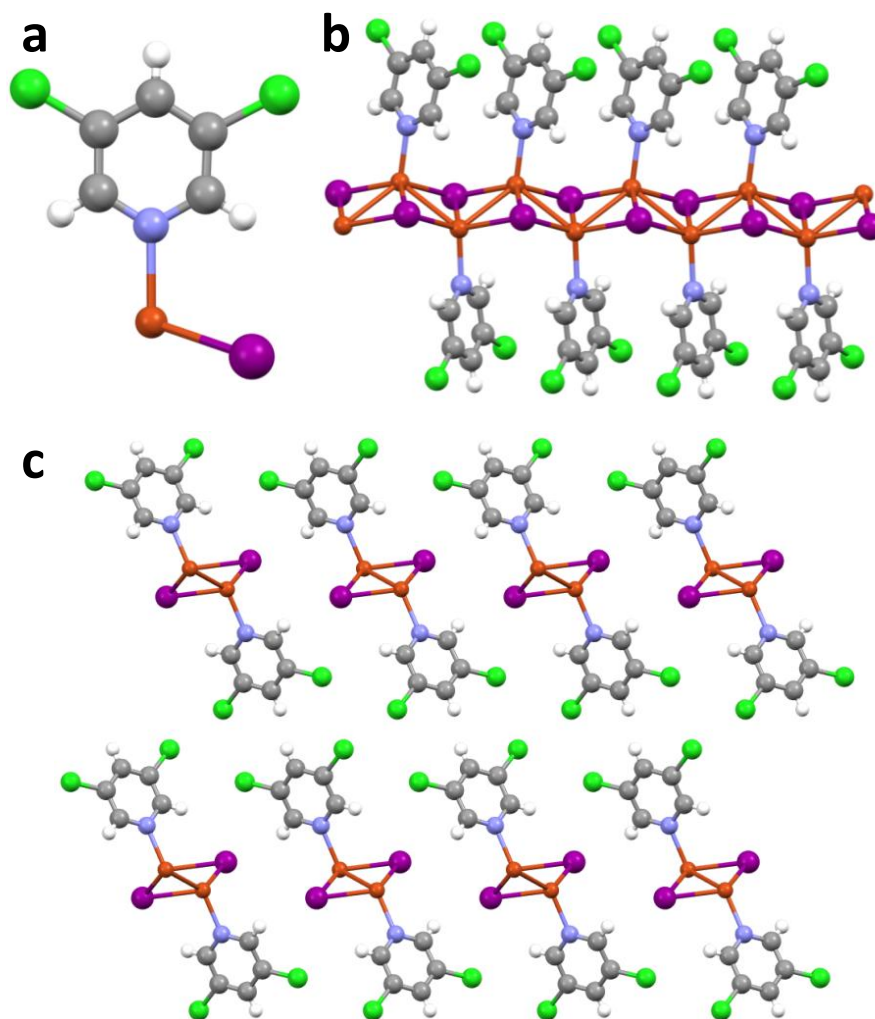


**Figure 3.7.** Crystal structure of compounds **8a** and **8b**: (a) asymmetric unit; (b) lateral view of a Cu(I)-I double *zigzag* chain; (c) View of the packing of the crystal structure from the crystallographic *b* axis. Cu: orange; I: purple; C: grey; H: white; N: blue; Cl: green.

Interestingly, compound **8b** is transformed in **8a** by slow recrystallization in acetonitrile at 25 °C. Additionally, when the reaction conditions were adjusted to produce an equimolecular mixture of **8a** and **8b** in acetonitrile (SI), recrystallization also led to the isolation of **8a** (Scheme 3.1). Therefore, these reactions confirm that the thermodynamic, and therefore the least defective material, corresponds to **8a**. It is worth mentioning that these reactions have been carried out several times and the results are highly reproducible.

Since the only synthetic difference in the formation of **8a** and **8b** is the solvothermal treatment of the initial CuI and 3,5-dichloropyridine acetonitrile solution, we have focused on the comparative analysis of two initial acetonitrile solutions: the one prepared at 25 °C and that obtained by solvothermal treatment.

The experimental difference observed upon the solvothermal treatment of the CuI and Cl<sub>2</sub>-py acetonitrile solution is the formation of a brown colloid that is removed before crystallization, in trace amount (0.5 mg per 100 mg of CuI added as starting reagent). The TXRF analysis of the solid confirms that it consists of just copper, and therefore a partial disproportionation of Cu(I) into Cu(0) and Cu(II) takes place (**Figure 3.8**).

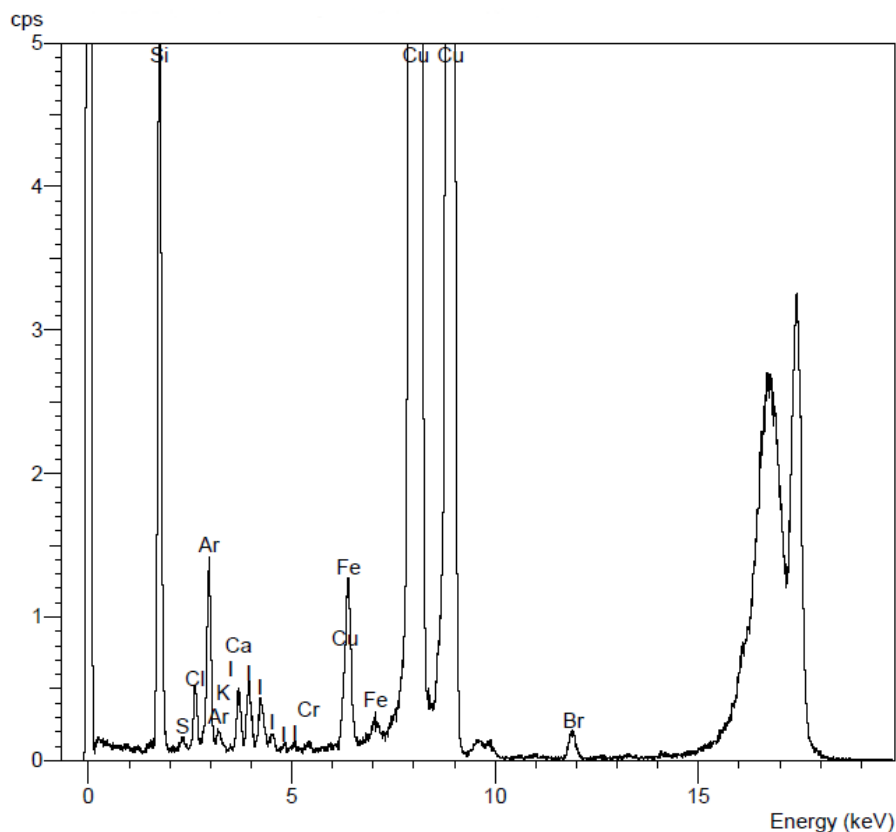


**Figure 3.8.** TXRF spectrum of the residual brown solid obtained in the synthesis of **8b**.

We have also discarded other potential processes that may occur and coexist during the solvothermal process such as: i) partial 3,5-dichloropyridine degradation, ii) Cu(I) reduction with iodide oxidation, leading to I<sub>2</sub> and Cu(0) formation; iii) insoluble CP formation.

Ligand degradation is discarded using NMR. The <sup>1</sup>H-NMR spectrum of the acetonitrile solution obtained after solvothermal process does not show any additional peak but just those corresponding to 3,5-dichloropyridine (**Appendix E, Figures E1-E4**).

On the other hand, the UV-visible spectrum of the solution obtained after the solvothermal process matches with the one obtained just by mixing the two building blocks in acetonitrile at 25 °C (**Figure 3.9**), therefore discarding the presence of iodine in solution (which would be observed by the presence of sharp and strong absorption bands centered at 242, 291 and 360 nm). Finally, the absence of iodine and chlorine in the TXRF (**Figure 3.8**) discard the possibility of an insoluble CP or metal complex.

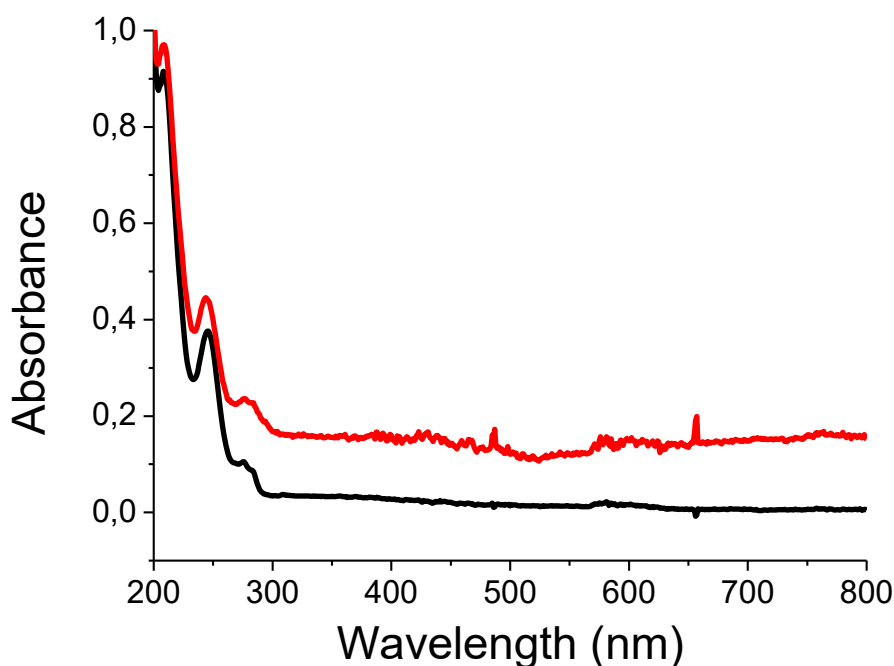


**Figure 3.9.** UV-visible spectra of the reaction solutions of **8a** (black) and **8b** (red).

Taking into account all of the explained above, we confirm that a partial disproportion reaction of CuI takes place with formation of elemental copper (trace amount), therefore, the solvothermal treatment implies a slight reduction of the CuI amount, relative to the Cl<sub>2</sub>-py, but also with the presence of trace quantities of Cu(II). Indeed, it has been previously reported that solvothermal conditions, can produce small amounts of metallic copper, which can slightly alter the reaction stoichiometry.<sup>20</sup>

Therefore, the slight alteration in the composition of the reaction mixture, together with a faster evaporation of acetonitrile, can explain the formation of more structurally defective CuI double chains (**8b**), that can be recrystallized in acetonitrile to eliminate the defects and produce a well-ordered structure (**8a**).

Trying to gain control over this process reactions in acetonitrile at room temperature with different CuI vs Cl<sub>2</sub>-py ratios (0.95:1 and 0.9:1), were carried out. However, in all these tests formation of **8a** was just observed upon crystallization. This observation suggests that the defects can only be generated under the specific experimental conditions obtained in the solvothermal process. Probably, the presence of small traces of Cu(II) and/or the presence of Cu(0) play a role in this process.

In any case, all these data confirm that the amount of defects present in **8b** is clearly below the detection limits of the spectroscopic and diffractometric techniques (in the scale of ppm).

Finally, XPS of **8a** and **8b** were measured to corroborate whether small amounts of Cu(0) or Cu(II) could be pre-sent as defects in the crystals of **8b**, since they are not detected by other techniques. Thus, both samples show analogous peaks, corresponding to the binding energies of the electrons coming from the core orbitals of carbon,



chlorine, nitrogen, iodine and copper (**Table 3.1**). As for the energy levels of copper, the emission bands relative to the 2p orbitals of copper for **8a** and **8b** confirm that all the metal centers present a +I oxidation state, since the Cu(II) bands present satellite signals which cannot be observed in the XPS spectra of the CPs (**Figure 3.10**), so this tells us that the amount of copper(II) is lower than a 0.1 %, which is negligible. To confirm the presence of Cu(0) centers in **8a** or **8b**, the Auger parameter of copper was studied. According to Battistoni and co-workers,<sup>21</sup> samples containing Cu(0) should have an Auger parameter about 2 or 3 eV lower than that of Cu(I). The results (**Table 3.1**) confirm that, since the Auger parameter does not vary from one sample to the other, all the metal centers in both samples are Cu(I).

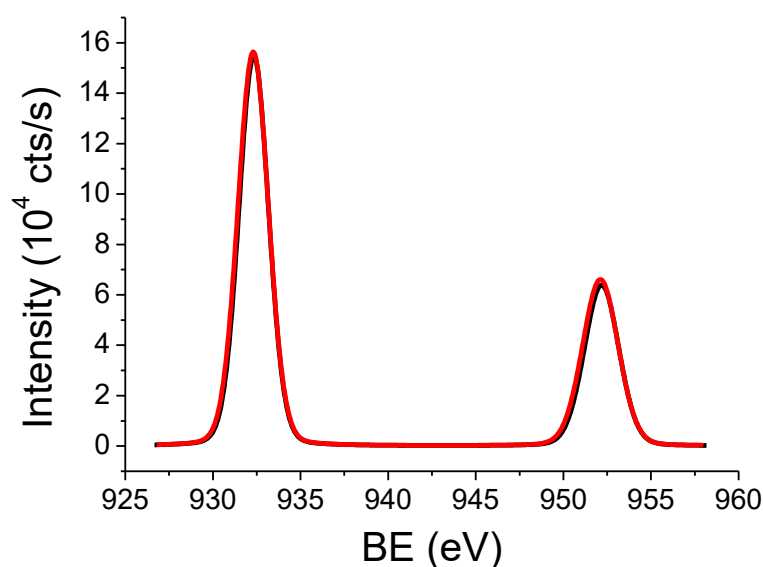


**Figure 3.10.** X-ray photoelectron spectra of **8a** (black) and **8b** (red) showing the 2p energy levels of the copper centers.

**Table 3.1.** Binding energy (BE) values of **8a** and **8b**.

Compound \ BE (eV)	C 1s	Cl 2p	Cu 2p <sub>3/2</sub>	I 3d	N 1s	Cu Auger parameter*
<b>8a</b>	284.8	200.3	932.3	619.3	398.0	1848.7
<b>8b</b>	284.8	200.2	932.3	619.3	397.9	1848.6

\*Auger parameter = 1253.6 + BE Cu2p<sub>3/2</sub> – BE Cu Auger<sup>22</sup>

Additionally, in order to check that no traces of solvents have been trapped within the structure of **8a** or **8b**, a thermogravimetric analysis coupled with mass spectrometry (TG-MS) of each form of the CP was collected. It is known that Cu(I)-I CPs start decomposing at about 80 °C, losing the ligand in the first place. Thanks to the TG-MS diagrams of **8a** and **8b** (**Figures D8-D9** in Appendix D) we know that this loss occurs in the shape of different fragments of the pyridine ring, or as py<sup>2+</sup>, but none of them correspond to acetonitrile or ethanol. On the other hand, at higher temperatures (400-



800 °C), the fragment at  $m/z$  which enters the mass detector corresponds to  $\text{Cu}^+$  or  $\text{I}^{2+}$  ions. Therefore, we can conclude that the shift in the luminescence of **8a** and **8b** is not due to the presence of solvents in the structure, thus reinforcing the hypothesis which implies the presence of defects in **8b**.

### 3.2.2. Luminescent properties

Building up onto the above theoretical description, we turned to investigate the impact of the structural defects on the photoluminescence behavior under different experimental conditions. Precisely, we carried out both temperature and pressure dependence photoluminescence assays for both compounds.

First, the emission spectra ( $\lambda_{\text{exc}} = 375 \text{ nm}$ ) of **8a** and **8b** was monitored at temperatures ranging from 80 to 300 K (**Figure 3.11**). Complex **8a** displays, at room temperature, an asymmetric broad emission band centered at 515 nm associated to photoluminescence quantum yield of 12 % and a  $\tau_{\text{av}}$  of 1.9  $\mu\text{s}$ . Upon decreasing the temperature, the intensity of the emission increases along with a gradually red-shift of the maximum wavelength to 530 nm with a new shoulder at *ca.* 550 nm at, for example, 80 K. Interestingly, the analysis at VT reveals that this red shift has its origin in the relative increase of a low energy structured band (530 max, 550*sh*) with respect to a second high energy component at  $\sim 495 \text{ nm}$ , clearly noticeable at intermediate temperatures (see 150K, for example). The noticeable increase in intensity and the vibrational spacing ( $\sim 680 \text{ cm}^{-1}$ ) of this low energy component points out to direct band gap emission associated to CuI core.

As discussed before, the general morphology of **8b** is similar to that of **8a**, while the structural defects introduce intra band gap states that can be radiatively active. Following this rationale, complex **8b** shows a weak orange/yellowish emission consisting of a low energy band at  $\sim 670 \text{ nm}$  ( $\tau_{\text{av}} = 0.5 \mu\text{s}$ ) with a broad shoulder at  $\sim 560 \text{ nm}$  (**Figure 3.11**) that are attributed to the intra band gap emission caused by structural defects and the direct band gap emission of the core, respectively. This dual emission is noticeable weaker than the one of **8a**, reaching photoluminescence quantum yields of 5%). In contrast to **8a**, the decrease of the temperature leads to i) a slight blue shift of the low-energy emission band from 670 nm to  $\sim 650 \text{ nm}$ , and ii) a significant increase in intensity of the  $\sim 560 \text{ nm}$  shoulder, that reveals itself as a prominent structured band at 80K (530*sh*, 560<sub>max</sub>, 590*sh*). This is expected since the deactivation pathway from the CB to the intra band gap defect states are hampered at low temperatures.

Joining both theoretical (*vide infra*) and photophysical evidences, **Figure 3.11c** displays the proposal for the emitting excited state scenario ruled by the structural defects. In short, the presence of the structural defects leads to reduced photoluminescence due to the presence of a low-energy emission with a zero energy of 2.03 eV (611 nm) and a high-energy band with a zero energy of 2.21 eV (560 nm) that becomes dominant at low temperature. Interesting, the difference between the zero energy values are in line with

those noted by the calculations (2.40 and 1.95 eV). In the case of **8a** as structural defect free compounds the emission only corresponds to the direct band gap (530 nm) with zero energy of 2.34 eV. Again, the differences between the zero energy of the direct band gap of **8a** and **8b** (0.13 eV) are also in good agreement with those noted by the calculations (2.40 eV).

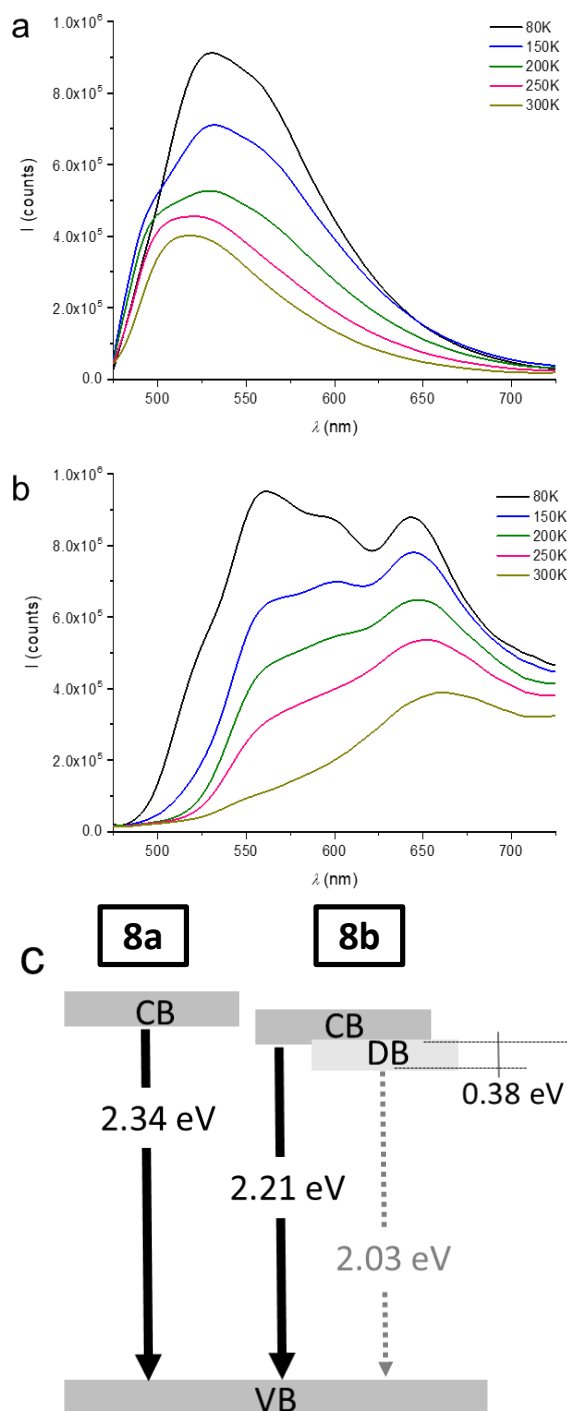


**Figure 3.11.** Thermal dependence of the luminescence spectra of **8a** (a) and **8b** (b).  $\lambda_{\text{exc}} = 375$  nm. (c) Emitting excited state scenario ruled by the structural defects.

Finally, we have also evaluated the emission properties of **8a** and **8b** under hydrostatic pressure (1 GPa, 3 GPa, 5 GPa) using pressed pellets of **8a** and **8b** crystals (**Figure 3.12**). **8a** shows an interesting behavior in which the direct band gap emission band is quenched at low applied pressures of 1 GPa. In contrast, **8b** shows negligible changes in the low-energy band, while the direct band gap emission also disappears at pressures >3 GPa.

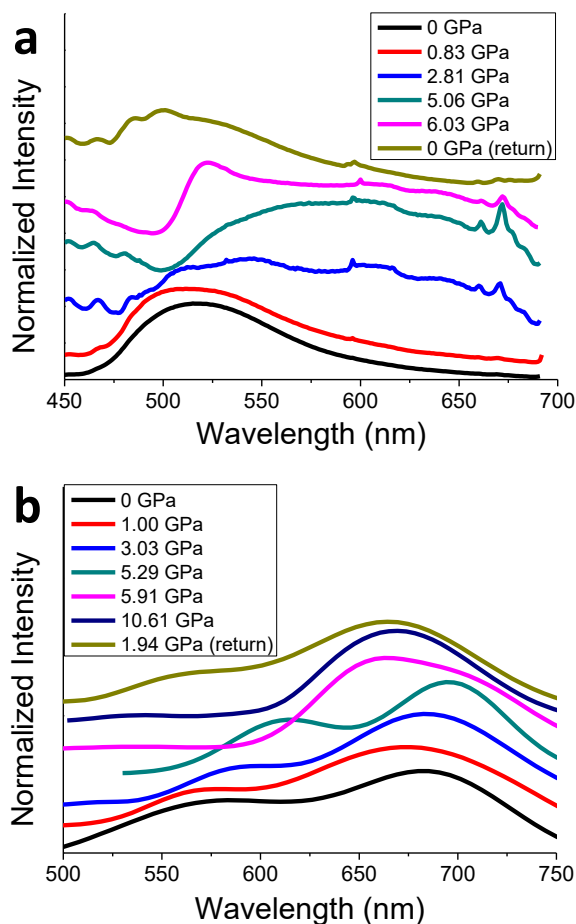


**Figure 3.12.** Mechanical dependence of the luminescence spectra of **8a** (a) and **8b** (b).  $\lambda_{\text{exc}} = 375$  nm and 300K.

In order to understand the deactivation of the direct band gap emission under pressure, we first analyze the powder X-ray diffraction patterns of the pressed pellets of **8a** after applying 5 GPa for 2 min. They show neither amorphization nor displacements of the signals with respect to the pristine crystals (**Figure C12** in appendix C). These results indicate that the changes suffered by the **8a** are reversible and only appreciable immediately after pressure is applied. Indeed, the emission is recovered after releasing the applied pressure (**Figure 3.12**). Next, we carried out the same analysis under different pressures. This allowed us to calculate the equations of state (EoS) and bulk modulus of **8a** and **8b**, indicating the degree of compressibility of these materials. Since **8a** deteriorated at low pressures, and considering the analogous behavior and identical crystal structures of **8a** and **8b**, the latter was taken as the reference for these studies. Its

bulk modulus ( $K_0 = 7.5 \pm 0.4$  GPa) is substantially smaller than the lower limit of the range expected for organometallic compounds (10-20 GPa), as a consequence of the deformability of the intermolecular interactions present in the structure. At pressures above 6 GPa a first order phase transition occurs, implying an isosymmetric transition without change of the space group. In these conditions, the bulk modulus triples its value, reaching  $K_0 = 24 \pm 2$  GPa. Therefore, after the phase transition the single crystal of **8b** loses elasticity, with reversible effects as pressure is released.

The increase of pressure induces a significant variation in some distances and angles of the structure (**Table A11 in Appendix A**). On one hand, the evolution of these parameters shows that the main changes produce a slight deformation of the Cu-I ladders. The softest distances are those of Cu...Cu interactions, being reduced significantly (up to a 7.5 % at 5.56 GPa) close to the point where the phase transition occurs. On the other hand, Cu-I bonds are stiffer. Cu-I-Cu and I-Cu-I angles along the chains also suffer important distortions, these ones lying between 3 and 4°. As usual for this kind of CPs, the layers maintain their planarity and orientation but the small displacement of the ligands over one another appears to be the cause for the changes in angles and, therefore, in the unit-cell parameters. As above mentioned, the behavior of the compound is reversible, returning to the initial distances and angles at 0 GPa. The theoretical PXRD patterns obtained at different pressures, taken from the respective SCXRD structures, allow the visualization of the variation in the diffraction peaks as a consequence of the modifications in the lattice parameters, distances and angles (**Figure 3.13**).

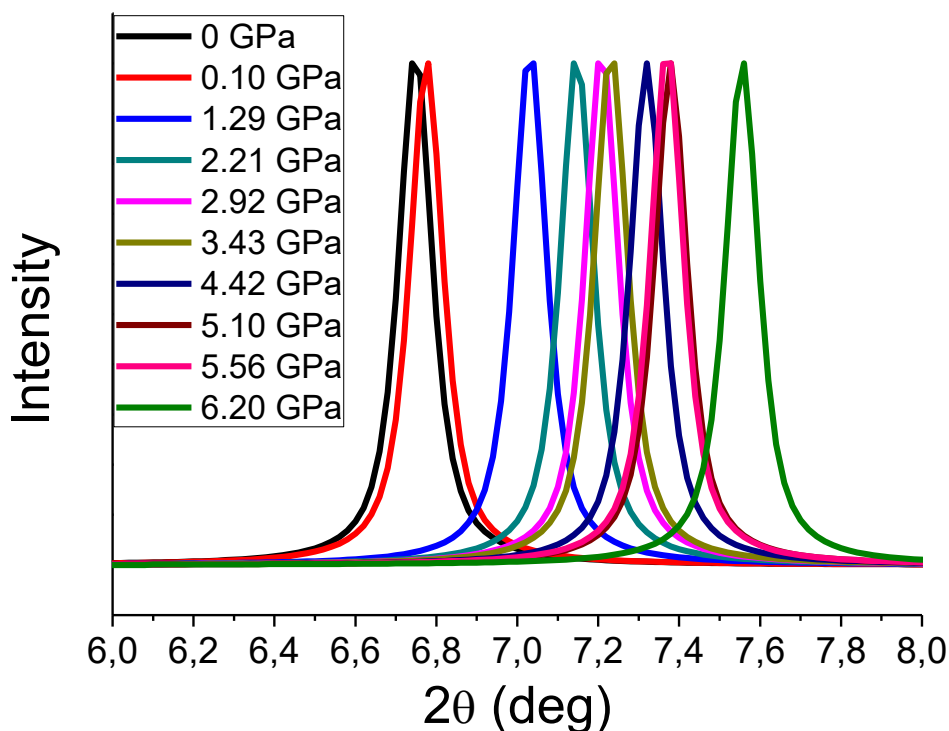


**Figure 3.13.** Theoretical PXRD of **8a** at different pressures, showing the diffraction peak corresponding to the (100) planes.

Something completely different happens above 6 GPa, after the crystal has suffered the phase transition. The shortenings of distances and the modifications in the angles are partially reverted, the asymmetry of the Cu-I changes and the structure itself becomes stiff. When pressure is raised above this point, distances and angles along the chains suffer changes almost negligible compared to those suffered at lower pressures.

Thus, the pressure dependent photoluminescence highlighted by the deactivation of the direct band emission is attributed to the above described decrease in structural network parameters involving i) a reduction of the volume of the cell in almost 20% and ii) a shortening in the Cu-I and Cu-Cu distances that produce a distortion in the angles, increasing the interligand interactions,<sup>23</sup> obtained in the single crystal XRD study at different pressures (**Table A11** in Appendix A).

Furthermore, the reversible emission behavior is in perfect agreement with the high flexibility of this type of Cu-I chains, where the small structural changes that occur when exerting pressure are usually reverted when it is stopped (see section 2.2.2.2). Indeed, this observation is not unusual, since something similar could be seen in the temperature-dependent luminescence study (**Figure 3.11**). However, it is very striking that the structural defects are not affected by both thermal and pressure stress scenarios.

### 3.2.3. Point defects: Theoretical calculations

In order to rationalize the differences observed between **8a** and **8b**, a theoretical study of the influence in their electronic structure *versus* the existence of structural defects in the Cu<sub>2</sub>I<sub>2</sub> double chains from the first-principles theoretical point of view has been carried out.

Here, we have used DFT theoretical calculations to model the pristine infinite chain (**Figure 3.14**) and different defective chain systems (**Figure 3.14 a, b and c**). This was realized on the basis of the structure obtained by X-ray diffraction experiments, and the relatively low bond energies of coordination bonds (15-50 kcal mol<sup>-1</sup>), which lead to a certain lability and in some cases kinetic reversibility of the coordination bonds.

As a proof of concept, three different point defects have been considered: the two first types of defects for representative chain fragments of three different lengths: 3, 5 and 9-units chain fragments, and the third one for a defective infinite chain.

The first type of defects consists of cutting a chain, leaving Cu<sup>+</sup> terminating atoms. Charge compensation has been realized by alternating OH<sup>-</sup> as counteranion and H<sub>2</sub>O groups (**Figure 3.14 a.3**). The second type of defect considered consists of cutting an infinite chain leaving I<sup>-</sup> terminating atoms, which, again, has been saturated to balance charge by alternating H<sup>+</sup> atoms (**Figure 3.14 a.4**). Finally, the third type of defect considered modelled on an infinite chain has been the lack of an organic ligand (with a defect density of 1/12). The Cu dangling bond after removing the ligand has been fully

relaxed and subsequently saturated by a water molecule yielding a bond-length of 2.36 Å (**Figure 3.14 a.2**). Nonetheless, among the rest of defect types, the latter seems to be the most unlikely; since a CI-NEB (climbing-image nudge elastic band) transition state calculation corresponding to the detachment of an organic ligand from the chain yields an energy barrier  $> 2.2$  eV, which turns this detachment mechanism unfeasible.

In order to check the influence of the modelled defects on the electronic properties of the compound, we have computed the density of electronic states (DOS) of the pristine infinite chain to be compared with that of the longest 9-units defective chain fragments and the defective infinite chain, normalized to the number of atoms per unit cell for a better comparison (**Figure 3.14 b.1-b.4**).

In **Figure 3.14**, the density of states shows a rich profile and yields an electronic band-gap between the valence and conduction bands (VB and CB, respectively) of around 0.9 eV (taking into account that the band gap is underestimated by 1.5 eV in the calculations, the actual value would be 2.4 eV). The pristine compound can be categorized as a narrow-gap n-type semiconductor with the Fermi energy very close to the conduction band. For the defective infinite chain with the lack of organic ligands (**Figure 3.14 a.2 and b.2**), the density of states profile remains almost unaltered with a similar band-gap and semiconducting character than that obtained for the pristine case, which indicates that, electronically, the system would not be substantially affected by this kind of defects (at least for a defect concentration of 1/12). For the 9-units defective chain fragment with the defect ( $\text{Cu}^+$  terminal) shown in **Figure 3.14 a.3 and b.3** its density of states profile has changed substantially. A direct comparison between this case and the DOS profile for the pristine infinite chain reveals the appearance of a defect state at around 0.2 eV below the Fermi energy within the mid-gap region. The new band-gap for this defective fragment is around 0.45 eV (1.95 eV after the correction). Finally, the 9-units defective chain fragment with the terminating ( $\text{I}^-$  terminal) defect shown in **Figure 3.14 (a.4, b.4)** shows a density of states profile also quite different to that of the pristine case. Again, a direct comparison between this situation and the DOS profile for the pristine infinite chain reveals a closing of the band-gap up to a value of 0.5 eV (2.0 eV after the correction), close to the obtained for the previous defective case. Thus, for these two defective cases we observe a reduction of the band-gap, although with two different origins, which will have a reflection in the optical properties of the system.

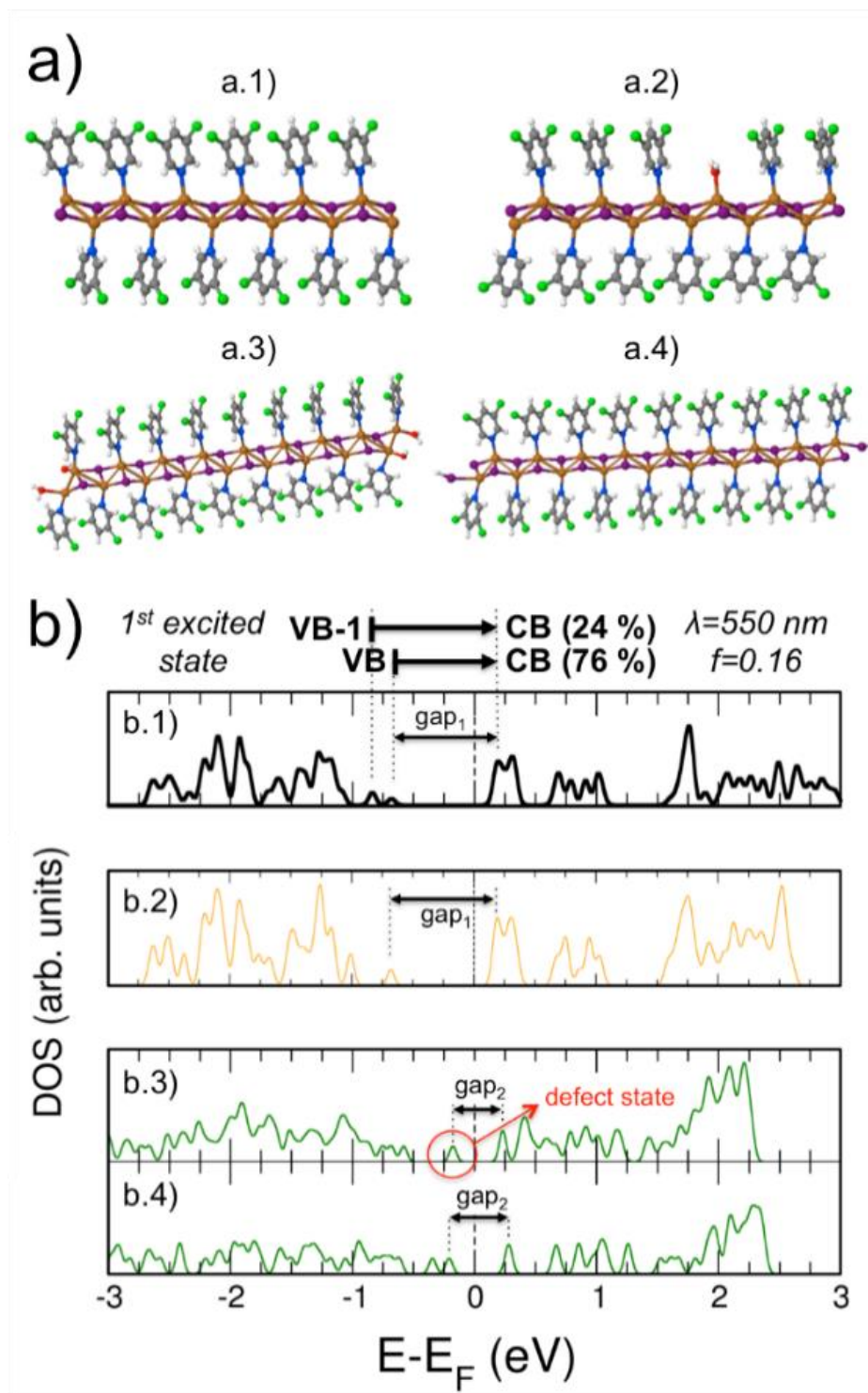


**Figure 3.14.** Computed density of states (in arb. units) as a function of the energy (referred to the Fermi energy) for: the pristine infinite chain case (a.1, b.1); an infinite defective chain with a lack of organic ligands (with a density of defects of 1/12) (a.2, b.2); 9-units defective chain fragments with two different terminating effects (a.3, a.4 and b.3 and b.4)). Electronic states involved, photon wavelength, oscillator strength and weight of the contributing transitions are shown for the most pronounced low-lying optical excitation in the infinite pristine chain. Structures are also shown for each case.



This observation can be reinforced by computing the most pronounced low-lying optical excitation for the infinite pristine chain. This computed excitation corresponds to a combination between two electronic transitions: one from VB  $\rightarrow$  CB (with a weight of around 75 %), and other from VB-1  $\rightarrow$  CB (with a weight of around 25 %) at a photon wavelength of 550 nm and with a computed oscillator strength of 0.16. Interestingly, the most important states involved in this optical transition, VB and CB, are spatially located, as usual in this kind of compounds, in the metallic skeleton and the organic ligands, respectively (**Figure 3.15**).

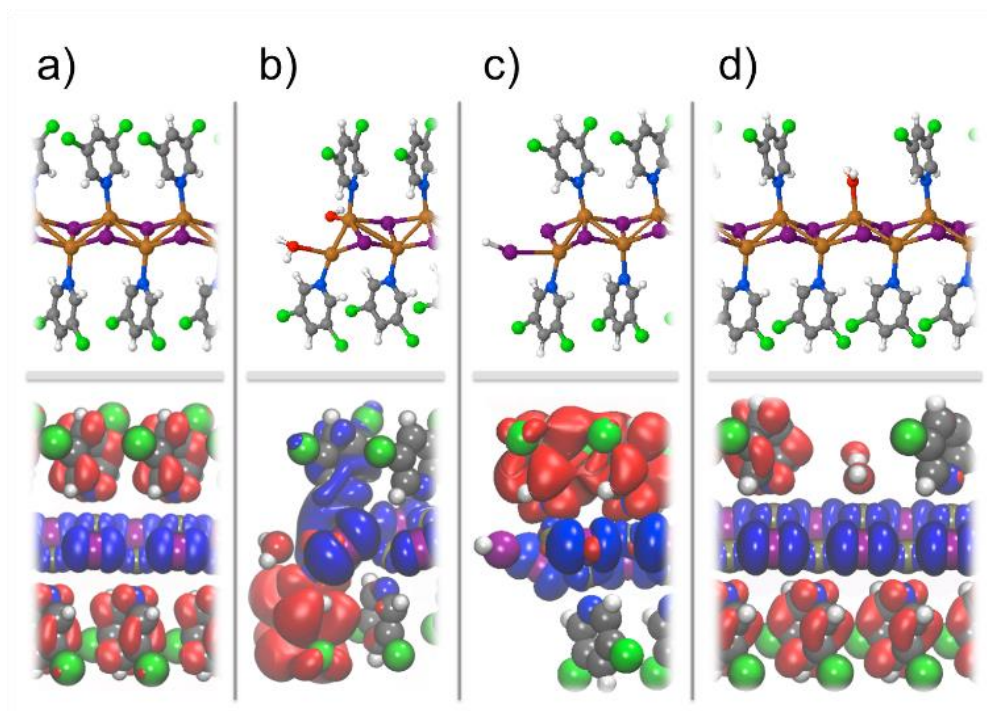


**Figure 3.15.** 3D orbital isodensities (all with a value of  $10^{-3}$  a.u.) corresponding to the valence (blue) and conduction (red) bands for: a) the pristine infinite chain case; b) and c) defective chain fragments with two different terminating effects; and d) an infinite defective chain with a lack of organic ligands with a density of defects of 1/12.

At this point, it would be interesting to check the spatial distribution of the CB and VB for the three defective chain fragments analyzed ( $\text{Cu}^+$ ,  $\text{I}^-$  terminal and remove the terminal ligand). **Figure 3.15b** shows that the spatial distribution of the new defect state appearing in the DOS profile of the defective chain  $\text{Cu}^+$  fragment is also located mostly in the skeleton chain, whilst the CB is mostly located on the ligands. This could yield similar photoexcitation efficiency as happens in the pristine case but with a red-shift in the wavelength of the main peak coming from the band-gap reduction. The same effect occurs for the defective  $\text{I}^-$  chain fragment of **Figure 3.15c**; VB and CB are once again located in the metallic chain and organic ligands, respectively. Similarly, one could expect similar photoexcitation efficiency as in the previous defective case exhibiting a similar associated red-shift in the wavelength of the main peak again coming from the



band-gap reduction. Nevertheless, no significant change in the photoexcitation efficiency is expected for the defective infinite chain of **Figure 3.15d** since their electronic properties rather vary w.r.t. the pristine case. Based on these findings one could expect a red-shift in the emission properties due to the presence of the terminating  $\text{Cu}^+$  and  $\text{I}$  defects, whilst not for the unlikely situation of lack of organic ligands. Interestingly, the almost 2<sup>nd</sup>-order electronic degeneracy observed in the conduction band for the case of the pristine infinite chain disappears as a consequence of a visible splitting into two peaks for the cases reported in **Figure 3.14**.

This could give rise to both, new absorption bands as highlighted by the color of the crystals and new photoluminescence features, that should correspond to transitions between VB-1 and VB  $\rightarrow$  CB and CB+1.

#### 3.2.4. Electrical conductivity

Conductivity measurements were carried out in order to study the sensibility change in the conductivity of **8a** and **8b** upon the exposition to acetic acid vapors. Interaction was demonstrated by the change in the conductivity of **8a** and **8b** by Electrochemical Impedance Spectroscopy (EIS).

The conductivity values  $\sigma$  ( $\text{Scm}^{-1}$ ) were determined from the Nyquist plot by arc extrapolation to the  $Z'$  real axis on the low frequency side. Each plot shows the presence of a depressed semicircular arc at high-medium frequencies (1 MHz-1 Hz), which is attributed to the bulk properties of the compound. The shapes of the Nyquist plots recorded after different exposure times for both **8a** and **8b** compounds are similar; however, the intercept of the semicircle with the  $Z'$  axis shifts towards lower  $Z'$  values with increasing exposition time (**Figure 3.16**).

Both materials present the same behavior;  $\sigma$  increases (*ca.* 3 orders of magnitude) with increasing exposition time to acetic acid vapors from starting values of  $7 \cdot 10^{-7}$  for **8a** and  $1.2 \cdot 10^{-7} \text{ S cm}^{-1}$  for **8b** ( $t = 0\text{h}$ ) respectively to values around  $1.5 \cdot 10^{-4}$  or  $8 \cdot 10^{-4} \text{ S cm}^{-1}$  for **8a** and **8b** ( $t = 24\text{h}$ ) respectively (**Figure 3.17**), and reaches saturation after *ca.* 24h of exposure. Therefore, vapors of acetic acid produce a similar effect in **8a** and **8b**.

In agreement with the Bode diagram, the semicircle representing the bulk properties of compounds shifted to higher frequencies when the acetic acid exposure time increases. This fact indicates that the material/electrode interphase capacitive character becomes less important, and the highly conductive phase of **8a** and **8b** appears. When saturated acetic acid pellets were exposed to air for longer times a poor value of conductivity was obtained. If we compare these results with the experiments involving different exposure times to Acetic acid vapor, the behavior clearly indicates the crucial role of the acetic acid molecules in establishing the conductivity pathway. In addition, there are not important differences between **8a** and **8b**.

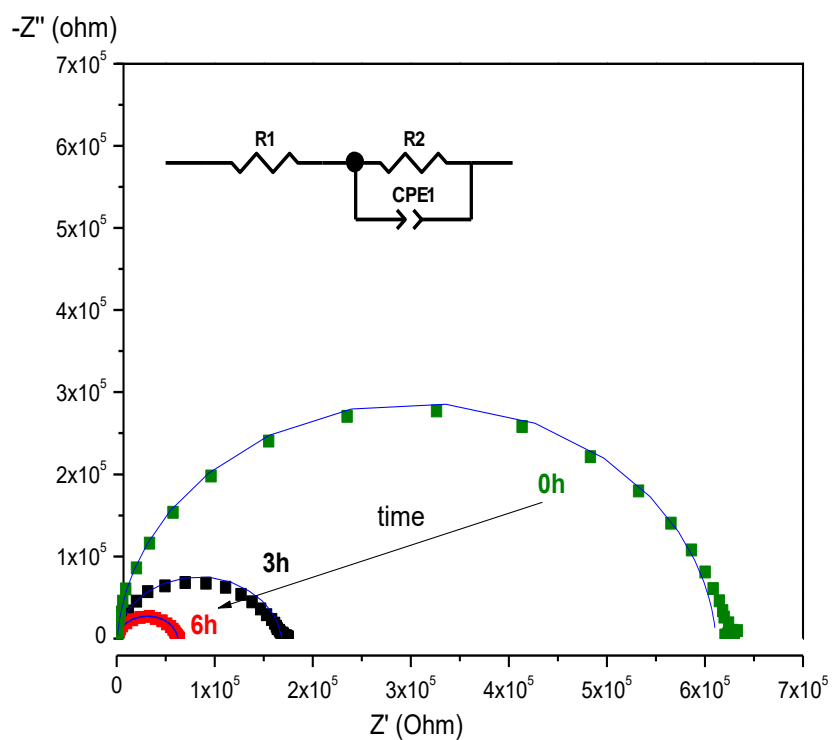


**Figure 3.16.** Nyquist plot of **8a** after 0, 3, 6 h of exposure to acetic acid vapors at 298K, with the fitting circuit: Experimental values (■), fitting values (-).

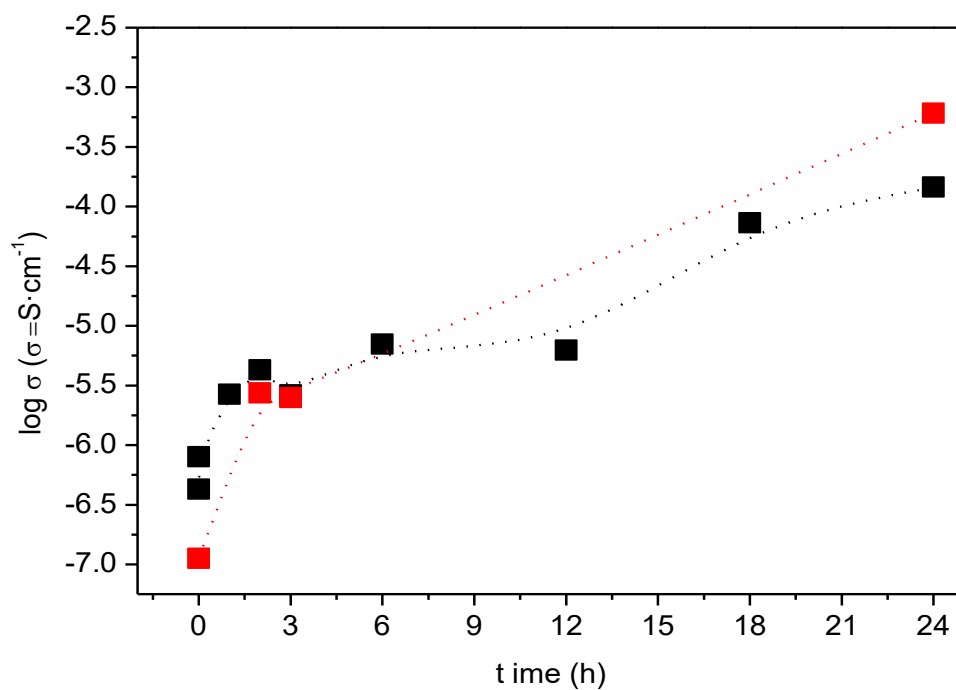


**Figure 3.17.** Electrical response of **8a** (black) and **8b** (red) with different exposition time to vapors of acetic acid.

### 3.3. Conclusions

The direct reaction between copper(I) iodide and 3,5-dichloropyridine leads to the formation of a one-dimensional CP which is analogous to those presented in chapter 2. However, the synthetic method employed in the preparation of this compound generates important variations in their luminescent properties: at room temperature we obtain the **8a** form, which presents a green emission; in solvothermal conditions the **8b** form is obtained, with an orange emission. The structural characterization does not allow the distinction of the two forms of this CP. Albeit, a DFT theoretical calculation allows demonstrating that the different behavior of the **8b** form is due to the presence of point defects along its Cu(I)-I chain.

### Conclusiones

La reacción directa entre yoduro de cobre(I) y 3,5-dicloropiridina conduce a la síntesis de un CP monodimensional análogo a aquellos presentados en el capítulo 2. Sin embargo, el método de síntesis empleado en su preparación produce importantes variaciones en sus propiedades luminiscentes: al prepararlo a temperatura ambiente se obtiene la forma **8a**, que presenta emisión verde, y en condiciones solvotermales se obtiene la forma **8b**, de emisión naranja. La caracterización estructural de ambas formas no permite diferenciarlas, pero un cálculo teórico por DFT permite demostrar la presencia de defectos puntuales en la cadena Cu(I)-I de la forma **8b**, explicando así el diferente comportamiento.

### 3.4. References

1. Callister, W. D., Jr., Imperfections in Solids. In *Fundamentals of Materials Science and Engineering*, Fifth ed.; Anderson, W., Ed. John Wiley and Sons: New York, 2001; pp 102-122.
2. Assefa, Z.; Omary, M. A.; McBurnett, B. G.; Mohamed, A. A.; Patterson, H. H.; Staples, R. J.; Fackler, J. P., Syntheses, Structure, and Photoluminescence Properties of the 1-Dimensional Chain Compounds [(TPA)<sub>2</sub>Au][Au(CN)<sub>2</sub>] and (TPA)AuCl (TPA = 1,3,5-Triaza-7-phosphaadamantane). *Inorganic Chemistry* **2002**, *41* (24), 6274-6280.
3. Qi, Y.; Xu, H.; Li, X.; Tu, B.; Pang, Q.; Lin, X.; Ning, E.; Li, Q., Structure Transformation of a Luminescent Pillared-Layer Metal–Organic Framework Caused by Point Defects Accumulation. *Chemistry of Materials* **2018**, *30* (15), 5478-5484.
4. Fang, Z.; Bueken, B.; De Vos, D. E.; Fischer, R. A., Defect-Engineered Metal–Organic Frameworks. *Angewandte Chemie International Edition* **2015**, *54* (25), 7234-7254.

5. Hernandez, W. Y.; Centeno, M. A.; Romero-Sarria, F.; Odriozola, J. A., Synthesis and Characterization of  $\text{Ce}_{1-x}\text{Eu}_x\text{O}_{2-x/2}$  Mixed Oxides and Their Catalytic Activities for CO Oxidation. *J. Phys. Chem. C* **2009**, *113* (14), 5629-5635.
6. Bispo, A. G., Jr.; Ceccato, D. A.; Lima, S. A. M.; Pires, A. M., Red phosphor based on  $\text{Eu}^{3+}$ -isoelectronically doped  $\text{Ba}_2\text{SiO}_4$  obtained via sol-gel route for solid state lighting. *Rsc Advances* **2017**, *7* (85), 53752-53762.
7. Byzynski, G.; Ribeiro, C.; Longo, E., Blue to Yellow Photoluminescence Emission and Photocatalytic Activity of Nitrogen Doping in  $\text{TiO}_2$  Powders. *International Journal of Photoenergy* **2015**.
8. Ahn, T.-S.; Müller, A. M.; Al-Kaysi, R. O.; Spano, F. C.; Norton, J. E.; Beljonne, D.; Brédas, J.-L.; Bardeen, C. J., Experimental and theoretical study of temperature dependent exciton delocalization and relaxation in anthracene thin films. *The Journal of Chemical Physics* **2008**, *128* (5), 054505.
9. Wang, Y.; Ma, Y., Perspective: Crystal structure prediction at high pressures. *The Journal of Chemical Physics* **2014**, *140* (4), 040901.
10. McAnally, R. E.; Bender, J. A.; Estergreen, L.; Haiges, R.; Bradforth, S. E.; Dawlaty, J. M.; Roberts, S. T.; Rury, A. S., Defects Cause Subgap Luminescence from a Crystalline Tetracene Derivative. *The Journal of Physical Chemistry Letters* **2017**, *8* (24), 5993-6001.
11. Fusella, M. A.; Schreiber, F.; Abbasi, K.; Kim, J. J.; Briseno, A. L.; Rand, B. P., Homoepitaxy of Crystalline Rubrene Thin Films. *Nano Letters* **2017**, *17* (5), 3040-3046.
12. Wang, W.; Wang, L.; Zhou, Q., Effect of solvents on morphologies of PbTe nanostructures: Controllable synthesis of hollow and solid PbTe nanocubes by a solvothermal method. *Journal of Solid State Chemistry* **2012**, *188*, 72-76.
13. Kanmani, S. S.; Ramachandran, K., Role of aqueous ammonia on the growth of ZnO nanostructures and its influence on solid-state dye sensitized solar cells. *Journal of Materials Science* **2013**, *48* (5), 2076-2091.
14. Xia, X.; Xie, S.; Liu, M.; Peng, H.-C.; Lu, N.; Wang, J.; Kim, M. J.; Xia, Y., On the role of surface diffusion in determining the shape or morphology of noble-metal nanocrystals. *Proceedings of the National Academy of Sciences of the United States of America* **2013**, *110* (17), 6669-6673.
15. Kiprotich, S.; Onani, M. O.; Dejene, F. B., Effect of growth temperature on the structural, optical and luminescence properties of cadmium telluride nanoparticles. *Journal of Materials Science: Materials in Electronics* **2018**, *29* (7), 6004-6011.
16. Ray, S.; Nair, G. B.; Tadge, P.; Malvia, N.; Rajput, V.; Chopra, V.; Dhoble, S. J., Size and shape-tailored hydrothermal synthesis and characterization of nanocrystalline  $\text{LaPO}_4:\text{Eu}^{3+}$  phosphor. *Journal of Luminescence* **2018**, *194*, 64-71.

17. Ares, P.; Amo-Ochoa, P.; Soler, J. M.; Jose Palacios, J.; Gomez-Herrero, J.; Zamora, F., High Electrical Conductivity of Single Metal-Organic Chains. *Advanced Materials* **2018**, *30* (21), 1705645.
18. Song, Y.; Fan, R.; Wang, P.; Wang, X.; Gao, S.; Du, X.; Yang, Y.; Luan, T., Copper(i)-iodide based coordination polymers: bifunctional properties related to thermochromism and PMMA-doped polymer film materials. *Journal of Materials Chemistry C* **2015**, *3* (24), 6249-6259.
19. Li, J.-C.; Li, H.-X.; Li, H.-Y.; Gong, W.-J.; Lang, J.-P., Ligand Coordination Site-Directed Assembly of Copper(I) Iodide Complexes of ((Pyridyl)-1-pyrazolyl)pyridine. *Crystal Growth & Design* **2016**, *16* (3), 1617-1625.
20. Li, Y.; Wang, Q.; Liu, P.; Yang, X.; Du, G.; Liu, Y., Facile synthesis and capacitive performance of Cu@Cu<sub>2</sub>O/graphene nanocomposites. *Ceramics International* **2015**, *41* (3, Part A), 4248-4253.
21. Battistoni, C.; Mattogno, G.; Paparazzo, E.; Naldini, L., An XPS and Auger study of some polynuclear copper compounds. *Inorganica Chimica Acta* **1985**, *102* (1), 1-3.
22. Moretti, G.; Filippone, F.; Satta, M., Use of Auger parameter and Wagner plot in the characterization of Cu-ZSM-5 catalysts. *Surface and Interface Analysis* **2001**, *31* (4), 249-254.
23. Benito, Q.; Baptiste, B.; Polian, A.; Delbes, L.; Martinelli, L.; Gacoin, T.; Boilot, J. P.; Perruchas, S., Pressure Control of Cuprophilic Interactions in a Luminescent Mechanochromic Copper Cluster. *Inorganic Chemistry* **2015**, *54* (20), 9821-9825.

## **Chapter 4. Smart composite films based on Cu(I)-I CPs**

## 4.1. Introduction to composite materials and mixed-matrix membranes (MMMs)

Despite their outstanding properties and the easy way to be generated as nanostructures, Cu(I)-I coordination polymers do not present the mechanical properties needed to be used in certain applications. Therefore, their use as raw materials at the industrial scale is very limited. A solution which has been presented to face this disadvantage is to use them as dopants in composite materials.

Composite materials, also called hybrid materials, are conformed by a mixture of two components: a matrix, which is the majoritarian one and the responsible of the shape of the final material (and, usually, of its mechanical properties), and a dopant, which includes an extra property which is desired. For example, in reinforced concrete the matrix would be the cement, whereas the dopants are iron bars which enhance the mechanical properties of the material. Functional composites usually include a dopant which adds other features to the material, usually electronic properties such as those of quantum dots (QD).<sup>1</sup>

In the case of hybrid materials including CPs, these would act as dopants, while the chosen matrices are organic polymers; the resulting composites are known as mixed-matrix membranes (MMM). The advantages of organic matrices over glasses are their flexibility and an easier way to process them (even in extrusion processes these polymers do not need temperatures higher than 180 °C); this, apart from the good optical quality (including transparency and a high refractive index) shown by some of them, makes them great candidates to be used. For instance, two popular matrices which are normally used to create composite materials including coordination compounds are polymethyl methacrylate (PMMA) and polyvinylidene difluoride (PVDF). The former, despite its rigidity, shows great transparency; this turned it into the most popular matrix used to engulf some CPs containing d<sup>10</sup> metals, especially Cu(I).<sup>2-3</sup> Moreover, the high refractive index of PMMA allows it to be used as optical fiber devices and amplifiers and optical glasses.<sup>2</sup>

In the case of PVDF, it shows a great flexibility and deformability, therefore increasing the durability of the manufactured devices. These advantages prompted its use in the last five years, due to the possibilities of using it as plastic coverages, *e.g.* for farms. Other flexible polymers used as matrices for the preparation of MMMs are polylactic acid (PLA), a biopolymer with high biocompatibility and biodegradability, polyimide-based polymers<sup>4</sup> and polyethyl-vinyl-acetate (EVA). The first attempt to prepare flexible MMMs was published in 2015 by Rodenas *et al.*,<sup>4</sup> and it consisted of nanosheets of the two-dimensional MOF [Cu(BDC)]<sub>n</sub> (BDC = 1,4-benzenedicarboxylate, terephthalate) implemented inside a polyimide-based organic polymer in weight ratios between 2 and 12%. The resulting materials showed the same adsorption properties than the pristine MOF, due to the homogeneous distribution of the CP along the matrix and the higher surface area exposed to the gas. In a similar way, Denny *et al.*<sup>5</sup> prepared a series of MMMs starting from several MOFs and PVDF,

obtaining flexible materials which retained the original properties (adsorption and mechanical properties) of both dopant and matrix (**Figure 4.1**).

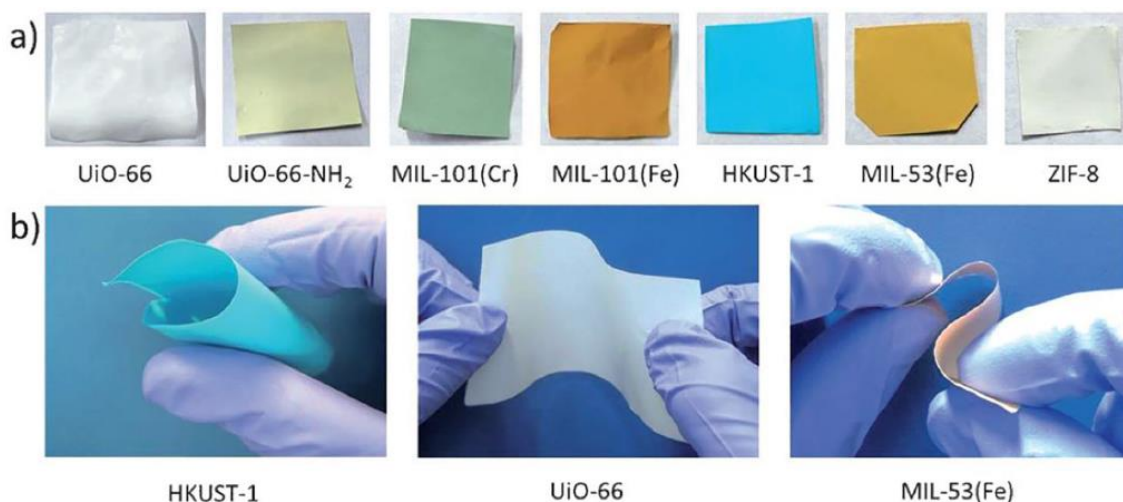


**Figure 4.1.** a) Free-standing MMMs ( $1 \times 1 \text{ cm}^2$ ) produced from a variety of MOFs embedded in PVDF. b) Photographs demonstrating that large area MMMs containing HKUST-1, UiO-66, and MIL-53 (Fe) ( $3 \times 5 \text{ cm}^2$ ) are resilient to mechanical stress and can be easily handled. Taken from reference <sup>5</sup>.

Focusing on luminescent composites, the main drawbacks of rare earth containing MMMs are the high dopant concentration and the single luminous color, apart from the high cost of the raw materials needed to prepare the coordination complexes. This is why the use of d<sup>10</sup> metals, more common in the Earth's crust and cheaper, has become of widespread interest to prepare CPs which can be used as dopants for MMMs. Furthermore, the easy nanoprocessability of these CPs (see chapter 2) offers the possibility to manufacture thin films of these composites, with thicknesses of microns or even in the nanoscale. A recent example, published by Troyano *et al.*,<sup>6</sup> consists of nanosheets of two CPs based on Cu(I) and sulfur-donor ligands, which were used to prepare flexible and homogeneous films of MMMs, with thicknesses ranging from 35 to 75  $\mu\text{m}$  (**Figure 4.2**). The process to prepare these MMMs was very simple: a solution of PVDF which contained the desired CP in suspension was treated in an ultrasound bath to favor the dispersion of both components; afterwards, the suspensions were deposited on flat glass surfaces by drop-casting and the solvent was evaporated at 85 °C.



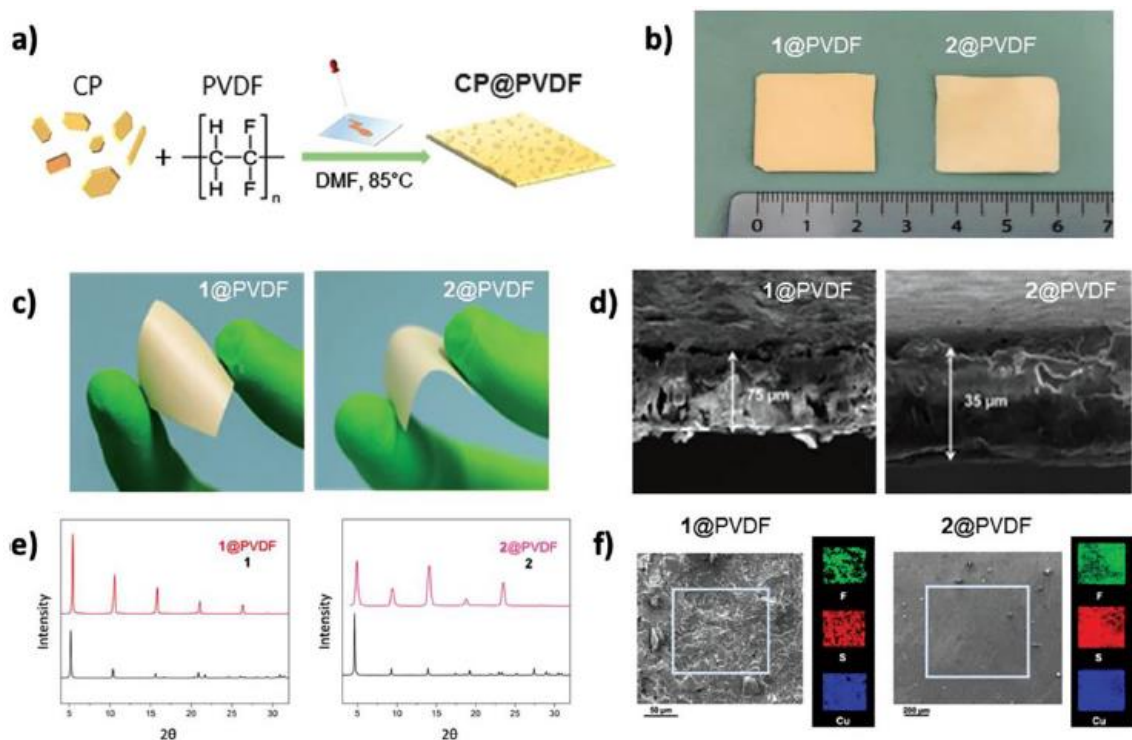


**Figure 4.2.** a) Schematic diagram of the fabrication of **CP@PVDF** composites via drop casting. b) Picture of as-prepared **1@PVDF** and **2@PVDF** thin films with 50% (w/w) of **1** and **2**, respectively. c) Pictures of **1@PVDF** and **2@PVDF** thin films showing their flexibility. d) Cross-section FE-SEM images of **1@PVDF** and **2@PVDF** thin films. e) PXRD patterns of **1@PVDF** (left) and **2@PVDF** (right) compared to the corresponding polycrystalline solids. f) SEM-EDX elemental mapping images of the outward facing surfaces of **1@PVDF** (left) and **2@PVDF** (right), showing the homogeneous distribution of fluorine (green), sulfur (red), and copper (blue). **1** =  $[\text{Cu}(\text{CT})]_n$ , where CT = 4-carboxylthiophenolate; **2** =  $[\text{Cu}(\text{MCT})]_n$ , where MCT = 4-methoxycarbonylthiophenolate.<sup>6</sup>

## 4.2. Results and discussion

### 4.2.1. Preparation of MMMs of different thicknesses

The outstanding optical sensing properties of compounds **5** and **6**, as well as the mechanical properties of polyvinylidene difluoride (PVDF) and polylactic acid (PLA), prompted us to produce composites of potential interest for the fabrication of new devices. In particular, the production of thin films is of potential interest towards applications. However, the preparation of film composites of nanometric thickness is hampered by the size of the integrated materials. Thus, composites with CPs have been limited to the bulk scale<sup>5, 7-10</sup> because of their macroscopic dimensions. Following this basis, we have very recently demonstrated that the nanoscale production of CP nanolayers enables us to produce composites of submicrometric thickness. As **5** and **6** consist of nanostructures (nanofibers and nanosheets, respectively), they are excellent

candidates for thin-film fabrication. Additionally, **5** shows the ability to reversibly dissolve and recrystallize from a DMF solution and **6** is able to form stable colloids in chloroform under ultrasound conditions. This feature has been still little explored but, as we previously demonstrated, it is very useful for the fabrication of CP-based nanomaterials.<sup>11-12</sup> However, it has never been used for composite thin-film preparation.

Thus, following the first strategy, a dispersion of nanofibers of **5** in DMF has been prepared at over-saturated concentrations (leading to final concentrations of 15 and 30 % w/w of **5** in the PVDF matrix). Alternatively, a bottom-up strategy based on in situ fibers of **5** formed from a DMF solution of **5** with PVDF, in a final concentration of 4% w/w in the matrix, was tested. For both approaches, the thin-film composites were prepared either by drop-casting (**Figure 4.3**), dip-coating or spin-coating on different substrates (**Figure 4.5**), and the solvent was eliminated upon soft heating. The so-formed composite-films **5@PVDF** were fully morphologically and structurally characterized (**Figures 4.3-4.5**). IR and PXRD data confirm that the original structure of **5** is retained after the composite formation process in all the cases (**Figures 4.3e** and **C13** in appendix C).

Additionally, AFM, SEM and EDX analyses confirm the formation of highly homogeneous films with thicknesses ranging from 40 nm for the drop-casting method, to thicknesses between 25 and 60 nm for the films prepared by dip-coating or spin-coating (**Figures 4.3c-d, 4.4, 4.5c-d**). The AFM measurements confirmed that, independently from the concentration of **5** in the film composites, those prepared by spin or dip-coating show a roughness of 20-60 nm, likely due to the intrinsic morphology of PVDF, while, for the films prepared by drop-casting, the roughness rises up to 40 nm, without significant differences between concentrations. Therefore, the most significant effect on the thickness of the film composite depends on the method used for its fabrication. Thus, just spin- and dip-coating methods allow us to form **5@PVDF** films of nanometric thicknesses. It is also worth mentioning that the **5** nano-structuration procedure does not significantly affect the **5@PVDF** thin-film formation. This is understandable because the low dimensions of **5** fibers produced are significantly smaller than the thickness of the **5@PVDF** thin-film formed. The **5@PVDF** films show both good elasticity and flexibility.

The process followed to prepare **6@PLA** composite films is very similar to that followed for **5@PVDF**. The process to obtain the composite materials involves dissolving the PLA in chloroform, the addition of **6** (1, 4, and 30 w/w %) and the sonication of the suspensions to form a homogeneous colloid (**Figure 4.6**) which upon slow solvent evaporation gives rise to the formation of flexible films of composite materials. The analytical, diffractometric, and spectroscopic analyses confirm the integration of **6** in the PLA matrix without alteration of its structure and composition (**Figure C14** in Appendix C). The obtained films are extremely flexible, and their transparency depends on the concentration of **6**: **6@PLA** films with 1% w/w of **6** are translucent, films with 4% w/w of **6** are almost opaque, and films with 30% w/w are fully opaque (**Figure 4.7**).

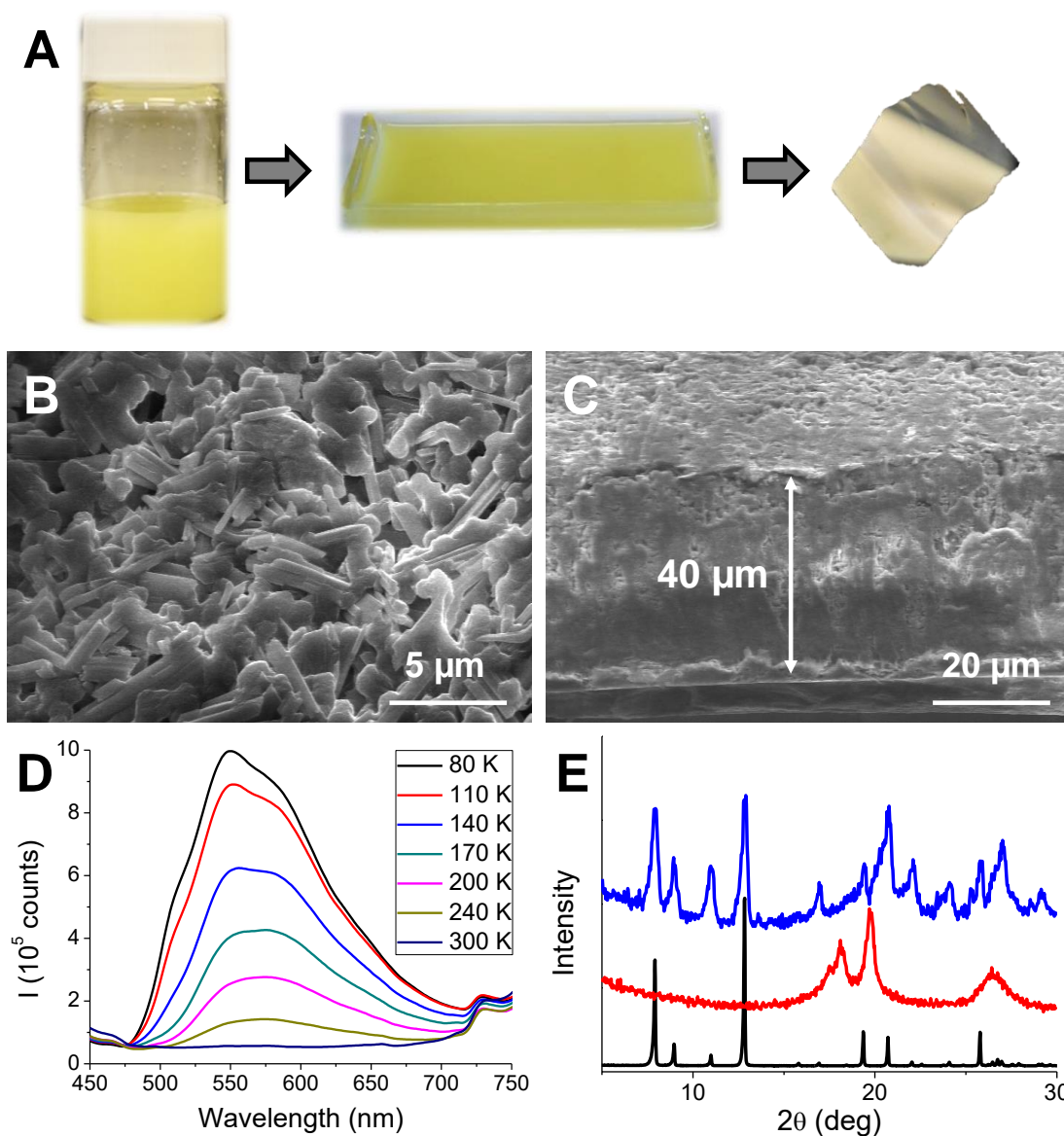


**Figure 4.3.** (a) Scheme of the slow-evaporation synthesis (DMF suspension) of the **5@PVDF** hybrid materials. (b, c) SEM images of the **5@PVDF** film, with 30 % w/w of **5**. (d) Luminescence spectra of the **5@PVDF** film, with 30% w/w of **5**, at several temperatures ( $\lambda_{\text{exc}} = 375$  nm). (e) PXRD patterns of **5** (black), PVDF (red) and the **5@PVDF** film, with 30 % w/w of **5** (blue).

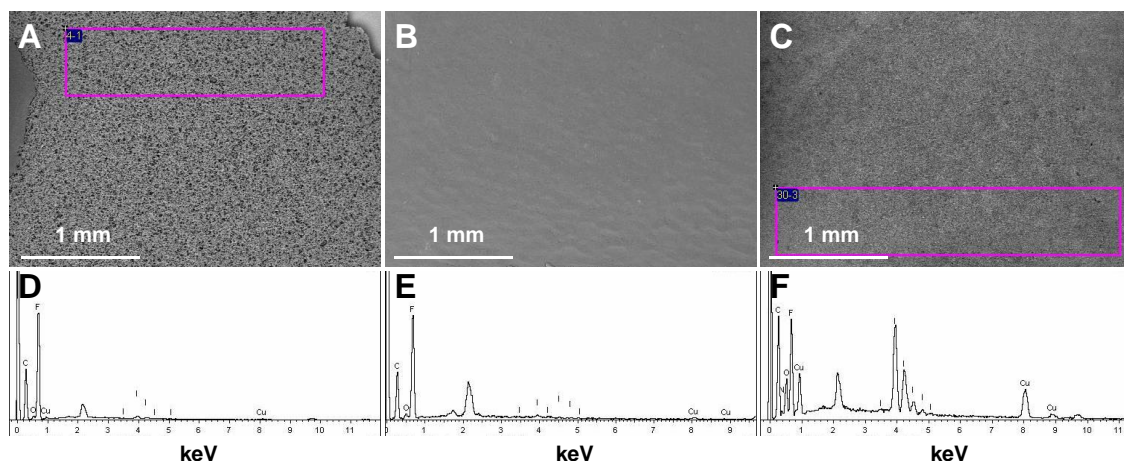


**Figure 4.4.** (a-c) Backscattered electrons SEM images of the **5@PVDF** films with 4% (a), 15% (b) and 30% w/w of **5** (c) prepared by drop-casting. (d-f) EDX analysis of the same **5@PVDF** films with 4% (d), 15% (c) and 30% w/w of **5** (f). The analyses confirm that the Cu/I proportion is always 1:1.

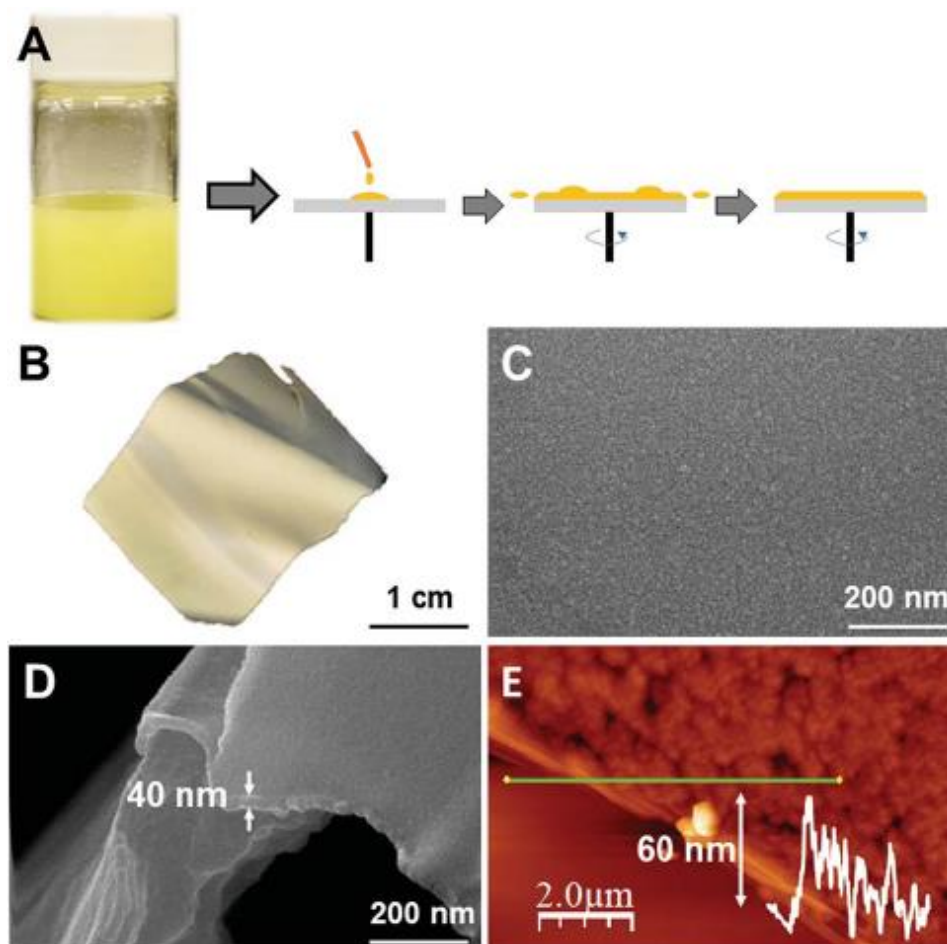


**Figure 4.5.** (a) Scheme of the spin-coating synthesis of the **5@PVDF** composite. (b) Photography of a  $2 \times 2$  cm **5@PVDF** thin-film. (c and d) SEM images of the **5@PVDF** thin-film with 4% w/w of **5**. (e) AFM image of the **5@PVDF** thin film with 4% w/w of **5**, and its height profile across the line.



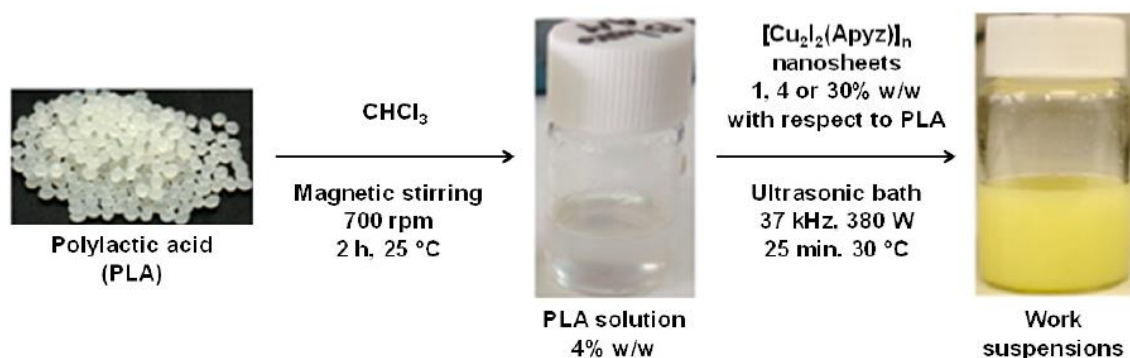


**Figure 4.6.** Scheme of the process that leads to the obtainment of homogeneous suspensions of **6@PLA**.

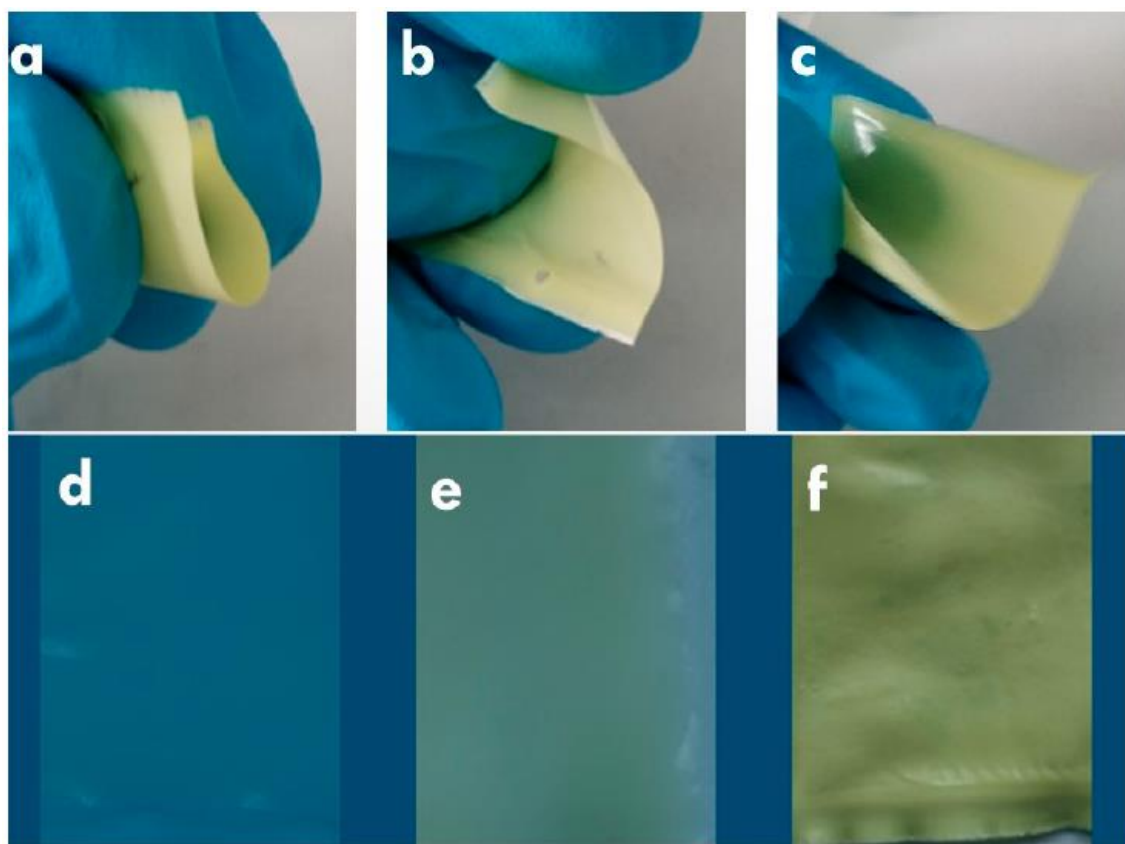


**Figure 4.7.** Flexibility of **6@PLA-30%** (a,b,c) and degree of visual transparency of the **6@PLA -1%** (d), **6@PLA-4%** (e) and **6@PLA-30%** (f).

The homogeneity of the nanosheets of **6** dispersed in the PLA matrix has been studied by FE-SEM (**Figure 4.8**) and SEM-EDX (**Figure 4.9**). High resolution SEM images give a first approximation of the high homogeneity of the **6@PLA** (1%, 4%, and 30%) films, showing surfaces with low roughness ( $R_a$  (mean arithmetic roughness) = 0.24, 0.23, and 0.20  $\mu\text{m}$  and  $R_q$  (mean square roughness) = 0.31, 0.34, 0.29  $\mu\text{m}$ , respectively); moreover, the CP is well dispersed within the matrix, with no fibers poking out of it. In addition to this, the SEM-EDX data confirm both the homogeneity of the samples and the 1:1 proportion between copper and iodine in the composites.

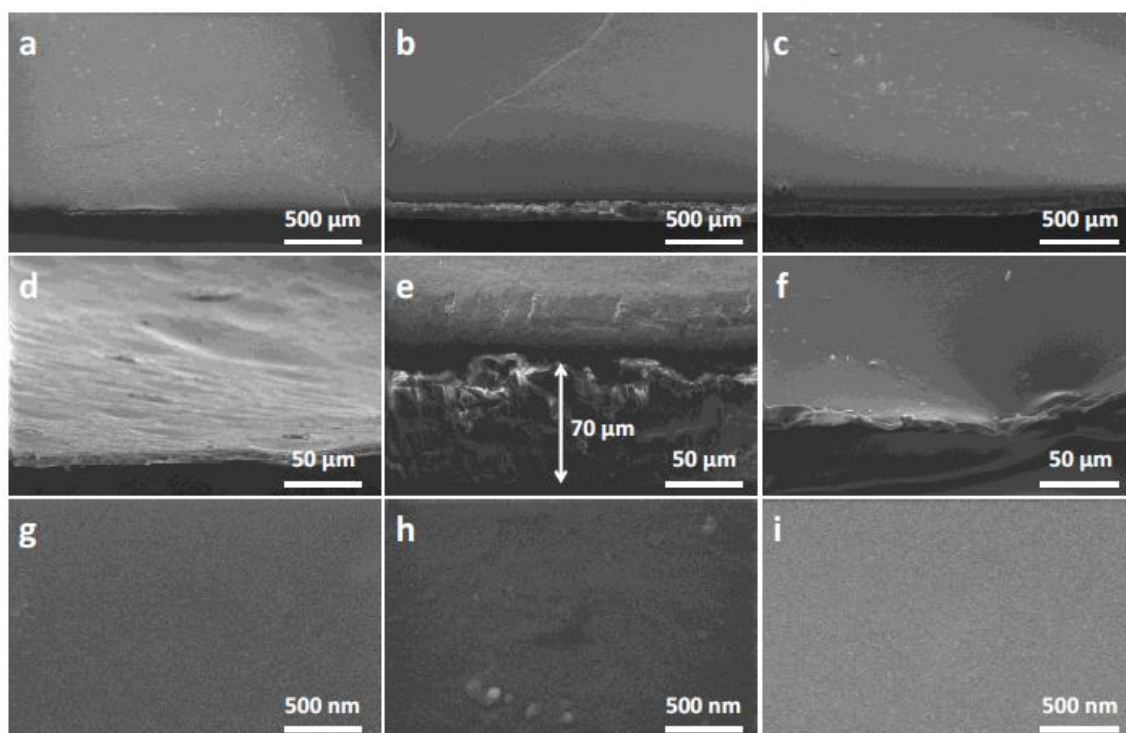


**Figure 4.8.** FE-SEM images of the **6@PLA** thin films with 1% w/w (a, d, g), 4% w/w (b, e, h) and 30% w/w of **6** (c, f, i) prepared by drop casting of the corresponding suspension.

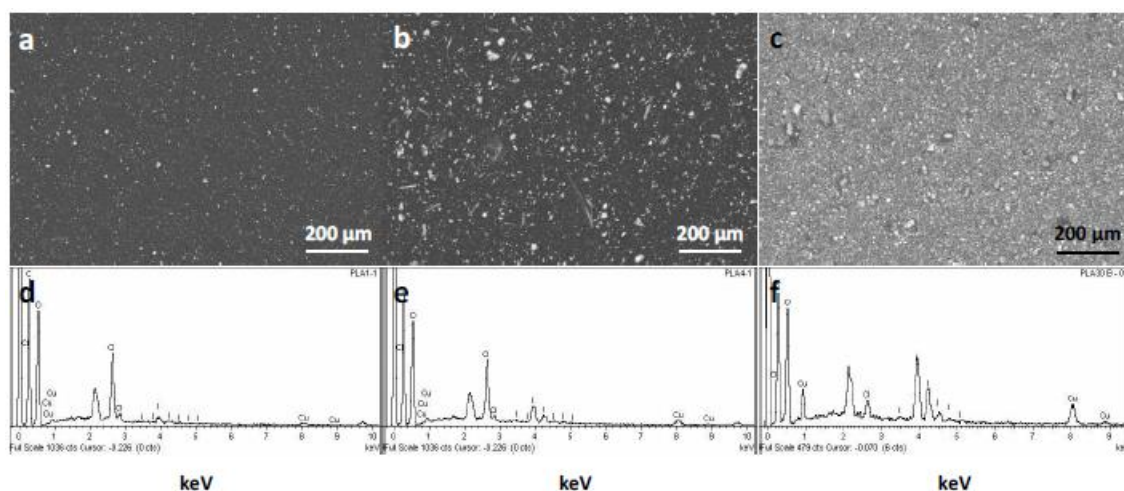


**Figure 4.9.** (a-c) Backscattered electrons SEM images of the **6@PLA** thin films with 1% w/w (a), 4% w/w (b) and 30% w/w of **6** (c) prepared by drop casting of the corresponding suspension. (d-f) EDX analyses of the same **6@PLA** thin films with 1% w/w (d), 4% w/w (e) and 30% w/w of **6** (f).

Once again, the thickness of film-composites can be controlled by changing the deposition method, from few microns for films prepared by drop-casting (**Figure 4.10a,d**) to few tens of nanometers for thin films generated by spin-coating or dip-coating (**Figure 4.10b-c,e-h**).

The thicknesses of the films have been studied by means of scanning electron microscopy (SEM) and atomic force microscopy (AFM) (**Figure 4.10**). When the composite material is generated by drop-casting, the SEM images of the films supported on SiO<sub>2</sub> show lateral thicknesses between 25 and 70 microns (**Figure 4.10d**). However, the thicknesses of the films obtained by spin coating or deep coating observed by AFM show heights between 20 and 40 nanometers (**Figure 4.10e-h**).

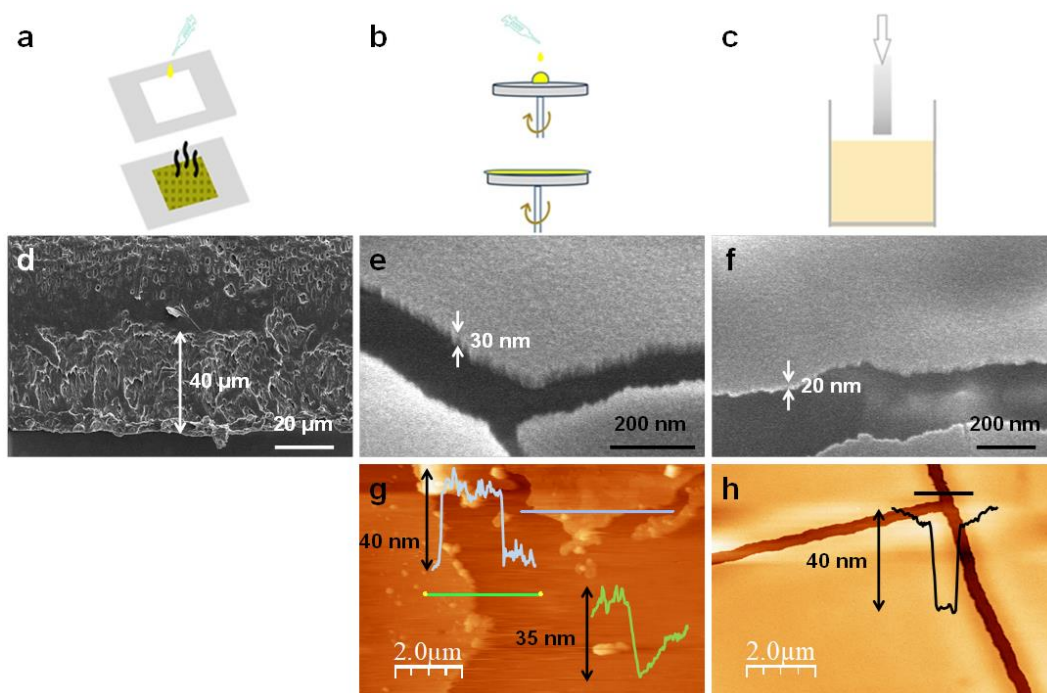


**Figure 4.10.** (a-c) Scheme of the deposition methods used to get **6@PLA** thin films: (a) Drop casting, (b) spin coating, (c) dip coating. (d) FE-SEM image of the **6@PLA** film with 30% w/w of **6** obtained using drop-casting as deposition method. (e,g) FE-SEM (e) and AFM (g) images of the **6@PLA** thin film with 30% w/w of **6** obtained using spin-coating as deposition method. (f,h) FE-SEM (f) and AFM (h) images of the **6@PLA** thin film with 30% w/w of **6** obtained using dip-coating as deposition method.

The thicknesses of the films prepared via drop-casting appear in the ranges reported for similar hybrid materials, also known as mixed-matrix membranes (MMMs). Usually, the thicknesses reported for MMMs fall in the range between 35 to 100 microns.<sup>5-6</sup> On the other hand, the use of spin-coating has allowed the preparation of thin-films in which the thicknesses can be controlled with the centrifugation speed up to few nanometers. At smooth speeds, the resulting films can have thicknesses of 50 to 100 microns if the rotation speed is low,<sup>13-14</sup> or in the rank between 300 and 470 nm at speeds up to 800 rpm.<sup>15</sup> However, at higher spinning rates (17000 rpm) we have been able to obtain films with nanometric thicknesses (under 100 nm).

#### 4.2.2. Luminescent response to temperature and pressure

The spectroscopic characterization of **5@PVDF** composites shows that the optical bulk properties of compound **5** are retained in the composite films showing weak yellow emission (571 nm at 298 K,  $\lambda_{\text{exc}} = 400$  nm) that is enhanced upon lowering the temperature (549 and 580 nm at 80 K,  $\lambda_{\text{exc}} = 400$  nm) with a similar lifetime, 1.42 ms, to that observed for **5** (**Figure 4.11**). Additionally, the emission spectra of **5@PVDF** materials excited at 375 nm have also been measured at ambient and high pressures (**Figure 4.12**). The main difference found between **5@PVDF** and **5** is the presence of a high energy (HE) band at ca. 435 nm. In particular, the emission of the 4% w/w **5@PVDF** sample consists of a single asymmetric band that can be de-convoluted into three components, two HE (424 nm and 454 nm) ones with a strong contribution and a weak LE (510 nm) contribution. However, for 15 and 30% w/w **5@PVDF** samples the spectra can be clearly divided into two different bands, one HE (435 nm) and one LE (577 nm and 558 nm), respectively. Unfortunately, due to the band overlapping with the diamond emission of the DAC, because of the UV excitation in 375 nm, and the HE emissions in the UV of the samples, it is not possible to resolve these bands for high pressures and, therefore, we can only focus on the pressure evolution of the LE emission bands. Thus, in the 4% w/w **5@PVDF** sample regarding the LE component of the band (510 nm), it remains almost constant in wavelength from 0 to 10 GPa, as well as the integrated intensities. On the other hand, the behavior of 15 and 30% w/w **5@PVDF** is similar to that observed for **5**, thereby showing different tendencies. Hence, in both samples the intensity gradually decreases by around 80% with the pressure at 5 GPa compared to their values at 0 GPa, and a red-shift of the LE emission bands is also noticeable. However, in 15% w/w **5@PVDF** this red-shift is linear with a slope of around  $330 \text{ cm}^{-1}$  per GPa, whereas a more complicated behavior is observed for 30% w/w **5@PVDF**, in which from 2 to 4.7 GPa the red-shift can be considered as linear (ca.  $326 \text{ cm}^{-1}$  per GPa). Therefore, a different origin for the transition observed for the 4% w/w **5@PVDF** sample with respect to 15 and 30% w/w **5@PVDF** samples is expected. Analyzing the pressure induced spectral behavior of the hybrid samples, some conclusions can be extracted; focusing only on the LE band of the 4% w/w **5@PVDF** sample, cuprophilic interaction ( $^3\text{MMC}$ ) can be disregarded due to the absence of a red shift in the emission band; however, in the other two samples 15 and 30% w/w **5@PVDF**, different behaviors are observed showing red-shifts with different rates and quenching of the emission, similar to those considered for compound **5**.



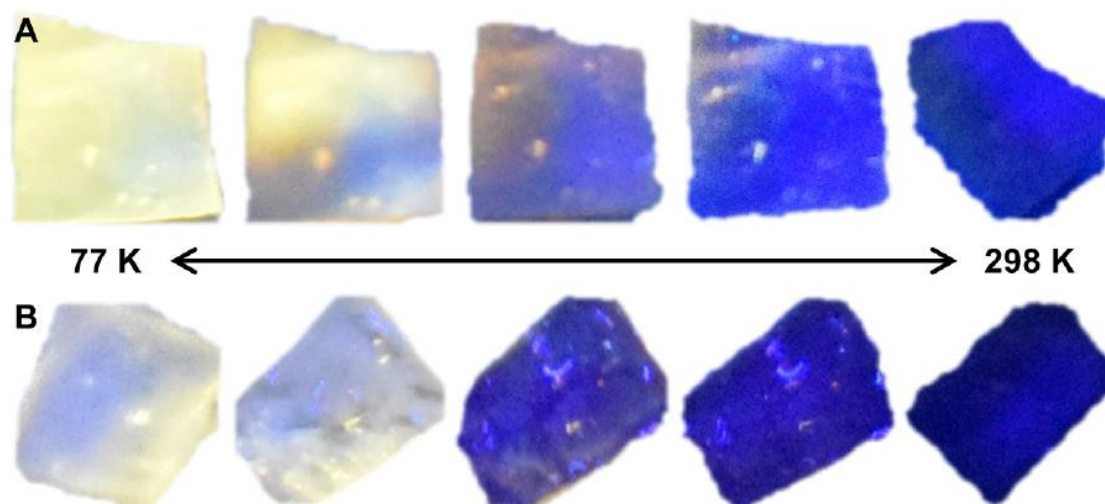


**Figure 4.11.** Thermoluminescent behavior of **5@PVDF** thin film with 30 % w/w of **5** before (a) and after applying a 5 GPa pressure (b).  $\lambda_{\text{exc}} = 312 \text{ nm}$ .

The same studies were carried out for **6@PLA** composites. **Figure 4.13** shows the luminescence spectra of **6@PLA** films (**Figure 4.13b**) and the pristine **6** (**Figure 4.13a**) with the temperature. We can observe that, while no significant changes in the emission bands are showed between the film composites and the pristine CP, the emission intensities of the **6@PLA** films decrease. As an example, **6@PLA** 30% w/w film and **6** show a very weak band emission centered at 630 nm at 300 K, which increases in intensity upon lowering the temperature (30 times higher from 300 to 100 K), and both materials show a progressive blue-shift. Since naked PLA does not show emission, the emission bands observed for the composites arise from metal-halide skeleton to ligand charge transfer triplet states ( $^3(\text{M}+\text{X})\text{LCT}$ ) of the CP. Therefore, these observations corroborate the potential use of the **6@PLA** thin-films as temperature sensors.

Additionally, since the emission of **6** is very sensitive to the pressure, we have studied the variations of the **6@PLA** thin-films' emission with the pressure. It would be expected that **6@PLA** composite films displayed mechanical response as well as the thermal one. However, it has been found that the PLA matrix absorbs the effect of pressure. This has been observed in a naked-eye experiment where **6@PLA** films with the studied concentrations of **6** were compressed at pressures up to 6 GPa. Whereas the naked **6** would have lost its luminescence at 77 K, the hybrid materials kept their previous luminescent behavior. Although this fact rules out the possibility to use our composite as pressure sensors, they reveal the high resistance to impacts that these materials display.

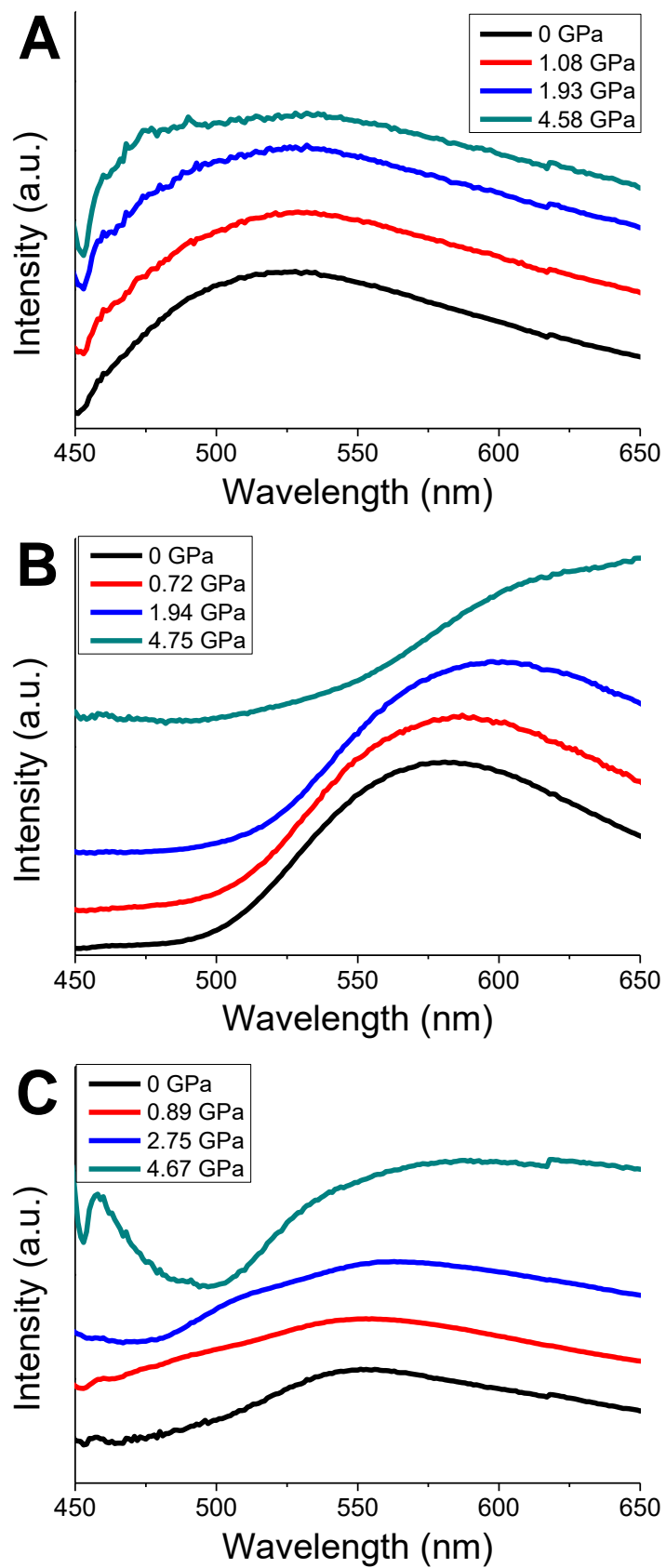


**Figure 4.12.** Luminescence spectra of the **5@PVDF** thin films with 4 % (a), 15 % (b) and 30 % w/w (c) of **5** at different pressures ( $\lambda_{\text{exc}} = 375$  nm).

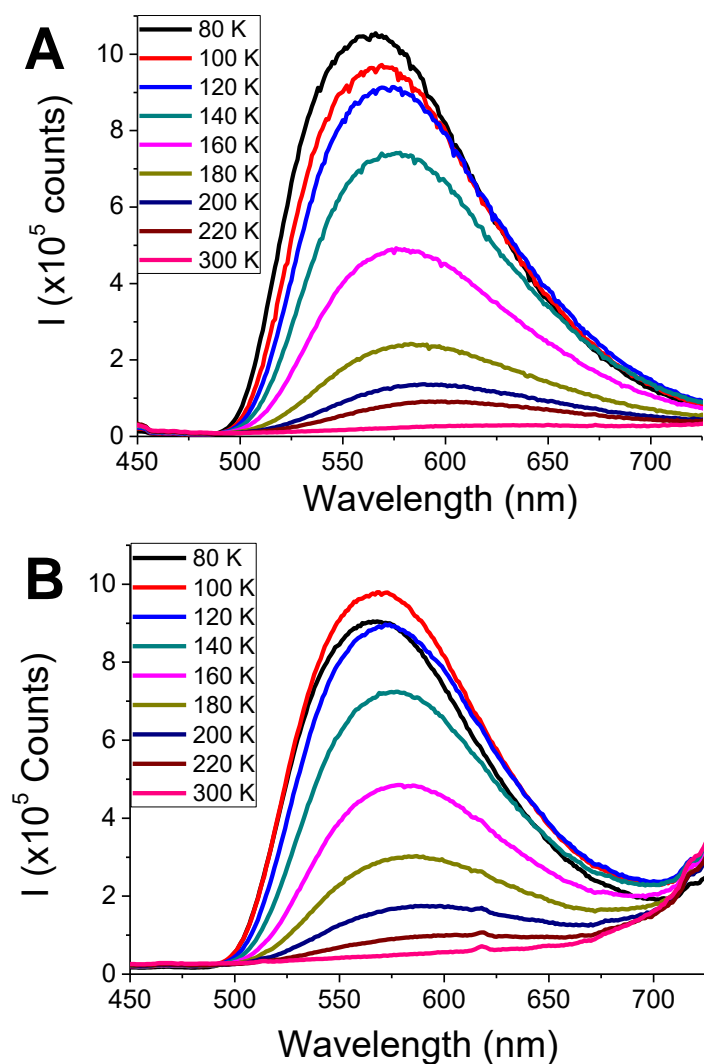


**Figure 4.13.** Thermal dependence of the luminescence spectra of **6** (a) and the **6@PLA** thin film with 30% w/w of **6** (b).

#### 4.2.3. Mechanical properties

The mechanical behavior of pristine PVDF and **5@PVDF** thin-films are shown in **Figure 4.14-4.17**.

The addition of small amounts of **5** (4% w/w) to the PVDF matrix does not seem to alter the ultimate tensile strength of the **5@PVDF** thin-films, but higher concentrations (15 and 30% w/w) provoke a gradual diminishing of this parameter (**Figure 4.15**). Remarkably, the elastic modulus (Young modulus) of these composites remains invariable regardless of the amount of **5** that is added to the PVDF matrix. This is indicative of good adhesion between the polymeric matrix and the CP nanofibers (**Figure 4.16**). Finally, as should be expected, the elongation at failure point decreases as the concentration of **5** increases; nonetheless, the difference between concentrations of 15% and 30% of **5** in the **5@PVDF** thin-films is not significant (**Figure 4.17**).

**Table 4.1.** Tensile strength (TS), Young Modulus or Elastic Modulus (E) and total elongation of the composite films **5@PVDF** with different amounts of **5**.

Sample	TS (MPa)	E (MPa)	Total Elongation (%)
<i>PLA</i>	$23 \pm 4$	$385 \pm 146$	$13 \pm 1$
<i>5@PVDF 4%</i>	$23 \pm 4$	$375 \pm 96$	$11 \pm 3$
<i>5@PVDF 15%</i>	$14 \pm 6$	$393 \pm 120$	$7 \pm 1$
<i>5@PVDF 30%</i>	$11 \pm 1$	$392 \pm 10$	$6 \pm 2$

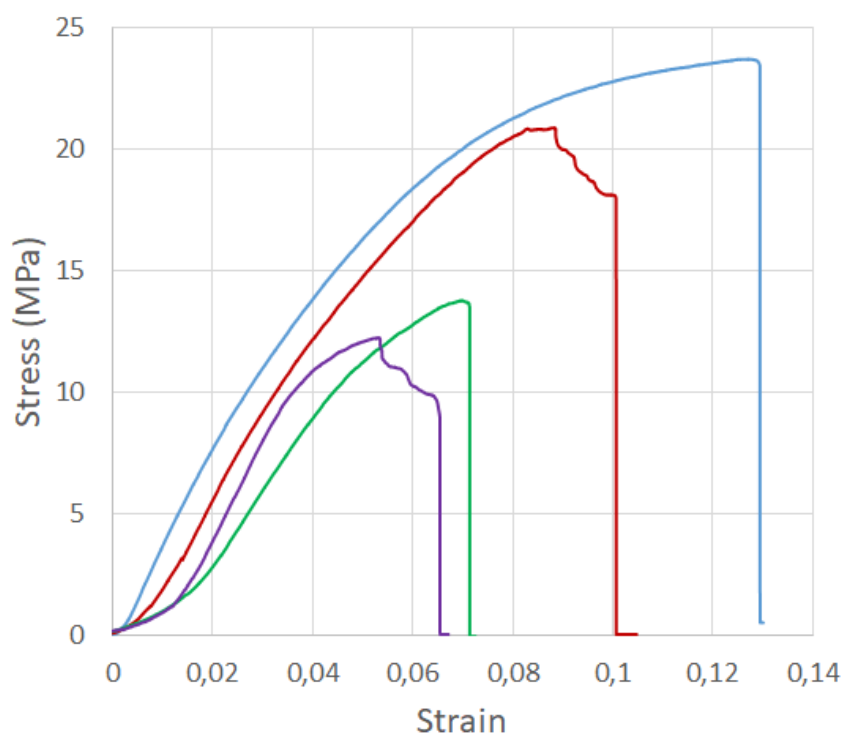


**Figure 4.14.** Stress-strain curves for pristine PVDF (blue line) and **5@PVDF** thin-films (red line 4% w/w, green line 15% w/w, and purple line 30% w/w).

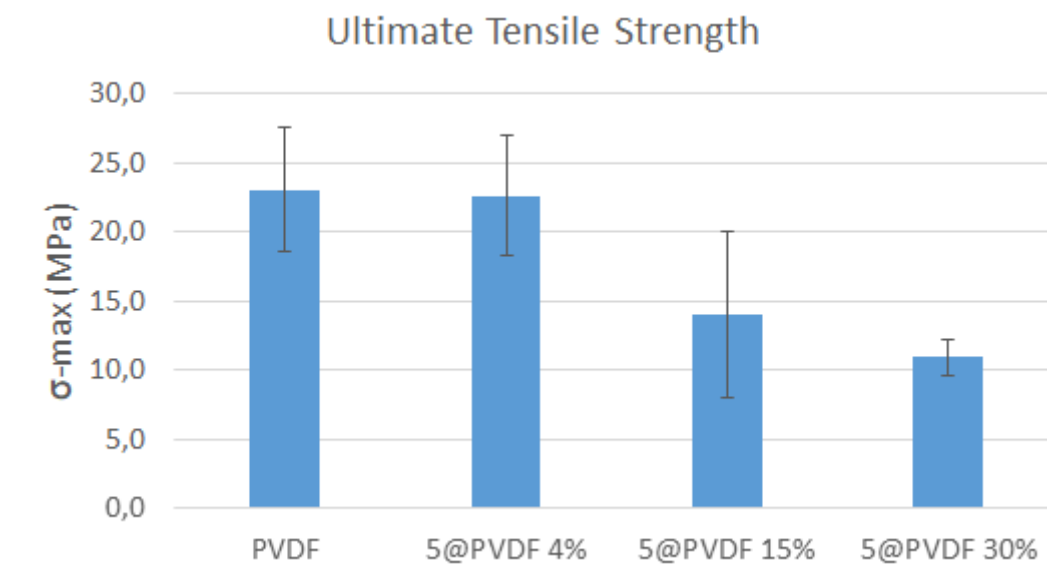


**Figure 4.15.** Ultimate tensile strength for naked PVDF film and **5@PVDF** thin films composites with 4%, 15% and 30% (w/w) of **5**. Different amounts of **5** produce slight changes in the ultimate tensile strength.

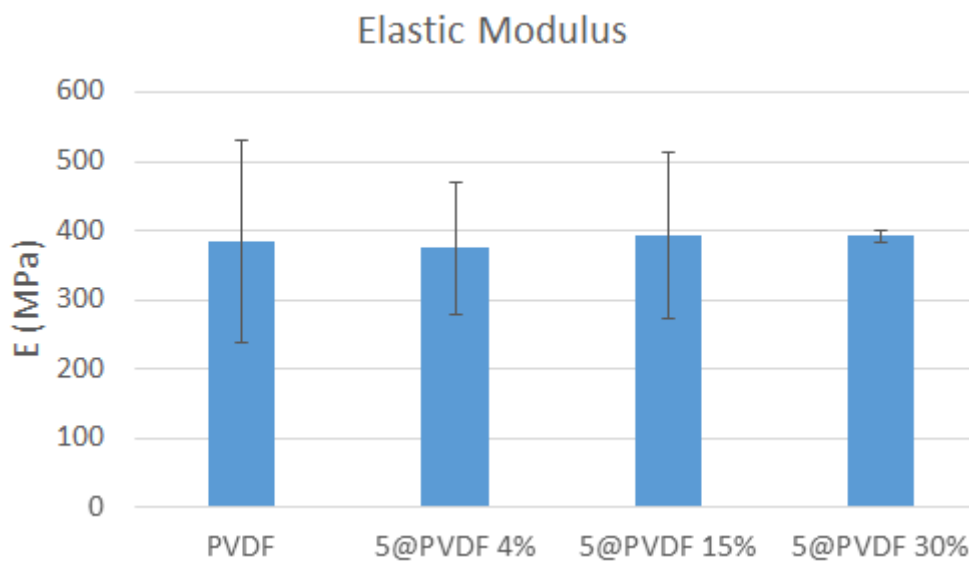


**Figure 4.16.** Elastic tensile modulus (Young Modulus) for naked PVDF film and thin films composites with 4%, 15% and 30% (w/w) of **5**. An increase in the quantity of CP does not alter the elastic modulus.

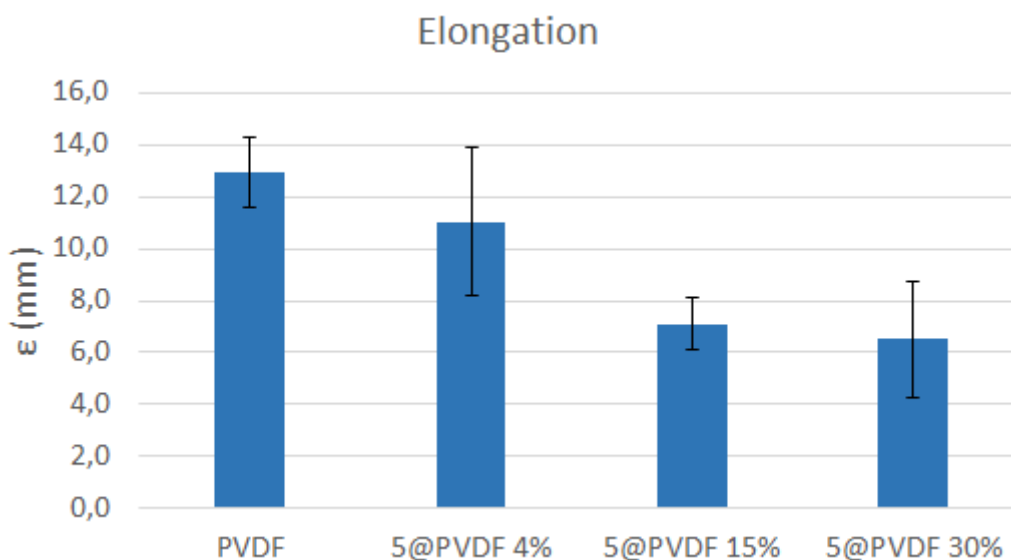


**Figure 4.17.** Elongation (%) at failure point for naked PVDF film and film composites with 4%, 15% and 30% (w/w) of **5**. Any amount of CP in the composite films produces a decrease of the total elongation of the material.

On the other hand, the mechanical behavior of pristine PLA and **6@PLA** thin-films are shown in **Figures 4.18-4.21**.

The addition of different amounts of **6** to the PLA matrix does not induce changes in the tensile strength of the films. Although there seems to be a slight increase in the ultimate tensile strength for the samples **6@PLA-1%** with respect to that observed for naked PLA (**Figure 4.19**), the statistical analysis indicates that there are no significant differences between them. A different behavior can be observed in the stiffness of the polymer (**Figure 4.20**), since the **6@PLA-1%** films showed an increase of 14% in the elastic modulus (E) when compared with PLA films (with a statistically significant difference,  $p$ -value = 0.017). The increase in the elastic modulus with this few amount of CP is indicative of good adhesion between polymer matrix and CP nanosheets. However, the addition of a high quantity of **6** (4% and 30%) gives rise to significant reductions in the Elastic Modulus of the films. The Young Modulus decreases a 16.6% for samples **6@PLA-4%** and a 27.3% for samples **6@PLA-30%** when compared with the samples **6@PLA-1%** films, being the differences of 4.9% and 17.0% when compared with the raw **PLA** (**Figure 4.20**). The decrease in the Young Modulus with the increase of the CP concentration should be related with the agglomeration of the CP and with a weak interfacial interaction between the CP and the organic matrix.<sup>16</sup>

**Table 4.2.** Tensile strength (TS), Young Modulus or Elastic Modulus (E), total elongation, plastic deformation and elastic elongation of the composite films **6@PLA** with different amounts of **6**.

Sample	TS (MPa)	E (MPa)	Total Elongation (%)	Plastic Deformation (%)	Elastic Elongation (%)
<i>PLA</i>	41 ± 1	948 ± 42	33 ± 4	19 ± 2	14 ± 3
<i>6@PLA 1%</i>	44 ± 3	1081 ± 24	16 ± 1	9 ± 4	7 ± 3
<i>6@PLA 4%</i>	41 ± 1	902 ± 29	15 ± 2	6.1 ± 0.4	9 ± 1
<i>6@PLA 30%</i>	38 ± 1	786 ± 72	17 ± 4	3.6 ± 0.4	14 ± 4

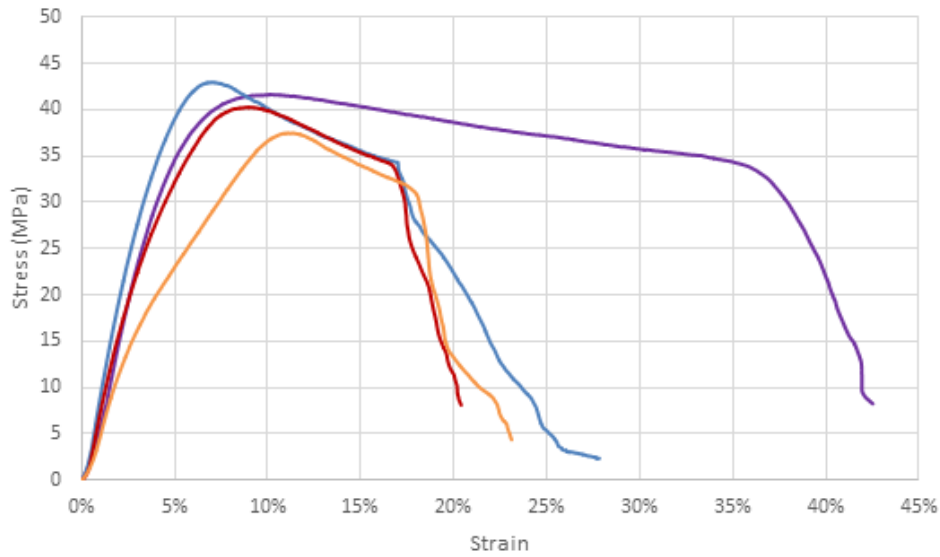


**Figure 4.18.** Stress-strain curves for pristine PLA (purple line) and **6@PLA** thin-films (blue line 1% w/w, red line 4% w/w, and orange line 30% w/w).

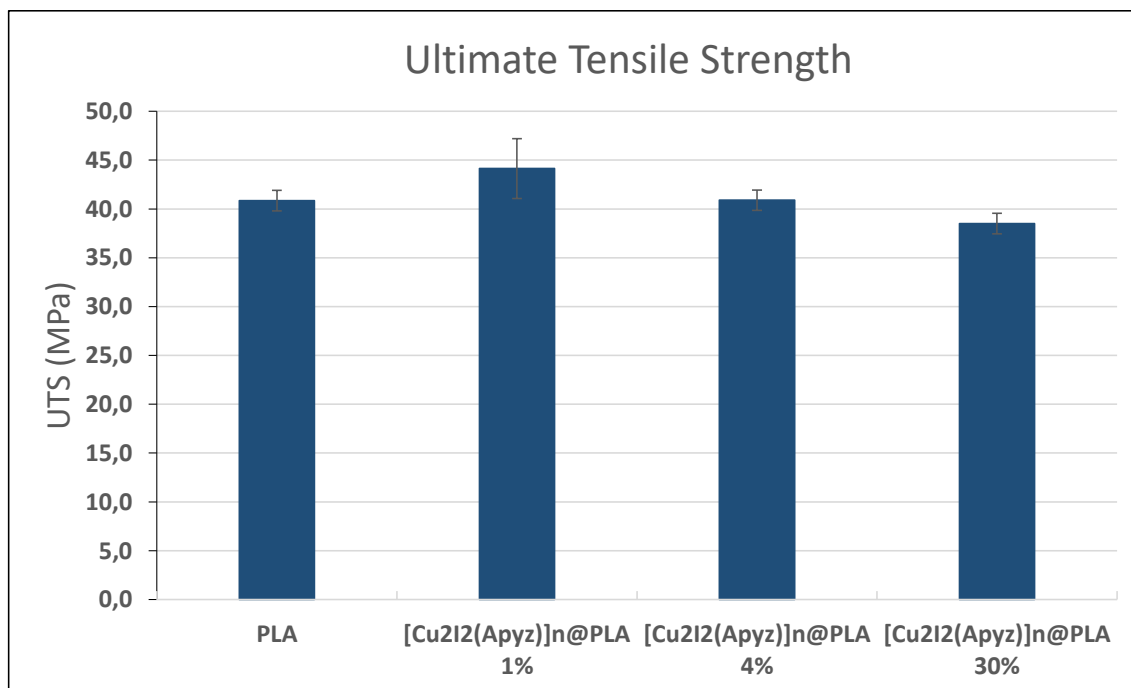


**Figure 4.19.** Ultimate tensile strength for naked PLA film and **6@PLA** thin films composites with 1%, 4% and 30% (w/w) of **6**. Different amounts of **6** produce slight changes in the ultimate tensile strength.

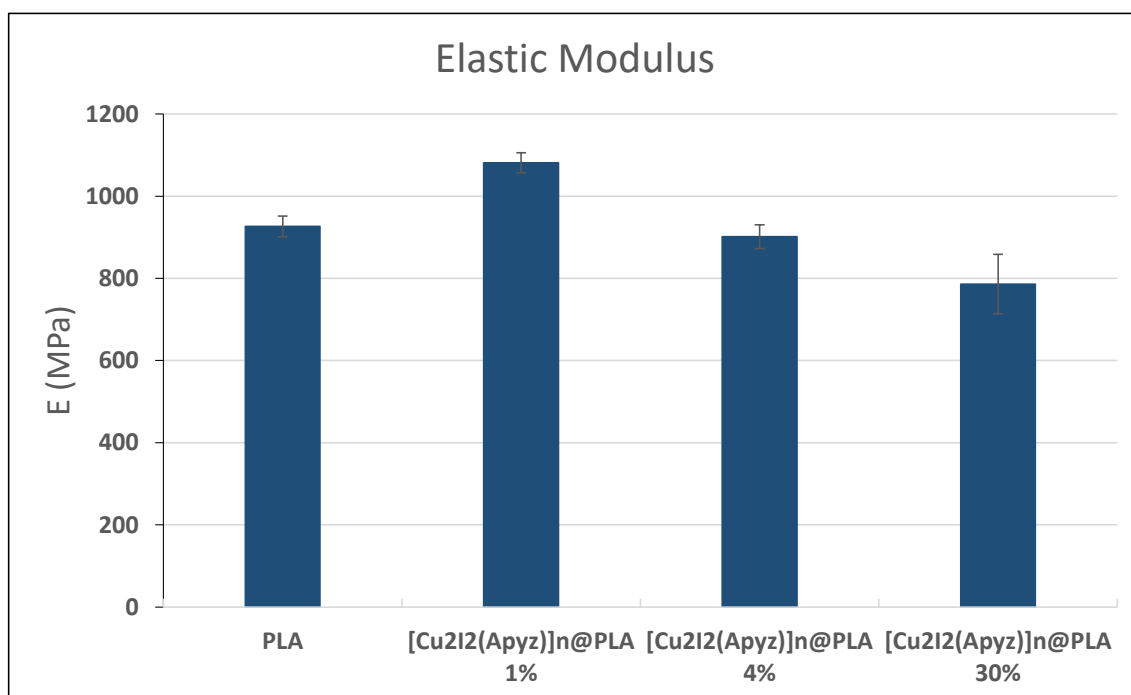


**Figure 4.20.** Elastic tensile modulus (Young Modulus) for naked PLA film and thin films composites with 1%, 4% and 30% (w/w) of **6**. A small amount of CP (1%) produces a slight increase in the Elastic modulus, while an increase in the quantity of CP causes the elastic modulus to decrease.



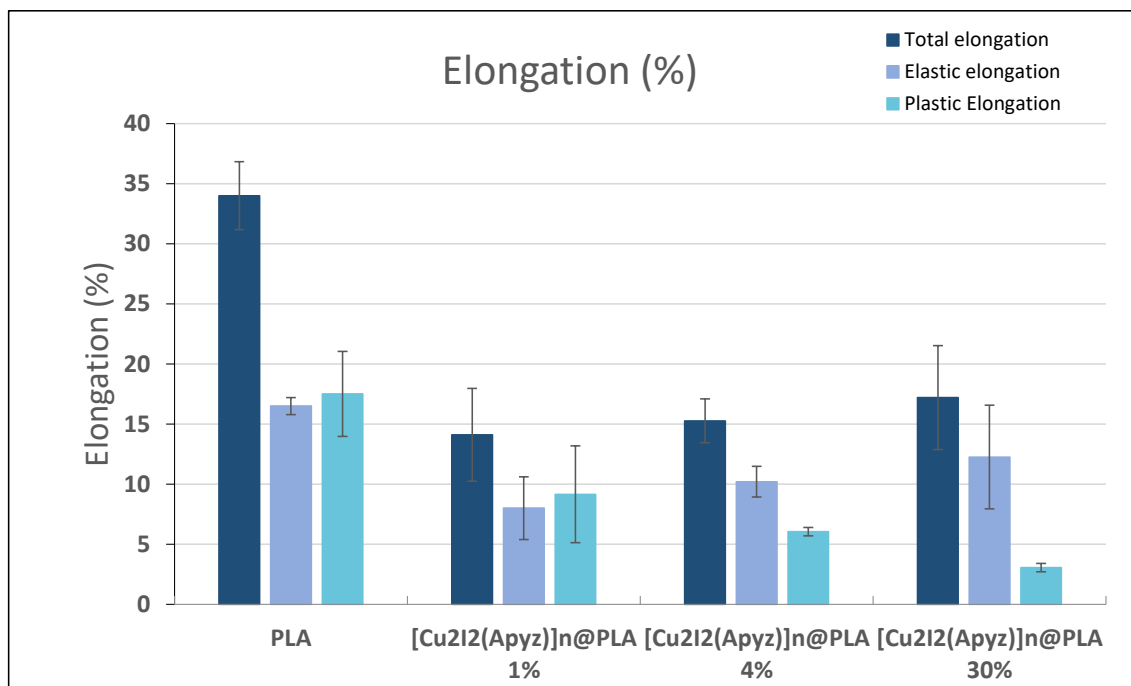


**Figure 4.21.** Elongation (%) at failure point for naked PLA film and film composites with 1%, 4% and 30% (w/w) of **6**. Any amount of CP in the composite films produces a decrease of roughly 50% in the total elongation of the material. As the amount of CP increases, so does the elastic elongation.

Moreover, **Figure 4.21** shows that any amount of **6** in the composite films produces a decrease, close to 50%, in the total elongation of the film composites. During the tensile test the films undergo two different types of elongation: the elastic elongation which reverses when the applied load is released or when the film breaks, and the plastic or permanent deformation which remains when the material breaks. **Figure 4.21** shows the total elongation, including plastic and elastic elongation. It is observed that increasing the content of **6** in the PLA composite from 1% w/w to 30% w/w produces no significant changes in the total elongation of the films. However, the samples exhibit a slight decrease in plastic deformation by increasing the amount of **6**, while the elastic elongation enhances due to its lower elastic modulus and, therefore, higher elasticity. Usually, MMMs based on porous or non-porous CP and a flexible organic matrix undergo a reduction in their ductility and ultimate tensile strength as the CP load increases. Taking these facts into account, **6@PLA** composite films show a mechanical behavior very close to that of analogous MMMs.<sup>5-6</sup>

### 4.3. Conclusions

Starting from suspensions of nanostructures of CPs **5** and **6** in solutions of, respectively, PVDF and PLA, highly homogeneous composite materials based on mixed-matrix membranes (MMMs) have been prepared. By means of a drop-casting deposition method, the obtained composite films show thicknesses of microns, whereas spin or dip-coating have allowed us to prepare nanometer-thick thin films. The CPs engulfed in the organic matrices contribute to the properties of the MMMs with thermochromism; as far as mechanochromism is concerned, **5@PVDF** composite films keep this behavior, slightly quenched by the flexibility of PVDF, while the great flexibility of PLA totally absorbs the effect of pressure on **6@PLA** composites. The presence of the CPs within the organic polymers slightly reduces their mechanical strength, embrittling the MMMs with respect to the naked matrices; all the same, our composites still show remarkable mechanical properties, allowing their use in potential applications.

### Conclusiones

A partir de suspensiones de nanoestructuras de los CPs **5** y **6** en disoluciones de, respectivamente, PVDF y PLA, se han preparado materiales híbridos basados en membranas de matriz mixta (MMMs), de alta homogeneidad. Mediante un método de deposición de gotas se generan láminas de micras de espesor, mientras que por recubrimiento por rotación o por inmersión somos capaces de reducir los espesores a unos pocos nanómetros. Los CPs embebidos en las matrices orgánicas aportan las propiedades termocrómicas de los CPs solos; en cuanto al mecanocromismo, los composites **5@PVDF** conservan dicho comportamiento, aunque ligeramente atenuado por la flexibilidad del PVDF, mientras que la gran flexibilidad del PLA absorbe totalmente el efecto de la presión sobre los composites **6@PLA**. La presencia de los CPs en el seno de la matriz orgánica reduce ligeramente su resistencia mecánica, haciendo que estos materiales sean más frágiles que los polímeros orgánicos de origen; a pesar de ello, conservan unas buenas propiedades mecánicas, haciendo a estos materiales aptos para diferentes aplicaciones.

#### 4.4. References

1. Martin, C.; Martin-Pacheco, A.; Naranjo, A.; Criado, A.; Merino, S.; Diez-Barra, E.; Herrero, M. A.; Vazquez, E., Graphene hybrid materials? The role of graphene materials in the final structure of hydrogels. *Nanoscale* **2019**, *11* (11), 4822-4830.
2. Song, Y.; Fan, R.; Wang, P.; Wang, X.; Gao, S.; Du, X.; Yang, Y.; Luan, T., Copper(i)-iodide based coordination polymers: bifunctional properties related to thermochromism and PMMA-doped polymer film materials. *Journal of Materials Chemistry C* **2015**, *3* (24), 6249-6259.
3. Zhao, C. W.; Ma, J. P.; Liu, Q. K.; Wang, X. R.; Liu, Y.; Yang, J.; Yang, J. S.; Dong, Y. B., An in situ self-assembled Cu<sub>4</sub>I<sub>4</sub>-MOF-based mixed matrix membrane: a highly sensitive and selective naked-eye sensor for gaseous HCl. *Chemical Communications* **2016**, *52* (30), 5238-5241.
4. Rodenas, T.; Luz, I.; Prieto, G.; Seoane, B.; Miro, H.; Corma, A.; Kapteijn, F.; Llabrés i Xamena, F. X.; Gascon, J., Metal-organic framework nanosheets in polymer composite materials for gas separation. *Nature Materials* **2015**, *14* (1), 48-55.
5. Denny, M. S., Jr.; Cohen, S. M., In Situ Modification of Metal-Organic Frameworks in Mixed-Matrix Membranes. *Angewandte Chemie International Edition* **2015**, *54* (31), 9029-9032.
6. Troyano, J.; Castillo, O.; Martinez, J. I.; Fernandez-Moreira, V.; Ballesteros, Y.; MasPOCH, D.; Zamora, F.; Delgado, S., Reversible Thermochromic Polymeric Thin Films Made of Ultrathin 2D Crystals of Coordination Polymers Based on Copper(I)-Thiophenolates. *Advanced Functional Materials* **2018**, *28* (5), 1704040.
7. DeCoste, J. B.; Denny, M. S., Jr.; Peterson, G. W.; Mahle, J. J.; Cohen, S. M., Enhanced aging properties of HKUST-1 in hydrophobic mixed-matrix membranes for ammonia adsorption. *Chemical Science* **2016**, *7* (4), 2711-2716.
8. Zhang, H.-J.; Fan, R.-Q.; Wang, X.-M.; Wang, P.; Wang, Y.-L.; Yang, Y.-L., Preparation, characterization, and properties of PMMA-doped polymer film materials: a study on the effect of terbium ions on luminescence and lifetime enhancement. *Dalton Transactions* **2015**, *44* (6), 2871-2879.
9. Zhai, L.; Zhang, W.-W.; Zuo, J.-L.; Ren, X.-M., A simple but efficient strategy to enhance hydrostability of intensely fluorescent Mg-based coordination polymer (CP) via forming a composite of CP with hydrophobic PVDF. *Dalton Transactions* **2016**, *45* (8), 3372-3379.
10. Zhao, C.-W.; Ma, J.-P.; Liu, Q.-K.; Wang, X.-R.; Liu, Y.; Yang, J.; Yang, J.-S.; Dong, Y.-B., An in situ self-assembled Cu<sub>4</sub>I<sub>4</sub>-MOF-based mixed matrix membrane: a highly sensitive and selective naked-eye sensor for gaseous HCl. *Chemical Communications* **2016**, *52* (30), 5238-5241.

11. Mas-Balleste, R.; Gonzalez-Prieto, R.; Guijarro, A.; Fernandez-Vindel, M. A.; Zamora, F., Nanofibers generated by self-assembly on surfaces of bimetallic building blocks. *Dalton Transactions* **2009**, (36), 7341-7343.
12. Gentili, D.; Givaja, G.; Mas-Balleste, R.; Azani, M. R.; Shehu, A.; Leonardi, F.; Mateo-Marti, E.; Greco, P.; Zamora, F.; Cavallini, M., Patterned conductive nanostructures from reversible self-assembly of 1D coordination polymer. *Chemical Science* **2012**, 3 (6), 2047-2051.
13. Monzón-Hierro, T.; Sanchiz, J.; González-Pérez, S.; González-Díaz, B.; Holinski, S.; Borchert, D.; Hernández-Rodríguez, C.; Guerrero-Lemus, R., A new cost-effective polymeric film containing an Eu(III) complex acting as UV protector and down-converter for Si-based solar cells and modules. *Solar Energy Materials and Solar Cells* **2015**, 136, 187-192.
14. González-Pérez, S.; Sanchiz, J.; González-Díaz, B.; Holinski, S.; Borchert, D.; Hernández-Rodríguez, C.; Guerrero-Lemus, R., Luminescent polymeric film containing an Eu(III) complex acting as UV protector and down-converter for Si-based solar cells and modules. *Surface and Coatings Technology* **2015**, 271, 106-111.
15. Kräuter, G.; Schumacher, A.; Gösele, U., Low temperature silicon direct bonding for application in micromechanics: bonding energies for different combinations of oxides. *Sensors and Actuators A: Physical* **1998**, 70 (3), 271-275.
16. Chuayjuljit, S.; Wongwaiwattanakul, C.; Chaiwutthinan, P.; Prasassarakich, P., Biodegradable poly(lactic acid)/poly(butylene succinate)/wood flour composites: Physical and morphological properties. *Polymer Composites* **2017**, 38 (12), 2841-2851.

## Chapter 5. Conclusions

The main conclusion of this PhD Thesis can be summarized as: **coordination polymers based on double Cu(I)-I chains decorated with a variety of N-donor aromatic ligands can be processed as multifunctional stimuli-responsive (nano)materials, retaining their features when they are integrated in composite materials.**

In this work we have been able to synthesize a series of coordination polymers bearing double *zigzag* Cu(I)-I chains decorated with a variety of N-donor aromatic ligands. The ten compounds have been characterized structurally, and their properties have been studied. The extraordinary structural flexibility of the Cu(I)-I chains bestows outstanding luminescence and multi-stimuli-responsive behaviors to our CPs. The easy processability in solution of these compounds makes our CPs great candidates for their fabrication as nanostructures, which can be embedded inside organic matrices in order to make smart composites. The inclusion of these CPs and composites in industrial fields or daily-life applications would allow the manufacture of cheaper opto-electronic devices and sensors, in opposition to those containing rare-earth elements.

## Conclusiones

La conclusión principal de esta tesis doctoral se resume en lo siguiente: **los polímeros de coordinación basados en cadenas dobles Cu(I)-I decorados con una variedad de ligandos aromáticos N-dadores pueden ser procesados como (nano)materiales multifuncionales estímulo-respuesta, conservando sus características cuando se integran en materiales compuestos.**

En este trabajo hemos sido capaces de sintetizar una serie de polímeros de coordinación que contienen dobles cadenas Cu(I)-I en *zigzag* decoradas con ligandos aromáticos N-dadores. Los diez compuestos se han caracterizado estructuralmente y se han estudiado sus propiedades. La extraordinaria flexibilidad estructural de las cadenas de cobre(I) y yodo otorgan una destacable luminiscencia y comportamiento multi-estímulo-respuesta a nuestros CPs. La facilidad para procesar estos compuestos en disolución permite prepararlos en forma de nanoestructuras, que pueden ser embebidas en matrices orgánicas para fabricar materiales compuestos inteligentes. La inclusión de estos CPs y composites en campos industriales y aplicaciones cotidianas permitiría la fabricación de dispositivos optoelectrónicos y sensores más baratos, en contraposición a aquellos que contienen elementos de tierras raras.

## **Chapter 6: Experimental procedures**

## 6.1. Materials

All starting reagents were purchased from commercial sources and used without further purification, unless otherwise stated. Copper(I) iodide (CuI) was purchased from Sigma-Aldrich and Tokyo Company International (TCI). Methyl isonicotinate (MeIN), ethyl isonicotinate (EtIN), isonicotinic acid (HIN), 3-chloroisonicotinic acid (Cl-HIN), methyl 2-aminoisonicotinate (NH<sub>2</sub>-MeIN), aminopyrazine (Apyz), 3,5-dichloropyridine (Cl<sub>2</sub>-py) and polyvinylidene difluoride (PVDF; M<sub>w</sub> = 180000, M<sub>n</sub> = 71000) were taken from Sigma-Aldrich. Biopolymer-quality polylactic acid (PLA; 3 mm mean granule diameter) was purchased from Goodfellow *via* Sigma-Aldrich. Benzimidazole, iodometane (MeI), 5-nitrobenzimidazol, sodium hydride (NaH) and sodium methoxide (NaOMe) were taken from TCI. All synthesis and ultrapure solvents were purchased from Scharlau except for acetonitrile (VWR Chemicals) and dry tetrahydrofuran (TCI), and were used without previous drying processes.

## 6.2. Methods

### 6.2.1. Fourier-Transform Infrared Spectroscopy (FT-IR).

IR spectra were registered in a Perkin-Elmer 100 spectrophotometer in the wavenumber range between 4000 and 650 cm<sup>-1</sup>, using a PIKE Technologies MIRacle Single Reflection Horizontal universal attenuated total reflectance (ATR) accessory.

### 6.2.2. Elemental Analysis.

The elemental analyses of all samples were conducted in a LECO CHNS-932 analyzer.

### 6.2.3. Powder X-ray Diffraction (PXRD).

The X-ray diffraction patterns of all samples were registered in a PANalytical X'Pert Pro diffractometer with  $\theta/2\theta$  primary monochromator and X'Celerator fast detector. The samples were analyzed by means of  $\theta/2\theta$  scanning.

### 6.2.4. Thermogravimetric analysis (TGA) and TGA coupled with mass spectrometry (TG-MS).

The thermogravimetric analyses of all samples and the TG-MS of compounds **8a** and **8b** were registered on a Q500 thermobalance from TA instruments, equipped with a platinum sample holder and a mass detector. The purge gas was nitrogen (N<sub>2</sub>), at a



constant flow speed of 90 mL·min<sup>-1</sup>. The samples were heated from 25 to 1000 °C, at a speed of 10 °C·min<sup>-1</sup>.

#### 6.2.5. Raman Spectroscopy.

The Raman spectra of compounds **8a** and **8b** were registered in a Bruker Senterra Raman microscope, using a 785 nm laser at a power of 25 mW as excitation source.

#### 6.2.6. Proton Nuclear Magnetic Resonance Spectroscopy (<sup>1</sup>H-NMR).

The <sup>1</sup>H-NMR spectra of compounds **8a** and **8b** were measured in a Bruker Advance III-HD Nanobay spectrometer, with an excitation frequency of 300 MHz for <sup>1</sup>H, using the TOPSPIN 3.2 program. All spectra were registered using deuterated acetonitrile (D<sub>3</sub>CCN) as solvent. Tetramethylsilane (TMS) was used as the reference (δ = 0 ppm).

#### 6.2.7. Diffuse reflectance UV-visible spectroscopy.

UV-visible spectra of all compounds were registered in the solid state using a Cary 5G spectrophotometer. A Praying Mantis solid sample holder was used in order to carry out diffuse reflectance measurements, and Teflon was used as the blank. The data were transformed by means of the Kubelka-Munk function.

#### 6.2.8. X-ray Photoelectron Spectroscopy (XPS).

The X-ray photoelectron spectra of **8a** and **8b**, were obtained with a VG Escalab 200R spectrometer equipped with a hemispherical electron analyzer and a Mg<sub>Kα</sub> (hν = 1254.6 eV, λ = 9.719 Å) X-ray source, powered at 120W. The contamination C<sub>s</sub> line was selected as the kinetic energies reference, at a value of 284.6 eV. Wagner sensitivity factors were used in order to quantify the different elements on the surface. Peaks were considered to be combinations of Gaussian and Lorentzian functions in an 80/20 ratio, working with a Shirley type baseline background subtraction by using XPS Peak Fit software. An estimated error of ±0.1 eV can be assumed for all measurements.

#### 6.2.9. Single Crystal X-ray Diffraction (SC-XRD).

The XRD data collections and structure determinations for all CPs detailed in this thesis at ambient pressure were conducted in a Bruker Kappa Apex II diffractometer with graphite-monochromated Mo<sub>Kα</sub> radiation (λ = 0.71073 Å). Measurements were carried out at 296K and 110K. The cell parameters were determined and refined by a least-

squares fit of all collected reflections, applying a semiempirical absorption correction (SADABS) in every case. All structures were resolved by direct methods using the SIR92 program<sup>1</sup> and refined by a full-matrix least-squares fit on  $F^2$  including all reflections with the SHELXTL97 program.<sup>2</sup> All non-hydrogen atoms were refined anisotropically. The hydrogen atoms were included in their calculated positions and refined riding on the respective parent atoms. All calculations were performed using the WINGX crystallographic software package.<sup>3</sup>

The structure determinations for compounds **5**, **6** and **8** at high pressure values were done using a Rigaku SuperNOVA diffractometer equipped with an EOS detector (CCD) and Mo radiation micro-source ( $\lambda = 0.71073\text{\AA}$ ). All measurements were conducted by means of the CrysAlisPro software.<sup>4</sup> The reference structures at room temperature and ambient pressure were determined by a dual-space algorithm using the SHELXT program<sup>5</sup> and refined by a full-matrix least-squares fit on  $F^2$  including all reflections with the SHELXL program.<sup>6</sup> All non-hydrogen atoms were refined anisotropically and hydrogen atoms were included in the model at calculated positions and refined with a rigid model where their  $U_{\text{iso}}$  value equals  $1.2U_{\text{eq}}$  of their parent atoms. The PLATON program<sup>7</sup> has been used for geometric calculations. For high pressure measurements, we have used a Diacell Bragg-S diamond anvil cell (DAC) from Almax-EasyLab, with an opening angle of  $90^\circ$  and anvil culets of  $600\text{ }\mu\text{m}$  diameter, fitted with a stainless gasket containing a hole of  $220\text{ }\mu\text{m}$  diameter and  $50\text{ }\mu\text{m}$  depth. A methanol-ethanol-water mixture (16:3:1) was used as pressure-transmitting medium, as it remains hydrostatic in the range of pressure used in our experiments.<sup>8,9</sup> In order to minimize deviatory stresses which can cause incorrect values for bulk modulus.<sup>10</sup> The sample was placed on one of the diamond anvils (diffraction side) together with a small ruby sphere as pressure sensor. The structure was refined, for each pressure, using previous results as starting point, on  $F^2$  by full-matrix least-squares refinement using the SHELXL program. Due to limitations of the opening angle of our DAC it is only possible to collect about 35% of the total reflections present in a full dataset at ambient conditions. In this situation, structure refinements were performed with isotropic displacement parameters for all atoms except for the heavy atoms (Cu and I) that were refined with anisotropic displacement parameters whenever they did not become non-positive definite. Hydrogen atoms were included in the final procedure in the same way as for ambient conditions. No restraints were used during this process.

#### 6.2.10. Luminescence Spectroscopy.

Luminescence excitation and emission spectra of all ligands and of compound **4** were performed at  $25\text{ }^\circ\text{C}$  on a 48000s (T-Optics) spectrofluorometer from SLM-Aminco. A front-face sample holder was used for data collection and oriented at  $60^\circ$  in order to minimize light scattering from the excitation beam on the cooled R-928 photomultiplier tube. Appropriate filters were used to eliminate Rayleigh and Raman scatters from the emission. Excitation and emission spectra were corrected for the wavelength

dependence of the 450 W xenon arc excitation but not for the wavelength dependence of the detection system. Spectroscopic properties were measured by reflection (front-face mode) on finely ground samples placed in quartz cells of 1 mm path length. No attempt was made to remove adsorbed or dissolved molecular oxygen from the materials. Reference samples that do not contain any fluorescent dopant were used to check the background and optical properties of the samples.

The thermal dependence of the luminescence spectra and the emission lifetimes of all compounds was measured in the temperature range between 80 and 300 K in a Jobin-Yvon Horiba Fluorolog FL-3-11 spectrometer using band pathways of 3 nm for both excitation and emission. Phosphorescence lifetimes were recorded with an IBH 5000F coaxial nanosecond flash lamp. Fluorescent lifetimes with a Data station HUB-B with a nanoLED controller and DAS6 software. The lifetime data were fitted with the Jobin-Yvon software package. Measurements at variable temperature were done with an Oxford Cryostat Optistat DN. The lifetime data were fitted using the Jobin-Yvon IBH software DAS6 v6.1.

The mechanical dependences of the luminescence emission spectra of compounds **5**, **6** and **8** were recorded exciting either with 375 nm or 457 nm diode lasers, respectively, using a 0.75 m single grating monochromator (Spex 750M) equipped with a cooled photomultiplier tube (Hamamatsu 928b). All spectra have been corrected for the instrument response. High pressure was generated with a miniature diamond anvil cell (mini-DAC), designed at The University of Paderborn (Germany), with low luminescent II-a type diamonds for optical, infrared and diffraction measurements. A stainless-steel gasket was pre-indented to 80  $\mu\text{m}$  and a centered hole of typical diameter of 150  $\mu\text{m}$  constitutes the sample chamber. Ruby chips were used as pressure calibrant using the ruby R1line fluorescence. A 16:3:1 methanol-ethanol-water mixture was used as pressure-transmitted medium since it provided hydrostatic pressures up to 14 GPa.<sup>8,9</sup>

#### 6.2.11. Electrical Conductivity and Electrochemical Impedance Spectroscopy (EIS).

Preliminary direct current (DC) electrical conductivity measurements were performed on different single crystals of all compounds, with graphite paste at 300 K and two contacts. The contacts were made from tungsten wires (25  $\mu\text{m}$  diameter). The samples were measured at 300 K by applying an electrical current with voltages from +10 to -10 V. The measurements were performed in the compounds along the crystallographic axis along which the Cu-I chain grows. The thermal dependence of the DC electrical conductivity was measured with the four (or two, depending on the size of the crystal) contacts method on up to four single crystals each compound, in the temperature range between 2 and 400 K. The contacts were made with Pt wires (25  $\mu\text{m}$  diameter) using graphite paste. The samples were measured in a Quantum Design PPMS-9 equipment connected to an external voltage source (Keithley model 2450 source-meter) and amperometer (Keithley model 6514 electrometer). All the quoted conductivity values

were measured in the voltage range where the crystals are Ohmic conductors. The cooling and warming rates were 1 and 2 K·min<sup>-1</sup>.

EIS measurements of compound **6** data at 298 K were collected using an Autolab electrochemical system II PGSTAT30 (Ecochemie, The Netherlands) impedance analyzer, from 1 Hz to 1 MHz with an applied voltage of 0.01 V using a two-probe method. AC measurements were performed to determine the conductivity parameters at different exposition times to acetic acid vapor (0, 4, 24 and 48 h). Through-plane conductivity was determined in three samples of this compound. Thus, *ca.* 5 mg of solid were pressed at up to *ca.* 5 GPa to form pellets with an approximate area of 0.071 cm<sup>2</sup> and a thickness around 0.30 mm. Symmetrical stainless steel electrodes were used as electrical contact. This was made by applying a pressure of 350 N cm torque in a conductivity cell configuration SS/ CP /SS, where SS refers to stainless steel. Each impedance measurement was repeated three times with different pellets to corroborate the consistency of the conductivity measurements. The subsequent Nyquist plots were obtained from the average of these three measurements.

#### 6.2.12. Field-Emission Scanning Electron Microscopy (FE-SEM).

FE-SEM images were taken in a Philips XL 30 S-FEG electron microscope, applying an electron beam of 300  $\mu$ A intensity and 10.0 kV potential, at a pressure of 10<sup>-7</sup> Pa. To obtain reproducible results, very flat substrates were used with precisely controlled chemical functionalities, freshly prepared just before the chemical deposition of the samples. Doped SiO<sub>2</sub> surfaces were sonicated in ultrasound bath (Elma, 37 kHz, 380 W), for 15 min in acetone and 15 min in 2-propanol, and then dried under an Argon flow. After sample preparation, the surfaces were metallized with a 10 nm thick Cr layer, at a pressure of 10<sup>-3</sup> Pa.

#### 6.2.13. Scanning Electron Microscopy coupled with analysis by Energy-Dispersive X-ray Spectroscopy (SEM-EDX).

SEM-EDX images and EDX spectra were taken in a Hitachi S-3000N microscope with an ESED detector coupled to an INCAx-sight EDX analyzer. For this technique, samples deposited on SiO<sub>2</sub> surfaces were metallized with a 15 nm thick Au layer, at a pressure of 10<sup>-3</sup> Pa.

#### 6.2.14. Atomic Force Microscopy (AFM).

AFM images were registered in a Nanotec Electronica microscope, at room temperature and in an open atmosphere, using Olympus cantilevers with a constant nominal force of 0.75 N/m. Images were processed by the use of the WSxM program.<sup>11,12</sup> To obtain

reproducible results, very flat substrates were used with precisely controlled chemical functionalities, freshly prepared just before the chemical deposition of the samples. Doped SiO<sub>2</sub> surfaces were sonicated in ultrasound bath (Elma, 37 kHz, 380 W), for 15 min in acetone and 15 min in 2-propanol, and then dried under an Argon flow.

#### 6.2.15. Theoretical Methodology.

These calculations have been used to compute mechanical and electronic properties, total energies, density of electronic states profiles and excitation spectra in the visible region. An efficient TDDFT formalism has been used to calculate the excitation spectra<sup>13-18</sup> as implemented within the plane wave (PW) basis set within the QUANTUM ESPRESSO distribution (<http://www.quantum-espresso.org>). In the calculations we have used the simulation cells and structures as obtained by X-ray diffraction experiments (for different T and P conditions), yielding residual forces acting on each atom below 0.1 eVÅ<sup>-1</sup>, sufficient to guarantee fully converged results. Spin-polarized calculations did not show any significant variation with respect to the spin-unpolarized tests. In all the calculations the Brillouin zones (BZs) were sampled by means of optimal Monkhorst–Pack grids.<sup>19</sup> We used the Perdew-Burke-Ernzerhof (PBE) XC-GGA functional, ultra-soft pseudopotentials<sup>20</sup> and a PW's basis set up to a kinetic energy cut-off of 40 Ry, as well as 300 Ry for the charge density. The excitation spectra are calculated as:  $I(\omega) \propto \omega \text{Im}[\alpha(\omega)]$ , where  $\alpha$  is the spherical average (average of the diagonal elements) of the dipole polarizability; an imaginary part of 0.002 Ry has been added to the frequency in order to smooth the emerging divergences of the polarizability. Additionally, once the different TDDFT spectra were obtained as aforementioned, we have carried out a battery of calculations with the GAUSSIAN09 package<sup>21</sup> to obtain oscillator strengths, and elucidate transitions and electronic states involved in the most intense excitations by using the same GGA-PBE functional and the rather large 6-311G\* basis set. To compute the individual transitions we have made use of the configuration interaction singles (CIS) method,<sup>22</sup> which requests a calculation on excited states using single-excitation CI (CI-Singles). This implementation provides excellent results in both closed-shell and open-shell systems.

### **6.3. Synthetic procedures**

#### 6.3.1. Synthesis of CPs with double zigzag Cu-I chains.

##### *6.3.1.1. Synthesis of [Cu(HIN)I]<sub>n</sub> (I) micro- and sub-microstructures*

This CP was prepared following a variation of a published method.<sup>23-25</sup> Copper(I) iodide (200 mg, 1.05 mmol) was dissolved in 10 mL of acetonitrile. On the other hand, HIN (130 mg, 1.05 mmol) was dispersed in 10 mL of ethanol and added to the copper iodide solution, both at 25 °C. The resulting orange-red suspension was stirred (500 rpm) for

30 min and filtered to remove the unreacted ligand. A 20  $\mu\text{L}$  drop of the solution was deposited on a doped  $\text{SiO}_2$  surface and left to evaporate completely; the resulting red solid consisted of submicroribbons and nanofibers. The rest of the solution was left to slowly evaporate at room temperature, obtaining red microcrystals after 72 h.

Total yield: 98 mg (30% based on Cu). Elemental analysis calculated (%) for  $\text{C}_6\text{H}_5\text{CuINO}_2$ : C 22.88, H 1.65, N 4.47; found: C 21.34, H 1.54, N 3.92. IR selected data (ATR):  $\tilde{\nu}$  ( $\text{cm}^{-1}$ ) = 3444 (w), 1697 (s), 1604 (m), 1556 (m), 1411 (s), 1324 (m), 1292 (s), 1209 (m), 1133 (s), 1058 (w), 917 (w), 825 (w), 759 (m), 696 (m), 676 (m).

The PXRD patterns show that both micrometric and sub-micrometric crystals have the same structure (**Figure C1** in appendix C).

#### 6.3.1.2. Synthesis of $[\text{Cu}(\text{EtIN})\text{I}]_n$ (**2**) nanostructures

This CP was prepared following a modified literature method.<sup>23,24,26</sup> To 15 mL of an acetonitrile solution of copper(I) iodide (0.53 mmol, 100 mg), 0.53 mmol (80  $\mu\text{L}$ ) of ethyl isonicotinate (EtIN) were added while magnetically stirring (500 rpm) the mixture. Immediately, the solution turned into a yellow suspension. The yellow solid was filtered off, washed carefully with acetonitrile (1 mL) and ethanol ( $2 \times 2$  mL), and dried in a vacuum.

Yield: 110 mg, 61% based on Cu. Elemental analysis calculated (found) % for  $\text{C}_8\text{H}_9\text{CuINO}_2$ : C 28.13 (28.20), H 2.66 (2.44), N 4.10 (4.02); selected IR data  $\tilde{\nu}$  ( $\text{cm}^{-1}$ ) = 3421 (w), 1716 (m), 1556 (w), 1414 (s), 1394 (w), 1363 (m), 1322 (m), 1288 (s), 1257 (m), 1226 (w), 1135 (w), 1114 (w), 1061 (m), 1018 (m), 856 (w), 759 (m), 698 (m). The homogeneity of the sample was confirmed by PXRD (**Figure C2** in appendix C).

In order to study the nanoribbons of **2** by SEM, 1 mL of the yellow suspension was centrifuged (5 min, 10000 rpm) and washed with ethanol ( $2 \times 1$  mL). Then the solid was redispersed in 1 mL of double-distilled water and 20  $\mu\text{L}$  of the yellow suspension were deposited over clean glass substrates and left to adsorb for 10 minutes. Afterwards, the surfaces were dried with an argon flow.

For their study by AFM, 400  $\mu\text{L}$  of the redispersed suspension were diluted with 3600  $\mu\text{L}$  of double-distilled water (the dilution factor is  $10^{-1}$ ), and 15  $\mu\text{L}$  of the new suspension were drop-cast onto doped  $\text{SiO}_2$  substrates. After 3 min of adsorption, the surfaces were dried under an argon flow.

#### 6.3.1.3. Synthesis of $[\text{Cu}(\text{ANP})\text{I}]_n$ (**3**) nanostructures

This CP was prepared following a modified literature method.<sup>23,26,27</sup> Two solutions of 0.53 mmol (100 mg) of copper(I) iodide in 10 mL of acetonitrile and 0.53 mmol (73 mg) of 2-amino-5-nitropyridine (ANP) in 5 mL of ethanol were prepared at 30  $^\circ\text{C}$ , and

then mixed with magnetic stirring at 500 rpm. Immediately, the solution turned from yellow to orange and an orange solid precipitated as nanocrystals after 1 min. The solid was filtered off, washed carefully with acetonitrile (1 mL) and ethanol ( $2 \times 2$  mL), and dried in a vacuum.

Yield: 62 mg, 26% based on Cu. Elemental analysis calculated (found) % for  $C_5H_5CuIN_3O_2$ : C 18.22 (18.90), H 1.53 (1.60), N 12.75 (12.93); selected IR data  $\tilde{\nu}$  ( $cm^{-1}$ ) = 3444 (m), 3323 (m), 3087 (w), 3056 (w), 1625 (s), 1601 (m), 1570 (m), 1491 (s), 1421 (m), 1329 (s), 1285 (s), 1161 (w), 1124 (m), 941 (m), 869 (w), 826 (vs), 760 (m), 723 (m), 667 (w). The homogeneity of the sample was confirmed by PXRD (**Figure C3** in appendix C).

For its study by SEM, 1 mL of the orange suspension was centrifuged (5 min, 10000 rpm) and washed with ethanol ( $2 \times 1$  mL). Then the solid was redispersed in 1 mL of double-distilled water and 20  $\mu$ L of the yellow suspension were deposited over clean glass substrates and left to adsorb for 10 minutes. Afterwards, the surfaces were dried with an argon flow.

In order to study the nanofibers by AFM, 40  $\mu$ L of the redispersed suspension were diluted with 3960  $\mu$ L of double-distilled water (the dilution factor is  $10^{-2}$ ), and 15  $\mu$ L of the new suspension were drop-cast onto doped  $SiO_2$  substrates. After 3 min of adsorption, the surfaces were dried under an argon flow.

#### 6.3.1.4. Synthesis of $[Cu(MeIN)I]_n$ (**4**)

Copper(I) iodide (201 mg, 1.05 mmol) was dissolved in 15 mL of acetonitrile. Methyl isonicotinate (126  $\mu$ L, 1.07 mmol) was added to the mixture; instantly, the solution turned orange, and an orange solid precipitated. The solid was immediately filtered, washed carefully with methanol ( $2 \times 3$  mL) and dried in vacuum. Single crystals were formed upon standing the mother orange solution at 25 °C for 72 h. The orange crystals obtained were filtered off, washed with methanol ( $2 \times 3$  mL) and dried in vacuum.

Yield: 170 + 59 mg, 49 + 17 % based on Cu. Elemental analysis calculated (%) for  $C_7H_7CuINO_2$ : C 25.66, H 2.15, N 4.28; found: C 25.72, H 2.15, N 4.28; IR selected data (ATR):  $\tilde{\nu}$  ( $cm^{-1}$ ) = 3039 (vw), 2950 (w), 1728 (vs), 1560 (w), 1433 (m), 1414 (m), 1321 (m), 1288 (s), 1184 (w), 1119 (m), 1061 (w), 955 (w), 854 (w), 758 (m), 700 (m), 690 (m). PXRD data of both nanofibers and crystals confirm their purity (**Figure C5** in appendix C).

In order to study the nanofibers of **4** by SEM, 30 mg of the orange solid were redispersed in 5 mL of double-distilled water, and 20  $\mu$ L of the suspension were deposited on a doped  $SiO_2$  surface; the drop was left to adsorb for 3 min. and dried with an Argon flow.

For their study by AFM, 1 mL of the orange suspension obtained in the synthetic process was centrifuged (5 min, 10000 rpm) and washed with methanol ( $2 \times 1$  mL). Then the solid was redispersed in 1 mL of double-distilled water and 40  $\mu$ L of the redispersed suspension were diluted with 3960  $\mu$ L of double-distilled water (the dilution factor is  $10^{-2}$ ), and 15  $\mu$ L of the new suspension were drop-cast onto doped SiO<sub>2</sub> substrates. After 3 min of adsorption, the surfaces were dried under an argon flow.<sup>24,28</sup>

#### 6.3.1.5. Synthesis of $[Cu(NH_2-MeIN)I]_n$ (**5**)

Copper(I) iodide (100 mg, 0.53 mmol) was dissolved in 8 mL of acetonitrile at 20 °C, and methyl 2-aminoisonicotinate (81 mg, 0.53 mmol) was dissolved in 8 mL of ethanol at 50 °C. Then, both solutions were mixed at 25 °C under magnetic stirring (500 rpm). A pale-yellow solid is immediately formed, filtered off, washed with acetonitrile ( $2 \times 5$  mL), ethanol ( $2 \times 5$  mL) and diethyl ether ( $2 \times 3$  mL), and dried in vacuum (Yield: 85 mg; 50 % based on Cu). Single crystals were formed upon standing the mother yellow solution at 25 °C for 48 h (Yield: 43 mg; 25 % based on Cu).

Yield: 85 + 43 mg, 50 + 25 % based on Cu. Elemental analysis calculated (%) for C<sub>7</sub>H<sub>8</sub>CuIO<sub>2</sub>N<sub>2</sub>: C 24.52, H 2.34, N 8.17; found: C 24.96, H 2.34, N 8.07; IR selected data (ATR):  $\tilde{\nu}$  (cm<sup>-1</sup>) = 3450 (s), 3345 (s), 3186 (w), 3078 (w), 2992 (w), 2945 (w), 2845 (w), 1788 (w), 1716 (vs), 1634 (vs), 1603 (m), 1560 (vs), 1489 (w), 1448 (vs), 1432 (s), 1346 (m), 1308 (vs), 1270 (vs), 1249 (s), 1123 (s), 999 (s), 900 (m), 830 (w), 816 (m), 762 (vs), 737 (m), 697 (w). PXRD data of both nanofibers and crystals confirm their purity (**Figure C6** in appendix C).

In order to study the nanofibers of **5** by SEM, 30 mg of the yellow solid were redispersed in 5 mL of double-distilled water, and 20  $\mu$ L of the suspension were deposited on a doped SiO<sub>2</sub> surface; the drop was left to adsorb for 3 min. and dried with an Argon flow.

For their study by AFM, 1 mL of the yellow suspension obtained in the synthetic process was centrifuged (5 min, 10000 rpm) and washed with ethanol ( $2 \times 1$  mL). Then the solid was redispersed in 1 mL of double-distilled water and 40  $\mu$ L of the redispersed suspension were diluted with 3960  $\mu$ L of double-distilled water (the dilution factor is  $10^{-2}$ ), and 15  $\mu$ L of the new suspension were drop-cast onto doped SiO<sub>2</sub> substrates. After 3 min of adsorption, the surfaces were dried under an argon flow.<sup>28</sup>

#### 6.3.1.6. Synthesis of $[Cu_2I_2(Apyz)]_n$ (**6**)

Copper(I) iodide (51 mg, 0.27 mmol) was dissolved in 10 mL of acetonitrile; on the other hand, 2-aminopyrazine (13 mg, 0.14 mmol) was dissolved in 3 mL of distilled water. Both solutions were mixed and magnetically stirred at 25 °C for 5 min, at a speed of 500 rpm. The resulting mixture was consisted of a yellowish solution and a yellow



solid formed of nanosheets. The solid was filtered off, washed with acetonitrile ( $2 \times 5$  mL), water ( $2 \times 5$  mL), and ethanol ( $2 \times 3$  mL), and dried in vacuum.

Total yield: 43 mg (67% based on Cu). Elemental analysis calculated (%) for  $C_4H_5Cu_2I_2N_3$ : C 10.09, H 1.06, N 8.83; found: C 10.53, H 1.18, N 8.82; IR-selected data (ATR):  $\tilde{\nu}$  ( $cm^{-1}$ ) = 3426 (s), 3321 (s), 3190 (w), 3024 (w), 1901 (w), 1615 (vs), 1606 (vs), 1584 (vs), 1524 (vs), 1471 (s), 1437 (vs), 1351 (s), 1317 (s), 1208 (vs), 1169 (m), 1069 (s), 1049 (m), 1027 (vs), 898 (m), 820 (vs), 744 (m). PXRD data of both nanofibers and crystals confirm their purity (**Figure C8** in appendix C).

In order to study the nanosheets of **6** by SEM, 30 mg of the yellow solid were redispersed in 5 mL of double-distilled water, and 20  $\mu$ L of the suspension were deposited on a doped  $SiO_2$  surface; the drop was left to adsorb for 3 min. and dried with an Argon flow.

For their study by AFM, 1 mL of the yellow suspension obtained in the synthetic process was centrifuged (5 min, 10000 rpm) and washed with double-distilled water ( $2 \times 1$  mL). Then the solid was redispersed in 1 mL of double-distilled water and 40  $\mu$ L of the redispersed suspension were diluted with 3960  $\mu$ L of double-distilled water (the dilution factor is  $10^{-2}$ ), and 15  $\mu$ L of the new suspension were drop-cast onto doped  $SiO_2$  substrates. After 3 min of adsorption, the surfaces were dried under an argon flow.<sup>29</sup>

#### 6.3.1.7. Synthesis of $[Cu(Cl-HIN)I]_n$ (**7**)

Copper(I) iodide (200 mg, 1.05 mmol) was dissolved in 10 mL of acetonitrile; in contrast, Cl-HIN (167 mg, 1.05 mmol) was dispersed in 5 mL of ethanol, at 50 °C. Both solutions were mixed and stirred (1000 rpm) at 25 °C for 3 min. The resulting mixture consisted of a dark yellow solution and an orange solid consisting of  $[Cu(Cl-HIN)I]_n$  nanofibers. The solid was filtered off, washed with acetonitrile ( $2 \times 5$  mL), ethanol ( $2 \times 5$  mL), and diethyl ether ( $2 \times 3$  mL), and dried in vacuo. The solution was left to crystallize at room temperature, obtaining red needle-like microcrystals after 48 h.

Total yield: 254 mg (69% based on Cu): 151 mg of nanofibers (41%) and 103 mg of microcrystals (28%). Elemental analysis calculated (%) for  $C_6H_4CuIClO_2N$ : C 20.69, H 1.15, N 4.02; found: C 20.93, H 1.24, N 3.88. IR selected data (ATR):  $\tilde{\nu}$  ( $cm^{-1}$ ) = 3024 (w), 2885 (w), 2643 (w), 2524 (w), 1711 (vs), 1698 (vs), 1589 (w), 1530 (w), 1473 (m), 1391 (vs), 1275 (vs), 1264 (vs), 1217 (vs), 1140 (w), 1090 (s), 1055 (s), 876 (m), 854 (vs), 784 (m), 733 (vs), 690 (s), 666 (vs).

The PXRD patterns show that both micrometric and nanometric crystals have the same structure (**Figure C10** in appendix C).

In order to study the nanostructures by SEM, the solid (61 mg) was redispersed in 1000  $\mu$ L of double-distilled water, and 20  $\mu$ L of the suspension were deposited on a doped

SiO<sub>2</sub> surface. The drop was left to adsorb until it dried and the surface was purged under an argon flow.

In order to study the nanostructures by AFM, copper(I) iodide (200 mg, 1.05 mmol) was dissolved in 10 mL of acetonitrile; in contrast, Cl-HIN (167 mg, 1.05 mmol) was dispersed in 5 mL of ethanol, at 50 °C. Both solutions were mixed and stirred (1000 rpm) at 25 °C for 3 min. The resulting mixture consisted of a dark yellow solution and an orange solid consisting of [Cu(Cl-HIN)I]<sub>n</sub> nanofibers. Then, 400 µL of this suspension were diluted with 3600 µL of acetonitrile (the dilution factor is 10<sup>-1</sup>). Next, 15 µL of this new suspension was deposited on a doped SiO<sub>2</sub> surface. The drop was left to adsorb for 1 min, and the surface was purged under an argon flow.<sup>25</sup>

#### 6.3.1.8. Synthesis of [Cu(Cl<sub>2</sub>-py)I]<sub>n</sub> (**8**)

**8a**: 200 mg (1.05 mmol) of copper(I) iodide are dissolved in 10 mL of acetonitrile. On the other hand, 167 mg (1.05 mmol) of 3,5-dichloropyridine are dissolved in 5 mL of ethanol. Both solutions are mixed under magnetic stirring (1000 rpm), giving rise to a greenish yellow suspension of **8a** after 3 minutes. The solid is filtered off, washed with acetonitrile (2 × 2 mL) and ethanol (2 × 3 mL), and dried in vacuum. Yellow rod crystals of **1** were obtained after 2 days of evaporation of the mother solution. Yield: 244 mg (66% based on Cu). Elemental analysis calculated (%) for C<sub>5</sub>H<sub>3</sub>CuICl<sub>2</sub>N: C 17.74, H 0.89, N 4.14; found: C 18.04, H 1.02, N 4.10; IR selected data (ATR):  $\tilde{\nu}$  (cm<sup>-1</sup>) = 3123 (vw), 3063 (vw), 3044 (w), 1867 (w), 1837 (w), 1810 (w), 1781 (w), 1561 (ms), 1551 (ms), 1415 (vs), 1387 (s), 1290 (m), 1217 (m), 1109 (s), 1094 (s), 1036 (m), 1015 (m), 903 (w), 873 (vs), 848 (m), 818 (vs), 678 (vs). TG-MS: 80-200 °C: m/z = 38, 48, 50, 63, 64, 78; 600-800 °C: m/z = 63.

The characterization data confirmed that both the solid and crystals correspond to **8a**. PXRD data confirmed the purity of both crystals and solid (**Figure C11** in appendix C).

**8b**: 100 mg (0.53 mmol) of copper(I) iodide and 83 mg (0.53 mmol) of 3,5-dichloropyridine are dissolved in 15 mL of acetonitrile. The solution is sealed in a glass vial with a Teflon cap, heated at 120 °C for 72 hours and cooled to 20 °C at a speed of 4.2 °C/h. The resulting yellow solution is filtered to eliminate impurities and left to slowly evaporate. After 2 days, yellow rod-like crystals (**8b**) form. The crystals are filtered off, washed with acetonitrile (2 × 2 mL) and ethanol (2 × 3 mL), and dried in vacuum. Yield: 23 mg (26% based on Cu). Elemental analysis calculated (%) for C<sub>5</sub>H<sub>3</sub>CuICl<sub>2</sub>N: C 17.74, H 0.89, N 4.14; found: C 18.38, H 1.04, N 4.34; IR selected data (ATR):  $\tilde{\nu}$  (cm<sup>-1</sup>) = 3063 (vw), 3044 (w), 1867 (w), 1837 (w), 1810 (w), 1782 (w), 1560 (ms), 1551 (ms), 1415 (vs), 1387 (s), 1290 (m), 1217 (m), 1110 (s), 1094 (s), 1037 (m), 1015 (m), 903 (w), 874 (vs), 846 (m), 817 (vs), 678 (vs). TG-MS: 80-200 °C: m/z = 38, 48, 50, 63, 64, 78; 600-800 °C: m/z = 63.

The PXRD data confirmed the purity of **8b** and the similarity of its structure to that of **8a** (**Figure C11** in appendix C).

Thermal stability studies by thermogravimetric analysis (TGA) and TG-MS confirm that both crystals (**8a** and **8b**) exhibit the same behavior (**Figures D6-D9** in appendix D).

### 6.3.2. Preparation of composite materials based on CPs engulfed in a flexible organic polymeric matrix.

#### *6.3.2.1. Preparation of 5@PVDF composites*

Polyvinylidene difluoride (PVDF) was mixed with compound **5** in weight concentrations of 4, 15 and 30% w/w. Compound **5** was dispersed in acetone, and PVDF was dissolved in DMF. Both components were mixed in different ratios and dispersed with sonication for 30 min., allowing an almost total solution of **5**. The resulting homogeneous suspension was used to prepare different-sized **5@PVDF** films: thicker ones were prepared by casting the suspension on microscope slides and drying at 75 °C for 1 h to remove DMF; the films were delaminated via immersion in water and dried in air. Thin films were prepared by depositing the suspension on SiO<sub>2</sub> surfaces by dip-coating for 2 min. or spin-coating for 30 sec. at 17000 rpm and dried with an Argon flow. IR, PXRD and TGA data showed the presence of **5** in the films (**Figure C13** in appendix C and **Figures D10-D11** in appendix D).

#### *6.3.2.2. Preparation of 6@PLA composites*

Poly(lactic acid) (PLA) was mixed with compound **6** in weight concentrations of 1, 4 and 30% w/w. PLA was dissolved in chloroform at a weight concentration of 4% w/w. When it was fully dissolved, an amount of compound **6** (dependent of the final concentration of the MMM) was added to the solution, and both components were dispersed with sonication for 30 min., allowing a perfect scattering of **6**. The resulting homogeneous suspension was used to prepare different-sized **6@PLA** films: thicker ones were prepared by casting the suspension on microscope slides and drying at 25 °C for 24 h to remove chloroform; the films were delaminated manually. Thin films were prepared by depositing the suspension on SiO<sub>2</sub> surfaces by dip-coating for 2 min. or spin-coating for 30 sec. at 17000 rpm and dried with an Argon flow. IR, PXRD and TGA data showed the presence of **6** in the films (**Figure C14** in appendix C and **Figures D12-D13** in appendix D).

## 6.4. References

1. A. Altomare, M. Cascarano, C. Giacovazzo, A. Guagliardi, *Journal of Applied Crystallography* **1993**, 26, 343-350.
2. G. M. Sheldrick, SHELXL-97, Program for Crystal Structure Refinement; Universität Göttingen, Göttingen (Germany), **1997**.
3. M. J. Prakash, M. S. Lah, *Chemical Communications* **2009**, 3326-3341.
4. Rigaku Oxford Diffraction, CrysAlisPro Software system, version 1.171.38.41 (Rigaku Corporation), **2016**.
5. Y. H. Luo, H. W. Liu, F. Xi, L. Li, X. G. Jin, C. C. Han, C. M. Chan, *Journal of the American Chemical Society* **2003**, 125, 6447.
6. J. M. González-Pérez, C. Alarcón-Payer, A. Castiñeiras, T. Pivetta, L. Lezama, D. Choquesillo-Lazarte, G. Crisponi, J. Niclós-Gutiérrez, *Inorganic Chemistry* **2006**, 45, 877.
7. A. Spek, *Acta Crystallographica Section D* **2009**, 65, 148.
8. (a) S. Klotz, J. C. Chervin, P. Munsch, G. L. Marchand, *J. Phys. D: Appl. Phys.* **2009**, 42, 075413; (b) T. H. Kim, Y. W. Shin, J. S. Kim, S. S. Lee, J. Kim, *Inorganic Chemistry Communications* **2007**, 10, 717.
9. R. J. Angel, M. Bujak, J. Zhao, G. D. Gatta, S. D. Jacobsen, *Journal of Applied Crystallography* **2007**, 40, 26.
10. D. Errandonea, A. Muñoz J. Gonzalez-Platas, *Journal of Applied Physics* **2014**, 115, 216101.
11. M. Usman, S. Mendiratta K. L. Lu, *Advanced Materials* **2017**, 29, DOI: 10.1002/adma.201605071.
12. I. Horcas, R. Fernández, J. M. Gómez-Rodríguez, J. Colchero, J. Gómez-Herrero, A. M. Baro, *Review of Scientific Instruments* **2007**, 78, 013705.
13. D. Rocca, R. Gebauer, Y. Saad, S. Baroni, *The Journal of Chemical Physics* **2008**, 128, 154105.
14. B. Walker, R. Gebauer, *The Journal of Chemical Physics* **2007**, 127, 164106.
15. B. Walker, A. M. Saitta, R. Gebauer, S. Baroni, *Physical Review Letters* **2006**, 96, 113001.
16. S. Baroni, S. De Gironcoli, A. Dal Corso, P. Giannozzi, *Review of Modern Physics* **2011**, 73, 515.
17. X. Gonze, *Physical Review A* **1995**, 52, 1096.

18. S. Baroni, P. Giannozzi, A. Testa, *Physical Review Letters* **1987**, 58, 1861.
19. H. J. Monkhorst, J. D. Pack, *Physical Review B* **1976**, 13, 5188.
20. D. Vanderbilt, *Physical Review B* **1990**, 41, 7892.
21. M. J. Frisch, Gaussian 09, Revision E.01 (Gaussian, Inc.), **2009**.
22. S. Sakai, *The Journal of Physical Chemistry* **1992**, 96, 131.
23. K. Hassanein, One Dimensional Coordination Polymers with Molecular Recognition Capability as Dynamic and Multifunctional Materials. PhD Thesis, Universidad Autónoma de Madrid, Madrid (Spain), **2016**.
24. K. Hassanein, J. Conesa-Egea, S. Delgado, O. Castillo, S. Benmansour, J. I. Martinez, G. Abellan, C. J. Gomez-Garcia, F. Zamora, P. Amo-Ochoa, *Chemistry – A European Journal* **2015**, 21, 17282.
25. J. Conesa-Egea, C. D. Redondo, J. I. Martínez, C. J. Gómez-García, O. Castillo, F. Zamora, P. Amo-Ochoa, *Inorganic Chemistry* **2018**, 57, 7568.
26. J. Conesa-Egea, K. Hassanein, M. Muñoz, F. Zamora, P. Amo-Ochoa, *Dalton Transactions* **2018**, 47, 5607.
27. P. Amo-Ochoa, K. Hassanein, C. J. Gomez-Garcia, S. Benmansour, J. Perles, O. Castillo, J. I. Martinez, P. Ocon, F. Zamora, *Chemical Communications* **2015**, 51, 14306.
28. J. Conesa-Egea, N. Nogal, J. I. Martínez, V. Fernández-Moreira, U. R. Rodríguez-Mendoza, J. González-Platas, C. J. Gómez-García, S. Delgado, F. Zamora, P. Amo-Ochoa, *Chemical Science* **2018**, 9, 8000.
29. J. Conesa-Egea, J. Gallardo-Martínez, S. Delgado, J. I. Martínez, J. Gonzalez-Platas, V. Fernández-Moreira, U. R. Rodríguez-Mendoza, P. Ocón, F. Zamora, P. Amo-Ochoa, *Small* **2017**, 13, 1700965.

## Appendix A: Crystallographic tables

**Table A1.** Crystal structure parameters of compounds **1** and **7**.

	<b>1 (296 K)</b>	<b>7 (296 K)</b>	<b>7 (150 K)</b>
<b>Empirical formula</b>	C <sub>6</sub> H <sub>5</sub> CuINO <sub>2</sub>	C <sub>6</sub> H <sub>4</sub> CuIClNO <sub>2</sub>	C <sub>6</sub> H <sub>4</sub> CuIClNO <sub>2</sub>
<b>Formula weight</b>	313.55	347.99	347.99
<b>Space group</b>	<i>P</i> 2 <sub>1</sub> / <i>c</i>	<i>P</i> -1	<i>P</i> -1
<b>Crystal System</b>	Monoclinic	Triclinic	Triclinic
<b>a (Å)</b>	14.6503(7)	4.1563(1)	4.1277(3)
<b>b (Å)</b>	4.1198(2)	6.8049(2)	6.7277(3)
<b>c (Å)</b>	14.3078(7)	15.9619(6)	15.910(1)
<b>α (°)</b>	90	95.998(2)	96.336(4)
<b>β (°)</b>	104.892(2)	92.787(2)	92.834(4)
<b>γ (°)</b>	90	95.733(2)	96.282(4)
<b>V (Å<sup>3</sup>)</b>	834.56(7)	445.94(2)	435.64(5)
<b>Z</b>	4	2	2
<b>ρ<sub>calc</sub> (g·cm<sup>-3</sup>)</b>	2.496	2.592	2.653
<b>μ (mm<sup>-1</sup>)</b>	6.263	6.164	6.310
<b>Reflections collected/R<sub>int</sub></b>	11064/0.0514	12775/0.0341	21566/0.0988
<b>Unique data/parameters</b>	1526/101	1614/110	1568/110
<b>Goodness of fit (<i>S</i>)</b>	1.176	1.018	1.164
<b><i>R</i>1/<i>wR</i>2 [<i>I</i>&gt;2σ(<i>I</i>)]</b>	0.0286/0.0668	0.0184/0.0350	0.0291/0.0668
<b><i>R</i>1/<i>wR</i>2 [all data]</b>	0.0515/0.0998	0.0224/0.0364	0.0451/0.0993

**Table A2.** Selected distances (Å) and angles (°) of compounds **1** and **7**.

	<b>1 (296 K)</b>	<b>7 (296 K)</b>	<b>7 (150 K)</b>
<b>Cu-I1<sub>rail</sub></b>	2.632(1)	2.6568(5)	2.644(1)
<b>Cu-I1<sup>i</sup><sub>rail</sub></b>	2.631(1)	2.6351(4)	2.625(1)
$\Delta$ [ <b>Cu-I1<sub>rail</sub></b> ]	0.001	0.0217	0.019
<b>Cu-I1<sub>rung</sub></b>	2.658(1)	2.6296(5)	2.620(1)
<b>Cu-N1</b>	2.054(5)	2.059(3)	2.059(6)
<b>Cu-Cu<sup>ii</sup></b>	2.872(1)	2.8141(8)	2.786(2)
<b>Cu-Cu<sup>iii</sup></b>	2.872(1)	2.7546(8)	2.719(2)
$\Delta$ [ <b>Cu-Cu</b> ]	0.000	0.0595	0.067
<b>I1-Cu1-I1<sup>i</sup></b>	103.01(3)	103.51(2)	103.13(3)
<b>I1-Cu1-I1<sup>ii</sup></b>	114.24(3), 114.27(4)	115.68(2)	116.10(4)
<b>I1<sup>i</sup>-Cu1-I1<sup>i</sup></b>	114.27(4), 114.24(3)	116.90(2)	117.55(4)
<b>Cu1-I1-Cu1<sup>ii</sup></b>	65.74(3), 65.75(3)	64.32(2)	63.90(4)
<b>Cu1-I1-Cu1<sup>iii</sup></b>	103.01(3)	103.51(2)	103.13(3)
<b>Cu1<sup>ii</sup>-I1-Cu1<sup>iii</sup></b>	65.75(3), 65.74(3)	63.10(2)	62.45(4)
<b>Dihedral angle</b>	119.3	122.3	122.7
<b>Tilt angle</b>	90.6	88.3	89.2
<b>Twist angle</b>	61.0	57.4	59.3

**Table A3.** Crystal structure parameters of **4** and **5**.

	<b>4 (296 K)</b>	<b>4 (200 K)</b>	<b>4 (110 K)</b>	<b>5 (296 K)</b>	<b>5 (110 K)</b>
<b>Empirical formula</b>	C <sub>7</sub> H <sub>7</sub> CuINO <sub>2</sub>	C <sub>7</sub> H <sub>7</sub> CuINO <sub>2</sub>	C <sub>7</sub> H <sub>7</sub> CuINO <sub>2</sub>	C <sub>7</sub> H <sub>8</sub> CuIN <sub>2</sub> O <sub>2</sub>	C <sub>7</sub> H <sub>8</sub> CuIN <sub>2</sub> O <sub>2</sub>
<b>Formula weight</b>	327.58	327.58	327.58	342.59	342.59
<b>Space group</b>	<i>P</i> 2 <sub>1</sub> / <i>c</i>	<i>P</i> 2 <sub>1</sub> / <i>c</i>	<i>P</i> 2 <sub>1</sub> / <i>c</i>	<i>P</i> -1	<i>P</i> -1
<b>Crystal System</b>	Monoclinic	Monoclinic	Monoclinic	Triclinic	Triclinic
<b>a (Å)</b>	4.1603(1)	4.128(1)	4.1003(1)	4.2503(2)	4.2103(3)
<b>b (Å)</b>	24.2918(8)	24.186(6)	24.1725(7)	10.1169(4)	9.9279(6)
<b>c (Å)</b>	9.5711(3)	9.370(3)	9.3158(3)	11.3784(5)	11.2864(7)
<b>α (°)</b>	90	90	90	81.030(3)	82.189(3)
<b>β (°)</b>	99.171(2)	97.62(1)	96.696(2)	88.843(3)	89.223(3)
<b>γ (°)</b>	90	90	90	82.580(4)	83.312(3)
<b>V (Å<sup>3</sup>)</b>	954.90(5)	927.1(4)	917.03(5)	479.24(4)	464.21(5)
<b>Z</b>	4	4	4	2	2
<b>ρ<sub>calc</sub> (g·cm<sup>-3</sup>)</b>	2.279	2.347	2.372	2.374	2.451
<b>μ (mm<sup>-1</sup>)</b>	5.479	5.643	5.705	5.467	5.644
<b>Reflections collected/R<sub>int</sub></b>	15471/ 0.0305	6987/ 0.0412	3329/ 0.0315	2481/-	1691/-
<b>Unique data/parameters</b>	1734/110	1684/110	1609/109	2481/127	1691/119
<b>Goodness of fit (S)</b>	1.259	1.157	1.089	1.036	1.319
<b>R1/wR2 [I&gt;2σ(I)]</b>	0.0342/ 0.0635	0.0293/ 0.0805	0.0342/ 0.0596	0.0247/ 0.0477	0.0189/ 0.0548
<b>R1/wR2 [all data]</b>	0.0472/ 0.0671	0.0436/ 0.1050	0.0446/ 0.0647	0.0292/ 0.0493	0.0235/ 0.0740



**Table A4.** Selected distances (Å) and angles (°) of **4** and **5**.

	<b>4 (296 K)</b>	<b>4 (200 K)</b>	<b>4 (110 K)</b>	<b>5 (296 K)</b>	<b>5 (110 K)</b>
<b>Cu-I1<sub>rail</sub></b>	2.6678(9)	2.663(1)	2.6616(8)	2.643(2)	2.6257(6)
<b>Cu-I1<sup>i</sup><sub>rail</sub></b>	2.6507(9)	2.639(1)	2.6408(8)	2.733(2)	2.7181(6)
<b>Δ[Cu-I1<sub>rail</sub>]</b>	0.0171	0.024	0.0208	0.090	0.0924
<b>Cu-I1<sub>rung</sub></b>	2.647(1)	2.641(1)	2.6376(8)	2.680(2)	2.6682(6)
<b>Cu-N1</b>	2.051(5)	2.057(6)	2.057(4)	2.04(1)	2.028(4)
<b>Cu-Cu<sup>ii</sup></b>	2.751(2)	2.719(2)	2.698(1)	2.682(4)	2.627(1)
<b>Cu-Cu<sup>iii</sup></b>	2.823(2)	2.764(2)	2.724(1)	3.514	3.523
<b>Δ[Cu-Cu]</b>	0.072	0.045	0.026	0.832	0.896
<b>I1-Cu1-I1<sup>i</sup></b>	102.93(3)	102.25(4)	101.30(3)	104.33(8)	103.96(2)
<b>I1-Cu1-I1<sup>ii</sup></b>	115.83(3)	117.19(4)	118.13(3)	99.05(7)	98.31(2)
<b>I1<sup>i</sup>-Cu1-I1<sup>i</sup></b>	117.44(3)	118.02(4)	118.51(3)	119.51(8)	120.50(2)
<b>Cu1-I1-Cu1<sup>ii</sup></b>	64.17(3)	62.81(4)	61.87(3)	80.95(7)	81.69(2)
<b>Cu1-I1-Cu1<sup>iii</sup></b>	102.93(3)	102.25(4)	101.30(3)	104.34(8)	103.96(2)
<b>Cu1<sup>ii</sup>-I1-Cu1<sup>iii</sup></b>	62.56(3)	61.99(4)	61.49(3)	60.49(8)	59.50(2)
<b>Dihedral angle</b>	122.1	122.9	122.9	112.22	111.65
<b>Tilt angle</b>	88.7	88.3	88.0	87.47	88.19
<b>Twist angle</b>	59.1	58.3	58.1	53.52	52.87

**Table A5.** Crystal structure parameters of **6**.

	<b>6 (296 K)</b>	<b>6 (110 K)</b>
<b>Empirical formula</b>	C <sub>4</sub> H <sub>5</sub> Cu <sub>2</sub> I <sub>2</sub> N <sub>3</sub>	C <sub>4</sub> H <sub>5</sub> Cu <sub>2</sub> I <sub>2</sub> N <sub>3</sub>
<b>Formula weight</b>	475.99	475.99
<b>Space group</b>	<i>P</i> -1	<i>P</i> -1
<b>Crystal System</b>	Triclinic	Triclinic
<b>a (Å)</b>	4.2224(2)	4.2003(4)
<b>b (Å)</b>	7.6959(4)	7.6091(7)
<b>c (Å)</b>	7.7567(4)	7.7271(7)
<b>α (°)</b>	107.789(5)	107.773(5)
<b>β (°)</b>	97.912(4)	97.910(5)
<b>γ (°)</b>	101.030(4)	100.762(5)
<b>V (Å<sup>3</sup>)</b>	230.33(2)	225.98(4)
<b>Z</b>	1	1
<b>ρ<sub>calc</sub> (g·cm<sup>-3</sup>)</b>	3.424	3.498
<b>μ (mm<sup>-1</sup>)</b>	11.256	11.473
<b>Reflections collected/R<sub>int</sub></b>	4976/0.017	5808/0.0299
<b>Unique data/parameters</b>	1150/55	810/55
<b>Goodness of fit (<i>S</i>)</b>	1.054	1.283
<b><i>R</i>1/<i>wR</i>2 [<i>I</i> &gt; 2σ(<i>I</i>)]</b>	0.0184/0.0405	0.0228/0.0712
<b><i>R</i>1/<i>wR</i>2 [all data]</b>	0.0202/0.0415	0.0196/0.0701

**Table A6.** Selected distances (Å) and angles (°) of **6**.

	<b>6 (296 K)</b>	<b>6 (110 K)</b>
<b>Cu-I1<sub>rail</sub></b>	2.6500(7)	2.631(1)
<b>Cu-I1<sup>i</sup><sub>rail</sub></b>	2.6824(7)	2.6738(9)
$\Delta[\text{Cu-I1}_{\text{rail}}]$	0.0324	0.043
<b>Cu-I1<sub>rung</sub></b>	2.6576(7)	2.655(1)
<b>Cu-N1</b>	2.042(3)	2.035(6)
<b>Cu-Cu<sup>ii</sup></b>	2.715(1)	2.660(2)
<b>Cu-Cu<sup>iii</sup></b>	3.253	3.269
$\Delta[\text{Cu-Cu}]$	0.538	0.609
<b>I1-Cu1-I1<sup>i</sup></b>	104.74(2)	104.71(3)
<b>I1-Cu1-I1<sup>ii</sup></b>	118.47(2)	119.58(3)
<b>I1<sup>i</sup>-Cu1-I1<sup>i</sup></b>	104.93(2)	104.34(3)
<b>Cu1-I1-Cu1<sup>ii</sup></b>	61.53(2)	60.42(3)
<b>Cu1-I1-Cu1<sup>iii</sup></b>	104.74(2)	104.71(3)
<b>Cu1<sup>ii</sup>-I1-Cu1<sup>iii</sup></b>	75.07(2)	75.66(3)

**Table A7.** Most representative variation in the Cu-Cu distances (Å) and I-Cu-I and Cu-I-Cu angles (°) for **5** at ambient pressure (0 GPa) and 7.16 GPa.

	<b>5 (0 GPa)</b>	<b>5 (7.16 GPa)</b>	$\Delta$
<b>Cu-Cu<sup>ii</sup></b>	2.682(4)	2.53(1)	-0.15 (5.60 %)
<b>Cu-Cu<sup>iii</sup></b>	3.514	3.151	-0.363 (10.33 %)
<b>I1-Cu1-I1<sup>i</sup></b>	104.33(8)	100.7(1)	-3.6 (3.45 %)
<b>I1-Cu1-I1<sup>ii</sup></b>	99.05(7)	105.5(2)	+6.5 (6.56 %)
<b>I1<sup>i</sup>-Cu1-I1<sup>i</sup></b>	119.51(8)	121.7(3)	+2.2 (1.84 %)
<b>Cu1-I1-Cu1<sup>ii</sup></b>	80.95(7)	74.5(2)	-6.5 (8.03 %)
<b>Cu1<sup>ii</sup>-I1-Cu1<sup>iii</sup></b>	60.49(8)	58.3(3)	-2.2 (3.64 %)

**Table A8.** Most representative variation in the Cu-Cu distances (Å) and I-Cu-I and Cu-I-Cu angles (°) for **6** at ambient pressure (0 GPa) and 8.35 GPa.

	<b>6 (0 GPa)</b>	<b>6 (8.35 GPa)</b>	$\Delta$
<b>Cu-Cu<sup>ii</sup></b>	2.715	2.543	-0.172 (6.34%)
<b>Cu-Cu<sup>iii</sup></b>	3.253	2.693	-0.560 (17.21%)
<b>I1-Cu1-I1<sup>i</sup></b>	104.74	101.83	-2.91 (2.78%)
<b>I1-Cu1-I1<sup>ii</sup></b>	118.47	121.01	+2.54 (2.14%)
<b>I1<sup>i</sup>-Cu1-I1<sup>i</sup></b>	104.93	116.15	+11.22 (10.69%)
<b>Cu1-I1-Cu1<sup>ii</sup></b>	61.53	58.99	-2.54 (4.13%)
<b>Cu1<sup>ii</sup>-I1-Cu1<sup>iii</sup></b>	75.07	63.85	-11.22 (14.95%)

**Table A9.** Crystal structure parameters of **8a** and **8b**.

	<b>8a (296 K)</b>	<b>8a (110 K)</b>	<b>8b (296 K)</b>
<b>Empirical formula</b>	C <sub>5</sub> H <sub>3</sub> Cl <sub>2</sub> CuIN	C <sub>5</sub> H <sub>3</sub> Cl <sub>2</sub> CuIN	C <sub>5</sub> H <sub>3</sub> Cl <sub>2</sub> CuIN
<b>Formula weight</b>	338.42	338.42	338.42
<b>Space group</b>	<i>P2<sub>1</sub>/c</i>	<i>P2<sub>1</sub>/c</i>	<i>P2<sub>1</sub>/c</i>
<b>Crystal System</b>	Monoclinic	Monoclinic	Monoclinic
<b>a (Å)</b>	13.1164(6)	12.961(2)	13.1301(6)
<b>b (Å)</b>	4.2363(2)	4.2177(5)	4.2377(2)
<b>c (Å)</b>	15.1474(5)	15.008(2)	15.1614(7)
<b>α (°)</b>	90	90	90
<b>β (°)</b>	94.613(4)	94.247(5)	94.623(4)
<b>γ (°)</b>	90	90	90
<b>V (Å<sup>3</sup>)</b>	838.94(6)	818.2(2)	840.86(7)
<b>Z</b>	4	4	4
<b>ρ<sub>calc</sub> (g·cm<sup>-3</sup>)</b>	2.679	2.747	2.673
<b>F(000)</b>	624	624	624
<b>μ (mm<sup>-1</sup>)</b>	6.840	7.013	6.824
<b>Reflections collected/R<sub>int</sub></b>	3723/0.0189	12661/0.0320	2141/0.0160
<b>Unique data/parameters</b>	2059/91	1495/91	1211/91
<b>Goodness of fit (S)</b>	1.089	1.280	1.079
<b>R1/wR2 [<i>I</i>&gt;2σ(<i>I</i>)]</b>	0.0330/0.0550	0.0144/0.0420	0.0223/0.0425
<b>R1/wR2 [all data]</b>	0.0464/0.0596	0.0200/0.0699	0.0291/0.0454

**Table A10.** Selected distances (Å) and angles (°) of **8a** and **8b**.

	<b>8a (296 K)</b>	<b>8a (110 K)</b>	<b>8b (296 K)</b>
<b>Cu-I1<sub>rail</sub></b>	2.6159(6)	2.6163(6)	2.6173(6)
<b>Cu-I1<sup>i</sup><sub>rail</sub></b>	2.6812(6)	2.6742(6)	2.6832(6)
$\Delta$ [ <b>Cu-I1<sub>rail</sub></b> ]	0.0653	0.0579	0.0659
<b>Cu-I1<sub>rung</sub></b>	2.6415(6)	2.6352(6)	2.6427(7)
<b>Cu-N1</b>	2.083(3)	2.084(3)	2.083(4)
<b>Cu-Cu<sup>ii</sup></b>	2.8092(7)	2.7689(6)	2.8118(8)
<b>Cu-Cu<sup>iii</sup></b>	2.8092(7)	2.7689(6)	2.8118(8)
$\Delta$ [ <b>Cu-Cu</b> ]	0.000	0.000	0.000
<b>I1-Cu1-I1<sup>i</sup></b>	106.20(2)	105.73(2)	106.16(2)
<b>I1-Cu1-I1<sup>ii</sup></b>	116.97(2), 114.72(2)	117.77(2), 115.72(2)	116.95(2), 114.68(2)
<b>I1<sup>i</sup>-Cu1-I1<sup>i</sup></b>	114.72(2), 116.97(2)	115.72(2), 117.77(2)	114.68(2), 116.95(2)
<b>Cu1-I1-Cu1<sup>ii</sup></b>	64.59(2), 63.70(2)	63.64(1), 62.86(1)	64.63(2), 63.73(2)
<b>Cu1-I1-Cu1<sup>iii</sup></b>	106.20(2)	105.73(2)	106.16(2)
<b>Cu1<sup>ii</sup>-I1-Cu1<sup>iii</sup></b>	63.70(2), 64.59(2)	62.86(1), 63.64(1)	63.73(2), 64.63(2)
<b>I1-Cu1-N1</b>	110.3(1)	109.65(9)	110.3(1)
<b>I1<sup>i</sup>-Cu1-N1</b>	101.8(1)	105.1(1)	101.9(1)
<b>Dihedral angle</b>	125.38	127.22	125.25
<b>Tilt angle</b>	89.89	89.62	89.86
<b>Twist angle</b>	59.15	58.43	59.17
<b>Interchain distance</b>	2.834	2.730	2.839

Symmetry codes: i) x-1, y, z; ii) -x, -y, -z+1; iii) -x+1, -y, -z+1

**Table A11.** Variation of Cu···Cu distances and I-Cu-I and Cu-I-Cu angles for compound **8b** with pressure.

Distances (Å) and angles (°)	<b>8b</b> (0 GPa)	<b>8b</b> (5.56 GPa) (variation w.r.t. 0 GPa)	<b>8b</b> (6.20 GPa) (variation w.r.t. 0 GPa)
Cu-Cu <sup>ii</sup>	2.8118(8)	2.602(9) (-7.5%)	2.73(1) (-2.8%)
Cu-Cu <sup>iii</sup>	2.8118(8)	2.602(9) (-7.5%)	2.73(1) (-2.8%)
I1-Cu1-I1 <sup>i</sup>	106.16(2)	103.6(5) (-2.4%)	104.7(7) (-1.4%)
I1-Cu1-I1 <sup>ii</sup>	116.95(2)	121.0(3) (+3.4%)	118.6(4) (+1.4%)
I1 <sup>i</sup> -Cu1-I1 <sup>i</sup>	114.68(2)	118.4(3) (+3.2%)	115.0(4) (+0.3%)
Cu1-I1-Cu1 <sup>ii</sup>	64.63(2)	60.7(2) (-6.0%)	63.8(3) (-1.2%)
Cu1 <sup>ii</sup> -I1-Cu1 <sup>ii</sup>	63.73(2)	59.9(2) (-6.0%)	62.5(3) (-1.9%)

Symmetry codes: i) x-1, y, z; ii) -x, -y, -z+1; iii) -x+1, -y, -z+1

## Appendix B: Pressure-dependent SC-XRD studies

### B1. Compound 5

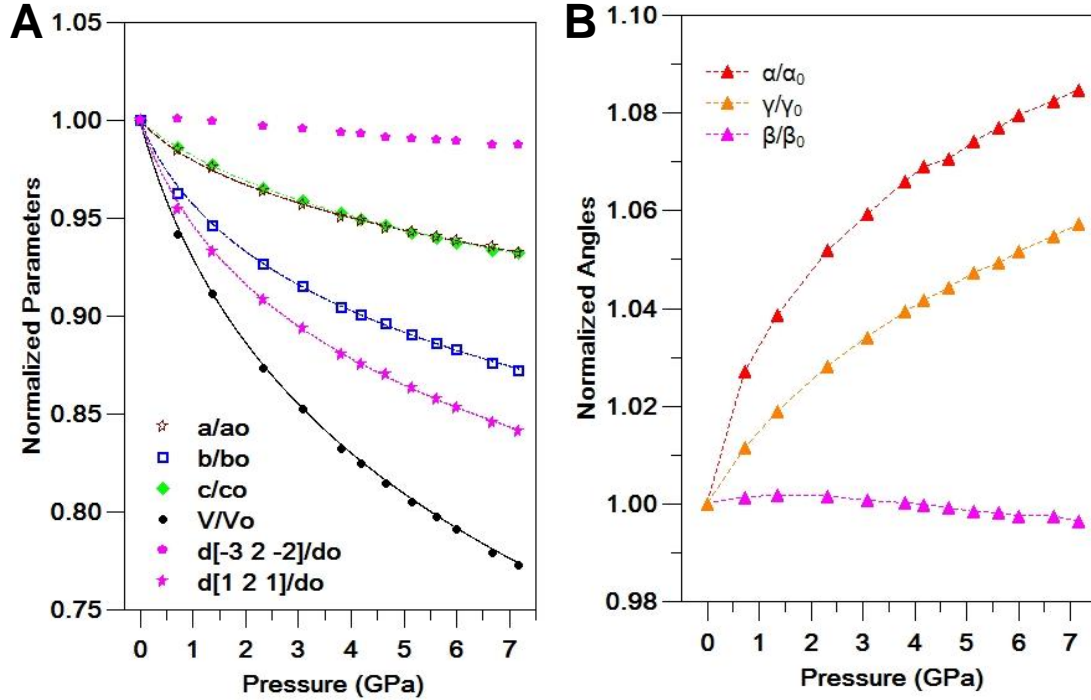


**Figure B1.** Variation of the cell distances and volume (a) and angles (b) of **5** with pressure. Error bars are smaller than their respective size symbols. Curve lines in (a) correspond to the respective EoS model fit.

Evolution of all unit cell parameters is smoothed up to the maximum pressure achieved. The  $b$ -axis is substantially softer than  $a$  and  $c$ -axes while the  $\alpha$  angle is the most variable angle and  $\beta$  angle remains almost unchanged but with a maximum around 1.5 GPa. The softest direction found for this compound is  $[1\ 2\ 1]$  as is showed on **Figure B1a**.

For EoS calculations we have selected the 3rd-order Birch-Murnaghan (BM) according to the information obtained from the plots of the axes and  $V$  unit-cell parameters as normalized pressure ( $F$ ) pressure against finite strain ( $f$ ) (i.e.  $f$ - $F$  plots, **Figure B2**). The  $f$ - $F$  plots for unit-cell parameters exhibit a curvature at low pressures indicating that values at zero pressure are not strictly consistent with the higher-pressure data. However, comparison of data collected from crystals within the DAC but without pressure fluid and data from crystals in air, shows that the formal uncertainties obtained for the unit-cell parameters are underestimated, and this accounts for the observed curvature in the  $f$ - $F$  plots.



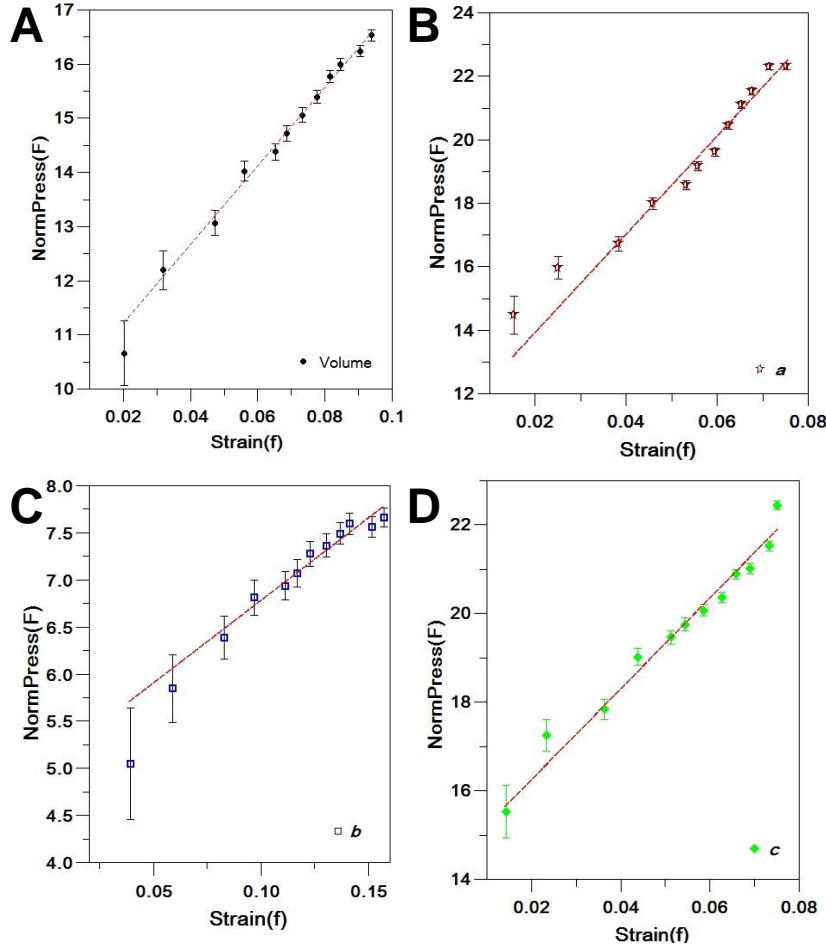


**Figure B2.**  $f$ - $F$  plots for Volume (a) and cell parameters (b-d) for **5**.

The volume ( $V$ ) and cell parameters ( $a$ ,  $b$  and  $c$ ) at equilibrium are displayed as  $V_0$  and  $L_0$ , in **Table B1**, linear and bulk moduli  $M_0$  and  $K_0$ , both in GPa, and their first derivative  $M'_0$  and  $K'_0$  for each axis and the bulk respectively. The fitting procedure was done with the *EosFit7-GUI* programme<sup>1</sup> using the BM EoS, with the linear modification of Angel *et al.* used to fit individual cell parameters and directions. The refinements of EoS all yield  $w\chi^2 < 1$  because of the overestimation of the  $\sigma(P)$ , but none of the fits show any systematic variation of  $P_{obs} - P_{Calc}$  with pressure, indicating that the reported parameters represent the data well. Lines on **Figure B1a** show the fitted EoS models.

**Table B1.** EoS parameters for **5**.

Parameter	EoS Model	$L_0$ (Å)	$M_0$ (GPa)	$M'_0$ (GPa)
$a$	BM3	4.25029(3)	32(2)	40(3)
$b$	BM3	10.1169(6)	15.1(6)	19.0(8)
$c$	BM3	11.3784(8)	42(2)	26(2)
$d[1\ 2\ 1]$	BM3	25.5519(8)	12.4(3)	13.8(3)
		$V_0$ (Å <sup>3</sup> )	$K_0$ (GPa)	$K'_0$ (GPa)
$V$	BM3	479.24(4)	9.7(2)	9.0(3)

The value of  $K_0$  falls in the lower limit of the range typical for organometallic compounds (10-20 GPa),<sup>2-3</sup> whereas the diamond anvil shows a  $K_0$  value of 440 GPa.<sup>4</sup> This, and the fits shown in **Table B1**, confirm that the hydrostatic compression of this material is very anisotropic, with the  $b$ -axis being much softer than the other two unit-cell axes. However, this material is triclinic and therefore the compression of the unit-cell axes alone does not necessarily represent the true compressibility tensor. The true pattern of compressibility is represented by the strain ellipsoid due to compression; two of the principal axes of this ellipsoid represent the directions of minimum and maximum compression, which can rotate with respect to the unit-cell axes during compression. The principal strains from the measured unit-cell parameters at each pressure and the room-pressure unit-cell were calculated with the Win\_Strain programme<sup>5</sup> We used the Eulerian finite strain definition because this is the same as used for BM EoS calculations; the orientation of the strain ellipsoid is not sensitive to the choice of strain definition. The softest direction was determined as  $[1\ 2\ 1]$  direction and not so far with values obtained for the  $b$ -axis.

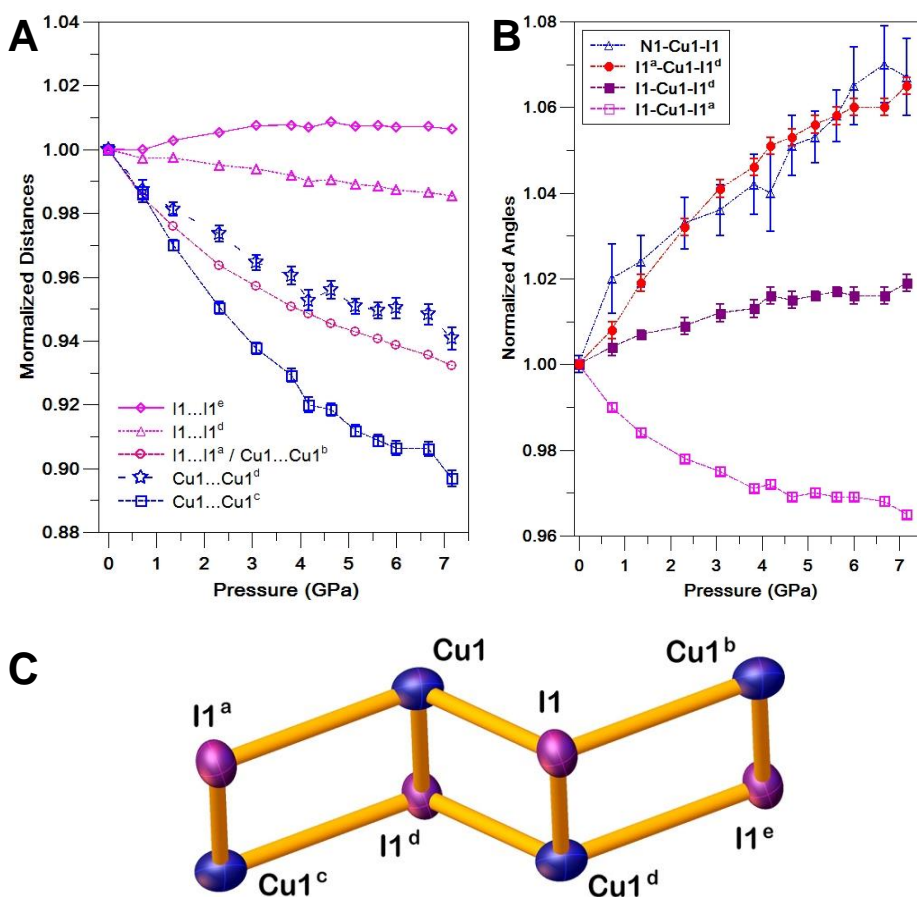


**Figure B3.** (a,b) Variation of the Cu...Cu and I...I distances (a) and angles (b) of **5** with pressure. Error bars represent the standard deviation for each value. c) Schematic representation of the Cu<sub>2</sub>I<sub>2</sub> chain in **5**. Symmetry codes: *a*:  $-1+x, y, z$ ; *b*:  $1+x, y, z$ ; *c*:  $1-x, -y, 1-z$ ; *d*:  $2-x, -y, 1-z$ ; *e*:  $3-x, -y, 1-z$ .

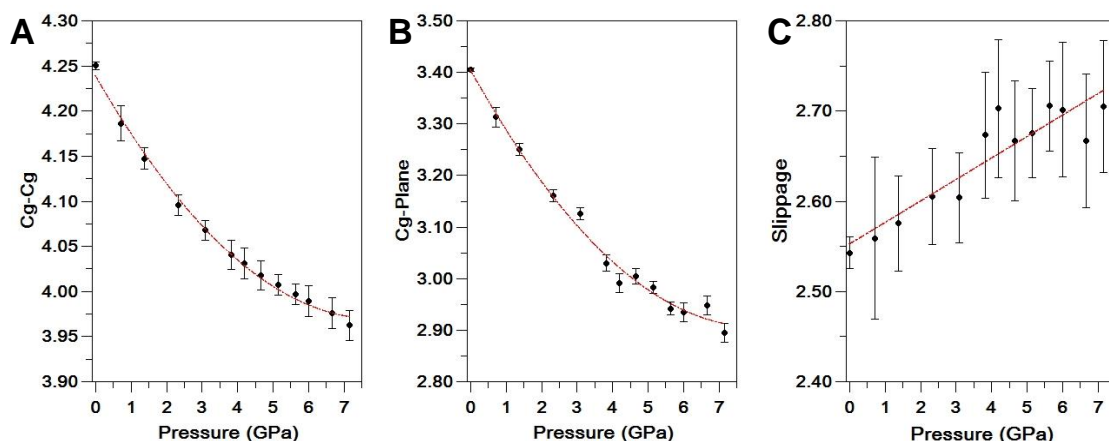


**Figure B4.** Perpendicular distances between layers (a, b) and their respective mutual slippage (in-plane component of relative displacement) (c) with pressure.

## B2. Compound 6

**Figure B5** presents the behavior of the main bond distances and angles of compound **6** with pressure. The evolution of these parameters shows that, in a similar way than in the case of compound **5**, the main change is a slight deformation of the Cu-I ladders. The layers maintain their planarity and orientation but the small displacement of the ligands over one another (**Figure B6**) appears to be the cause for the changes on the  $\alpha$  and  $\beta$  angles with pressure (**Figure B7**).

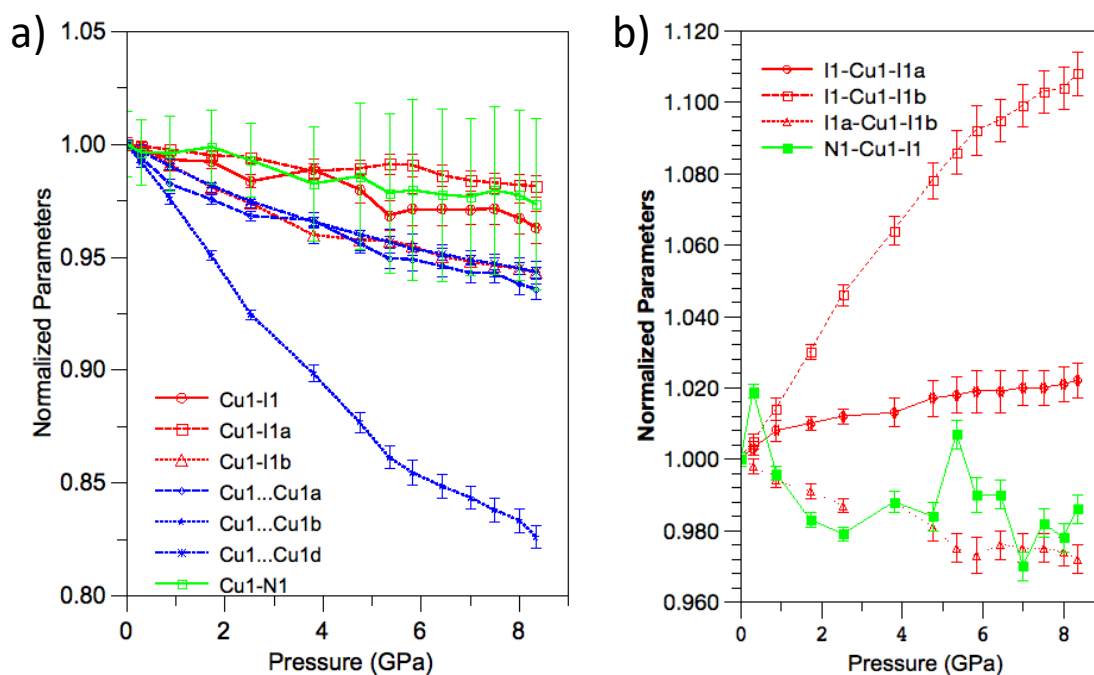


**Figure B5.** Variation of the Cu...Cu, Cu-N and Cu-I distances (a) and angles (b) with pressure for compound **6**. Error bars represent the standard deviation for each value.

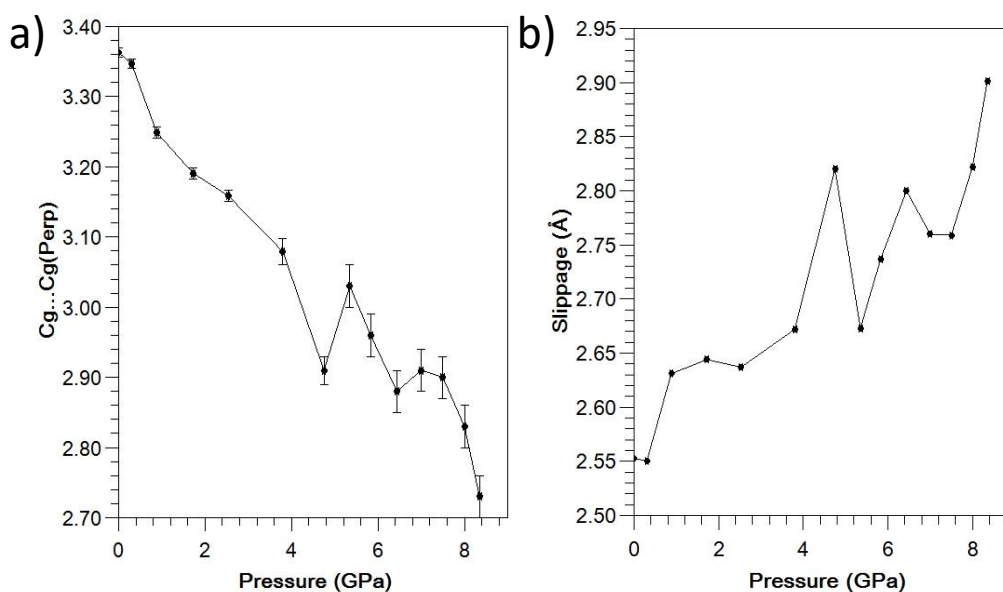


**Figure B6.** Perpendicular distances between **6** layers (a) and their respective mutual slippage (in-plane component of relative displacement) (b) with pressure.

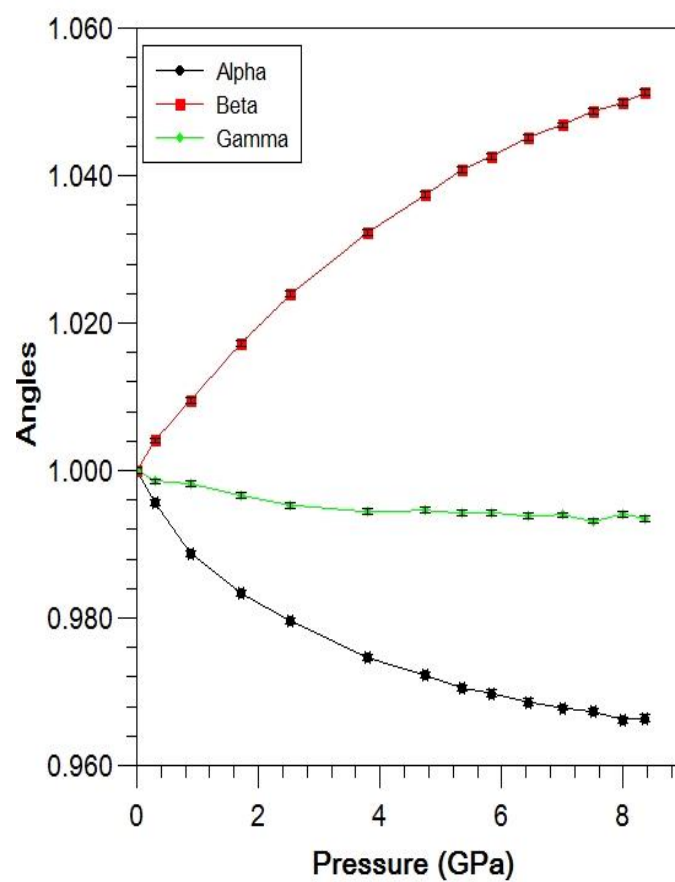


**Figure B7.** Variation of the crystallographic angles  $\alpha$ ,  $\beta$  and  $\gamma$  of compound **6** with pressure. The angles are normalized with respect to their values at 0 GPa.

The study of the isothermal EoS gives details of interatomic interactions that are influenced by the externally applied compressive stresses. From this study, it is possible to obtain the bulk modulus ( $K_0$ ), which measures the compressive strength of the material and in this case has a value of 14.1(3) GPa (**Table B2**). This value falls into the range of 10-20 GPa typical for organometallic compounds,<sup>2-3</sup> while diamond has a  $K_0$  of 440 GPa.<sup>4</sup> In general, these lower values are attributable to deformability of the intermolecular interactions or voids present in the structure. A similar CP based on a Cu(I)-I chain was studied by Aguirrechu *et al.*<sup>6</sup> yielding a  $K_0$  value of 10.2(2) GPa, so the values obtained for **5** and **6** suggest that their elastic properties are close to those of other similar CPs.

Moreover, the fits shown in **Table B2** confirm that the hydrostatic compression of this material is very anisotropic, with the  $b$ -axis being much softer than the other two unit cell axes (**Figure B8**). However, this material is triclinic and therefore the compression of the unit-cell axes alone does not necessarily represent a true compressibility tensor. The true pattern of compressibility is represented by the strain ellipsoid due to compression; two of the principal axes of this ellipsoid represent the directions of minimum and maximum compression, which can rotate with respect to the unit-cell axes during compression. The *Win\_Strain* program<sup>5</sup> was used to calculate the principal strains from the measured unit-cell parameters at each pressure and the room pressure unit-cell. We used the Eulerian finite strain definition because this is the same as used for BM EoS calculations; the orientation of the strain ellipsoid is not sensitive to the choice of strain definition. Unfortunately, some changes in the orientation were observed in the strain calculations. The softest direction points to [3 0 2] direction after 2 GPa. The stiffest direction is 90° from this direction and is thus close to the (-2 0 3) normal plane. The refined linear modulus is double respect to the soft  $b$ -axis but the main difference arises from the fact that pressure derivative of the linear modulus is like the  $c$ -axis but a quarter of the value for  $b$ -axis (**Table B2**).

Evolution of all unit cell parameters is smoothed up to the maximum pressure achieved. The  $b$  axis is substantially softer than  $a$  and  $c$  axes and the  $\beta$  angle is the most variable angle while  $\gamma$  angle remains almost unchanged. Plots of the axes and  $V$  unit-cell parameters as normalized pressure ( $F$ ) pressure against finite strain ( $f$ ) (i.e.  $f$ - $F$  plots) are straight lines with positive slopes within the uncertainties, indicating that they can be fit with 3rd-order Birch-Murnaghan (BM) EoS (**Figure B8**). The  $f$ - $F$  plots for unit-cell parameters exhibit a curvature at low pressures indicating that values at zero pressure are not strictly consistent with the higher-pressure data. However, comparison of data collected from crystals within the DAC but without pressure fluid and data from crystals in air, shows that the formal uncertainties obtained for the unit-cell parameters are underestimated, and this accounts for the observed curvature in the  $f$ - $F$  plots. The refinements of EoS all yield  $w\chi^2 < 1$  because of the overestimation of the  $\sigma(P)$ , but none of the fits show any systematic variation of  $P_{obs}-P_{Calc}$  with pressure, indicating that the reported parameters represent the data well (**Figure B9**).

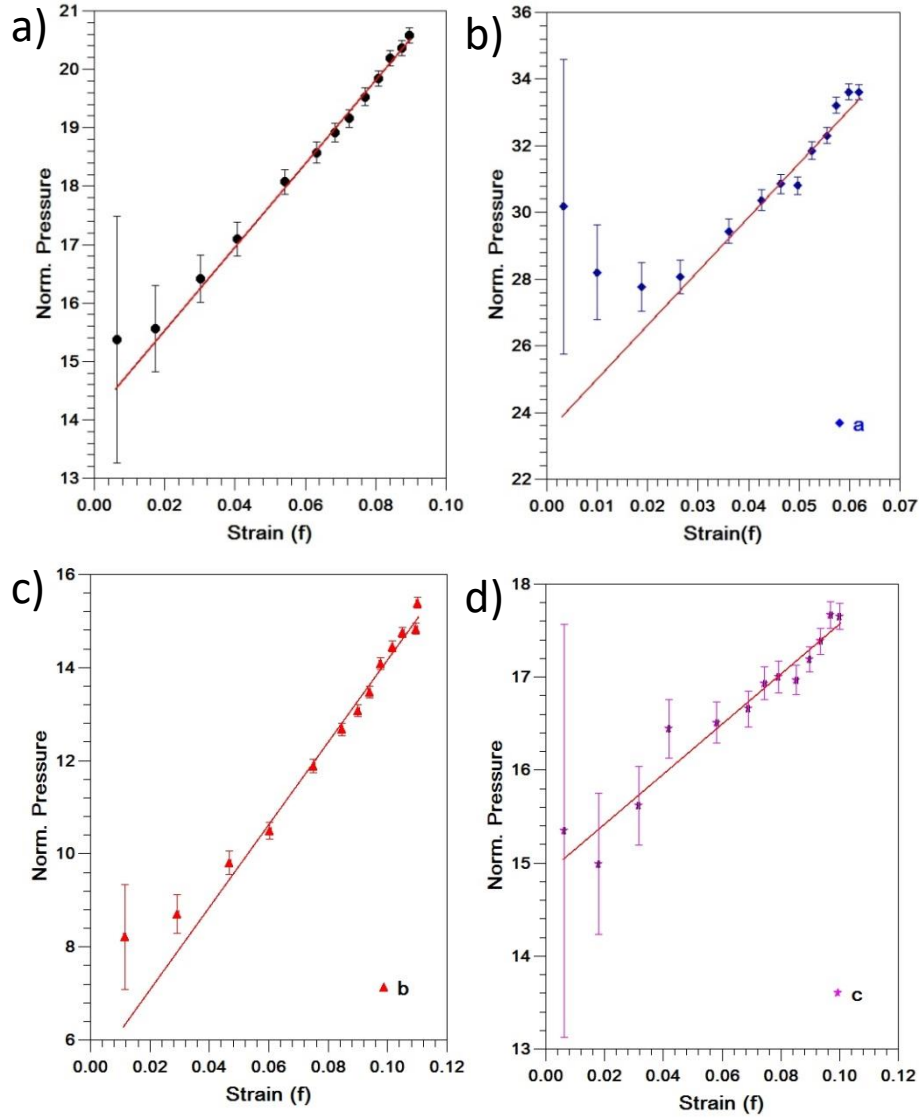


**Figure B8.**  $f$ - $F$  plots for Volume and cell parameters for **6**. The volume  $V$  (a) and cell parameters  $a$ ,  $b$  and  $c$ , b-d respectively, at equilibrium are displayed as  $V_0$  and  $L_0$ , in **Table B2**, along with the linear moduli  $M_0$  of each axis, the bulk modulus  $K_0$  (both in GPa) and the bulk modulus first derivative  $K'_0$ . The fitting procedure was done with the *EosFit7-GUI* program<sup>5</sup> using the BM EoS, with the linear modification of Angel *et al.*<sup>1</sup> used to fit individual cell parameters and directions.

**Table B2.** EoS parameters for **6**.

Parameter	EoS Model	$L_0$ (Å)	$M_0$ (GPa)	$M'_0$ (GPa)
$a$	BM3	4.222(1)	70(3)	26(2)
$b$	BM3	7.697(3)	16(1)	46(4)
$c$	BM3	7.752(2)	44.6(9)	15.6(5)
$d[3\ 0\ 2]$	BM3	18.622(5)	30.3(6)	11.5(3)
		$V_0$ (Å <sup>3</sup> )	$K_0$ (GPa)	$K'_0$ (GPa)
$V$	BM3	230.2(1)	14.1(3)	7.4(2)

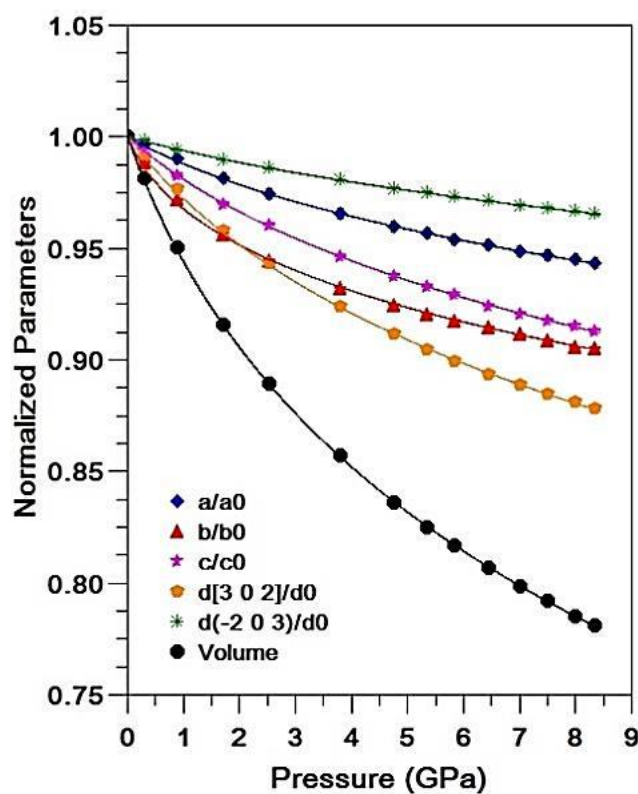


**Figure B9.** Normalized parameters for compound **6**. Curve lines correspond with the respective EoS model fit.

### B3. Compound 8

The differences between samples were negligible as can be observed on **Figure B10** except for  $b$ -axis. However, compound **8a** deteriorated after exceeding pressures of 6 GPa, so for the rest of experiments we will focus on compound **8b**.

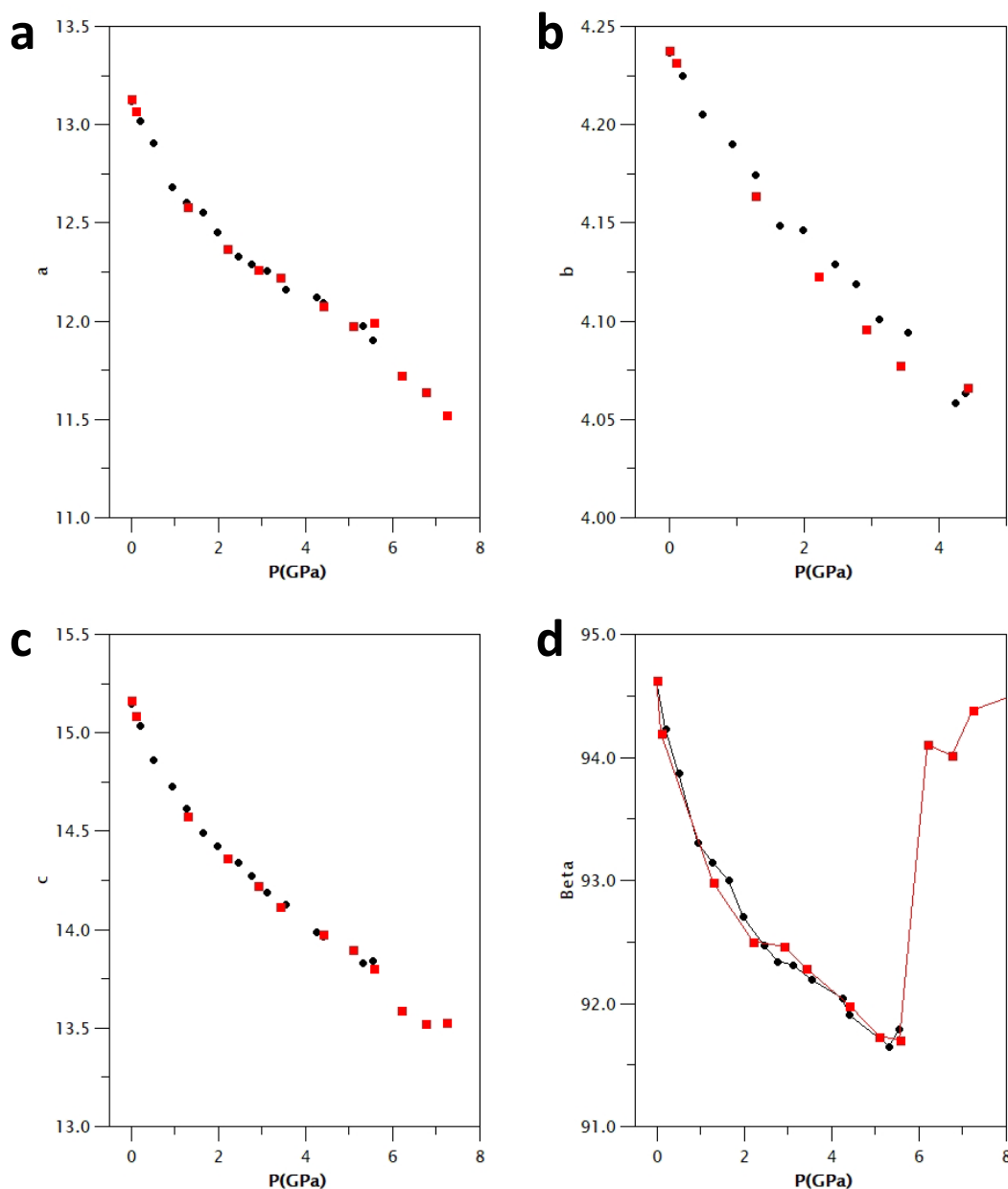


**Figure B10.** Evolution of cell parameters  $a$  (a),  $b$  (b),  $c$  (c) and  $\beta$  (d) with pressure for compound **8a** (black) and **8b** (red). Cell axis distances are expressed in Å; the  $\beta$  angle, in degrees.

**Figures B10 and B11** present the behavior of the cell parameters with pressure. The  $b$ -axis is substantially stiffer than  $a$  and  $c$ -axes. At around 6 GPa we can observe a discontinuity on the evolution of volume with pressure and a leap on the  $\beta$  angle. It is associated with a reversible isosymmetric phase transition, stating as a first order transition where there is no change in the space group.



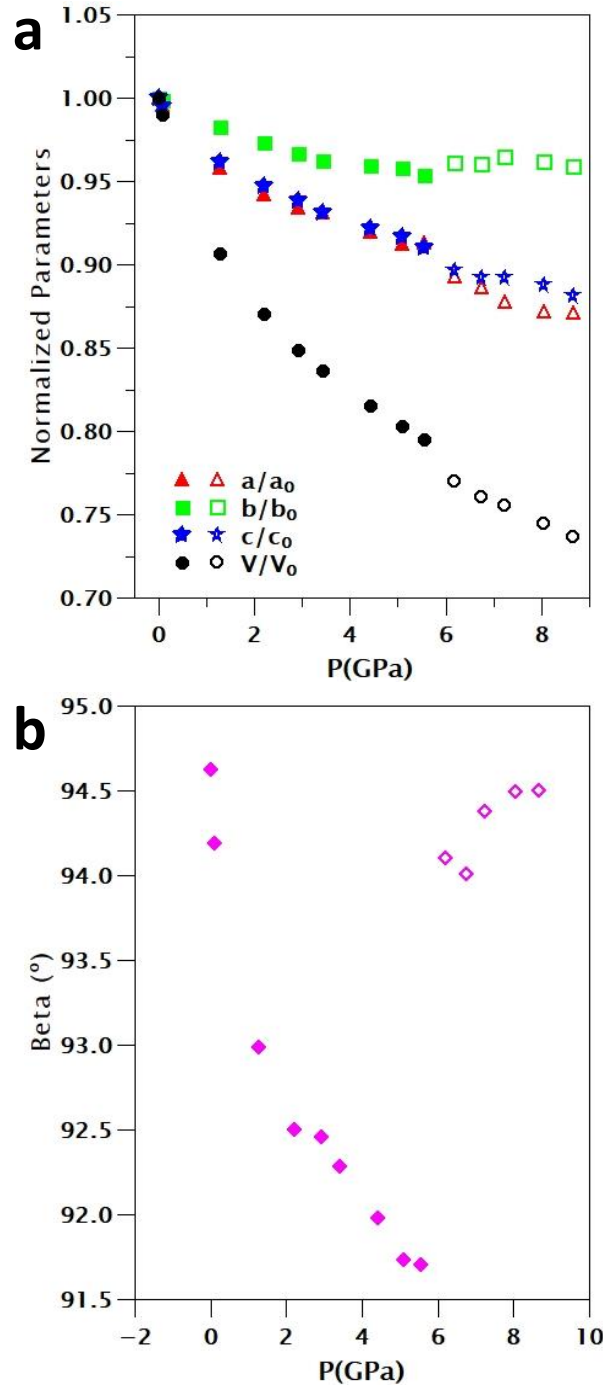


**Figure B11.** Variation of the cell parameters of **8b** with pressure. Error bars are smaller than their respective size symbols. Empty symbols represent the parameter after phase transition.

For equations of state (EoS) calculations we have selected the 3rd-order Birch-Murnaghan (BM) EoS according with the information obtained from the plots of  $V$  unit-cell parameters as normalized pressure ( $F$ ) pressure against finite strain ( $f$ ) (i.e.  $f$ - $F$  plots). The  $f$ - $F$  plots for unit-cell parameters exhibits a curvature at low pressures indicating that values at zero pressure are not strictly consistent with the higher-pressure data. However, comparison of data collected from crystals within the DAC but without

pressure fluid and data from crystals in air, shows that the formal uncertainties obtained for the unit-cell parameters are underestimated, and this accounts for the observed curvature in the  $f$ - $F$  plots.

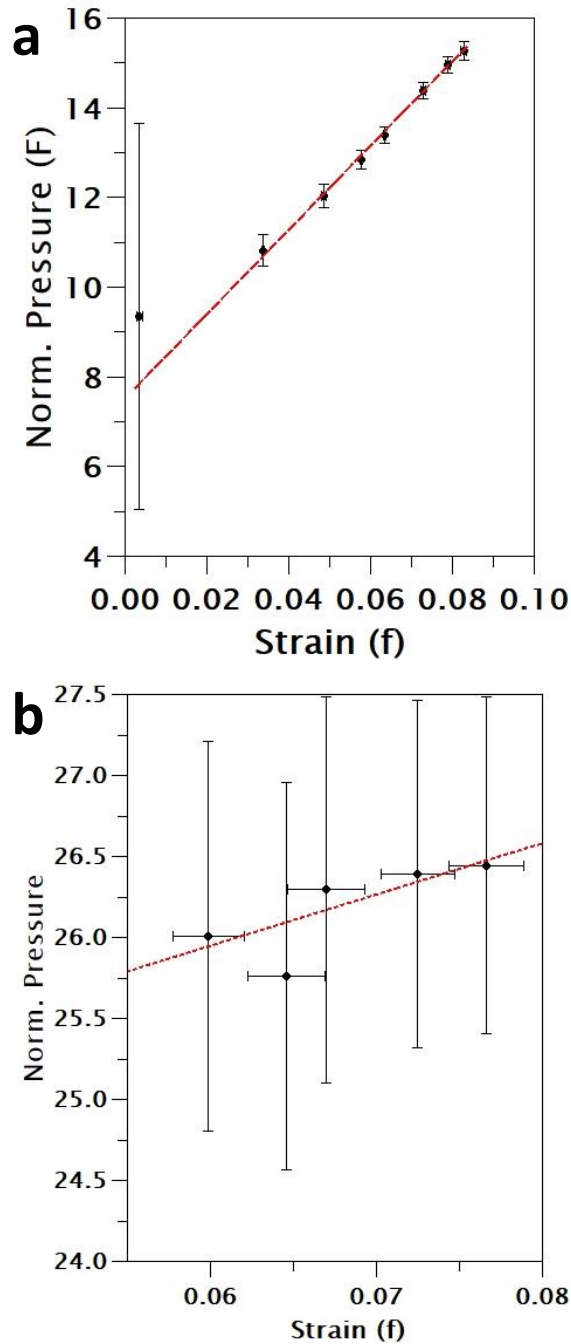


**Figure B12.**  $f$ - $F$  plots for Volume for **8b** before (a) and after phase transition (b).

The fitting procedure was done with the *EosFit7-GUI* program<sup>1-5</sup> using the BM EoS. The refinements of EoS all yield  $w\chi^2 < 1$  because of the over-estimation of the  $\sigma(P)$ , but none of the fits show any systematic variation of  $P_{obs} - P_{calc}$  with pressure, indicating that the reported parameters represent the data well. Lines on **Figure B12** show the fitted EoS models.

The bulk modulus obtained for  $C_5H_3CuINCl_2$  (**8a** and **8b**) before 6 GPa is softer than other similar copper iodide Cu-I ladders that have recently been studied under hydrostatic pressure, including compounds **5** and **6** and the CP described in reference 6. In general, these lower values are attributable to deformability of the intermolecular interactions present in the structure. The situation changes dramatically after 6 GPa where the bulk modulus increases by a factor of 3 (**Figure B13**).

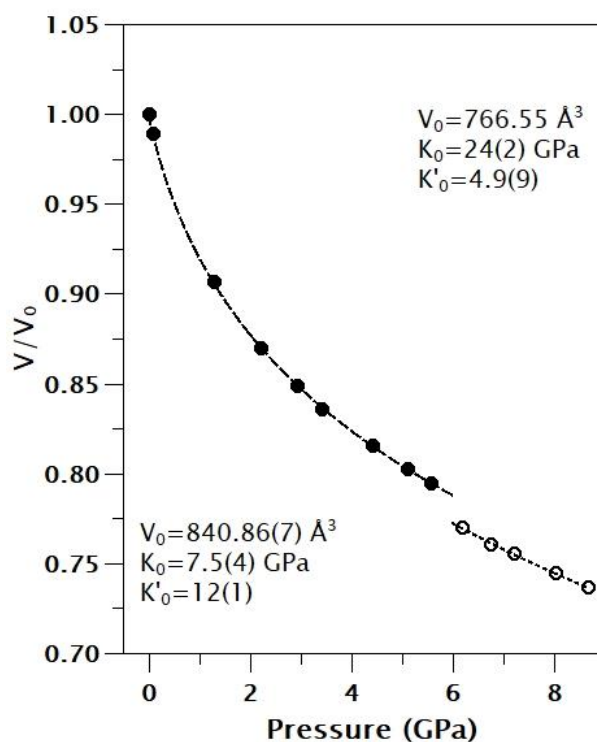


**Figure B13.** *EoS* fitting for **8b** before and after phase transition.

**Figures B14 and B15** present the behavior of the main bond distances and angles with pressure. The evolution of these parameters shows that the main changes produce a slight deformation of the Cu-I ladders. It is clear the different behavior after phase transition of the compound where the pyridine ring suffers a tilting and rotation.

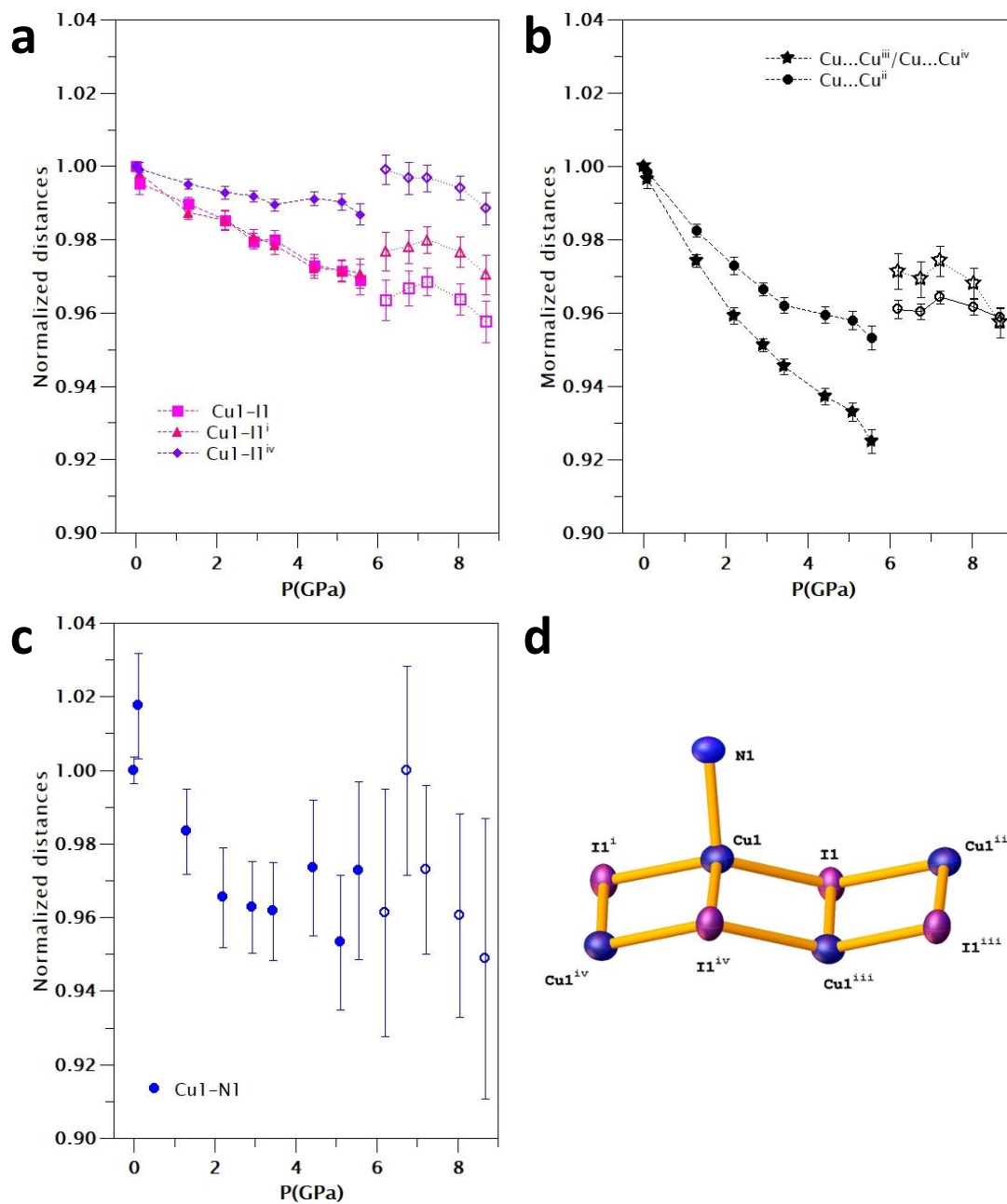


**Figure B14.** (a-c) Variation of the main distances on the Cu-I staircase. Error bars represent the standard for each value. (d) Referential fragment of the Cu-I staircase motif.

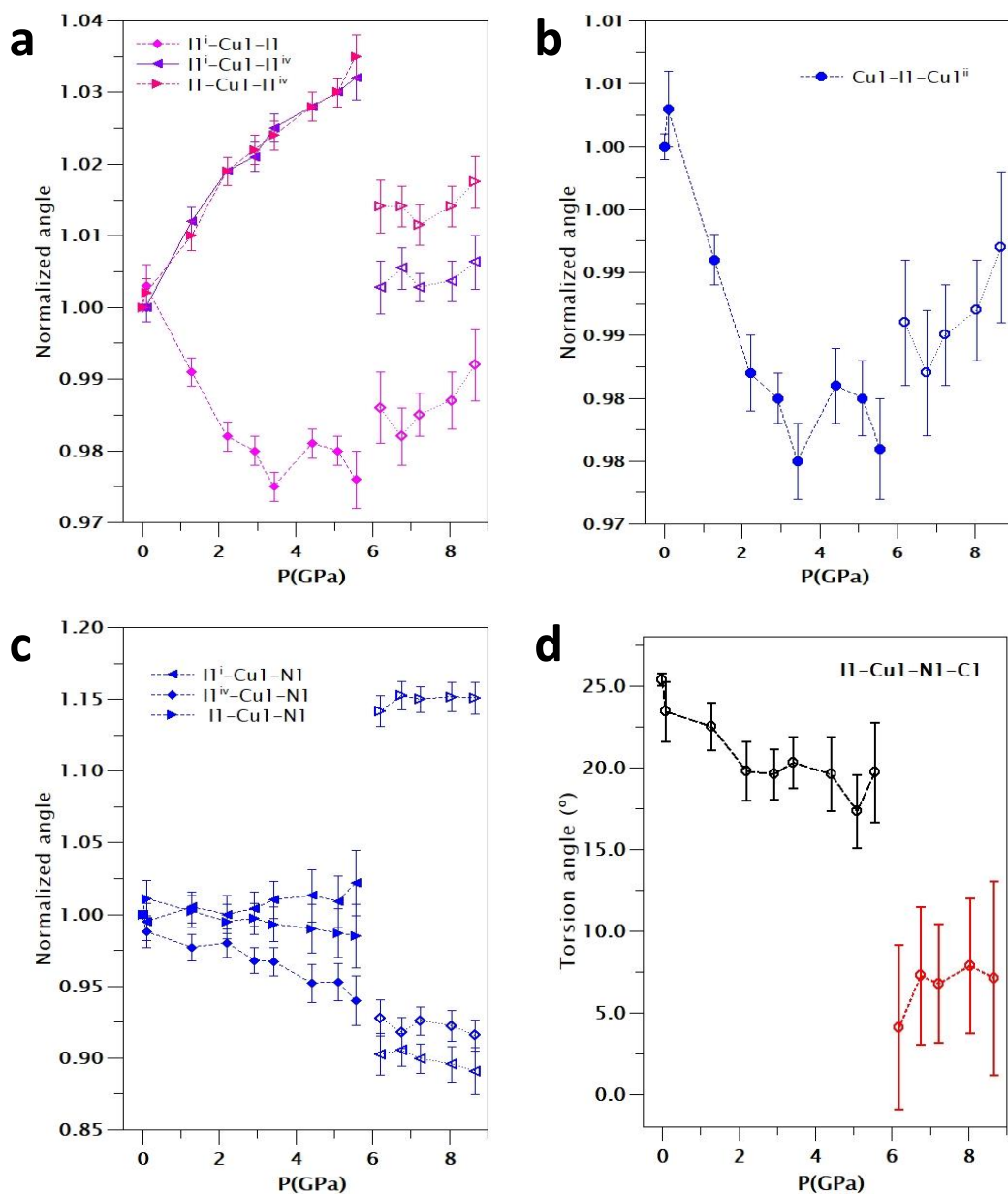


**Figure B15.** Variation of the main angles on the Cu-I ladder. Error bars represent the standard for each value.

The structure presents a weak  $\pi$ - $\pi$  stacked interactions between pyridine rings with Cg...Cg from 4.238(3) to 4.041(16) Å. Also, there is a C4-Cl2...Cg from 3.640(2) Å to 3.210(18) Å that change to 2.84(3) Å. After phase transition appears a C1-H1...Cg weak interaction with C...Cg around 3.25(3) Å (**Figure B16**).<sup>5</sup>

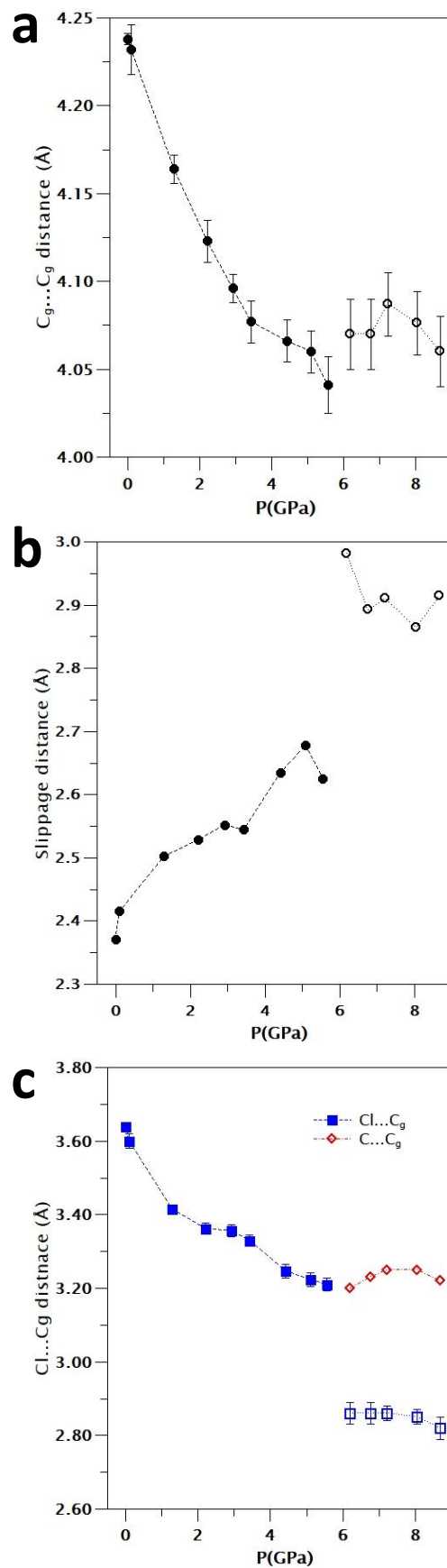


**Figure B16.** Variation of the  $C_g \dots C_g$  distances with pressure.

## References

1. Gonzalez-Platas, J.; Alvaro, M.; Nestola F.; Angel, R. J., *Journal of Applied Crystallography* **2016**, *49*, 1377.
2. Spencer, E. C.; Angel, R. J.; Ross, N. L.; Hanson, B. E.; Howard, J. A. K., *Journal of the American Chemical Society* **2009**, *131*, 4022.
3. Funnell, N. P.; Dawson, A.; Francis, D.; Lennie, A. R.; Marshall, W. G.; Moggach, S. A.; Warren, J. E.; Parsons, S., *CrystEngComm* **2010**, *12*, 2573.
4. Slebodnick, C.; Zhao, J.; Angel, R.; Hanson, B. E.; Song, Y.; Liu, Z.; Hemley, R. J., *Inorganic Chemistry* **2004**, *43*, 5245.
5. Angel, R. J., Win\_Strain program for Strain calculations (<http://www.rossangel.net>), **2015**.
6. Aguirrechú-Comerón, A.; Hernández-Molina, R.; Rodríguez-Hernández, P.; Muñoz, A.; Rodríguez-Mendoza, U. R.; Lavín, V. C.; Angel, R. J.; Gonzalez-Platas, J., *Inorganic Chemistry* **2016**, *55*, 7476.

## Appendix C: PXRD patterns

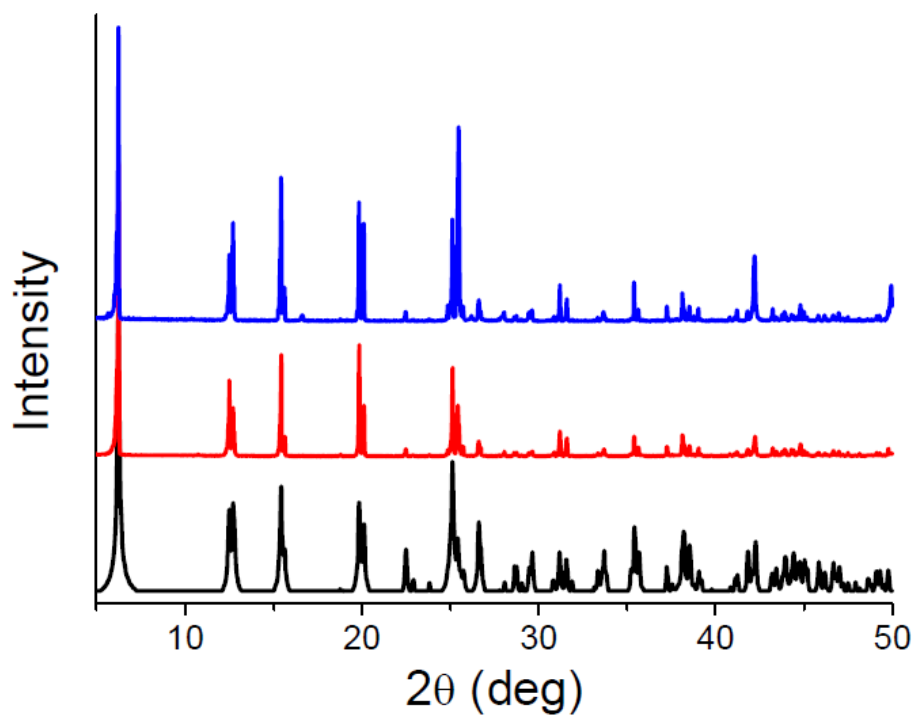


**Figure C1.** Simulated (black) and experimental PXRD patterns of **1** in micro- (red) and sub-microscale (blue).

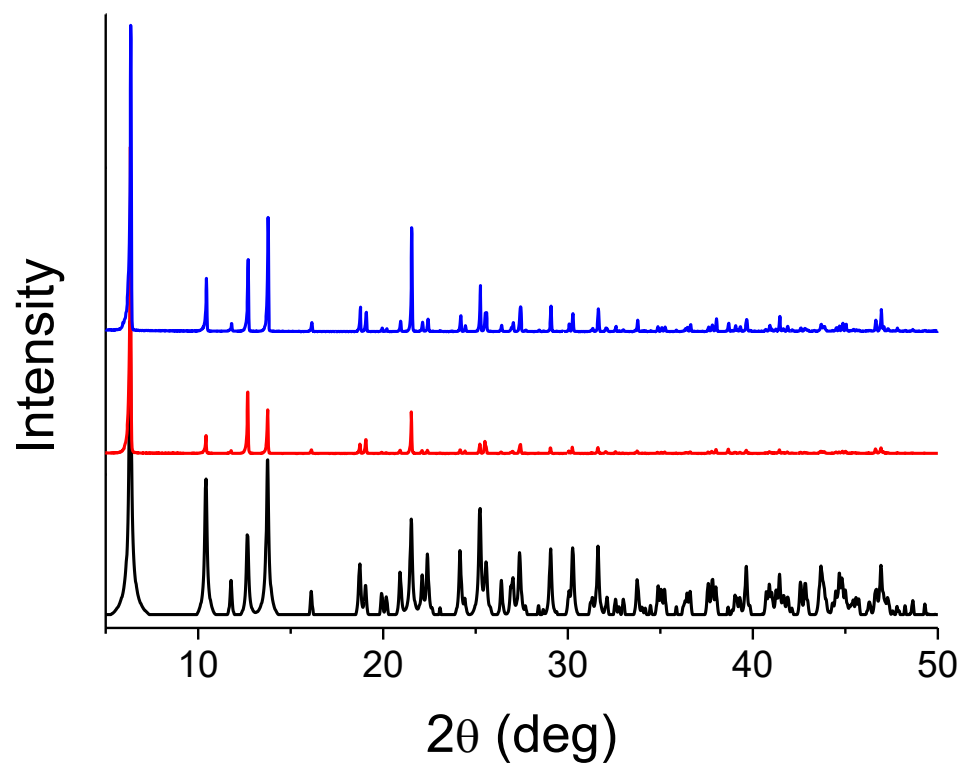


**Figure C2.** Simulated (black) and experimental PXRD patterns of **2** in micro- (red) and sub-microscale (blue).



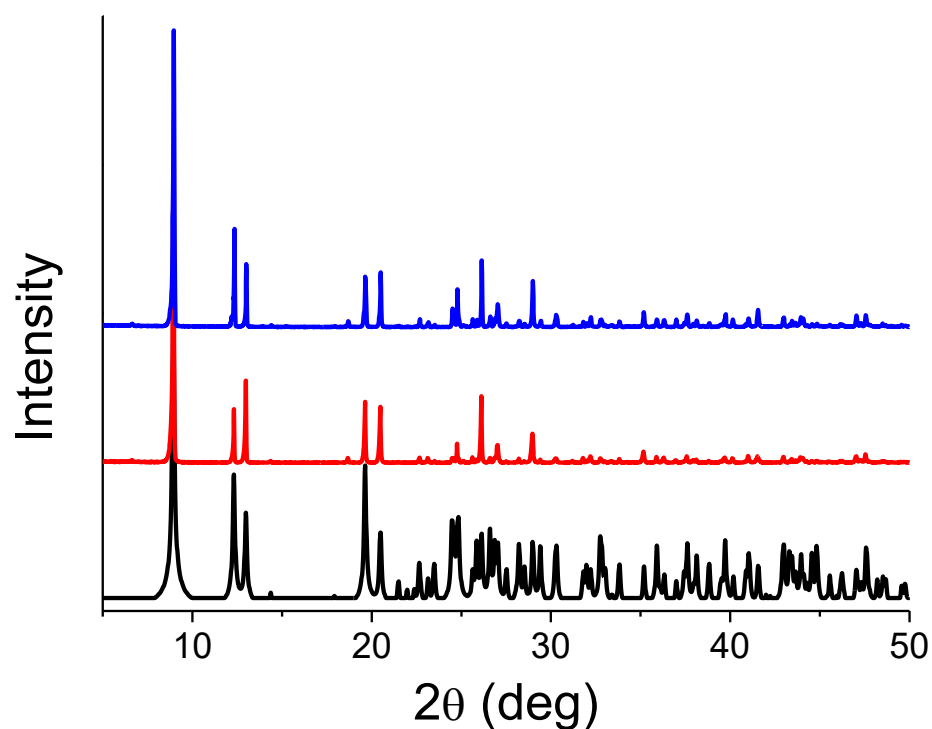


**Figure C3.** Simulated (black) and experimental PXRD patterns of **3** sub-microfibers prepared by magnetic stirring (500 rpm) (red) and sonication in ultrasound bath (1 min) (blue).

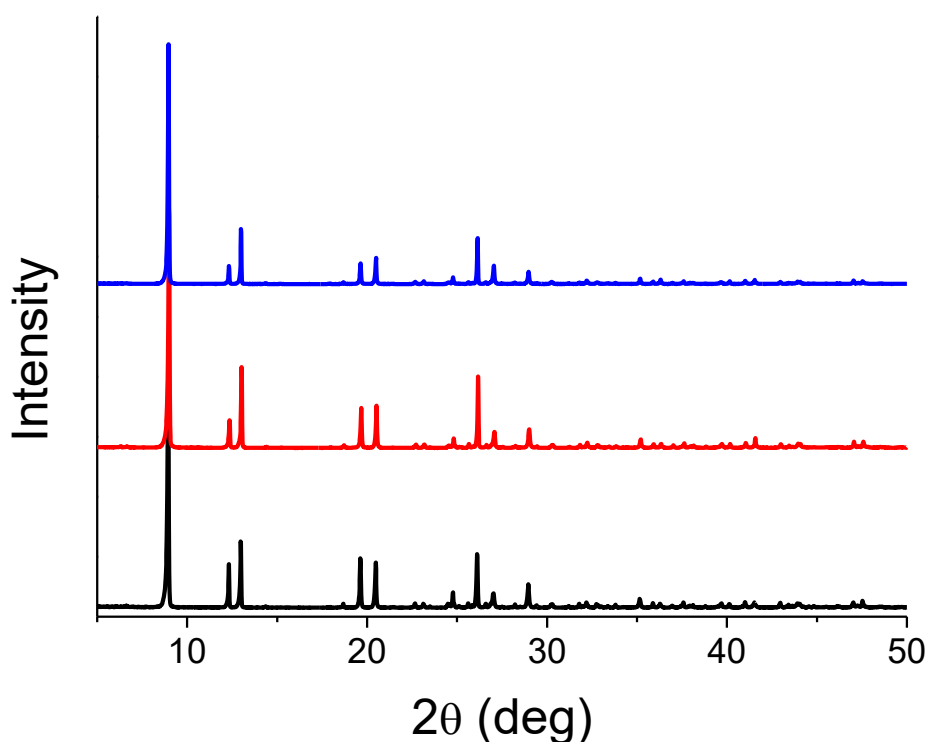


**Figure C4.** Experimental PXRD patterns of **3** submicrofibers: pristine (black), exposed to acetic acid vapors for 72 hours (red) and exposed to acetic acid for 72 hours and heated at 50 °C for 2 hours (blue).

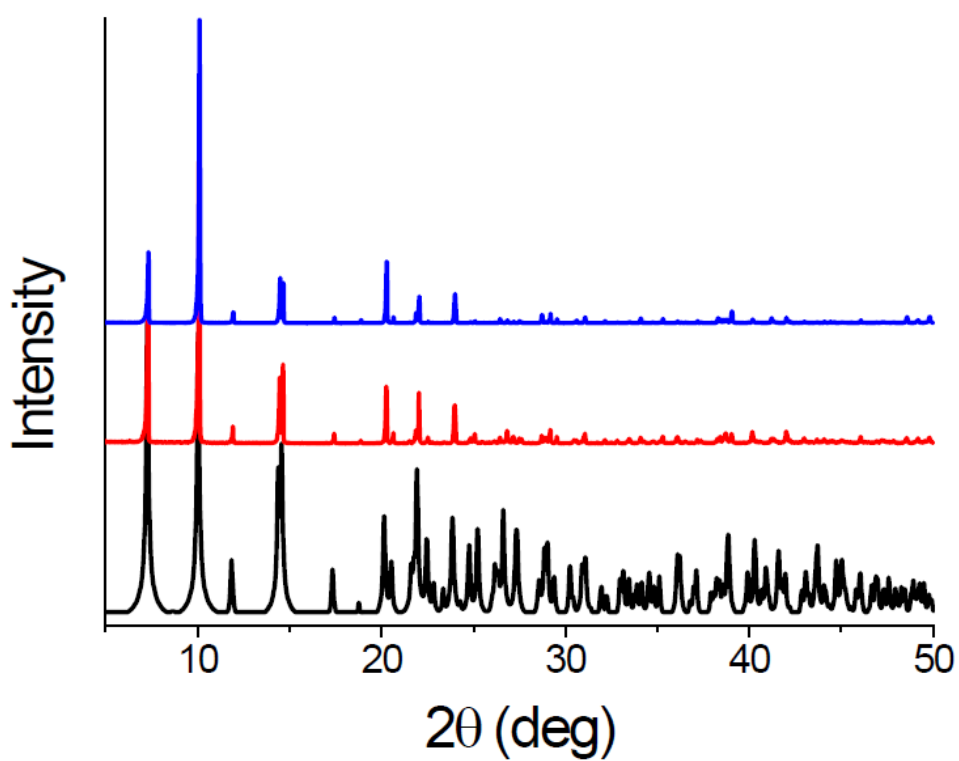


**Figure C5.** Simulated (black) and experimental PXRD patterns of **4** in micro- (red) and nanoscale (blue).

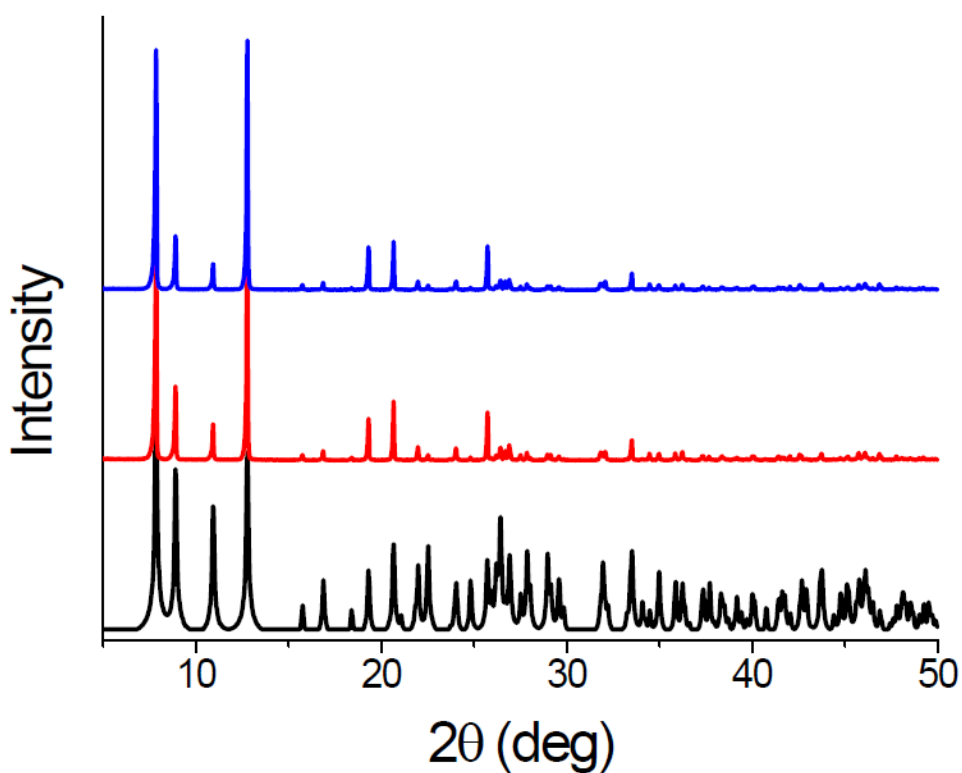


**Figure C6.** Simulated (black) and experimental PXRD patterns of **5** in micro- (red) and nanoscale (blue).

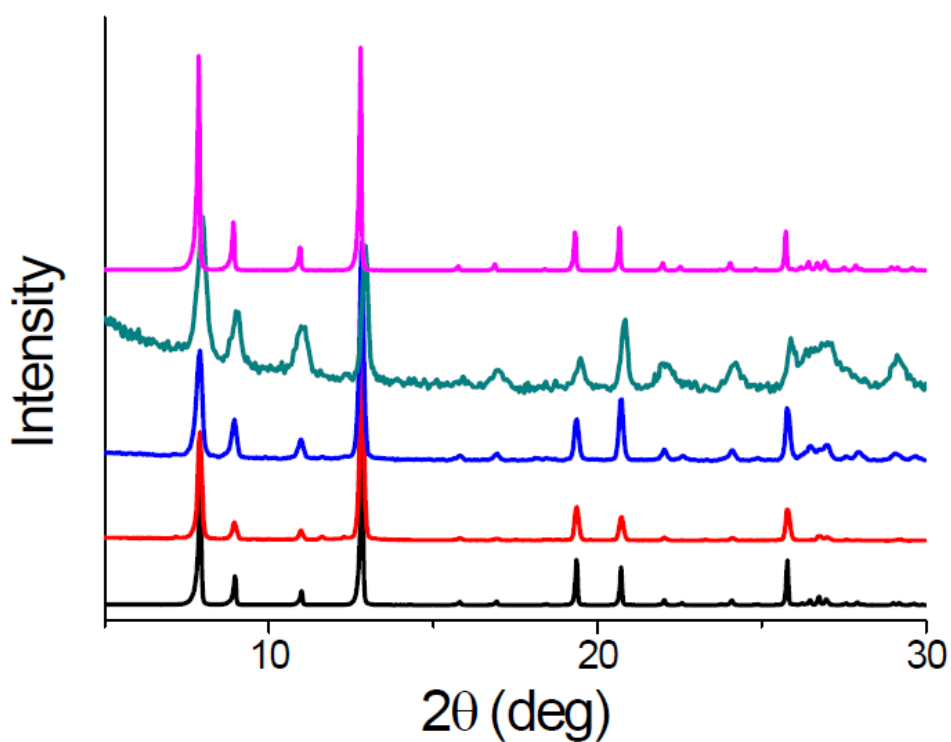


**Figure C7.** Experimental PXRD patterns of **5**: pristine nanofibers (black), pellets prepared at pressures of 1 GPa (red), 3 GPa (blue) and 5 GPa (green), and a ground pellet (pink).

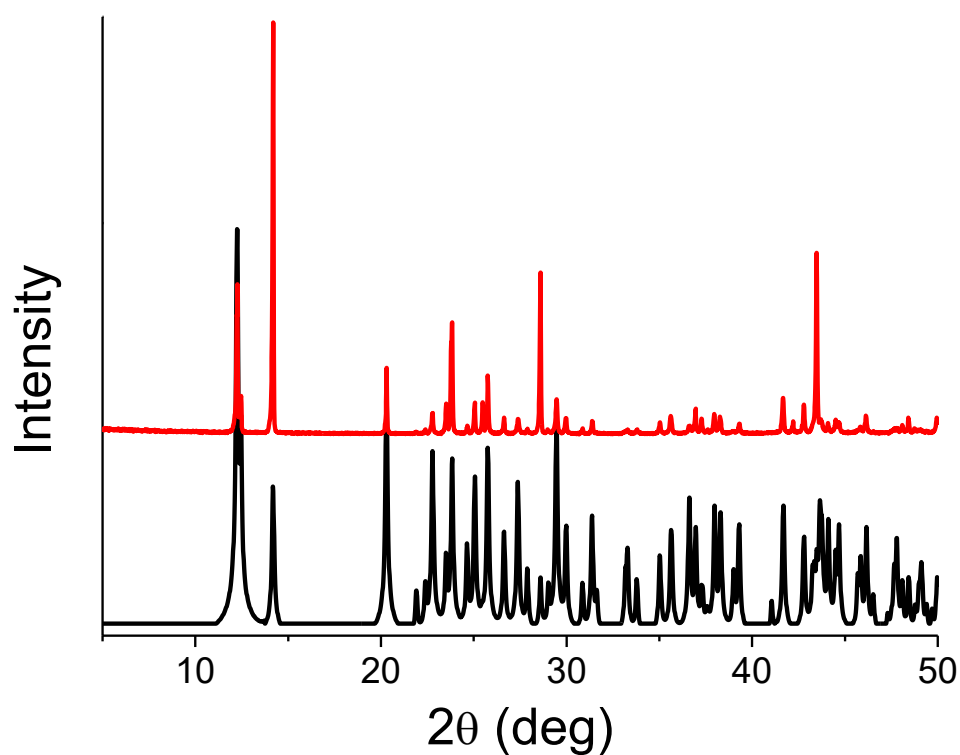


**Figure C8.** Simulated PXRD pattern of **6m** crystals (black) and experimental PXRD pattern of **6n** nanosheets (red; the same pattern is obtained for **6m** crystals).

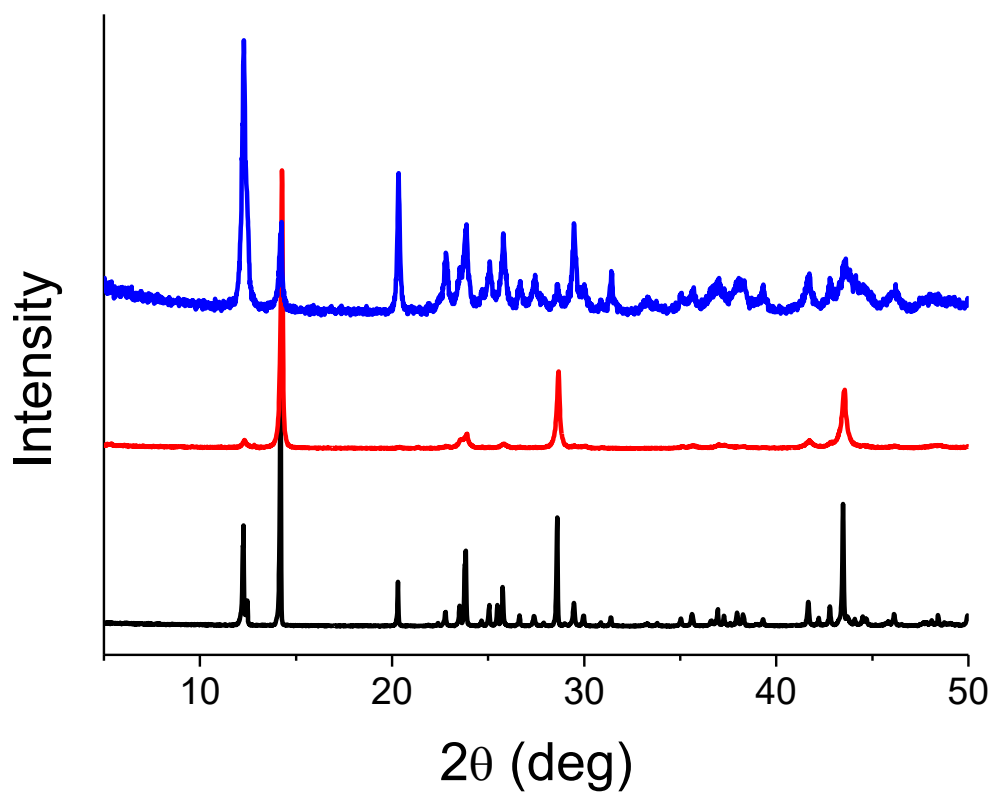


**Figure C9.** Experimental PXRD patterns of **6**: pristine nanosheets (black), a pellet prepared at a pressure of 5 GPa (red), and a ground pellet (blue).

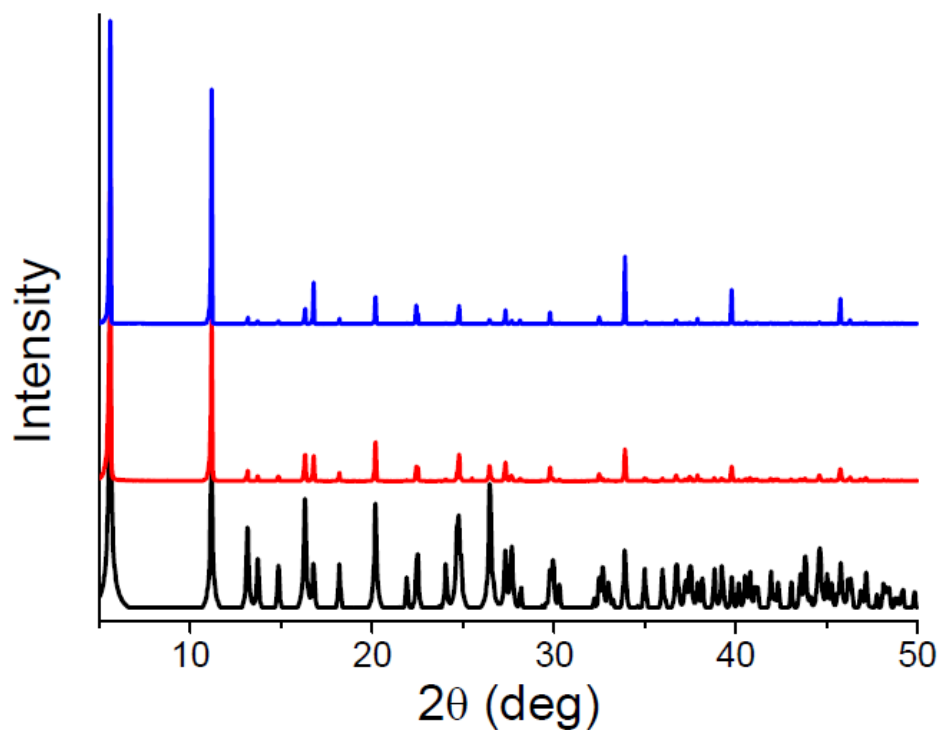


**Figure C10.** Simulated (black) and experimental PXRD patterns of **7** in micro- (red) and sub-microscale (blue).

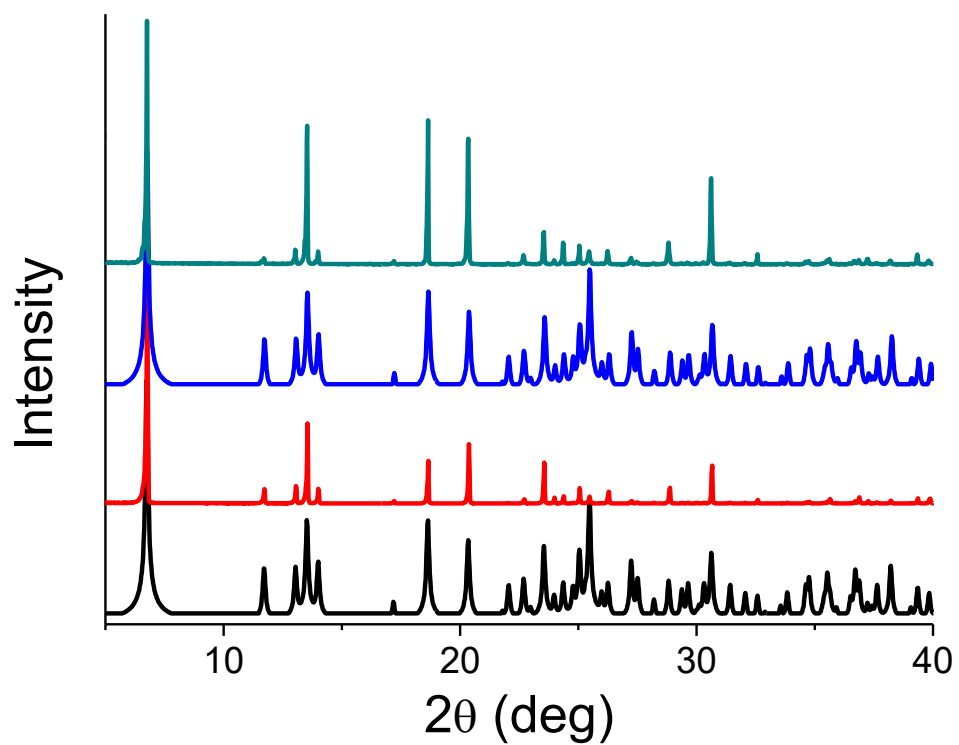


**Figure C11.** PXRD patterns of **8a** (simulated in black, experimental in red) and **8b** (simulated in blue, experimental in green).

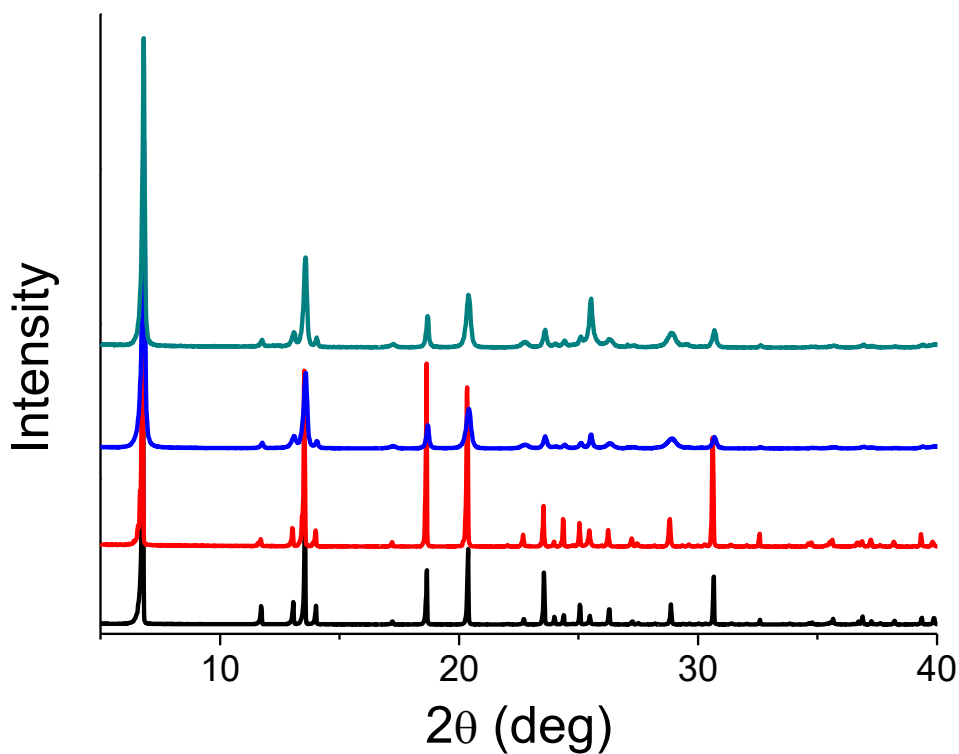


**Figure C12.** PXRD patterns of **8a** and **8b**: pristine solid (**8a** in black, **8b** in red) and pellets pressed at 5 GPa (**8a** in blue, **8b** in green).

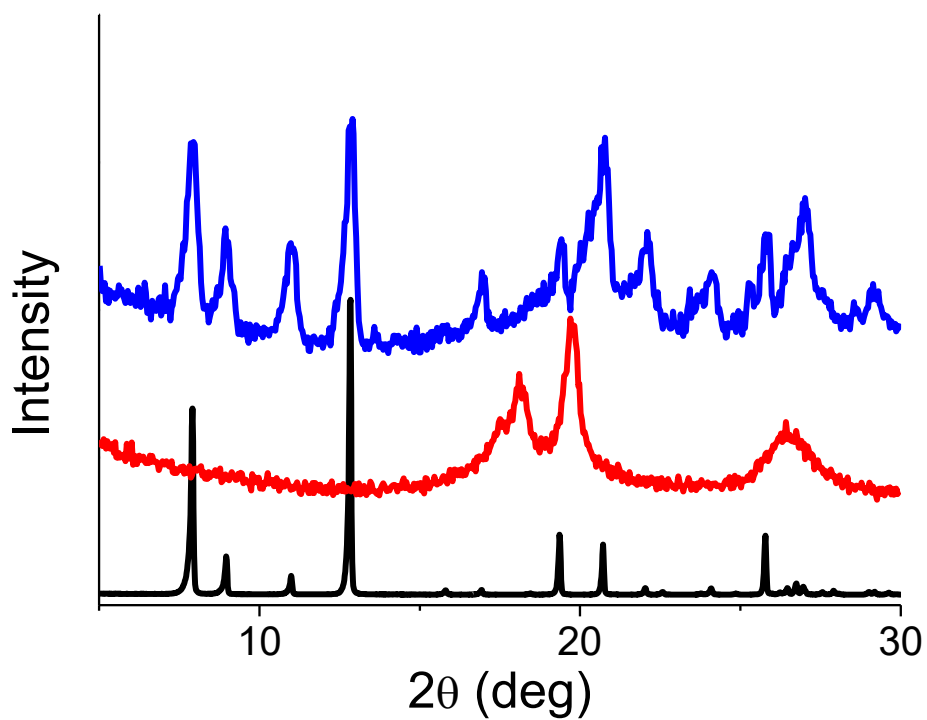


**Figure C13.** PXRD patterns of **5** (black), PVDF (red) and the **5@PVDF** film with 30 % w/w of **5** (blue).

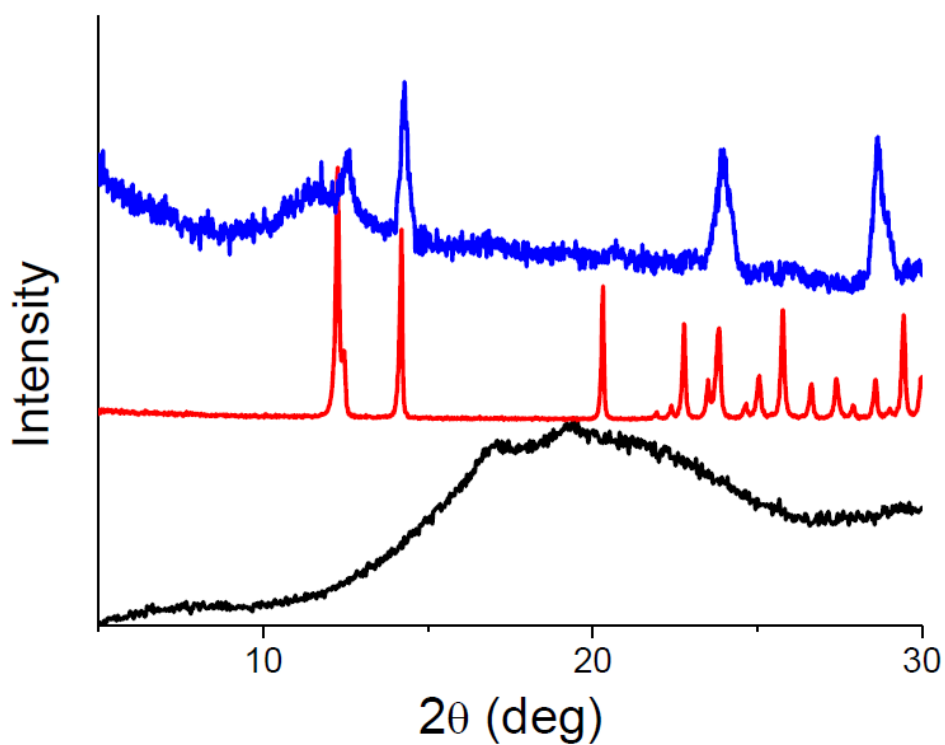


**Figure C14.** PXRD patterns of PLA (black), **6** (red) and the **6@PLA** film with 30 % w/w of **6** (blue).

## Appendix D: TGA analyses

### D1. Pristine CPs

As will be observed in all the figures depicted in this appendix, all the coordination polymers detailed in this thesis decompose following the same mechanism: from 100 to 300 °C, we see a first weight loss which corresponds to the ligand. The second loss, which occurs from 400 to 700 °C, corresponds to iodine and some volatile copper-iodine compounds. This behavior is observed for both micrometric crystals and nanometric fibers of these compounds.

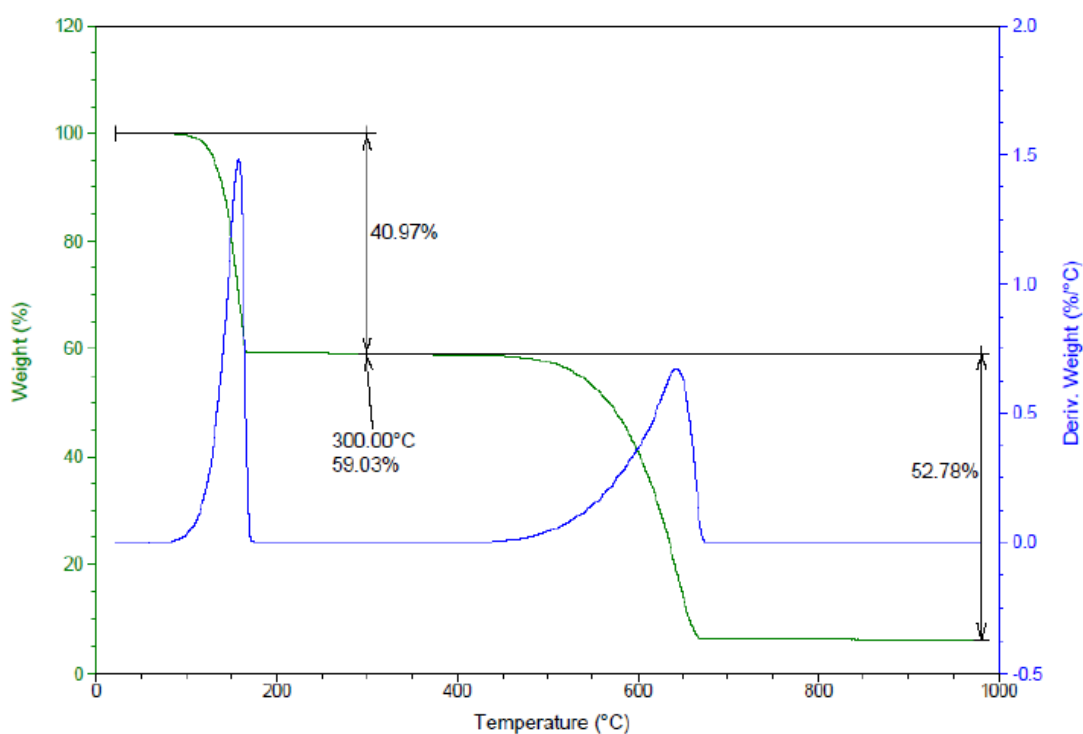


**Figure D1.** Thermogravimetric analysis of compound **4** at a heating rate of 10 Kmin<sup>-1</sup> under a nitrogen flow rate of 90 mL·min<sup>-1</sup>.

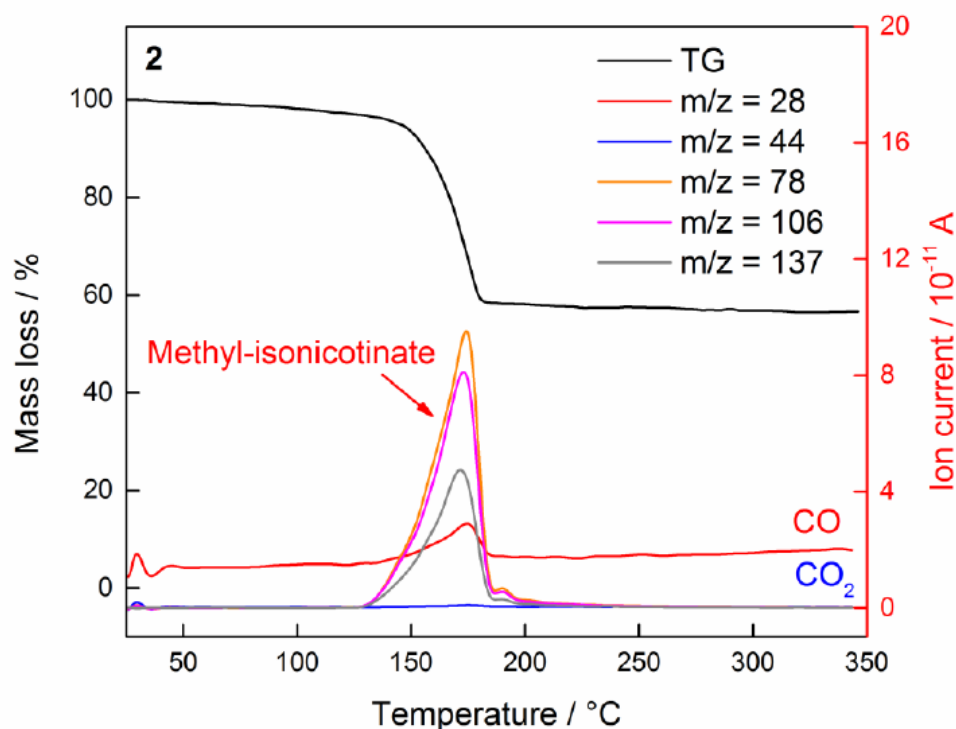


**Figure D2.** TGA-MS analysis of compound **4** using a heating rate of 10 K/min under helium. A continuous release of CO ( $m/z = 28$ ) and  $\text{CO}_2$  ( $m/z = 44$ ) can be detected. The intense peak mass loss takes place at ca. 175 °C. Depicted MS traces can be attributed to the 4-(methoxycarbonyl)pyridine fragments –  $m/z$  (78, 106, and 137).

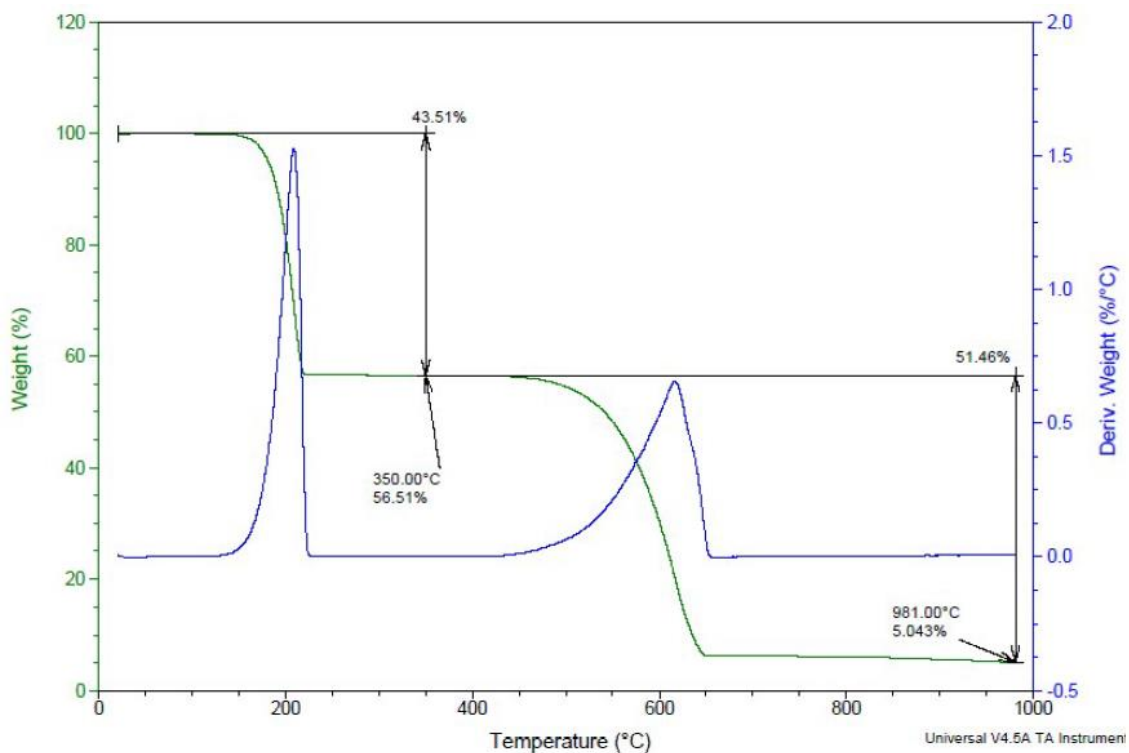


**Figure D3.** Thermogravimetric analysis of compound **5** at a heating rate of 10 Kmin<sup>-1</sup> under a nitrogen flow rate of 90 mL·min<sup>-1</sup>.



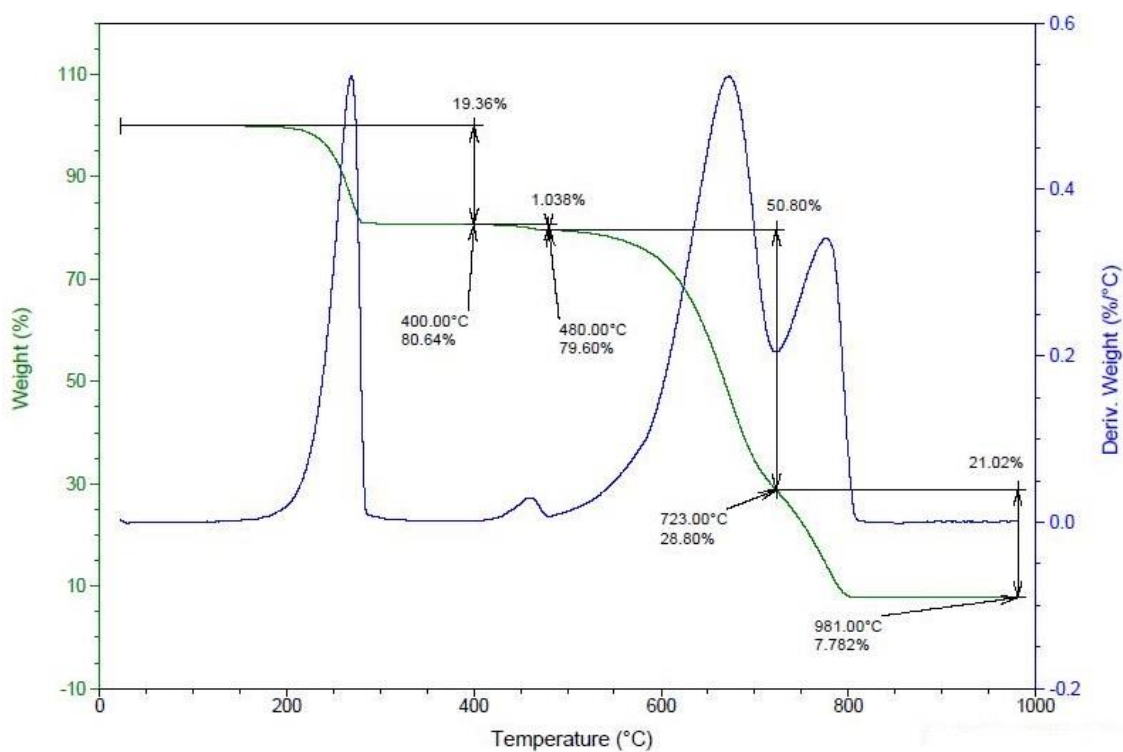


**Figure D4.** Thermogravimetric analysis of compound **6** at a heating rate of 10 Kmin<sup>-1</sup> under a nitrogen flow rate of 90 mL·min<sup>-1</sup>.

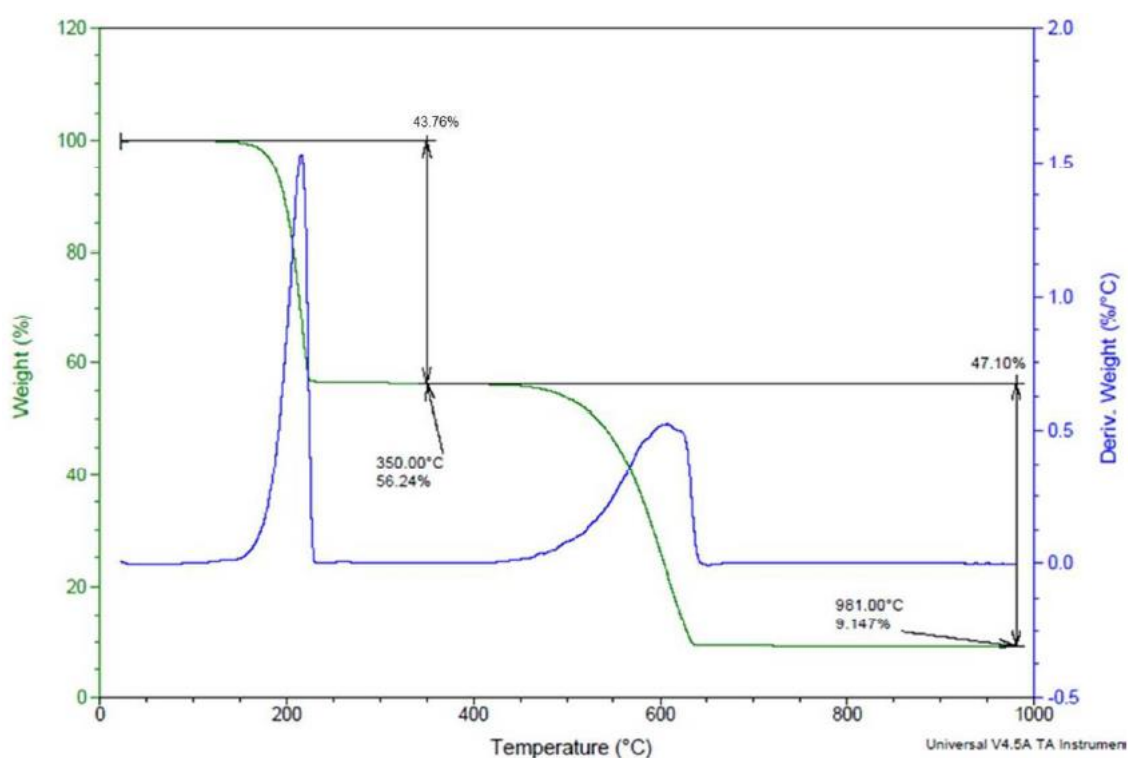


**Figure D5.** Thermogravimetric analysis of compound **7** at a heating rate of 10 Kmin<sup>-1</sup> under a nitrogen flow rate of 90 mL·min<sup>-1</sup>.

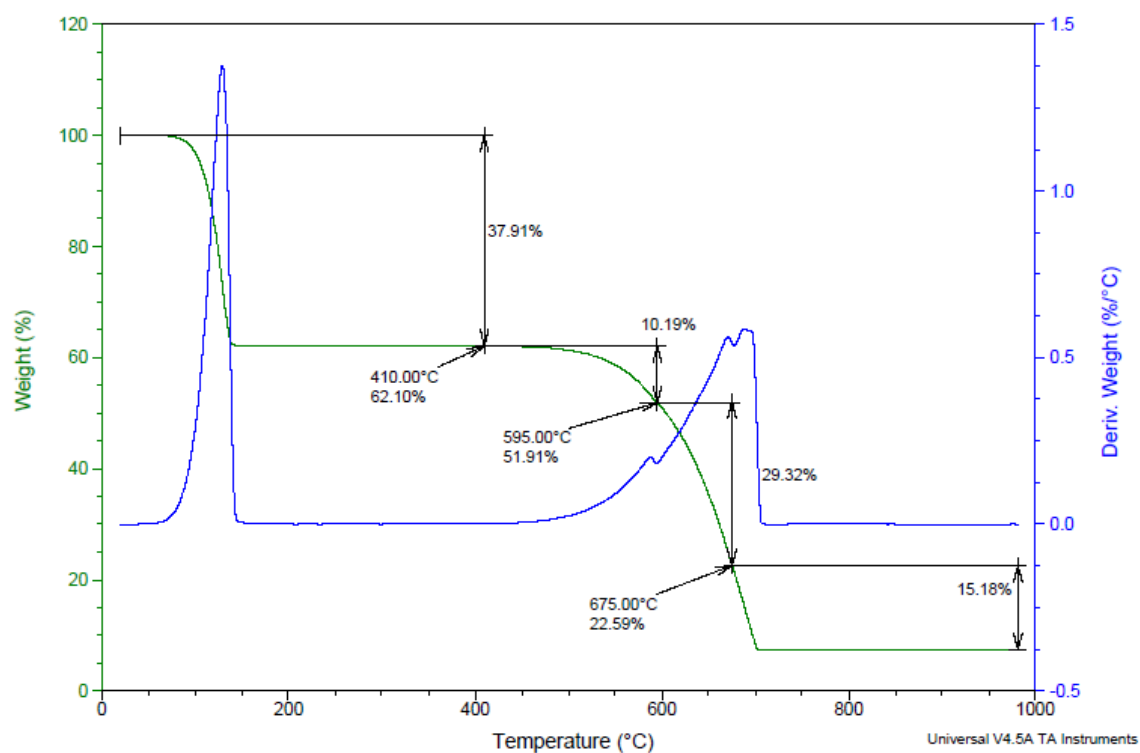


**Figure D6.** Thermogravimetric analysis of compound **8a** at a heating rate of 10 Kmin<sup>-1</sup> under a nitrogen flow rate of 90 mL·min<sup>-1</sup>.

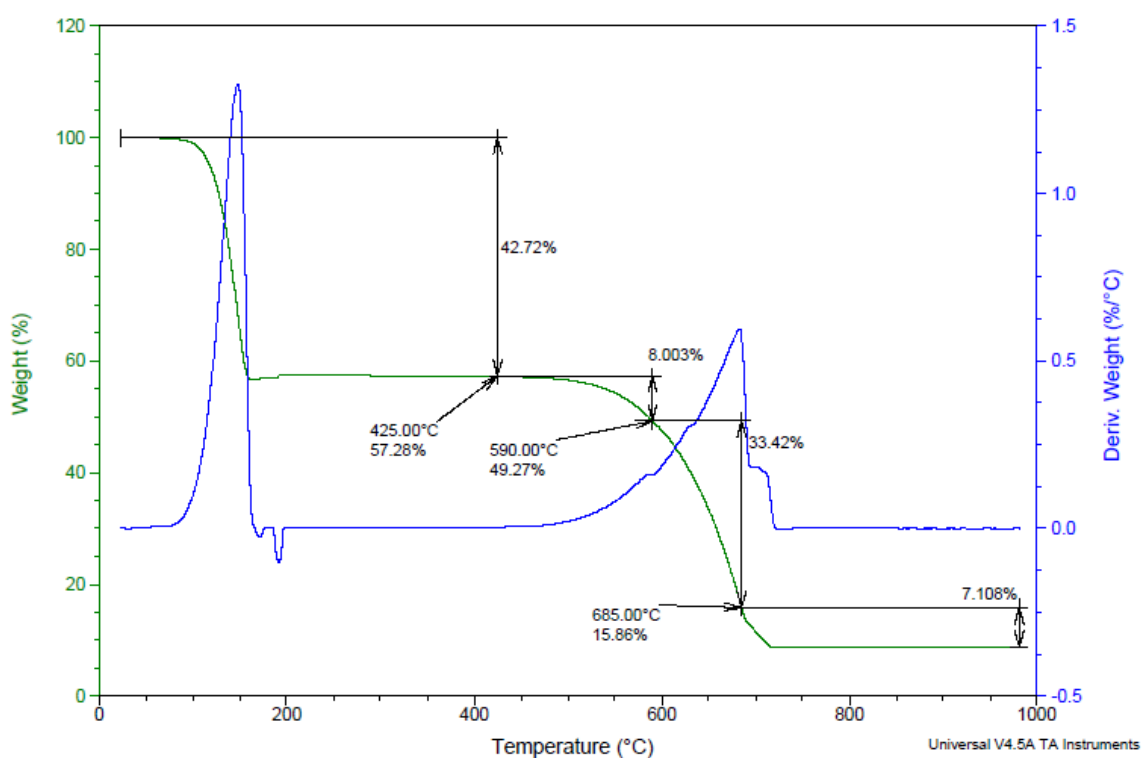


**Figure D7.** Thermogravimetric analysis of compound **8b** at a heating rate of 10 Kmin<sup>-1</sup> under a nitrogen flow rate of 90 mL·min<sup>-1</sup>.

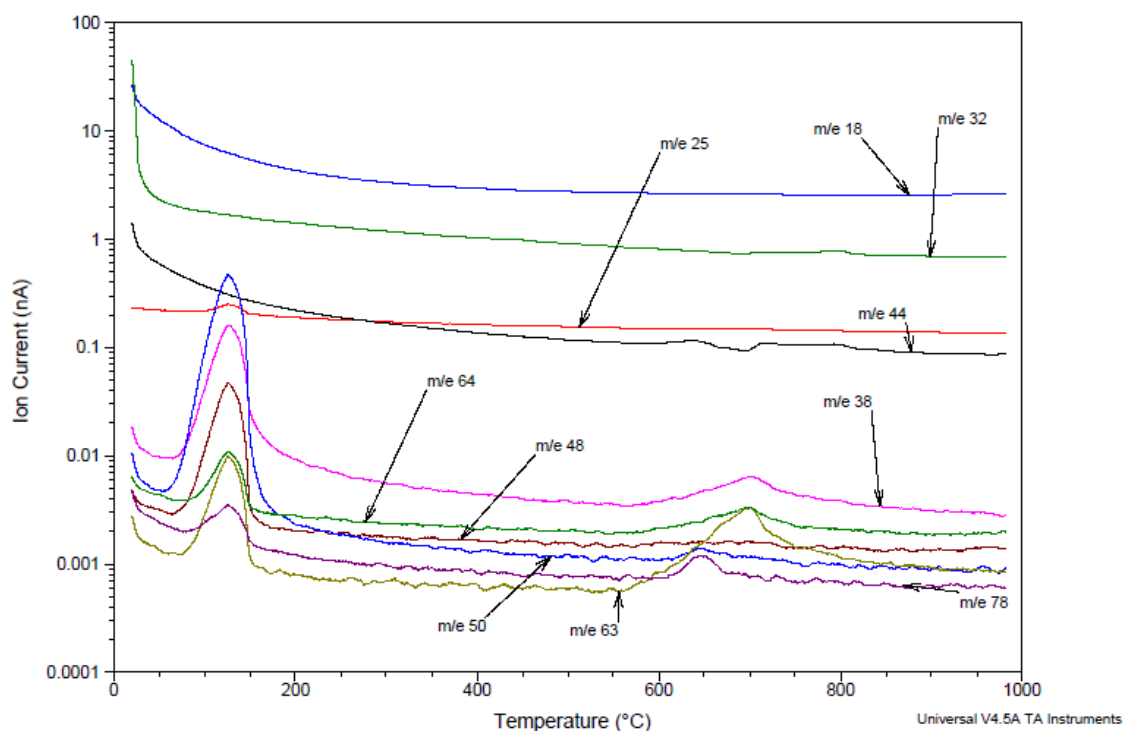


**Figure D8.** TG-MS analysis of compound **8a** at a heating rate of  $10\text{ K}\cdot\text{min}^{-1}$  under a nitrogen flow rate of  $90\text{ mL}\cdot\text{min}^{-1}$ . The ions detected between 80 and 150 °C correspond to different fragments of the 3,5-dichloropyridine ligand.

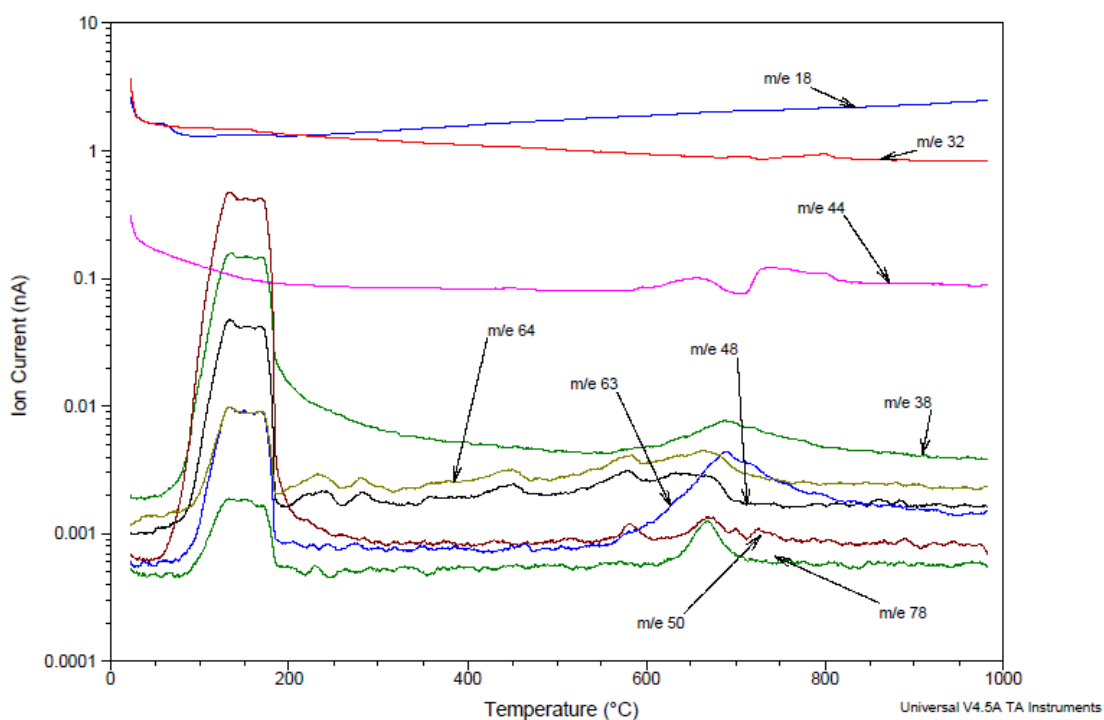


**Figure D9.** TG-MS analysis of crystals of **8b** at a heating rate of  $10\text{ K}\cdot\text{min}^{-1}$  under a nitrogen flow rate of  $90\text{ mL}\cdot\text{min}^{-1}$ . The ions detected between 80 and 150 °C correspond to different fragments of the 3,5-dichloropyridine ligand.

## D2. Composite thin films

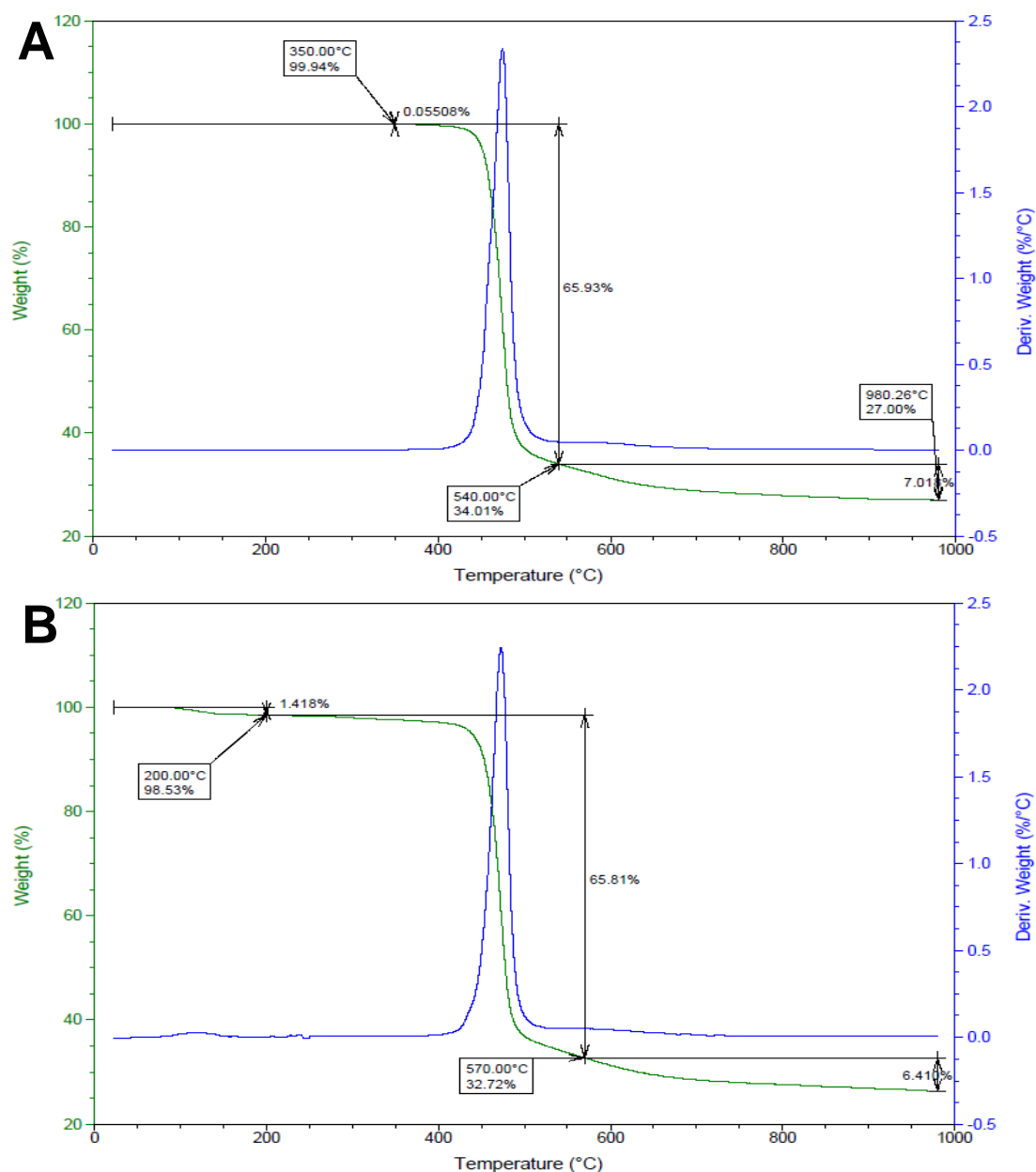


**Figure D10.** Thermogravimetric analysis of PVDF (a) and **5@PVDF** film with 4% w/w of **5** (b), under nitrogen gas with flow rate 90 mL/min and heating rate 10 °C/min. PVDF fully decomposes between 400 and 600 °C; therefore, about 70% of the carbon remains as a residue (100% would suppose 37.5% of the total mass of PVDF). **5@PVDF** films show the decomposition patterns of both **5** (Figure D3) and PVDF.

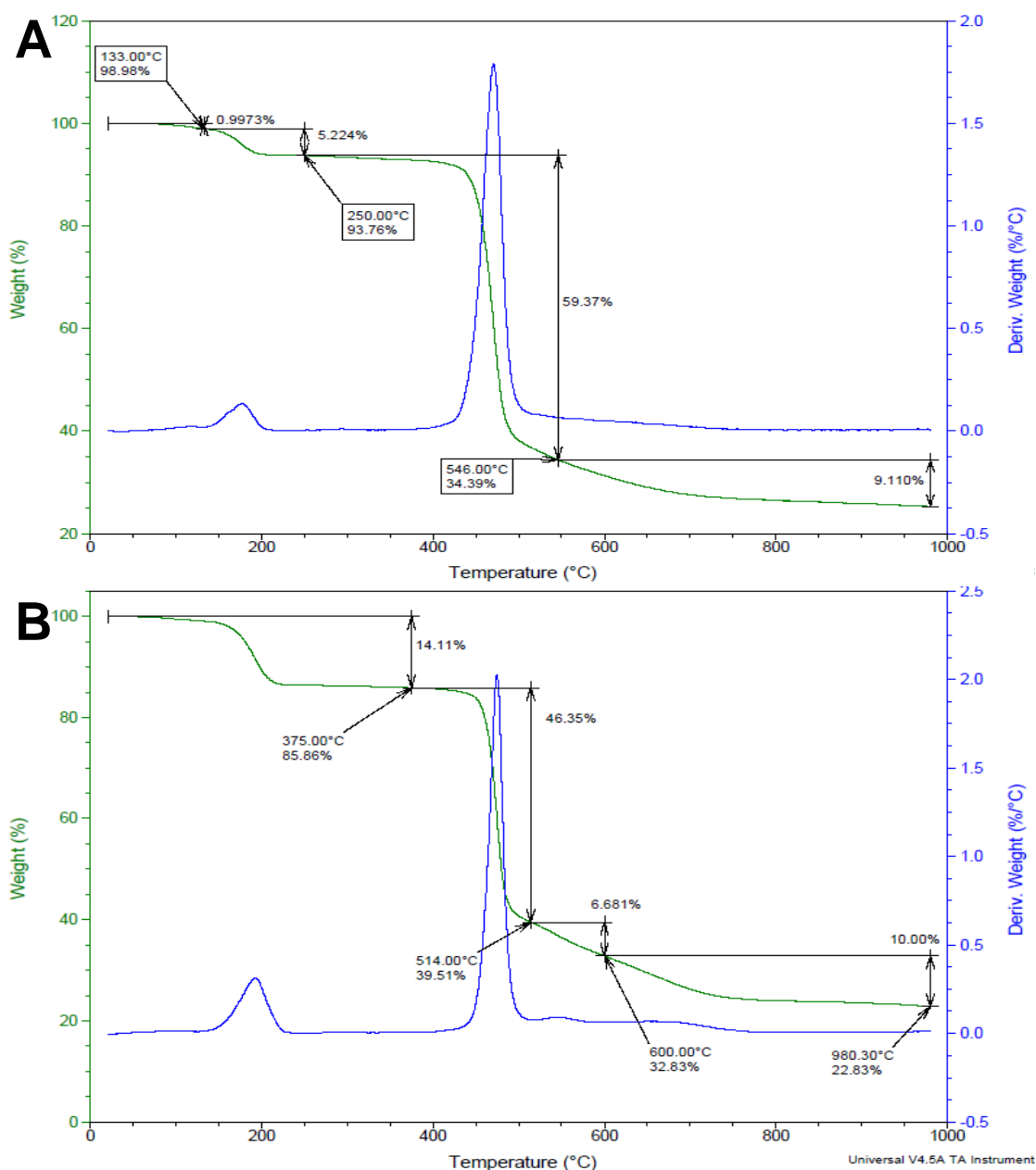


**Figure D11.** Thermogravimetric analysis of **5@PVDF** films with 15% (a) and 30% w/w of **5** (b), under nitrogen gas with flow rate 90 mL/min and heating rate 10 °C/min. PVDF fully decomposes between 400 and 600 °C; therefore, about 70% of the carbon remains as a residue (100% would suppose 37.5% of the total mass of PVDF). **5@PVDF** films show the decomposition patterns of both **5** (Figure D3) and PVDF.

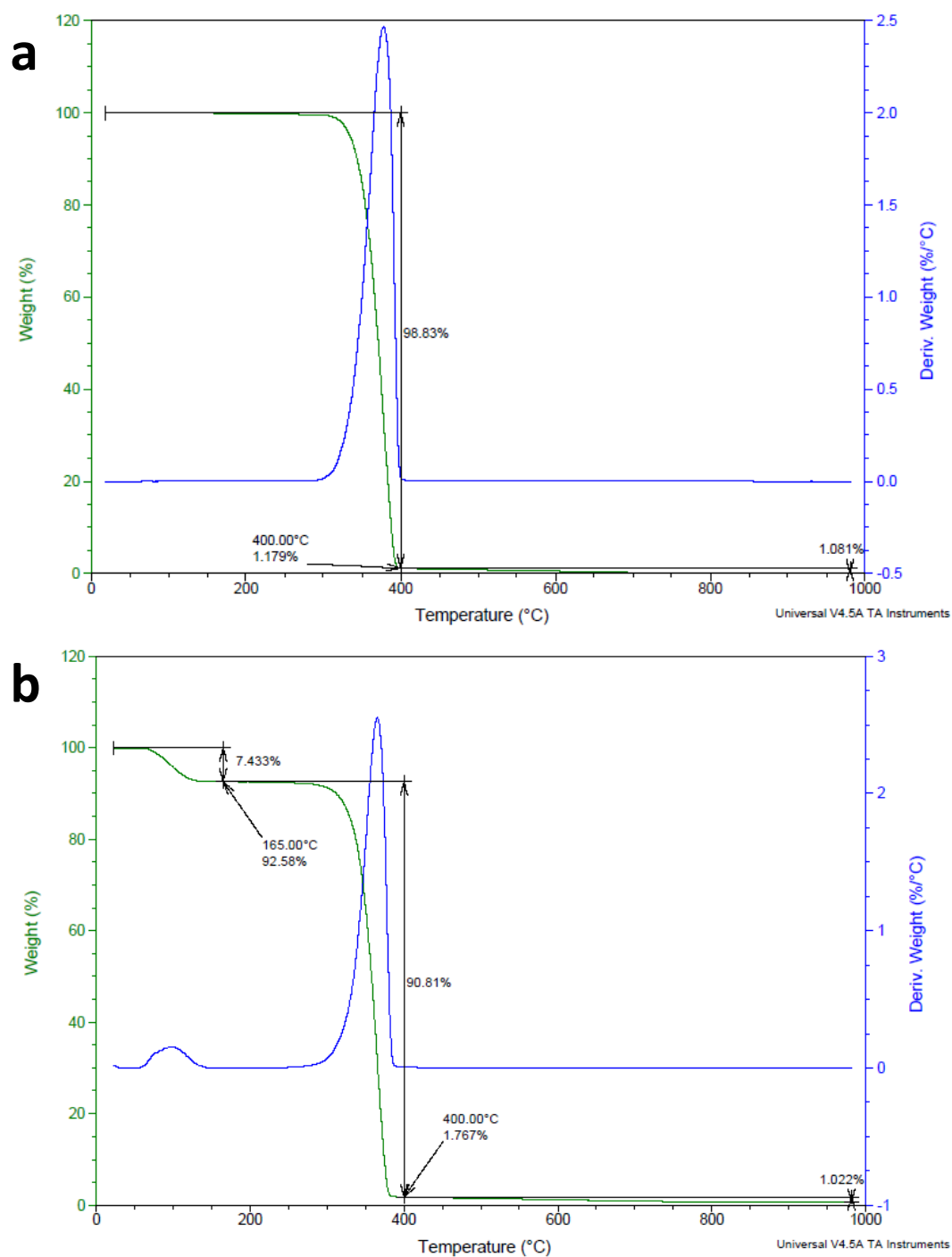


**Figure D12.** Thermogravimetric analysis of PLA (a) and **6@PLA** film with 1% w/w of **6** (b), under nitrogen gas with flow rate 90 mL/min and heating rate 10 °C/min. PLA fully decomposes between 300 and 400 °C, vanishing almost completely when this process is completely. **6@PLA** films show the decomposition patterns of both **6** (Figure D4) and PLA.

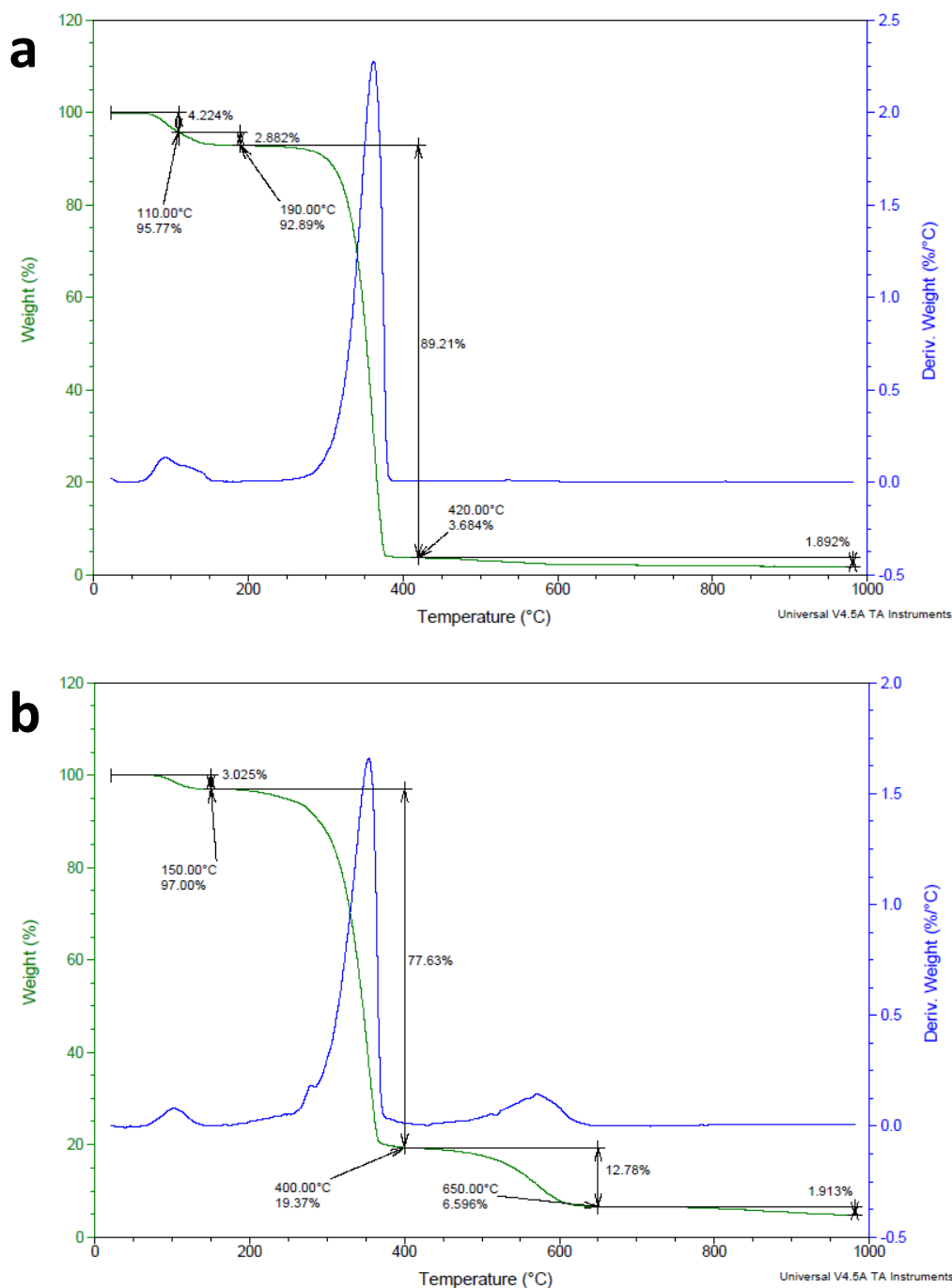


**Figure D13.** Thermogravimetric analysis of **6@PLA** films with 4% (a) and 30% w/w of **6** (b), under nitrogen gas with flow rate 90 mL/min and heating rate 10 °C/min. PLA fully decomposes between 300 and 400 °C, vanishing almost completely when this process is completely. **6@PLA** films show the decomposition patterns of both **6** (Figure D4) and PLA.

## Appendix E: $^1\text{H}$ -RMN studies of compound 8

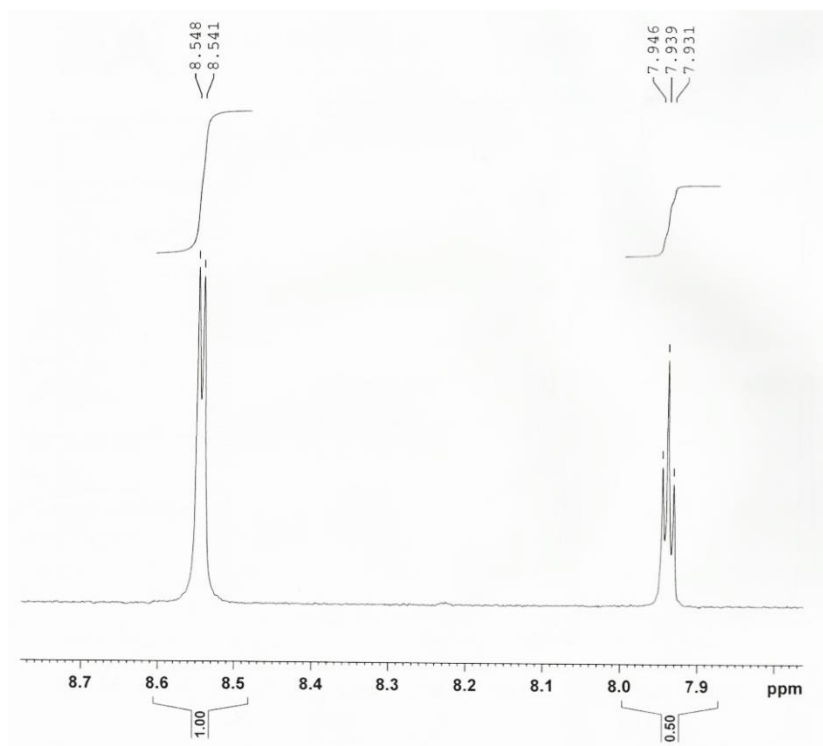


**Figure E1.**  $^1\text{H}$ -NMR spectrum of commercial  $\text{Cl}_2\text{-py}$  in  $\text{CD}_3\text{CN}$ .

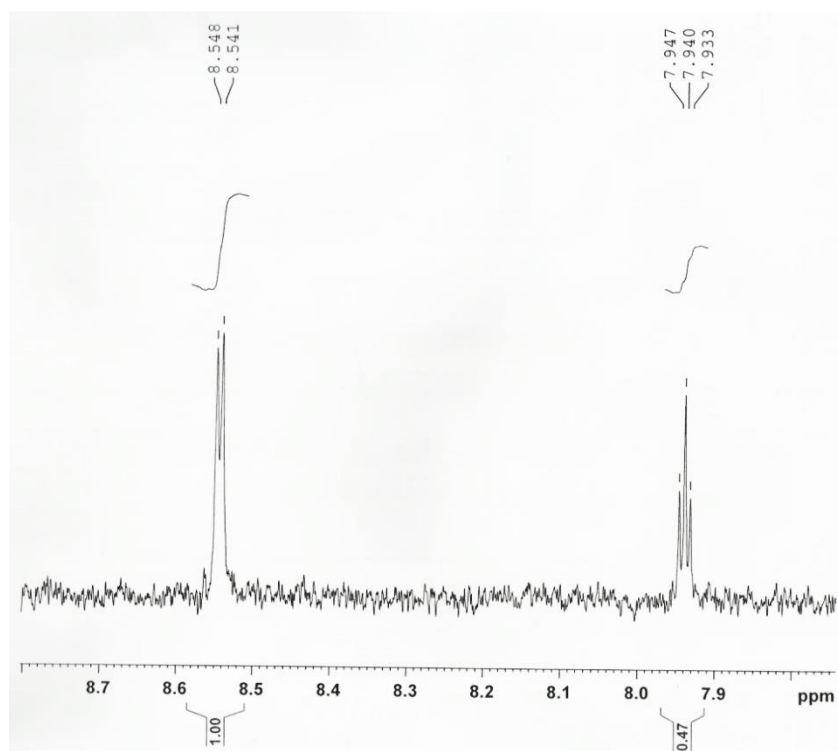


**Figure E2.**  $^1\text{H}$ -NMR spectrum of  $\text{Cl}_2\text{-py}$  treated in solvothermal conditions (acetonitrile, 120 °C, 72 hours) in  $\text{CD}_3\text{CN}$ . The high noise levels are due to a low sample concentration.



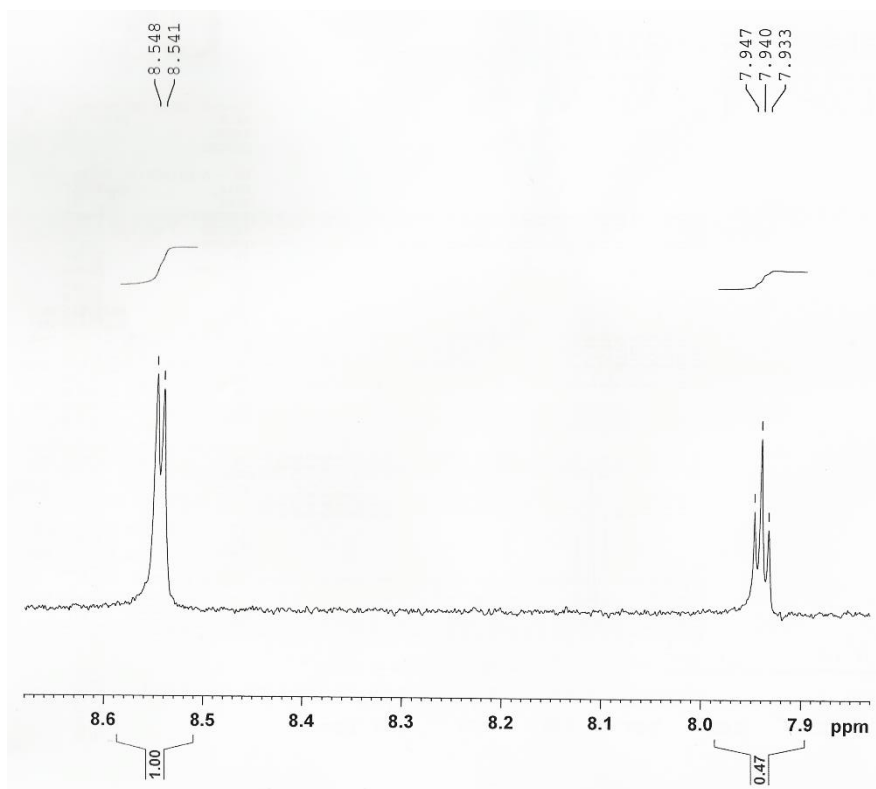


**Figure E3.** <sup>1</sup>H-NMR spectrum of redissolved crystals of **8a** in CD<sub>3</sub>CN.

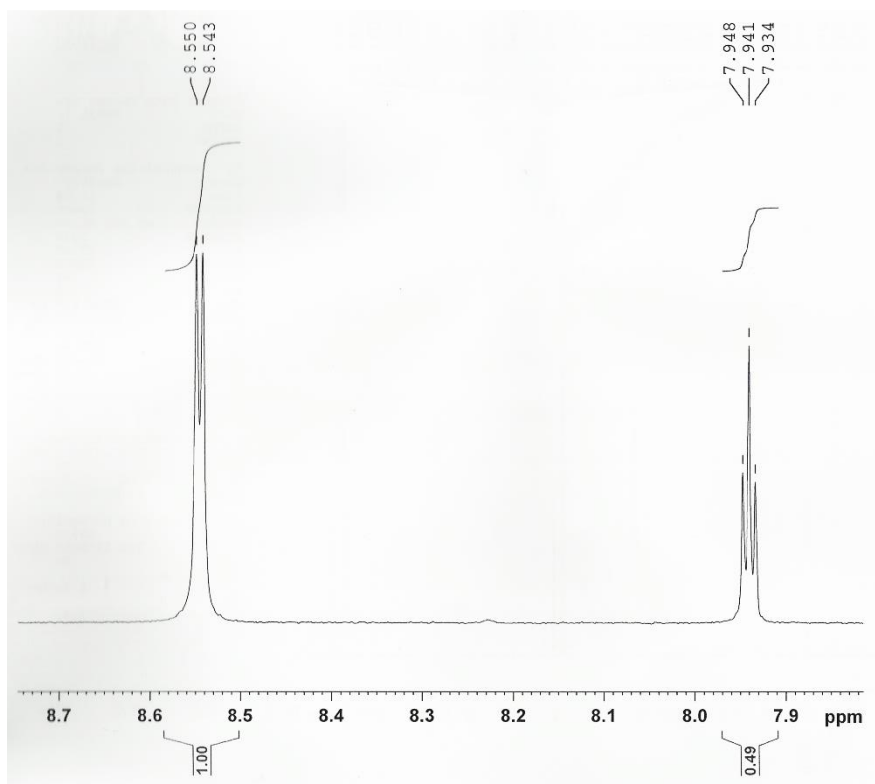


**Figure E4.** <sup>1</sup>H-NMR spectrum of redissolved crystals of **8b** in CD<sub>3</sub>CN.